# Analyse einer mit PbS-Nanopartikeln sensibilisierten Injektionssolarzelle mittels elektrochemischer und frequenzmodulierter Verfahren

## Characterisation of a PbS Nanoparticle sensitized Injection Solar Cell by means of Electrochemical and Frequency-modulated Methods

DISSERTATION

zur Erlangung des akademischen Grades

Doctor rerum naturalium
(Dr. rer. nat.)

vorgelegt

der Fakultät Mathematik und Naturwissenschaften
der Technischen Universität Dresden

von

Dipl. Chem. Susanne Krüger

geboren am 19.01.1983 in Cottbus

Eingereicht am 23.09.2011

Die Dissertation wurde in der Zeit von
August 2007 bis September 2011
in der Fachrichtung für Chemie und Lebensmittelchemie angefertigt

‘Science never solves a problem without creating ten more.’

George Bernard Shaw

# Contents

# List of Abbreviations

| | |
|---|---|
| ac | alternating current |
| Ag/AgCl | silver/silver chlorid electrode |
| $C_3$ | alkyl chain with 3 carbons, $-CH_2-CH_2-CH_2-$, annologous $C_6+C_{12}$ |
| CA | chronoamperometry |
| CB | conduction band |
| $Cd_3P_2$ | cadmium phosphide |
| CdS | cadmium sulfide |
| CdSe | cadmium selenide |
| CdTe | cadmium telluride |
| CE | counter electrode |
| CPE | constant phase element |
| CS | charge separation |
| CTRW | continuous-time random walk |
| CV | cyclic voltammetry |
| dc | direct current |
| DCM | dichloromethane |
| DSSC | dye sensitised solar cell |
| E | electrolyte |
| $e^-$ | electron, negative charge |
| EIS | electrochemical impedance spectroscopy |
| EY | eosin Y |
| FF | fill factor |
| FTIR | fourier transform infrared spectroscopy |
| FTO | flour tin oxide, flourine doped tin oxide |
| $h^+$ | hole, positive charge |

| | |
|---|---|
| HDT | 1,6-hexandithiol |
| HOMO | highest occupied molecular orbital |
| ICP-OES | inductively coupled plasma-optical emission spectrometry |
| IMPS | intensity modulated photocurrent spectroscopy |
| IMVS | intensity modulated photovoltage spectroscopy |
| InAs | indium arsenide |
| IPCE | incident photon to current conversion efficiency |
| IQE | internal quantum efficiency |
| IRM | interference reflection microscopy |
| ISC | injection solar cells |
| ITO | indium tin oxide, tin doped indium oxide |
| LCAO | linear combination of atomic orbitals |
| LED | light-emitting diode |
| LSV | linear sweep voltammetry |
| LUMO | lowest unoccupied molecular orbital |
| MA | oxalic acid |
| MEG | multiple exciton generation |
| MO | metal oxide |
| MPA | 3-mercaptopropionic acid |
| MPTMS | 3-(mercaptopropyl)trimethoxylsilane |
| MT | multiple trapping |
| MX | metal chalcogenides |
| $Na_2SO_3$ | sodium sulfite |
| $NaClO_4$ | sodium perclorate |
| NC | nanocrystall |
| NEXAFS | near edge X-ray absorption fine structure |
| NIR | near infrared |
| NP | nanoparticle |
| OA | oxalic acid |
| ocp | open circuit potential |
| OLED | organic light emitting diode |
| OTE | optically transparent electrode |
| Ox | oxidized species |

| | |
|---|---|
| PbS | lead sulfide |
| PbSe | lead selenide |
| PbTe | lead telluride |
| PD | photo diode |
| PS | polystyrene |
| QD | quantum dot |
| QDSSC | quantum dot sensitised solar cell |
| Red | reduced species |
| RVS | residual volume structure |
| scr | space charge region |
| SEM | scanning electron microscope |
| ShS | shell structure |
| SkS | skeleton structure |
| SR | sheet resistance |
| STC | standard test conditions |
| STM | scanning tunnelling microscopy |
| TAA | thioacetic acid |
| TCE | tetrachlorethylene |
| TCO | transparent conducting oxide |
| TEM | transmission electron microscopy |
| TGA | thioglycolic acid |
| THF | tetrahydrofuran |
| $TiO_2$ | titanium dioxide |
| $TiO_{2inv}$ | titan dioxide structured as inverse opal |
| TSC | thermally stimulated current |
| UPS | ultraviolet photoelectron spectroscopy |
| UV | ultraviolet |
| VASRA | variable angle specular reflectance accessory |
| VB | valence band |
| X-ray | Röntgen radiation |
| XPS | X-ray photoelectron spectroscopy |
| XRD | X-ray diffraction |

# Legend of Symbols

| **Symbols** | **Units** | **Explanation** |
|---|---|---|
| A | | constant |
| B | | constant |
| c | [m/s] | speed of the light in the vacuum [meter per second] |
| C | [F] | capacitance [Farad] |
| $C_{MPA-PbS}$ | [F] | capacitance of the MPA-PbS interface [Farad] |
| $C_{PbS-E}$ | [F] | capacitance of the PbS-electrolyte interface [Farad] |
| $CPE_{FTO-ZnO}$ | [F] | CPE capacitance of the FTO-ZnO interface [Farad] |
| $CPE_{ZnO}$ | [F] | CPE capacitance of the ZnO layer [Farad] |
| $CPE_{ZnO-E}$ | [F] | CPE capacitance of the ZnO-electrolyte interface [Farad] |
| $CPE_{ZnO-MPA}$ | [F] | CPEcapacitance of the ZnO MPA interface [Farad] |
| d | [nm] | particle diameter [nanometer] |
| $d_{hkl}$ | [nm] | interplane distance of the crystall [nanometer] |
| $d_{111}$ | [nm] | interplane distance of [111] crystal plane [nanometer] |
| e | | voltage drop across a series resistance between WE & RE |
| $E_{BG}$ | [eV]* | energy of the band gap[electron Volt] |
| $E_{B}$ | [eV]* | energy of the band bending [electron Volt] |
| $E_{CB}$ | [eV]* | position of the conduction band edge [electron Volt] |
| $E_{F}$ | [V] | Fermi-level [Volt] |
| $E_{h\nu}$ | [eV] | energy of photon [electron Volt] |
| $E_{oc}$ | [eV]* | occupied states of the redox couple [electron Volt] |

| Symbols | Units | Explanation |
|---|---|---|
| $E_{RedOx}$ | [V] | redox potential [Volt] |
| $E_{unoc}$ | [eV]* | unoccupied states of the redox couple [electron Volt] |
| $E_{VB}$ | [eV]* | position of the valence band edge [electron Volt] |
| $f_{fcc}$ | | packing density of the face-centered cubic (fcc) packing |
| j | | imaginary unit of complex number |
| i | [A] | current [Ampere] |
| $i_{ac}$ | [A] | amplitude of the current ac [Ampere] |
| $i_{dc}$ | [A] | backgound current [Ampere] |
| $i_{ph}(\omega)$ | [A] | photocurrent density [Ampere] |
| $I_{ac}$ | [1/cm·s] | amplitude of modulated ac photon flux [1/cm·s] |
| $I_{dc}$ | [1/cm·s] | background of the irradiation [1/cm·s] |
| $I_{ISC}$ | [A] | current of the injection solar cell [Ampere] |
| $I(\omega)$ | [1/cm·s] | light intensity (photon flux) [1/cm·s] |
| K | | shape factor |
| $P_{PD}$ | [W] | power of the calibrated photo diode [Watt] |
| R | [Ω] | resistance [Ohm] |
| $R_E$ | [Ω] | resistance of the elctrolyte [Ohm] |
| $R_{FTO}$ | [Ω] | resistance of the FTO coated glass [Ohm] |
| $R_{FTO-ZnO}$ | [Ω] | resistance of the FTO-ZnO interface [Ohm] |
| $R_{linker}$ | [Ω] | resistance of the linker moelcule [Ohm] |
| $R_{MPA}$ | [Ω] | resistance of the linker MPA [Ohm] |
| $R_{MPA-PbS}$ | [Ω] | resistance of the MPA-PbS interface [Ohm] |
| $R_{PbS-E}$ | [Ω] | resistance of the PbS-electrolyte interface [Ohm] |
| $R_{ZnO}$ | [Ω] | resistance of the ZnO layer [Ohm] |

| **Symbols** | **Units** | **Explanation** |
|---|---|---|
| $R_{ZnO-E}$ | [Ω] | resistance of the ZnO-electrolyte interface [Ohm] |
| $R_{ZnO-MPA}$ | [Ω] | resistance of the ZnO MPA interface [Ohm] |
| t | [s] | time [Second] |
| u | [V] | potential/voltage [Volt] |
| $u_{ac}$ | [V] | amplitude of the potential/voltage ac [Volt] |
| $X_{MPA}$ | | variable of the FTO/ZnO/MPA model |
| $X_{MPA/PbS}$ | | variable of the FTO/ZnO/MPA/PbS model |
| Z | [Ω] | impedance [Ohm] |
| $Z_I$ | [Ω] | ohmic resistance [Ohm] |
| $Z_U$ | [Ω] | capacitive reactance [Ohm] |
| $Z_{CPE}$ | [Ω] | CPE reactance [Ohm] |
| Z' | [Ω] | impedance of real part [Ohm] |
| Z" | [Ω] | impedance of imaginary part [Ohm] |
| $Z_{ph}(j\omega)$ | [Ω] | complex impedance in the case of IMPS [Ohm] |
| $\alpha$ | | absorption coefficient |
| $\alpha$ | | rotation angle of a purely capacitive line on the complex plane |
| $\beta$ | | full width at half maximum of the reflexes |
| $\theta$ | | diffraction angle |
| $\lambda$ | [nm] | wavelength[nanometer] |
| $\lambda_{max}$ | [nm] | wavelength of the absorptionmaximum of a material [nanometer] |
| $\lambda_{no.}$ | [nm] | wavelength of an specific PbS absorptionmaximum [nanometer] |

| **Symbols** | **Units** | **Explanation** |
|---|---|---|
| $\lambda_R$ | [nm] | opal reflection wavelength[nanometer] |
| $n_{eff}$ | | effective refraction index of the colloidal crystal |
| $n_{PS}$ | | refraction index of the polystyrol latex shperes |
| $n_{air}$ | | refraction index of the air |
| $\omega$ | [rad/s] | angular velocity [rad per second] |
| $\phi$ | [rad] | total phase shift [rad] |
| $\phi_i$ | [rad] | phase angle of the ac current [rad] |
| $\phi_u$ | [rad] | phase angle of the ac voltage [rad] |

---

[*] Unit description is against to the absolute vacuum energy band (AVS). If the variables are against to the normal hydrogen electrode (NHE) than the unit is quoted in [V] (Volt).

# 1

# Introduction and Motivation

In the latter half of the 20th century the first active environmentalist movements such as Greenpeace and the International Energy Agency were born and initiated a gradual rethinking of environmental awareness. Against all expectations the sole agency under international law for climate protection policy, called the United Nations Framework Convention on Climate Change, was formed 20 years later. Today the awareness of sustained, regenerative and environmental policies permeates throughout all areas of life, science and industry. But energy provision is the most decisive topic, especially since the discussions concerning the phase out of nuclear power where the voices calling for alternative energy sources have become much more vociferous. In addition the depletion of fossil fuels is expected to occur in the not too distant future. All new energy generation methods are required to meet the present and future energy demands, need to be ecological and need to exhibit the same or significantly lower cost expenditure than current energy sources. Unfortunately mankind is confronted with the problem that current commercial alternative energies are more expensive and not yet remotely as efficient as the present energy sources. Although energy provision based on water, wind, sun and geothermal sources have a huge potential because of their continuous presence, unfortunately, they are plagued by inefficient energy conversion caused by the state of technology i.e. the conversion of sun light into electricity loses energy through heat emission, reflection of the sun light, the inability of the material to absorb the entire sun spectrum and the ohmic losses in the transmission of electric current.

The sun power is the most exhaustless resource and moreover through photovoltaic action, one of the most direct and cleanest source for use in energy conversion. Presently incoming sun light is not transformed in its entirely, as much degradation occurs during photon absorption and electron transfer processes. A number of other innovative possibilities have also been researched. With respect to cost and efficiency one of the most promising devices is injection solar cells (ISC). By dint of the dye sensitised solar cell (DSSC) Grätzels findings provided the foundations for much research into this type of solar cell where the light absorbing molecule employed in is a dye.[1] The current is obtained through charge separation in the dye, which is initiated through the connection between the dye and a metal oxide on the one hand and a matched redox couple on the other. In a variant of the DSSC the charge separation processes can also occur between a nanoporous metal oxide and nanoparticles giving rise to a quantum dot sensitised solar cell (QDSSC).[2] The use of nanoparticle (NP) properties can be utilized for the harvesting of solar energy, as demonstrated by Kamat and coworkers[3] who were able to exploit these findings subsequently and prepare a number of nanoparticle based solar cells.

Nanoparticle research has comprised a wide field of science and nanotechnology for a number of years. As the size of a material approaches dimensions on the nm scale the surface properties contribute proportionally more to the sum of the properties than the volume due to the increase in the surface to volume ratio. These dimensions also constitute a threshold in which quantum physical effects need to be taken into account. Hence the properties of devices or materials in this size regime are inevitably size dependent. The basic principles can be described by two different theories, one of which is based on molecular orbital theory in which the particle is treated as a molecule. For this reason n atomic orbitals with the same symmetry and energy can build up n molecular orbitals through their linear combination based on the LCAO method (Linear Combination of Atomic Orbitals).[4] In the case of solids the orbitals build up energy bands, where the unoccupied states form the quasi continous conduction band (CB) and the occuppied states form the quasi continous valence band (VB). The energy "forbidden" area in between these two bands is called the band gap. The band gap is a fixed material property for bulk solids but depends on size in the case of the nanoparticles. In contrast to the LCAO method, simplified solid state theory will be used throughout the present work, the theoretical background of which is provided by the effective mass approximation.[5] When an absorption of a photon occurs, an exciton (electron-hole pair) can be generated. By promoting an electron ($e^-$) from the valence band into the conduction band a hole ($h^+$) may be said to remain in the valence band. By comparison to bulk solids, in a small particle the free charges can sense the potential barrier i.e. the edges of the nanoparticle. Analogous to the particle in a box model this potential barrier interaction results in an increase in the band gap as the particle size decreases.

In a solar cell NPs with a particle size which possess a band gap energy in the near infrared (NIR) may be utilised and therefore the NPs will be able to absorb in this spectral region. However NPs also have the ability to absorb higher energy photons due to the continuum present in their band structure, so that almost the entire sun spectral range from the NIR up to UV wavelengths may be absorbed just by using the appropriate NP material and size. Suitable NPs are metal chalcogenides e.g. MX (where M = cadmium, zinc or lead and X = sulfur, selenium or tellurium) because of their bandgap size[6–10] and their relative band positions compared to those of the semiconductor oxide states. Both the $TiO_2$/CdSe[11–14] and $TiO_2$/CdTe[15–18] systems have already been successfully fabricated and many of the anomalies reported.[3] Much interest in the lead chalcogenides has been generated by reports that they may feature the possibility to exhibit multiple exciton generation (MEG) where the absorption of one high energy photon can result in more than one electron-hole pairs.[19–25]

Currently electrochemical impedance spectroscopy (EIS) is being used more and more to clarify processes at polarisable surfaces and materials such as nanoparticles. Likewise this method has been rediscovered in photovoltaic research and its use in the characterisation of DSSCs has been discussed in the literature.[26–31] In a number of publications the evaluation of nanoporous and porous structures has been quite extensively explored.[28,29,32–34] Since the mid-20th century Jaffé's[35] theoretical work concerning the steady-state ac response of solid and liquid systems lead to the formation of the basics of EIS. Further developments in the measurement technology have lead to a broader range of analysis becoming possible. Nevertheless the most challenging part still remains the interpretation of the results and especially to merge the measured data with the theoretical model. EIS quantifies the changes in a small ac current response at electrode electrolyte interfaces i.e. the rate at which the polarized domain will respond, when an ac potential is applied. In this way dielectric properties of materials or composites, such as charge transfers, polarization effects, charge recombination and limitations can be measured as a function of frequency and mechanistic information may be unveiled. Hence EIS allows one to draw a conclusion concerning chemical reactions, surface properties as well as interactions between the electrodes and the electrolyte.

Other very useful tools that may be employed for quantifying electron transfer processes and their time domains are intensity modulated photocurrent spectroscopy (IMPS) and intensity modulated photovoltage spectroscopy (IMVS). IMPS permits the generation of time-resolved plots of particular photo-processes in the system, each of which may be specifically addressed through varying the excitation wavelength. For the IMPS technique a sinusoidal wave with a small amplitude is applied, analogous to that of electrochemical impedance spectroscopy, but in this case the modulation is applied to a light source and not to the electrochemical cell as in EIS.[35] The current response is associated with the photogenerated charge carriers which flow through the system and finally discharge into the circuit. The amount of generated and discharged charge carriers is often different due to the presence of recombination and capture processes in surface or trap states. Ultimately the phase shift and magnitude of these currents reveal the kinetics of such processes. The only processes that will be addressed will be those that occur in the same frequency domain or on the same time scale as that of the modulated frequency of the illuminated light. In the literature some explanation of the kinetics of simple systems can be found and basic theories and introductive disquisitions may be found elsewhere.[36–38] Furthermore in solar cell research a multiplicity of studies are available which give an account of IMPS measurements on $TiO_2$ nanoporous structures. Such studies permitted proof for the electron trapping and detrapping mechanism in $TiO_2$ surface states.[39,40] An analysis of $TiO_2$ electrodes combined with a dye sensitization step was established in the work of Peter and Ponomarev.[41–43] Hickey et.al.[44,45] have previously published kinetic studies on CdS nanoparticle (NP) modified electrodes. A theory was presented which allows for the IMPS data to be the interpreted in the case of CdS NP based electrodes. The back transfer, recombination and surface states have been demonstrated to be important as was determined from their inclusion in the theory. Similar attempts to explain the kinetics of CdS quantum dots are described by Bakkers et.al.[46].

In the present work the most important questions concern the behaviour of the photovoltaic assembly. Such assemblies can be equated with an electrode in contact with an electrolyte. Preliminary remarks about such electrodes as components of an electrochemical cell will be introduced in the first part of chapter 2. Thereafter the properties of electrodes in contact with the electrolyte and under illuminated conditions are illustrated. This is followed by a description of the important electrochemical and opto-electrochemical methods which have been employed in these studies. In particular, two separate subsections are dedicated to the methods of EIS and IMPS and the experimental section which are then linked to the theoretical section. The synthesis of all substances used and the preparation of the solar cell substrates are also dealt with in this section as will the equipment used and the instrument settings employed. The optical response of the working photoactive electrode is not only dependent on the substances used but also on their arrangement and linkage. The substrate which was employed in chapter 3 consists of a nanoporous ZnO gel layer upon which an organic linker has been placed in order to connect the oxide layer with the light absorbing component, the PbS NPs. Chapter 3 deals with the linker dependence on the ZnO layer and reports the typical optical characteristics and assembly arrangements of six different linkers on the ZnO layer which is an important intermediate stage in the fabrication of an ISC. The questions concerning how the type of linking affects the photo response and other electrochemical interactions of the complete solar cell substrate will be outlined in chapter 4. Further an examination of the electrochemical and opto-electrochemical behaviours of the samples will be presented similar to that presented in chapter 3. The most interesting substrate resulting from the investigations as described in chapter 3 and 4 will be used for a more in-depth characterisation by EIS in chapter 5. A suitable model and the results of the calculation of the ISC and the intermediate stages will be presented. The potential dependence, the dependence on the illuminated wavelength and also the size dependence of the PbS nanoparticles will be discussed. It will be revealed that ZnO is chemically unstable in contact with some of the linkers. For that reason the same linker study has been repeated with the more stable $TiO_2$ employed as the wide band metal oxide. Comparisons between the different semiconductor metal oxides are made in chapter 6. In addition a number of open questions which previously had remained unanswered due to the instability of the ZnO can now be answered. In chapter 7 another highly porous structure different from that of the ZnO gel structure has been studied to determine its suitability as an ISC substrate. The structure arises from the electrodeposition of a ZnO reactant in the presence of eosin Y dye molecules. In the end the desorption of the dye provides a substrate with a high degree of porosity. Compared to the ZnO gel which was prepared and used for measurements in chapter 3 and 4, the electrodeposited ZnO is of a higher crystallinity and possesses a more preferential orientation. This results in a lower amount of grain boundaries which in turn results in fewer trap processes and subsequently yields a higher effective diffusion of the electron through the layer.[47,48] Optical and (opto-)electrochemical methods have been used for the basic characterisation of the untreated ZnO/Eosin Y and all other materials used in the fabrication of the ISC and a comparison with the ZnO gel used in chapter 3 and 4 will be made. Finally in chapter 8 an alternative metal oxide structure will be discussed. The background to this last chapter is to examine the influence of the ISC where the oxidic layer is present as a highly periodic arrangement, known as a photonic crystal. The $TiO_2$ metal oxide which was also used in chapter 6 has been structured to form an inverse opal. First preparative findings and the first illustration of the (opto-)electrochemical results are presented. Consequently suggestions for improvements will be made.

It is envisaged that the information gathered and presented here will help to achieve a deeper understanding of solar cells and help to improve the device efficiency and the interplay of the materials. Elementary understanding paves the way for further developments which can also contribute to providing devices for more efficient energy conversion.

# 2

# Theoretical and Experimental Introduction

## 2.1 Basics of the (Opto-)Electrochemistry

For researchers working in the field of solar cells knowledge of spectroscopy and electrochemical methods are indispensable. As the method name reveals spectroscopy describes the interaction between matter and radiated energy. Especially for solar cells the radiation profile of the solar spectrum and its interaction with the solar cell materials is of utmost importance. For instance UV/Vis/NIR spectroscopy (Ultra Violet/Visual/Near InfraRed spectroscopy) can be used to explore the characteristic absorption range of nanoparticulate materials through their absorption spectra, maximum peak of absorbance and accordingly the particle size and particle quality. Also the optical band gap energy $E_{BG}$ of the material can be determined through the position of the maximum peak. But the most important aspect within the bounds of this thesis is electrochemistry. For this reason the description of relevant electrochemical and opto-electrochemical methods will be dealt with in slightly more theoretical detail. Usually the photovoltaic solar cell can be represented as an electrochemical system. If the photovoltaic substrate is in contact with an electrolyte the substrate is expected to follow the usual rules of electrochemistry. Semiconductors especially show quite complex interactions in an electrochemical system. By reason of employment of semiconducting materials in the present work, the first section will open with a detailed explanation concerning semiconductors in electrochemical environments and the principle of operation of the injection solar cell (ISC), followed by the introduction of the most important electrochemical characterization techniques employed.

## 2.1.1 Electrode-Electrolyte Interface Non-Illuminated

Electrochemistry is the science of interfaces. Whatever processes occur in an electrochemical cell are primarily visible through contact with the electrode surface and this is particularly true in the case of photoelectrochemical cells where the semiconductor electrolyte interface plays an important role. A schematic of an n-type semiconductor electrolyte interface at equilibrium is presented in Figure 2.1.

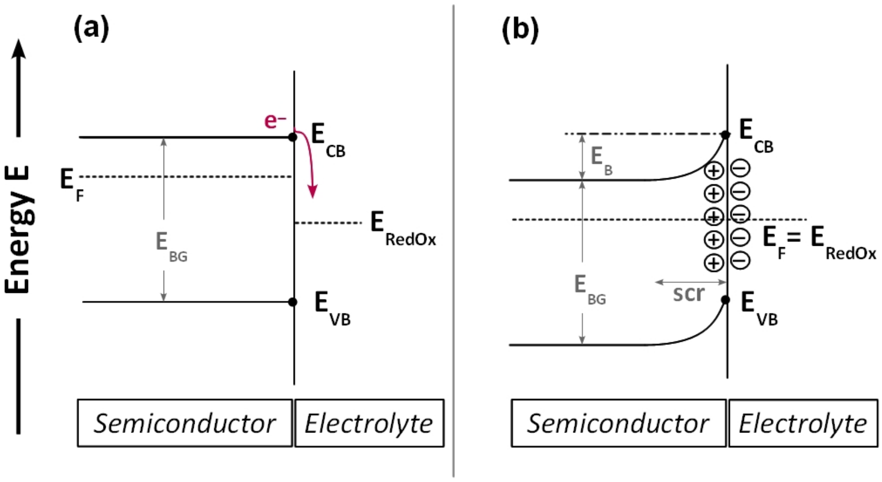

Figure 2.1: An energy diagram of an n-type semiconductor in contact with an electrolyte (a) in the very first instant before a potential is applied and charge equilibrium occurs and hence the energy of the conduction band ($E_{CB}$) and valence band ($E_{VB}$) are uniform at every distance from the interface and (b) after charging equilibrium occurs. The band edges of the semiconductor are pinned at the energy levels $E_{VB}$ and $E_{CB}$. The deeper band structure shows a downwards bending band ($E_B$) in the space charge region (scr). The energy of the band gap ($E_{BG}$) is still constant. After the equilibrium has been reached the $E_F$ equals the redox potential of the electrolyte ($E_{RedOx}$).

Generally semiconductors may be subdivided into n-type and p-type semiconductors. For a more detailed theoretical description of semiconductors the interested reader is referred to the literature.[49] For the purposes of this thesis n-type semiconductors have been employed and therefore will be used as the basis of all treatments and discussions. Typically the Fermi-level ($E_F$) of an n-type semiconductor at open circuit is higher than the redox potential of the electrolyte ($E_{RedOx}$)(Figure 2.1(a)). Therefore electrons present in the semiconductor transfer into the solution and leave positive charges behind in the semiconductor (Figure 2.1(b)). These charges affect the space charge region (scr) and induce a downward band bending of the band edges to the more positively bands located deeper within the structure. Contrariwise the p-type semiconductor contains an upward directed band bending due to the reverse electron transfer to the semiconductor. Such band changes, for instance band bending[50–52] and Fermi-level pinning[53] in the scr, is to be expected in all semiconductor solids. The dimensions of the scr depends on the conductivity of the semiconductor and the degree of band bending ($E_B$).[54] In the case of a too small nanoparticle size it is assumed that the potential drop remains within a few milivolts and is consequently negligible.[55] Depending on the band positions and redox potential of the electrolyte, an elementary electron transfer between electrode and electrolyte can be described as shown in Figure 2.2. In this figure it is assumed that the redox

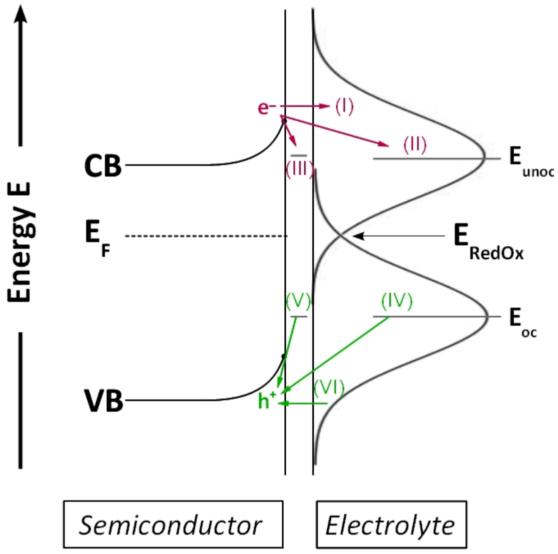

Figure 2.2: The above energy diagram shows various electron transfer processes for an n-type semiconductor in contact with an electrolyte. The isoenergetic electron transfers from (I) or to (VI) (from the semiconductor into the energy distribution of the unoccupied state ($E_{unoc}$) and occupied state $E_{oc}$ respectively) are possible. The inelastic transfer from (II) or to (IV) the $E_{unoc}$ and $E_{oc}$ may also occur as can the intermediate process where an electron is injected into the surface states of the semiconductor (III+V).

species is diluted in solution and the occupied and unoccupied states of the redox couple matches well with the band edges of the electrode. At first an isoenergetic transfer of electrons (Figure 2.2 (I)) from the CB to the lowest unoccupied state of the redox couple ($E_{unoc}$) can occur. A electron transfer from the highest occupied state of the redox couple ($E_{oc}$) to the hole ($h^+$) located in the VB of the semiconductor can also occur (Figure 2.2 (VI)). Furthermore two kinds of inelastic electron transfer processes are conceivable. The direct transfer from the CB of the semiconductor into $E_{unoc}$ (II) or from $E_{oc}$ (IV) directly into the $h^+$ in the semiconductor VB is possible. Last but not least the transfer of an electron into a semiconductor surface state (III) and from the surface state back to the semiconductor VB (V) cannot be ruled out.

## 2.1.2 Electrode-Electrolyte Interface Under Illumination

The photovoltaic phenomena, also known as the "Becquerel effect"[56], is the core process in any injection solar cell (ISC). The cornerstone for the understanding of the photovoltaic effect was developed by Brattain and Garett.[57] The primary idea behind the process is to gain electrical energy through the simple direct conversion of sunlight photons to electrons ($e^-$) in semiconductors which then close an electric circuit.

If a photon ($h\nu$) with an energy $E_{h\nu} > E_{BG}$ impinges on the semiconductor then the absorbed energy can generate an exciton ($e^-$-$h^+$ pair). In such cases the $e^-$ is promoted into the CB level whilst a $h^+$ remains in the VB of the semiconductor (Figure 2.3(a)). The $e^-$ may then discharge into the circuit.[52,53,58–60] The fast separation of the $e^-$-$h^+$ pair and the transfer of the $e^-$ are important processes and central to the design of an ISC. An $E_{unoc}$ far below the CB (Figure 2.3(a)) is desirable, because it prevents the promoted electrons from oxidizing the electrolyte species. On the other hand the $E_{RedOx}$ is then shifted more towards the lower level of the $h^+$ leaving it assessable. The $E_{oc}$ of the redox couple has a better overlap with the VB state of the semiconductor where the $h^+$ is located. Consequently a fast separation of the hole is given by the regeneration of the $h^+$ with the reduced species of the redox couple.

In the case of non-ideal semiconductor systems a more complex model for the generation is required. In Figure 2.3(b) the simplest model [1] and the more complex model with the involved intermediate states [2] up to [5] are presented. Given the assumption that defect and surface states (intermediate states) are located within the semiconductors band gap it becomes necessary to consider the dependence of different incoming photon energies $E_{h\nu}$ and their interaction with these states. Supposing that $E_{h\nu} < E_{BG}$ and intermediate states exist then such states can be addressed by these lower energies. For the electron transferred into the CB, where it can move, a second excitation in terms of a further absorbed photon [2] and transitions which can be thermally fed by kT [3] and [4] is necessary. Process [5] describes a refilling of an empty surface state by an interfacial electron process. This process only describes a way to push an electron into higher useable states but also a way in which to inject the electron in surrounding regions.[58]

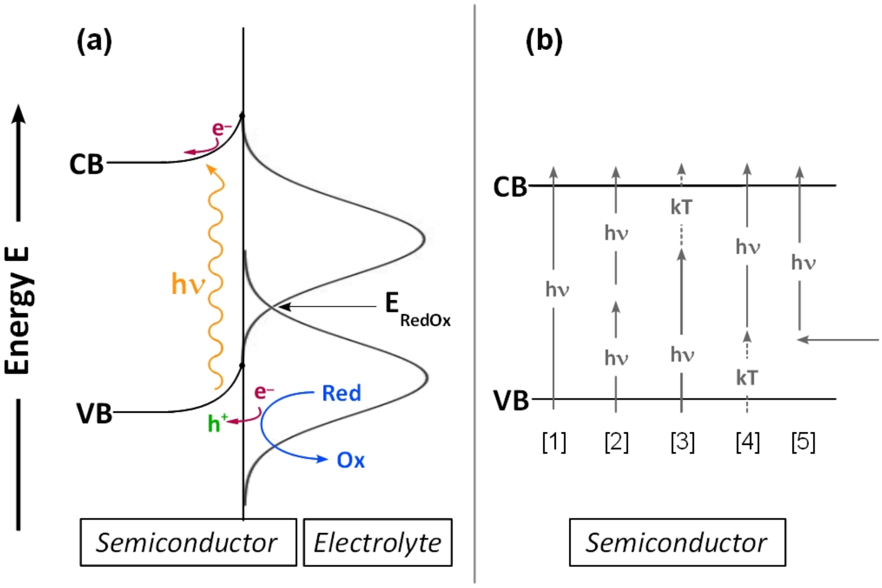

Figure 2.3: A schematic of the exciton ($e^-$-$h^+$ pair) generation and interaction of the $h^+$ with the redox system when $E_{h\nu} > E_{BG}$ ((a) and (b)[1]) and when $E_{h\nu} < E_{BG}$ ((b)[2]-[5]). Mechanisms of exciton generation are dependent on the photon energy $E_{h\nu}$ and the further states in the band gap (defect and surface states). The $e^-$ transferring out of the intermediate state can be promoted by further photon absorption (b[2]) or further energy may feed through thermal excitation (b[3], b[4]). In particular b[5] describes the refilling of an empty surface state by an interfacial electron process.

### 2.1.3 The Processes in the Injection Solar Cell (ISC)

Generally the charge carrier generation species is a dye or a semiconductor nanoparticle which is able to absorb the incoming sun light. Optimally the photoactive species should have a band gap energy of approx. $E_{BG}\sim 1$ eV. The possession of a narrow band gap allows a material to absorb much of the sun spectrum in the wavelength range stretching from NIR down to the UV. The nanoparticle (NP) is placed next to the surface of a wide band semiconductor with an $E_{BG}$ in the region of 2-3 eV. This wide band semiconductor is usually a metal oxide (MO) as most metal oxides have a band gap of such a width, and as such, in contact with the narrow band gap material, the nanoparticle band gap can be adjusted such that an efficient overlaid band profile can be achieved. In Figure 2.4 (a) the band diagram of the NP used as the photoactive species and the wide band metal oxide is illustrated as presented in the work of Vogel et.al.[2].

The nanoparticle layer is assumed to be present as a monolayer. The solar cell should be arranged in such a way that the $e^-$ and $h^+$ will separate quickly after the generation of the exciton. Therefore the position of the NP CB needs to be higher than that of the CB of the MO. The VB of the NP needs to be located quite far away from the CB of the MO, otherwise no charge separation (CS) will proceed[61] and a recombination of the $e^-$ and $h^+$ will occur. Few theoretical and practical treatments concerning the recombination processes and their dependence on the system parameters are to be found in the literature.[52,58,62,63] The promoted electron in the CB of the NP may then inject into the CB of the MO and it is this process that is mentioned in the term ISC. The $h^+$ will be regenerated by the reduced species (Red) of the redox couple analogous to that mentioned previously (Figure 2.3(a)). The subsequently oxidized species (Ox) may then diffuse towards the counter electrode (CE) and react returning to the Red species. The interfacial $e^-$ process which was introduced in section 2.1.2 in Figure 2.3(b) is important in the discussion of the electron transfer to the MO layers. In the present work the MO appears as a nanoporous layer. Such a layer consists of very small MO particles which stick together to form a fractal geometrical network analogous to that described by percolation theory and built up therefore from nanosized pores. The $e^-$ transfer within the MO layer

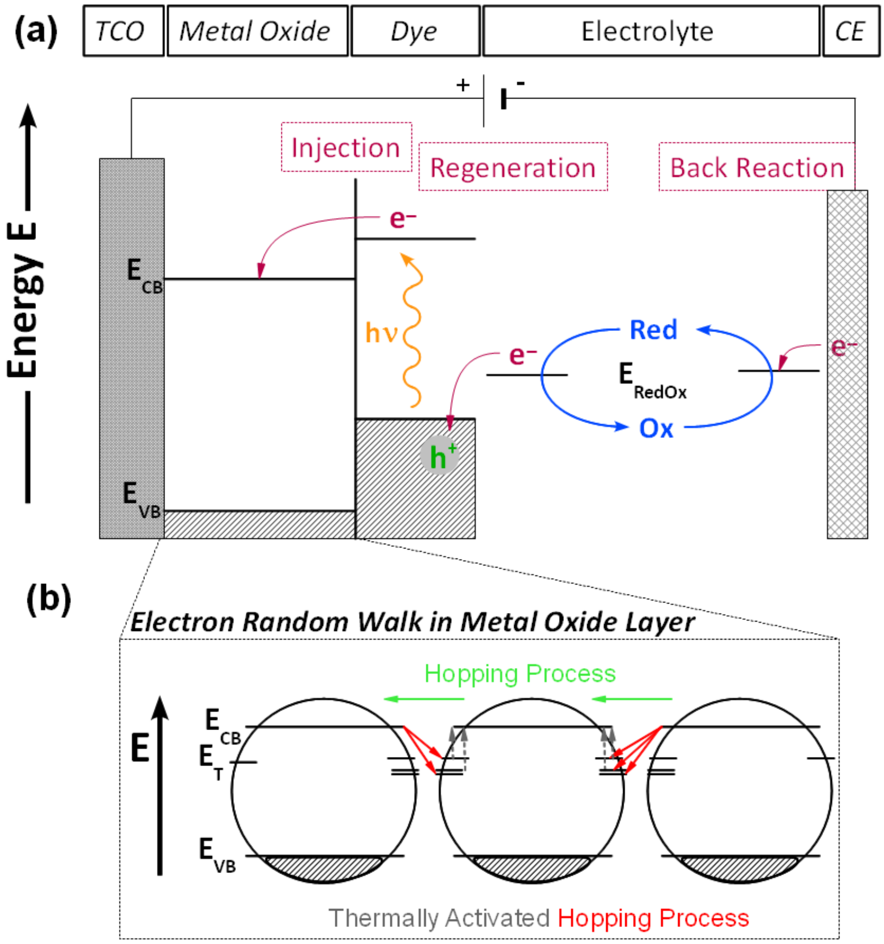

Figure 2.4: (a) Schematic showing the charge carrier transfer (CCT) in an ISC. The CCT consists of an exciton generation initiated by the photon h$\nu$, of CS via e$^-$ injection from the dye at the metal oxide and charge separation CS of the h$^+$ via regeneration with the redox couple as well as a back reaction on the CE. (b) In the MO layer the electron will move to the TCO through a hopping process also called a random walk.

may be affected by the transfer between the MO particles. Additionally it is assumed that some surface or trap states exist in the MO particles and for that reason the electron transfer becomes more complex. Besides the multiplicity of transfer possibilities which are located in the band gap, their potential dependence and accordingly the dependence of the Fermi-level $E_F$ position needs to be considered. In the literature the mechanism of the $e^-$ transfer through the MO, which is applied for theoretical treatments, will be termed a "hopping" process. There are different types or principles associated with these hopping processes. It is well known that most oxides have an ionic character. The polarisation of a crystal lattice is purely by the electronic effect (electronic polarisation) and the motion of ions in the lattice (ionic polarisation). The electronic effect is quite fast compared to ionic motion. In the end, if charge moves through the band, the ionic polarisation is too slow to follow efficiently and the stabilization will be affected. Therefore most of the stabilization occurs by lowering of the energy of the charge which appears through the displacement of the ions or by the polarisation of the lattice. The charge which is trapped by the local lattice polarisation will be termed a "small polaron".[64–67] The hopping process from atom to atom and from particle to particle may then occur by such polarons. Often the polaron movements are related through a thermally activated hopping process. This means that the absorption of thermal energy (kT) is necessary to transfer the polaron to the CB, where the polaron continues to move. This is also known as a trapping-detrapping process. A good visualisation of such a polaron transfer is reported by Cox.[66]

A theoretical description for simulations of these hopping processes is often reported through a variation of the Monte Carlo simulation[68], called the multiple trapping (MT) and continuous-time random walk (CTRW) model. This describes an electron transfer as a random walk hopping process between tail states. The tail states are localized trap levels. The differences between these two theories are as follows. In the CTRW the electrons move over the traps. In the case of MT the electrons move in the CB where sometimes electrons are trapped. Hence MT describes a thermally activated trapping process of charges.[61,69] In Figure. 2.4(b) a scheme depicting the hopping processes is presented. The direct hopping (light green arrow) transfers free charges from the CB of one particle to the CB of another particle. During the thermally activated hopping process the electrons are being trapped (red arrow) in lower energy states ($E_T$) which are also called trap or tail states. After being thermally promoted to higher energy levels (grey dotted arrow) the electron transfer continues. According to the model such trap states can also be located not only at the surface but also inside the particle.

### 2.1.4 Cyclic Voltammetry (CV)

Cyclic voltammetry is a potential sweep method which applies a triangular potential wave to the system. Significant for the upper and lower potential limit is the stability of the electrolyte used. Hence the working window will also be defined by the solvent and its dissolved species. The recorded current response evinces the occurring oxidation processes through an anodic current or the reduction processes through a cathodic current. Thereby the rate of the current is dependent on the concentration of the redox active species at the corresponding electrode.

$$\text{Anodic oxidation:} \qquad Red \longrightarrow Ox + ne^- \tag{2.1}$$

$$\text{Cathodic reduction:} \qquad Ox + ne^- \longrightarrow Red \tag{2.2}$$

When the voltage applied to the electrodes approaches the oxidation potential of the reduced species then the concentration ratio between the reduced species (Red) and oxidized species (Ox) will decrease due to the oxidation of the reduced species. On the electrode surface a concentration gradient and a diffusion layer will build up in accordance with Fick's second law. Analogous to Fick's first law the current density is reciprocally proportional to the concentration gradient and therefore the increasing gradient is seen in the cyclic voltammogram as a current peak. With further application of the voltage the concentration of the reduced species at the electrode converges to zero. Then the diffusion layer will expand which results in a decrease in the concentration gradient on the surface and therefore a decrease in the current. The theoretical background for such current-voltage curves was presented by Randles.[70] An extensive examination of the theory of reactions based on CV, the description of reversible, irreversible and more complex reactions were further presented by Nicholson et.al..[71] CV makes it possible to determine the electron transfer processes between the active redox species and the electrode which can occur through electrochemical reactions and adsorption processes. Under special conditions the position of the electrochemical band gap of solid materials as well as nanoparticles can be determined.[72,73]

### 2.1.5 Chronoamperometry (CA)

The simplest way to check the photoactivity of a solar cell is with CA. With a potential applied, the system is illuminated with an square wave modulated monochromatic light source. The resulting photocurrent transient shows the time dependent response to the light excitation.[36,74,75] First estimations concerning the rate of charge transfer processes and the magnitude of the photocurrent are obtained. The charge transfer processes immediately after the electron generation can be seen in the increase of the photocurrent upon initial illumination. The charge transfer process itself during the illumination period can be characterized through the profile when the current has reached steady state (plateau region). Then upon cessation of the illumination the currents return to the dark current level. Under specific circumstances a pulsed laser technique is helpful to separate the charge transfer process from the electron generation affected processes. The application of a short pulse gives information concerning the electron transfer transient.[76] Often using this technique a resolution on the $\mu$s time-scale is possible.

### 2.1.6 Incident Photon to Current Conversion Efficiency (IPCE)

The IPCE describes how many electrons transfer for a given number of photon impacts on the substrate. The mathematical description is:

$$IPCE(\%) = \frac{h \cdot c \cdot I_{ISC}}{\lambda \cdot P_{PD}} \cdot 100 \qquad (2.3)$$

whereby

$$E = \frac{h \cdot c}{\lambda} = h \cdot \nu = \frac{h \cdot \omega}{2\pi} \qquad (2.4)$$

The impacting photons of each wavelength are measured using a calibrated photo diode (PD) which is located at the same position as the photovoltaic cell. The resulting current of the ISC ($I_{ISC}$) is related to the recorded power as measured by the PD ($P_{PD}$). In this way the photoactivity of the ISC over all wavelengths can be measured.[77] Especially for the characterisation of dyes it is important to compare the optical absorption properties with the opto-electrochemical properties. The expected IPCE should mirror the optical absorption profile of the solar cell substrate. Because of recombination and other loss mechanisms of the system it is not possible to achieve an identical spectrum under real conditions.

### 2.1.7 Electrochemical Impedance Spectroscopy (EIS)

In EIS a sinusoidal alternating potential (ac) is applied to the solar cell between the substrate and the resulting alternating current is recorded. The excitation ac potential u can be the described by the following relationship:

$$u = u_{ac} \cdot \sin(\omega t) \tag{2.5}$$

The amplitude of the excitation potential is required to be small, so that the current response also prossesses sinusoidal characteristics such that:

$$i = i_{ac} \cdot \sin(\omega t + \phi) \tag{2.6}$$

where $u_{ac}$ and $i_{ac}$ are the amplitudes of the potential and current sinusoidal signals respectively. An important system parameter gained is the phase difference between the ac potential and the current response:

$$\phi = \phi_u - \phi_i \tag{2.7}$$

The magnitude of the phase shift gives information concerning the interfacial reactance of a system. If no phase shift has been recorded an ideal ohmic resistance is present (Figure 2.5(a)). A positive shift of $\pi/2$ is caused by an inductance (Figure 2.5(b)), a negative shift of $\pi/2$ by a capacitance (Figure 2.5(c)). For all electrochemical cells such as solar cells only resistances and capacitances are present and therefore need to be considered. Hence, within the framework of this thesis, it is not necessary to address further the issue of inductance.

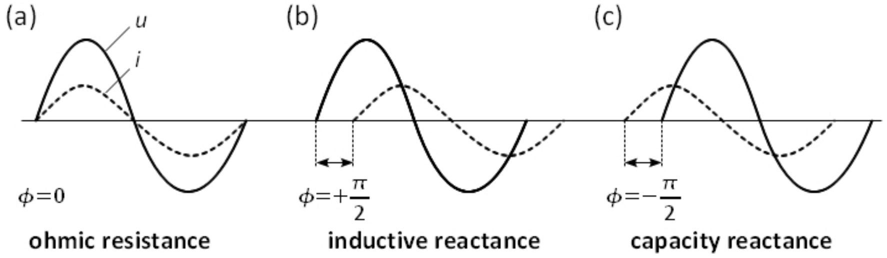

Figure 2.5: The overlay of the sinusoidally applied potential $u$ (line) and the sinusoidal current response $i$ (dashed line) offers valuable clues to the recorded impedance. When the phase of i is not shifted with respect to u then the impedance is an ohmic resistance (a). In the case of a phase shift of $\pi/2$ the impedance has an inductive contribution (b). A phase shift of -$\pi/2$ indicates the presence of a capacitive reactance (c).

Sequentially the total impedance consists of the ohmic resistance $Z_R$ (real part(Z')) and the capacitive reactance $Z_C$ (imaginary part (Z")).

$$Z = Z_R + Z_C = Z' + jZ'' \tag{2.8}$$

$$= R + j\left(\frac{1}{\omega C}\right) \tag{2.9}$$

$$= R - \frac{1}{j\omega C} \tag{2.10}$$

Through recording the ac current response to the applied ac potential at different frequencies (*f*) it is possible to gain information in the time domain about the electrochemical processes. For the description of the time domain, especially that of the phase shift, the mathematical relationship becomes quite complex with respect to *dt*. For ease of handling Fourier transformation, in which the complex number j is included, is applied. A response may occur if the applied frequency stimulates processes with an equal time domain.

The analysis of these results is very extensive and based on specific rules.[78,79] A model must be found which brings together the main electrochemical processes in the cell and the equivalent electrical circuit elements such as the resistors R and capacitors C. If the results of the calculations cannot be fit to the measured data than the search for an appropriate model must be continued. One of the simplest equivalent circuits is that shown in Figure 2.6(a) which consists of one resistor $R_2$ connected with a parallel linked RC element with a resistor $R_1$ and capacitor $C_1$. Normally this is the model used to describe a simple electron transfer at the electrode electrolyte interface (||RC) which contains an electrolyte resistor $R_2$=$R_E$. Generally a CE with a high surface area is used which results in a high capacitance and a low resistance, so the impedance of the counter electrode (CE) is observed in the high frequency range away from processes connected with the working electrode. For this reason the CE can be neglected when fitting the data. The Bode phase ($\phi$ against lg($f$)) and the Bode modulus (lg($Z$) against lg($f$)) of the system are presented in a Bode diagram for this model (Figure 2.6(c)). The current $i$ which passes through the system moves in such a way as to encounter the lowest impedance. Therefore the lowest impedance which the current needs to overcome may be seen from the diagram. In the high frequencies the lowest impedance is generally given by the ohmic resistance, the electrolyte resistor $R_2$=$R_E$. At lower frequencies the impedance of $C_1$ will be greater and may dominate the total impedance in the diagram. The $i$ passes through $R_2$ and $C_1$ of the circuit (Figure 2.6(a)). Eventually the impedance of $C_1$ increases with decreasing frequency of the applied $u$. In the Bode modulus the slope of lg($Z$) has a value of -1. Simultaneously the Bode phase logically decreases to -$\pi/2$. If the impedance of $C_1$ becomes higher than the impedance of the resistor sum ($R_1$+$R_2$) then $i$ will go through $R_2$ and $R_1$ of the circuit (Figure 2.6(a)), the phase will return to zero and the impedance become constant at $Z$=lg($R_2$ + $R_1$).

The Nyquist diagram of the model, i.e. the plot of Z" against Z', is a semicircle with a shift to higher Z'. The semicircle arises from the mathematical form of the total impedance:

$$
\begin{aligned}
Z &= Z' + jZ'' && (2.11)\\
&= R_2 + \frac{1}{\frac{1}{R_1} - j\omega C_1} && (2.12)\\
&= R_2 + \frac{R_1}{1 - j\omega C_1 R_1} && (2.13)
\end{aligned}
$$

The solution of the real part and the imaginary part arises from the binomial relation, which describes a semicircle analogous to:

$$
\begin{aligned}
Z' &= R_2 + \frac{R_1}{1 + \omega^2 C_1^2 R_1^2} && (2.14)\\
Z'' &= \frac{\omega C_1 R_1^2}{1 + \omega^2 C_1^2 R_1^2} && (2.15)
\end{aligned}
$$

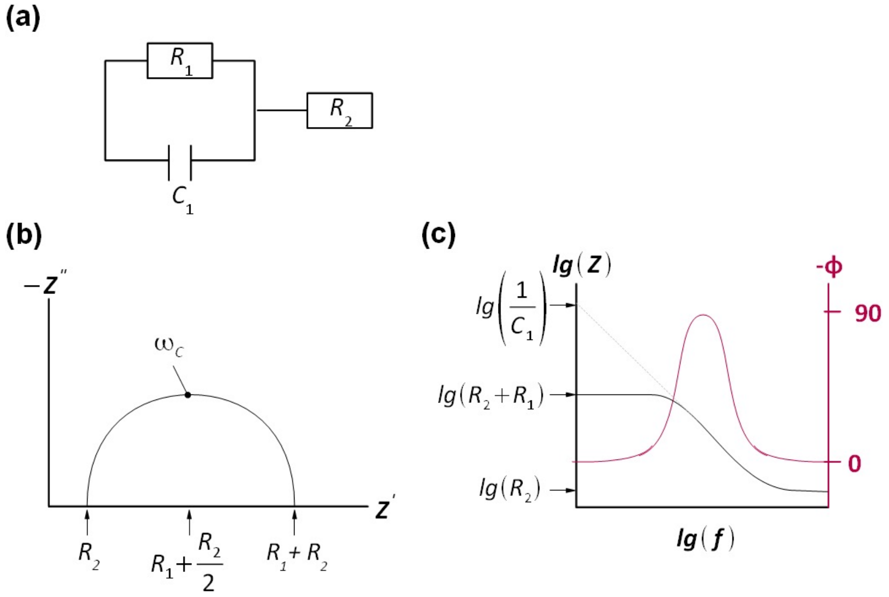

Figure 2.6: (a) The most straightforward model for a simple electron transfer at the electrode electrolyte interface with a resistor $R_2$ connected with a parallel linked RC element with $R_1$ and capacitor $C_1$ (b) The Nyquist diagram of the model.(c) The Bode diagram of the model.

Through elimination of the angular velocity $\omega$ the following relation ship results:

$$\left(\frac{R_1}{2}\right)^2 = \left(Z' - Z_2 - \frac{R_1}{2}\right)^2 + (Z'')^2 \tag{2.16}$$

which has the form of a semicircle with $z^2$:

$$z^2 = x^2 + y^2 \tag{2.17}$$

Another circuit element used in modelling is the constant phase element (CPE) which describes the inhomogeneous potential distribution at the surface. This view of the surface is important in case of a nanoporous MO layer because of its inhomogeneous surface which does not act as an ideal capacitor. As far as possible the CPE stands for a capacitance with a frequency independent phase shift and is described by an exponential expression.

$$Z_{CPE} = \frac{1}{(j\omega A)^{\alpha}} \tag{2.18}$$

with $\omega$ as the angular velocity, A as a constant with the dimensions of $\mathrm{Fcm}^{-2}\mathrm{s}^{\alpha-1}$ and $\alpha$ as the rotation angle of a purely capacitive line on the complex plane schematic.[80,81] In the case of $\alpha$=1 the CPE element will behave as an ideal capacitor according to equation 2.10 and 2.12. In the case of $\alpha$=0.5 diffusion processes are involved and yields the Warburg impedance.[80] For more details and theoretical background to EIS the interested reader is referred to the literature.[82–84]

### 2.1.8 Intensity Modulated Photocurrent Spectroscopy (IMPS)

IMPS is a method by which one may gain information concerning the kinetics within an ISC. As opposed to the technique of EIS for IMPS the light intensity is modulated and not the potential applied to the ISC. The light intensity (photon flux) consists of both an ac ($I_{ac}$) generated and a direct current (dc) generated ($I_{dc}$) component:

$$I(\omega) = I_{dc} + I_{ac}\sin(\omega t)) \tag{2.19}$$

The response will be a photocurrent density $\mathrm{i}_{ph}(\omega)$ which can be described by:

$$i_{ph}(\omega) = i_{dc} + i_{ac}\sin(\omega t + \phi) \tag{2.20}$$

whereas $\mathrm{i}_{dc}$ is the background current and $\mathrm{i}_{ac}$ is the amplitude modulated photocurrent density. The comparison of phase and the response takes place between the modulated light intensity of the light source and the resulting $i_{ph}(\omega)$ of the ISC. The complex impedance in stable systems is time independent and may be represented through Equation 2.21:

$$Z_{ph}(j\omega) = \frac{I_{ac}(j\omega)}{e i_{ac}(j\omega)} \tag{2.21}$$

with $e$ as the voltage drop across a series resistance between WE and RE and j as imaginary unit of the complex number.[82] Whereas EIS provides information concerning the impedance as a result of a frequency modulated potential, IMPS gives the frequency dependent photocurrent response arising due to the photo active processes. Hence an IMPS response will not be recorded for a non-photoactive system.

The analysis of the IMPS based results provides information concerning the kinetics. It is known that the total current $i$ is given by the amount of charge,

[Q] that passes through the circuit per unit time t.

$$i = \frac{d[Q]}{dt} \tag{2.22}$$

If a simple system of photoactive species according to Hickey et.al.[44] is assumed, then only the rate constant of the $h^+$ regeneration with the redox couple $k_h$, the rate of $e^-$ discharge to the circuit $k_e$, the rate of back transfer of the $e^-$ to the VB of the nanoparticle $k_b$ and the recombination of the exciton $k_r$ need to be considered (Figure 2.7). The generation of the exciton is a very fast process and does not of itself contribute to charge transfer hence this process is not observed using IMPS. Three different charges may exist in the system: a positively charged particle $[Q^+]$, negatively charged particle $[Q^-]$ and an excited state $[Q^*]$. The formulation of a kinetic equation for each charge is possible by setting up the differential equations for $d[Q^+]/dt$, $d[Q^-]/dt$ and $d[Q^*]/dt$. The modulated photon flux from the light source (Equation 2.13) will be absorbed by the particle and excite it. The relation of the absorbed photon flux to the nanoparticle is given by:

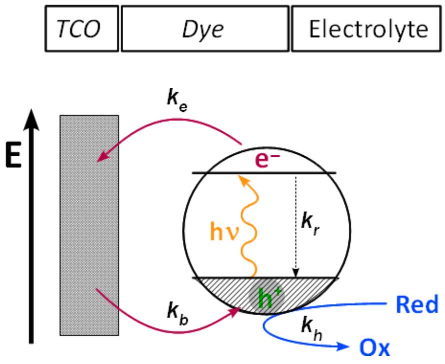

Figure 2.7: The simplest model for charge carrier transfer within an electrode nanoparticle-electrolyte interface. The rate constant of the $h^+$ regeneration with a redox couple $k_h$, the $e^-$ discharges to the circuit $k_e$, the back transfer from the $e^-$ to the VB of the NP $k_b$ and the recombination of the exciton $k_r$ need to be considered.

$$\text{absorbed photon flux} = \alpha(I_{dc} + I_{ac}e^{i\omega t}) \tag{2.23}$$

whereby $\alpha$ is the absorption coefficient of the nanoparticle. The subsequent solutions of the differential equation are calculated via the trial functions of each of the charges of [Q]. A final model $i_{ph}$ is added by summing all charges [$Q^+$], [$Q^-$] and [$Q^*$]:

$$\begin{aligned} i_{ph}(\omega) = \alpha e I_{ac} k_e \Bigg[ & \frac{k_r(k_e + k_r + k_h)}{(k_r + k_h)(k_r + k_e - k_b)} \left( \frac{1}{k_r + k_e + k_h + i\omega} \right) \\ & + \frac{k_h}{k_r + k_h} \left( \frac{1}{k_e + i\omega} \right) - \frac{k_b}{k_r + k_e - k_b} \left( \frac{1}{k_h + k_b + i\omega} \right) \Bigg] \\ & \left[ \frac{1}{1 + i\omega RC} \right] \end{aligned} \tag{2.24}$$

Similar rudiments and further theoretical details are given following literature.[36,38,40,42,45,46,82]

# 2.2 Experimental

## 2.2.1 Synthesis of ZnO Sol-Gel

ZnO was synthesized using zinc acetate ($Zn(Ac)_2$, 99.99%, Aldrich), lithium hydroxide monohydrate ($LiOH\ H_2O$, 98%, Aldrich) and dry ethanol (SeccoSolv, Merck). All water used was purified using a Milli-Q system and had a resistance of 18.2 MΩ/cm.

The ZnO synthesis employed was a modification of that described by Spanhel and Anderson[85] and optimized by Meulenkamp et.al.[86] The ZnO synthesis protocol was carried out under inert atmosphere conditions (Ar) using water free chemicals and hence the necessity for the boiling step was circumvented. In a typical synthesis $Zn(Ac)_2$ (1.464g, 5mmol) was dissolved in dried ethanol (75 ml/59.2g) whilst stringently maintaining the oxygen and water free conditions. A $LiOH\ H_2O$/ethanol solution (0.455g, 7mmol/75 ml) was prepared and the injection of this solution was performed at a temperature of ±2 °C. Subsequently the resulting clear solution was refluxed for 10 minutes at 65 °C. After heating the solution Milli-Q water was quickly added for as long as a precipitation was observed to occur. This treatment was followed by washing the ZnO gel three times with an ethanol/water mixture (95:5).

The precipitate was suspended in ethanol and used up within 3 days.

### 2.2.2 Synthesis of $TiO_2$ Sol-Gel

The titanium precursor was made by mixing titanium(IV)isopropoxide (Ti-IPO, 99.999%, Sigmal-Aldrich) and dry ethanol (SeccoSolv, Merck). In addition nitric acid (HNO3, 65%, Fluka), polyethylene glycol M-20000 (PEG, Fluka) and water (Milli-Q system, resistance 18.2 MΩ/cm) were used.

The $TiO_2$ synthesis employed here was a modification of the procedure as described by Srikanth et.al.[87] The $TiO_2$ synthesis was performed under conditions of inert atmosphere (Ar). In a typical synthesis Ti-IPO (4g/4.46 M) was dissolved in dried ethanol (4 g) whilst stringently maintaining oxygen and water free conditions to avoid any unwarranted $TiO_2$ formation. Subsequently the Ti-precursor was added drop wise to water at 0°C under vigorous stirring. The mass ratio of Ti-IPO:ethanol:water was chosen to be 1:1:10. After hydrolysis the resulting colorless suspension was acidified using approx. 200 $\mu$l $HNO_3$ until a pH value of 1.5 was reached. For the sol generation the suspension was refluxed for 8 hours at 80°C. This treatment was followed by centrifugation of the $TiO_2$ gel to separate out strongly agglomerated $TiO_2$ nanoparticles from non-agglomerated $TiO_2$. The overlaying $TiO_2$ suspension was concentrated using rotary evaporation at 40°C until the solution became strongly viscous. The sol was then mixed with a small amount of a highly diluted PEG solution.

The suspension is highly stable and could be stored for months.

### 2.2.3 Preparation of the ZnO/Eosin Y Substrate

For the ZnO/Ey film zinc chloride ($ZnCl_2$, 98%, Merck), potassium chloride (KCl, 99%, Sigma-Aldrich), potassium hydroxide (KOH, >85%, Carl-Roth) and eosin Y (disodium salt)(Ey, certified with 80% dye, Acros organics) were purchased. All water used had a resistivity of 18.2 MΩ/cm (SatoriusArium 611 DI). FTO was used as the TCO glass (U type TCO, <12 Ω/sq, Transmittance > 80%, AGC Fabritech Co., Ltd) and a zinc wire (99.95%, Alfa Aesar) as CE.

The ZnO deposition was carried out according to the previous work of Boeckler et.al.[88] with a three electrode arrangement in which the FTO coated glass acts as a working electrode (WE). The counter electrode is composed of a zinc wire and an Ag/AgCl reference electrode (type XR300, Radiometer Analytical) was also used. After 10 minutes pre-electrolysis in 0.1 M KCl solution at a potential of -0.91 V the electrodeposition was undertaken at approx. 70°C for 30 minutes in a mixture of 0.1 M KCl, 5 mM $ZnCl_2$ and 80 $\mu$M eosin Y. The deposition was carried out in potentiostatic mode (potentiostat model 7050 from Amel Instruments) at -0.91 V. The ZnO/Eosin Y (ZnO-Ey) film preparation is followed by an eosin Y desorption process in KOH solution at a pH value of 10.5 for 24 hours. The eosin Y desorption does not occur completely and a remnant of 1-2% eosin Y in the ZnO substrate is present. The desorbed film was rinsed with water and dried in air at room temperature.

### 2.2.4 Syntheses and Preparation of the Inverse Opal

#### Preparation of Opal Substrate

As conducting substrate indium tin oxide (ITO, Luminescence Technology Corp., sheet resistance $\leq$20 $\Omega$/sq) was used. The ITO has been cleaned with Milli-Q water, ethanol (p.a., Merck), hydrogen peroxide (100 volume, >30 w/v, Fisher Scientific) and ammoniac (28-30%, p.a., Merck). The polystyrene latex spheres used for the opal substrate have been purchased (PS, microParticles GmbH, diameters 535 and 471 nm, stock solution c = 10 mg/ml). All water was purified using a Milli-Q system (18.2 M$\Omega$/cm).

The opal deposition and pretreatment of the ITO coated glass substrates was a modification of Juárez et.al..[89] First the ITO substrates have been cleaned using ethanol and water. The cleaning step was followed by their surface hydrophilization by placing them in a water/ammoniac/hydrogen peroxide mixture $H_2O$/35% $NH_3$/$H_2O_2$ of 17:3:1 (78.03 ml/30.37 ml/16.60 ml) for 20 minutes and subsequent placement in an ultrasonic bath. After 20 minutes in the ultrasonic bath the ITO substrates were washed with ample amounts of water and dried under a $N_2$ flow.

The cleaned ITO coated glass has then been placed into a snap-cap glass and fixed by a transversely supported platelet. For the opal deposition a 10% polystyrene stock solution has been diluted to give a 0.25% PS suspension, homogenized in an ultrasonic bath for 45 minutes and added into the snap-cap glass. The deposition has been carried out in an oven at 50°C. For vibration minimisation the PS suspension addition has been performed directly by placing a long cannula of a syringe to the wall of the snap-cap glass which was located in a pre-heated oven. For evaporation control the snap-cap glass has been covered by an open 400 ml upside down beaker. The complete evaporation was carried out in a vibration free space over 5-7 days. After the deposition the opal coated ITO has been removed and air-dried for 3 h.

### Preparation of the Inverse Opal

The inverse opal was prepared using the $TiO_2$ gel synthesized analogous to section 2.2.2. For $TiO_2$ gel dilution ethanol (p.a., Merck) and water have been used. All water was purified using a Milli-Q system (18.2 MΩ/cm).

For the opal inversion the opals have been heated close to the glass temperature, in the range between 60° and 90°C. The aim was to determine the optimal conditions to fuse but not liquefy the PS sphere network. The Opal substrates have been heated up to 65°C for 30 minutes. The contact points of the PS spheres have melted together and formed a stable opal framework without any shape loss. The inverse opals have been gained by infiltration of the $TiO_2$ gel suspended in a water/ethanol mixture of proportions 8:2. A dip coating technique has been carried out in a safety cabinet (Herasafe KS, class II) in order to minimise contamination. The opals have been dipped carefully into the $TiO_2$/water/ethanol solution and withdrawn at a speed of 5 $\mu$m/s and the procedure repeated 8 times.

To achieve a more stable structure the infiltrated substrate was dried first at 50°C for 30 minutes. The PS spheres were subsequently eliminated by sintering the substrate at 450°C for 30 minutes.

## 2.2.5 The Syntheses for PbS Nanoparticle

### Synthesis of PbS (Chapter 3 and 4)

For the PbS synthesis the following materials were used: bis(trimethylsilyl)sulfide (purum, Fluka), butanol (p. A., AppliChem), dimethylformamide anhydrous (99.8%, Aldrich), diphenylether (>98%, Acros), lead acetate (99.999%, Sigma-Aldrich), oleic acid (90%, Aldrich), thioacetamide (>99+%, Sigma-Aldrich), tetrachlorethylene (anhydrous 99+%, Sigma-Aldrich), toluene (p.A.), trioctylphosphine (90%, Fluka). For the PbS synthesis all chemicals were used as received with the exception of TOP which was doubly distilled.

The PbS nanocrystals were synthesized in a three-necked flask under an inert atmosphere of $N_2$. A mixture of lead acetate (2 mmol), 1.5 ml oleic acid (4.4 mmol), 2 ml diphenylether (12.6 mmol) and 8 ml of trioctylphosphine (17.9 mmol) was heated under vacuum for 1 h at 80 °C to form lead oleate. The resulting clear and colorless solution was then heated to the injection temperature (140 °C) and a mixture of 0.1 ml thioacetamide (0.67 mmol), 0.1 ml bis(trimethylsilyl)sulfide (0.53 mmol) and 6 ml of trioctylphosphine (13.4 mmol) was injected. The color changed instantly to black and after a growth time of 10 minutes the solution was cooled down to room temperature. For the cleaning-up procedure the particles were precipitated twice using butanol and re-dissolved in toluene. For spectroscopic investigations solutions of the nanocrystals in tetrachlorethylene were used.

### Synthesis of PbS for Ligand exchange (Chapter 4)

For the PbS synthesis the following materials were used: butanol (p. A., AppliChem), lead acetate (99.999%, Sigma-Aldrich), lead(II) oxide ($\leq$ 99%, Sigma-Aldrich), octadecene (90%, technical grade, Aldrich), oleic acid (90%, Aldrich), (trimethylsilyl)sulfide (Aldrich), toluene (p. A.).

The PbS nanoparticles with an absorption wavelength maximum of 1013 nm (sample Pr92) were also synthesized in a three-necked flask under $N_2$. A mixture of 0.4 mmol lead acetate, 3.75 ml octadecene and 0.25 ml oleic acid was heated under vacuum for 1 hour at 80°C to form lead oleate. The clear and colorless oleate solution was heated to the injection temperature (120°C) under $N_2$ and a mixture of 42 $\mu$l (trimethylsilyl)sulfide (0.22 mmol) in 2 ml octadecene was injected. The color changes instantly to black and after a growth time of 10 minutes the solution was cooled down to room temperature. For the cleaning-up procedure the particles were precipitated twice with butanol and re-dissolved in toluene. For spectroscopic investigations tetrachlorethylene was used as solvent. The PbS nanoparticles with an absorption wavelength maximum of 1345 nm (sample Pr67) were again synthesized in a three-necked flask under $N_2$ atmosphere. A mixture of 0.4 mmol lead(II) oxide, 3.75 ml octadecene and 0.25 ml oleic acid was heated under vacuum for 1 hour at 80°C to form lead oleate.

The clear and colorless oleate solution was heated to the injection temperature (160°C) under $N_2$ and a mixture of 42 $\mu$l (trimethylsilyl)sulfide (0.22 mmol) in 2 ml octadecene was injected. The color changes instantly to black and after a growth time of 10 minutes the solution was cooled down to room temperature. For the cleaning-up procedure the particles were precipitated twice with butanol and re-dissolved in toluene. For spectroscopic investigations tetrachlorethylene was used as solvent.

### Synthesis of PbS for the Size Dependence Studies (Chapter 5)

For the PbS synthesis the following materials were used: butanol (p. A., AppliChem), dimethylformamide anhydrous (99.8%, Aldrich), diphenylether (>98%, Acros), lead acetate (99.999%, Sigma-Aldrich), oleic acid (90%, Aldrich), thioacetamide (Sigma-Aldrich), anhydrous tetrachlorethylene, (99+%, Sigma-Aldrich), toluene (p. A.), trioctylphosphine (90 %, Fluka). For the PbS synthesis all chemicals were used as received with the exception of TOP which was doubly distilled.

Three different synthesis were carried out to obtain the four different NP sizes with absorption wavelength maxima of 868 nm (1.47 eV), 1033 nm (1.24 eV), 1169 nm (1.09 eV) and 1570 nm (0.8 eV). The procedures are similar in their steps and synthesis conditions. Only the amount of reagents used in the nanoparticle synthesis and the growth times were varied. The description of the nanoparticle synthesis may be found elsewhere.[90] In brief, the smallest PbS nanocrystals with an absorption maximum at 868 nm were synthesized in a three-necked flask under an inert atmosphere of $N_2$. A mixture of lead acetate (2.1 mmol), 1.5 ml oleic acid (4.7 mmol), 6 ml diphenylether (37.8 mmol) and 4 ml of trioctylphosphine (9 mmol) was heated under vacuum for 1 h at 80 °C to form lead oleate. The resulting clear and colorless solution was then heated to the required injection temperature (150 °C) and a mixture consisting of 0.25 ml thioacetamide (0.67 mmol) and 6 ml of trioctylphosphine (13.45 mmol) was injected. The color changed instantly to black and after a growth time of 5 minutes the solution was quickly cooled down to room temperature. For the cleaning-up procedure the particles were precipitated twice using butanol and subsequently re-dissolved in toluene. For all spectroscopic characterizations solutions of the nanocrystals in tetrachlorethylene were used. A second fraction obtained from this synthesis provided nanocrystals with an absorption maximum at 1033 nm.

The procedure to acquire nanocrystals with an absorption maximum at 1169 nm is almost identical to that described above but with the growth time increased to 10 minutes. To obtain nanocrystals with an absorption maximum at 1570 nm the reaction mixture contained lead acetate (2.2 mmol), 1.5 ml oleic acid (4.7 mmol), 2 ml diphenylether (12.6 mmol) and 8 ml of trioctylphosphine (17.9 mmol) and a mixture containing 0.5 ml thioacetamide (1.3 mmol) and 6 ml of trioctylphosphine (13.45 mmol) was injected. In addition the time of growth was 10 minutes.

### Synthesis of PbS (Chapter 6)

The synthesis of the PbS NPs with an absorption wavelength maximum of 1130 nm, used for the $TiO_2$ studies, is analogous to the synthesis for sample Pr92 used for the ligand exchange as described above.

### Synthesis of the PbS (Chapter 7)

For the PbS synthesis the following materials were used: bistrimethylsilylsulfide (purum, Fluka), butanol (p. A., AppliChem), dimethylformamide anhydrous (99.8%, Aldrich), diphenylether (>98%, Acros), lead acetate (99.999%, Sigma-Aldrich), oleic acid (90%, Aldrich), thioacetamide (Sigma-Aldrich), tetrachlorethylene anhydrous (99+%, Sigma-Aldrich), toluene (p. A.), trioctylphosphine (Fluka).

The PbS nanoparticles were synthesized in a three-necked flask under $N_2$. A mixture of 2 mmol lead acetate, 1.5 ml oleic acid (4.4 mmol), 2 ml diphenylether (12.6 mmol) and 8 ml distilled trioctylphosphine (17.9 mmol) was heated under vacuum for 1 hour at 80°C to form lead oleate. The clear and colorless oleate solution was heated to the injection temperature (150°C) under $N_2$ and a mixture of 0.1 ml thioacetamide (0.67 mmol) in dimethylformamide (0.5 g/ml), 0.1 ml bis(trimethylsilyl)sulfide (0.53 mmol) and 6 ml distilled trioctylphosphine (13.4 mmol) was injected. The color changes instantly to black and after a growth time of 10 minutes the solution was cooled down to room temperature. For the cleaning-up procedure the particles were precipitated twice with butanol and re-dissolved in toluene. For spectroscopic investigations tetrachlorethylene was used as solvent. The particles have an absorption maximum at 1056 nm (1.17 eV)

#### Synthesis of PbS (Chapter 8)

For the PbS synthesis the following materials were used: butanol (p. A., AppliChem), diphenylether (>98%, Acros), lead acetate (99.999%, Sigma-Aldrich), oleic acid (90%, Aldrich), (trimethylsilyl)sulfide (Aldrich), trioctylphosphine (90 %, Fluka), toluene (p. A.).

The PbS nanoparticles were synthesized in a three-necked flask under $N_2$. A mixture of 2 mmol lead acetate, 10 ml diphenylether and 1.5 ml oleic acid was heated under vacuum for 1 hour at 80°C to form lead oleate. The clear and colorless oleate solution was heated to the injection temperature (125°C) under $N_2$ and a mixture of 0.15 ml (trimethylsilyl)sulfide in 2 ml trioctylphosphine was injected. The color changes instantly to black and after a growth time of 10 minutes the solution was cooled down to room temperature. For the cleaning-up procedure the particles were precipitated twice with butanol and re-dissolved in toluene. For spectroscopic investigations tetrachlorethylene was used as solvent.

### 2.2.6 Preparation of the PbS Coated Substrates

#### The Ligand exchange at PbS

The ligands normally at the PbS NP surface have been exchanged using 3-(mercaptopropyl)trimethoxylsilane (MPTMS, >97% (GC), Fluka) and hexane (p.a., Merck).

For the ligand exchange 20 $\mu$l MPTMS have been added to 100 $\mu$l of a concentrated PbS solution (in toluene) in a 2 ml centrifuge tube. The mixture has been suspended in an ultrasonic bath for a maximum of 5 minutes and subsequently washed 2-3 times by the addition of 300 $\mu$l hexane and centrifuged at 13k rpm for 5 minutes. The precipitation and centrifugation of the PbS in hexane is easily achieved for relatively big nanoparticles with an absorption maximum down to approx. 1300 nm. Smaller particles, with an absorption maximum from approx.

1200 nm down to the visible range, have to be cooled with liquid nitrogen before the centrifugation has been initiated, otherwise precipitation will not occur.

#### Deposition of the PbS on ITO Coated Glass

Dichloromethane (DCM, puriss. absolute, over molecular sieves, $H_2O \leq 0.005\%$, Sigma-Aldrich) was used as solvent. As conducting substrate indium tin oxide (ITO, Luminescence Technology Corp., Sheet Resistance $\leq$20 Ω/sq) was used and cleaned by Extran solution (Extran MA 01, Merck). All water was purified using a Milli-Q system (18.2 MΩ/cm).

The ITO substrates have been cleaned by immersion in a 10% Extran solution and placement in an ultrasonic bath for 10 minutes. After the first cleaning the ITO glasses have been washed well with Milli-Q water and have been placed again in a beaker with Milli-Q water in an ultrasonic bath for a further 10 minutes. Each cleaned ITO substrate has then been placed in a 100 ml Erlenmeyer flask with the conductive side facing up.

The cleaned PbS precipitate and the Erlenmeyer flasks have been placed in the glovebox. Under a water and oxygen free atmosphere the PbS has been dissolved in 4 ml anhydrous DCM and poured into the Erlenmeyer flasks containing the ITO. The PbS coated ITO can be removed after 24 hours deposition time and the unconductive side cleaned with sulphuric acid. The deposition has been achieved by agitation in a shaker (model GFL3006).

### 2.2.7 Preparation of the ISC

#### Preparation of the ISC using ZnO or $TiO_2$ gel

As conducting substrates indium tin oxide (ITO, Merck, Sheet Resistance $\leq$20 Ω/sq) and flourine doped tin oxide (FTO, Sheet Resistance $\leq$5 Ω/sq) were used and cleaned using an Extran solution (Extran MA 01, Merck). The preparation of the ZnO/linker/PbS substrates was carried out from solutions in tetrahydrofuran (THF, Acros Organics). All water used was purified using a Milli-Q system and had a resistance of 18.2 MΩ/cm. The molecules employed in this study to link the PbS nanoparticles to the ZnO were thioacetic acid (TAA, 96%, Aldrich), thioglycolic acid (TGA, >98%, Fluka), 3-mercaptopropionic acid (MPA, >98%, Fluka), 1,6-hexandithiol (HDT, >97%, Fluka), oxalic acid (OA, 99%, KMF) and malonic acid (MA, 99%, AppliChem).

The metal oxide was coated onto a transparent conducting oxide (TCO) coated glass substrate of either FTO or ITO. The metal oxides synthesized by sol-gel methods have been applied to the TCO surface by spin coating. In all cases the TCO had previously been boiled in a 5 % extran-solution for approx. 15 minutes. This is required for surface cleaning and also for the functionalization of the surface to provide a stronger metal oxide attachment to the TCO. The conditions employed were such that layers could be prepared to be of the same thickness each time. The thickness plus its reproducibility were verified using UV/Vis spectra in the case of the metal oxides synthesized by the sol-gel technique. After sintering, the TCO/metal oxide substrate was placed into a solution of the linker in THF (0.2 M) for approx. 4 hours. Subsequently the substrate was washed with THF and then added to a solution of the PbS nanoparticles in THF (0.0002 mM) for 12 hours. The substrate may thus be visualized to be composed of a layer-by-layer structure whereby the PbS is bound to the metal oxide layer through a linker. Generally the substrate structure may be described as TCO/metal oxide/linker/PbS. The kind of linker, TCO, metal oxide material and PbS sizes that have been used are noted separately in each chapter.

### Preparation of the ISC for the ZnO/Eosin Y and Inverse Opal Substrate

Because of the complex structuring of the metal oxides in the case of ZnO/Eosin Y and the inverse opal the preparation of the FTO/ZnO-EY and ITO/inverse opal substrate is connected to the synthesis of these materials. Hence the reader is referred to section 2.2.3 for the FTO/ZnO-EY substrate preparation and to section 2.2.4 for the ITO/inverse opal substrate preparation. Here only the deposition step for the MPA linker and the PbS NP is analogous to the procedure above.

The TCO/metal oxide substrate was placed into a solution of the linker in THF (0.2 M) for approx. 4 hours. Subsequently the substrate was washed with THF and then added to a solution of the PbS nanoparticles in THF (0.0002 mM) for 12 hours. Generally the substrate structure may be described as TCO/metal oxide/linker/PbS as mentioned above.

### 2.2.8 Material Characterisations and Instrument Settings

UV/Vis absorption spectra of the substrate were collected using a Cary 5000 spectrophotometer (Varian). For the absorption measurements of the substrate a blank TCO (ITO or FTO) has been used as a background reference. In reflection mode the Cary 5000 was used with the VASRA attachment (variable angle specular reflectance accessory). All VASRA measurements were done at an angle of 20°.

FTIR spectra were recorded on a Nicolet 5700 FTIR spectrometer (Thermo). To minimise as far as possible the water adsorption onto the surface immediately after the deposition of the linker on the ZnO surface each substrate was placed into a desiccator. Afterwards the samples were purged for 5 minutes under an Argon flow and purged for further 30 minutes in the FTIR instrument with $N_2$. The water vapour signals higher than 3500 $cm^{-1}$ and between 2000 $cm^{-1}$ and 1300 $cm^{-1}$ and a $CO_2$ signal at 2300 $cm^{-1}$ were however corrected for by using an ITO/ZnO substrate as reference. The number of scans recorded was 200.

The X-ray diffraction (XRD) measurements were carried out on a D5000 diffractometer (Siemens, Cu $K_\alpha$ radiation). For all measurements of the ZnO/linker/PbS layered structures ITO was used as the substrate support. Only in the case of the reference XRD measurement of the PbS nanoparticles was this altered and a Si wafer was used as substrate.

The ICP-OES determinations were realized using a Perkin-Elmer Optima 7000DV with a wavelength range of 160-900 nm, a $CaF_2$ prism and SCD-detector. The PbS nanoparticles were dissolved in 3 M $HNO_3$ solution.

SEM images were taken on a Zeiss Gemini 982 spectrometer with a thermal field emission cathode and on a Zeiss SMT with a field emission cathode Ultra55 as well as a SE2- and in-lense detector for secondary electrons. TEM images were obtained on a Phillips EM208 microscope.

The light source for the wavelength dependent photocurrent transients and IPCE measurements was a 75 Watt Xenon lamp (Oshio) dispersed using an MD-

1000 monochromator. For the IPCE measurements an Autolab PGSTAT302 potentiostat (Ecochemie BV), 7265DSP Lock-In Amplifier (Signal Recovery) and C-995 Optical Chopper (Terahertz Technologies Inc.) were used. This instrumentation was controlled using the NOVA 1.6 (Metrohm) and the Signal Recovery Acquire 4.0 software. A calibrated silicon photodiode (model FDS100-CAL from Thorlabs Inc.) was used to determine the lamp photon flux density. Further (opto-)electrochemical measurements were undertaken using a Zahner IM6 equipped with a CIMPS (XPOT) system and controlled and recorded by the proprietary software Thales. The LEDs used for illumination had a peak intensity at 370nm (3.33 eV) and 470 nm (2.62 eV) and were powered using a BUVZ01 integrated LED light source system. The LED LW570 and LW630 light with a maximum peak intensity at 570 nm (2.16 eV) and 630 nm (1.96 eV) were powered using the Zahner light source holder T01. The illumination intensity range, across which the intensity response was linear, was determined and in this study an illumination intensity of 10 $W/m^2$, which was within this linear region, was used. The measured EIS data was fit to the model using the proprietary software package NOVA 1.6 (Metrohm).

For analysis of the injection solar cell a three electrode alignment has been employed. A Pt-sheet was utilized as a counter electrode (CE) and a 0.1 M sodium sulfite solution ($Na_2SO_3$, p.a., Grüssing), a well established hole scavenger,[44,45,91–93] was employed as the background electrolyte with an Ag/AgCl/3M NaCl (BAS inc.) electrode being used as the reference (RE). All electrochemical potentials reported within are relative to this reference electrode. The sensitized substrate, whose preparation was depicted above, was employed as the working electrode (WE). Under conditions of irradiation the light will illuminate the cell as depicted in Figure 2.8.

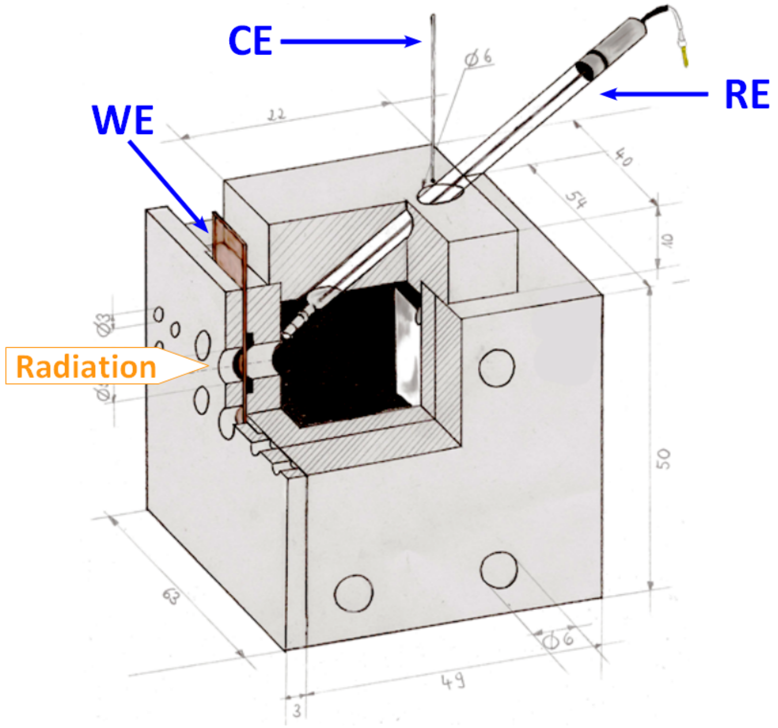

Figure 2.8: The injection solar cell electrochemical compartment in three electrode assembly. The counter electrode (CE) is a Pt-sheet and an Ag/AgCl electrode was used as reference electrode (RE). The prepared substrate acts as the working electrode (WE). The light impacts on the 0.5 cm diameter hole and onto the WE substrate which illuminates the substrate in the sequence: glass/TCO/ZnO/linker/PbS.

# 3

# The Linker Attachment on a ITO/ZnO Substrate

## 3.1 Introduction

Many kinds of injection solar cells are now part and parcel of modern research. More and more the technologies used for ISC performance enhancement are intertwining with nanotechnology. This alliance is also reflected as a basic part of this thesis. The essential construction of the ISC studied here includes a transparent conducting oxide, a nano-structured wide band gap metal oxide, PbS nanoparticles, a linker to connect the NPs to the MO surface as well as an electrolyte containing a hole scavenger and a Pt-sheet as counter electrode.

The TCO is employed because of its multiplicity of advantages, for instance the high transparency and conductivity, chemical stability, low cost and non-toxicity.[94] In contrast to metal films and foils TCOs also feature a long term stability and hardness.[95] For the following studies indium tin oxide (ITO), a common TCO in many photoactive devices[96–100], was selected. Further details concerning the characteristics of the material, such as its electron transfer properties and optical effects may be found in the literature.[94,95,101]

On the ITO a further metal oxide, nanoporous ZnO, has been deposited. In the literature ZnO is a well known material which combines the typical metal oxide stability in air and advantageous electronic properties. The electronic characteristics of ZnO allow new industrial and technological applications in optical and electro-optical devices, in ceramics as well as in the fields of lasing and photovoltaics.[95,102] In addition to the most investigated MO $TiO_2$[103–105] ZnO therefore represents an alternative material. In contrast to the more common $TiO_2$ the electron mobility of ZnO is generally an order of magnitude larger.[106] The dimension of the electron mobility is dependent on the fabrication, film structure and the cristallinity, so that for ZnO the range of the electron mobility is between 1 and 155 $cm^2/V{\cdot}s$[107,108] and for $TiO_2$ between $10^{-6}$ and 1 $cm^2/V{\cdot}s$[109–111] can be found. A similar behavior can be found in the electron transport times and the light intensity dependence where the electron lifetime in ZnO is significantly higher than that of $TiO_2$.[112] Therefore the ZnO is deemed to be a material which can also be used as a thin transparent conducting[95] layer as is the case for ITO. The synthesis and preparation methods of such materials are as diverse as the properties of the ZnO films themselves. The sol-gel synthesis yields ZnO particles with a quite narrow size distribution which crystallize in the hexagonal wurtzite (B 4-type) lattice.[95,102] But a major benefit is that of network formation, also called gelation and explained within the framework of percolation theory. The ZnO particles align themselves by stringing together to form a nanoporous network (Figure 3.1(a)).[113,114] The coating of such a gel has been achieved by spin coating techniques[115,116] but there are a number of alternative methods existing for the preparation of thin ZnO films for instance sputtering[95,117,118], spray pyrolysis[95,119,120], chemical vapor deposition[95,121,122] or electrodeposition[123,124] methods. These nanoporous networks provide a huge surface area which allows a high degree of material loading. For that reason a large amount of absorbing material in photovoltaic applications can be incorporated because of the provision of sufficient space. Another beneficial property is the energetically wide band gap of this material[55] which makes it possible to control the transfer of the electron from the excited state of the absorber, in this thesis the PbS NPs, to the ITO/ZnO substrate.[2,12] Certainly the regeneration of the hole in the PbS VB, which occurs generally at the PbS-electrolyte interface, must not be forgotten from the complete mechanism of electron-hole separation (see section 2.1.3). But in the first instance the ZnO-PbS interface is most important in this chapter. The connection between the ZnO and PbS is dependent on their surface functionalization. Often a physisorption of the NCs is not efficient or stable enough

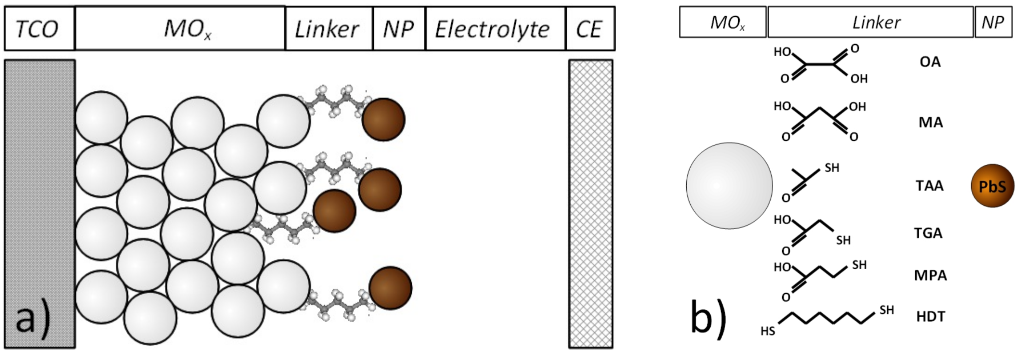

Figure 3.1: The substrate composed of a layer-by-layer structure. a) A transparent conducting oxide (TCO) is covered by a metal oxide ($MO_x$) film of a specific thickness. This film is sensitized by PbS nanoparticles which are linked to the $MO_x$ surface through a carpet of linker molecules. b) The ISC substrates which were used in this thesis consist of a $MO_x$ (either ZnO or $TiO_2$), one of 6 linkers and the PbS NPs.

which then necessitates the use of special linker molecules. The surface functionalization of each material decides which kind of functional groups the linker must possess to ensure an effective bond.[125] Accordenly for the ZnO a hydroxide stabilized surface is expected. Ergo, it is obvious to choose an approach in which the linker has a carboxylic group which can bind covalently to the Zn-OH surface. For the PbS a very good attachment was observed with thiol functionalized organic molecules. Such thiols have also been used as stabilizers in nanocrystal synthesis.[126] However, this kind of stabilization of PbS NPs does not mean that other kinds of linker with different functional groups for instance carboxylic, hydroxide, amine or silane groups would not be able to attach to the PbS surface. Also the assumption that the ZnO can link only to carboxylic groups is also quite implausible.

The kind of the solvent used during the deposition steps also has a strong influence on the quality of the self assembled monolayer. The orientation and quality of the monolayer are influenced by the presence of ions during the deposition step and is an observation that has been reported in the literature.[127,128] The deposition step in these studies was performed in the relatively inert solvent THF so that such negative influences have been minimized.

In the end the linkage is far more complex and involves more than just the connection between the NP onto the metal oxide surface. Through the intermolecular and intramolecular interactions a linker can effect band edge changes in semiconductors, the trap depth[129,130], the surface functionalization[125] (which is directly related to the kind of linker bound to the surface), the distance between the QD and metal oxide surface[131,132] (which is related to the linker and consequently to the charge tunneling rates), as well as directly influence charge separation. Therefore the influence that the linker has on these processes has to be separated, quantified and placed within a framework that allows us to understand them better.

In the next two chapters a study concerning the ISC assembly of ITO/ZnO/linker/PbS with a structure as shown in Figure 3.1(a) is presented. Six different linkers were used in the study. The linkers are distinguished by varying the alkyl chain length and the choice of either acid and/or thiol groups employed as the attachment moieties at the linker ends. The different linkers employed are oxalic acid (OA), malonic acid (MA), thioacetic acid (TAA), thioglycolic acid (TGA), 3-mercaptopropionic acid (MPA) and 1,6-hexandithiol (HDT) (Figure 3.1(b)). First this chapter will present the characteristics of the ITO/ZnO film and ITO/ZnO/linker film and in particular some essential questions concerning the kind of attachment of the linker to the ZnO surface will be considered. Subsequently the orientation of the linker, which functional group is located on the ZnO surface and which interaction is generated between the ZnO surface and the linkers, will be addressed.

## 3.2 The ITO/ZnO Film

### 3.2.1 The ZnO Layer and the ITO/ZnO Substrate Preparation

The synthesis of the ZnO resulted in a colorless gel with an absorption onset at 380 nm which generated a broad emission band at 540 nm as a result of trap and defect states.[85,133] The yellow emission results from incorporation of lithium, which acts as an acceptor, into the ZnO, the lithium initially being present during the synthesis.[102,134] The ZnO thickness was observed to have an important influence on the measured photocurrent response profile. From the ZnO thickness versus photocurrent profiles (Figure 3.2) it can be seen that a linear increase in the photocurrent response resulted for the different thicknesses of the ZnO layers. The on/off illumination experiments gave a sharp cornered square wave shaped photocurrent response for thin and strong rounded square wave shape for thick ZnO layers. It was also observed that the samples with the thickest ZnO layers reach an expected maximum in the photocurrent magnitude. Consequently the ability to obtain electrodes containing a reproducible ZnO layer thickness is of importance if valid comparisons are to be made. Conditions were employed such that layers could be reproducibly prepared to be of the same thickness, the thickness of the ZnO layer being selected such that no thickness induced limitations in the photocurrent magnitudes resulted, and the thickness plus its reproducibility were verified using UV/Vis spectra (Figure 3.3).

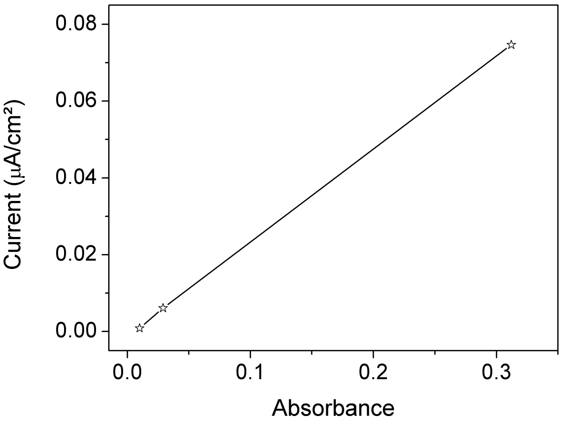

Figure 3.2: Measured photocurrent as a function of the absorbance at 470 nm for three different thicknesses of ZnO layer. The excitation wavelength employed for the photocurrent measurement is 470 nm which is equal to the absorbance wavelength.

Generally the samples show an absorption profile as shown in Figure 3.3(a). The most noticeable characteristic is the scattering down to 375 nm although it was possible once to achieve a synthesis which yielded a ZnO film with low scattering. The synthesized ZnO which was used for the linker dependence study was obtained from a suspension solution with very low scattering (Figure 3.2(b)) due to its small particle sizes, however this synthesis was not reproducible. The values in the absorbance profile of the sample at wavelengths at 270 nm and

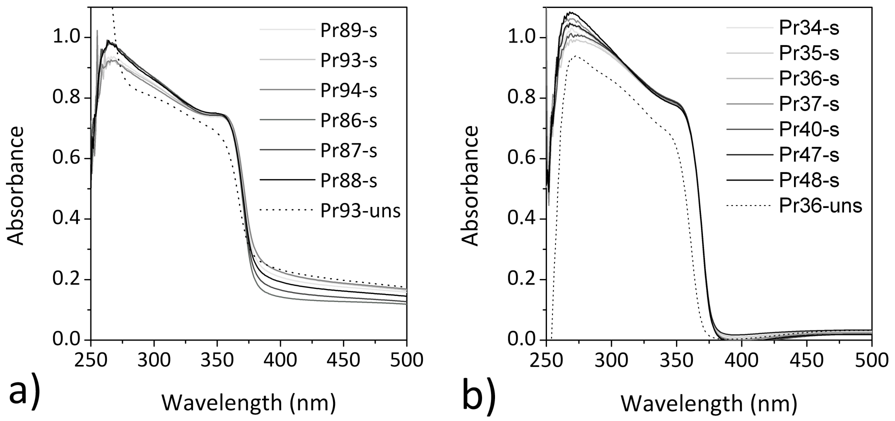

Figure 3.3: UV/Vis spectra of sintered ZnO layers (PrX-s where X is an internal sample reference number) on ITO. The sintering at 300°C results in a slight red-shift of the peak and an increase in the absorption when compared with the unsintered ZnO layers (PrX-uns). The a) ZnO absorbance with scattering b) ZnO absorbance without scattering is shown. The samples in b) have been used for the linker dependence study.

shorter decreases due to the high absorbance of the bare ITO substrate used as reference.

From SEM images (Figure 3.4) the ZnO films were confirmed to be homogenous and have a thickness of between 300 and 400 nm. From further SEM images

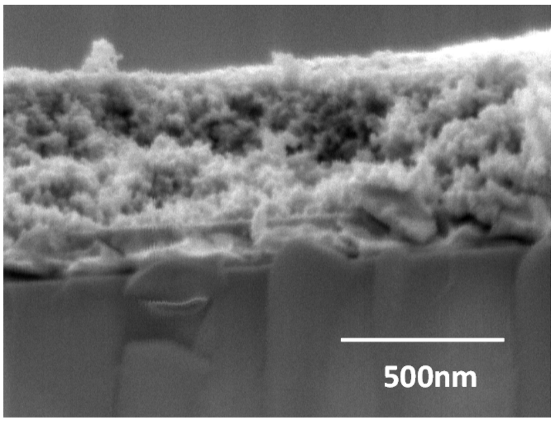

Figure 3.4: SEM-image of a 400 nm thick homogenous nanoporous ZnO layer on ITO.

(not presented) an average ZnO crystallite diameter of from 10 nm up to 16 nm has been observed for samples which were sintered at 300°C. Earlier studies on ZnO layers have shown equivalent particle sizes and ZnO-layer properties[135] as well as a thickness dependence of the photocurrent transient profiles within such systems as investigated here.[76]

### 3.2.2 The ZnO Structure as a Function of the Sintering Temperature

Not only does the thickness of the ITO/ZnO film have an influence on the photocurrent but also the sintering temperature plays an important role in determining the ZnO layer properties. In the work of Noack[135] the structure and electrochemical characterisation of the prepared ITO/ZnO film as a function of the sintering temperature has been studied. Different ITO/ZnO films have been sintered at 100°C, 200°C, 300°C, 400°C and 500°C. An unsintered ITO/ZnO film was used as reference. The absorption spectra of the ITO/ZnO films were observed to display distinct differences (Figure 3.5). A red shift of the absorption band with higher sintering temperatures is seen. At 400°C and 500°C the absorption band structure is also seen to possess a separate absorption maximum. Furthermore for temperatures up to 300°C the ZnO structure is not strongly altered.

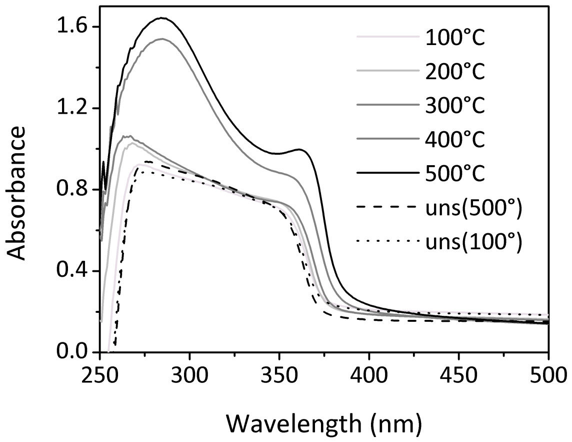

Figure 3.5: UV/Vis spectra of ITO/ZnO layers sintered at different temperatures (100°C up to 500°C). Before the sintering of the films the absorption spectra was also measured (unsintered samples = uns)

XRD measurements of the ZnO film on pure glass have been undertaken to ensure that no modification changes have occurred (Figure 3.6) and it can be seen that the XRD reflex positions of the sintered films do not show any changes. But the full width at half maximum and their sharpness provide evidence of changes in the sizes of the ZnO particles. The reflexes are broader in the case of smaller particles due to the fewer atomic planes which contribute to the diffraction signal. The transitions between destructive interference and diffraction are distinctly diffuse.[136]. The defects and inhomogeneities in their crystallinity also cannot be averaged out resulting in a broader XRD signal.[137] Hence the XRD measurements also reflect the increase in the particle sizes with increasing sintering temperature. It is possible to calculate the size of the ZnO modifications from an XRD diffractogram using the Debye-Scherrer relation. The freshly made ZnO gel had an average diameter of 18 nm whereas the ZnO gel aged for one week had an average diameter of approx. 28 nm due to agglomeration. Generally homogenous films will not be obtained with ZnO gels which are older than 3 days. For this reason the results of the Debye-Scherrer calculation are not be presented for these samples.

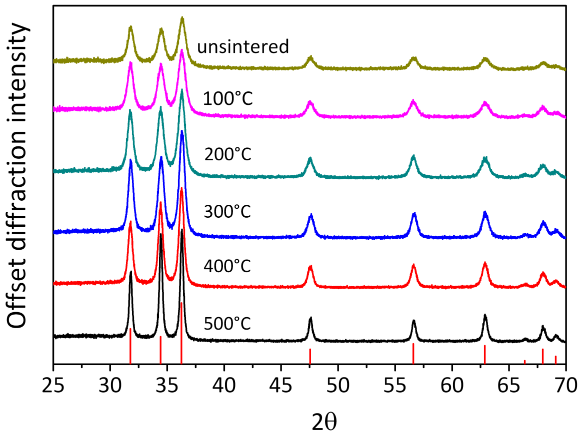

Figure 3.6: XRD diffractogram of a thick layer of ZnO on normal glass after sintering at different sintering temperatures. The red lines along the x-axis represent the position and relative intensities expected for ZnO.

In addition SEM measurements of freshly prepared ITO/ZnO films have been made. Whereas the structure and the shape of the ZnO films can be observed in the SEM, it is also possible to determine the sizes of the ZnO particles. In Figure 3.7 the SEM images of selective samples are shown. The ITO/ZnO sample sintered at 300°C was not measured because no significant differences between the 200°C and 400°C samples could be seen.

Generally it can be observed that the layers have a nanoporous structure. Due to the pore diameters of approx. 20 nm, as determined from the SEM images, a mesoporous structure can be inferred. The porous topology is formed from a loosely packed structure of small ZnO nanocrystals as is expected. The unsintered and the sintered films up to 300°C shows no significant changes. If the size distributions in Figure 3.7 are examined it is possible to observe slight differences between sample a), b) and c). After sintering at 100°C a shrinking of the particles as well as the structure is found which could be as a result of the drying effect of the ZnO. At 200°C a small expansion in the particle size distribution occurs. The distribution ratios shift to larger sizes which is clearly seen in Figure 3.7(d) at a sintering temperature of 400°C. However, large differences have not been observed. A strong change appeared only after sintering at 500°C. The size distribution is observed to be in the range between 24 and 70 nm. The shape to the porous structure is more compact and the necks between the particles start to grow and quite often the spherical shape of the particles can no longer be identified. ZnO is not an easy material to handle in the SEM microscope as during the recording of the SEM images it was noted that the image often shifted out of the display due to strong charging of the layers. For this reason a high capacitance for the material is expected. Due to the existing conductivity of the ZnO film no gold was required to be sputtered onto the ZnO surface. With the increase in the sintering temperature from 400°C to 500°C the charging of the sample strongly decreased. The compact structure, as seen in Figure 3.7(e) and the additional connections between each particle formed during the necking process is a reason for the strong change in the electrical properties.

A similar response for the ITO/ZnO films was ascertained in the cyclic voltammetry. The cyclic voltagram under dark conditions (Figure 3.8(a)) and under UV irradiation (Figure 3.8(b)) shows different I/E behavior. The curves are quite similar at potentials higher than -0.3 V under non-illuminated conditions. Under UV (370 nm) irradiation a strong response change was measured in this range. It appears that with the increase in the sintering temperature the resistance of the layer becomes lower. Excitation generation and consequent recording of the

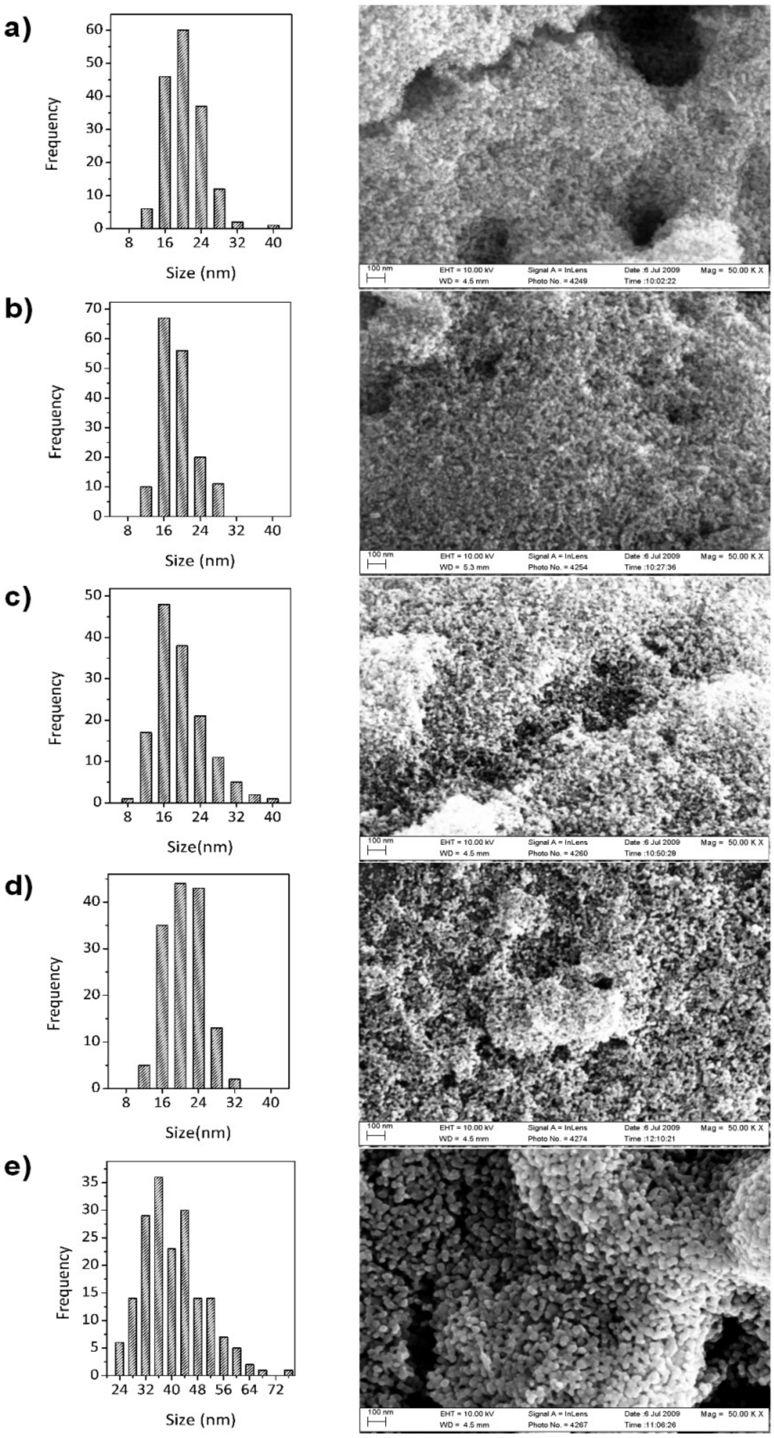

Figure 3.7: SEM-image of the homogenous mesoporous ZnO layer on ITO by using different sinter temperatures. (a) unsintered (b) 100°C (c) 200°C (d) 400°C (e) 500°C

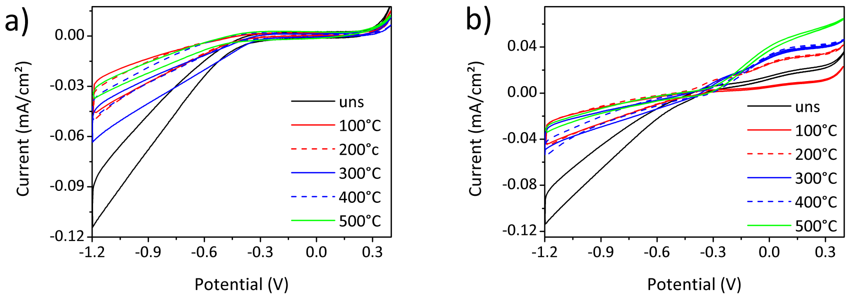

Figure 3.8: The cyclic voltagram of the ITO/ZnO film under different sintering temperatures (100°C - 500°C). The unsintered sample (uns) is employed as reference. Under dark conditions (a) the curves are quite similar at potentials higher than -0.3 V. These responses changed strongly under UV illumination (370 nm).

photocurrent is possible under UV illumination. This effect is similar to the impinging electron beam in the SEM. The electrons enter the ZnO layer and charge it and subsequently the film then needs to be discharged. How efficiently the charges move to the back contact is dependent of the sintering temperature. The more compact the ZnO network the more the ZnO particles are bound to each other and consequently the higher the conduction of the ZnO layer.

The above mentioned photocurrent response is presented in Figure 3.9. The unsintered and the 100°C sintered sample show the lowest photocurrent. All samples which were sintered at a higher temperature than 100°C show almost the same photocurrent intensity. These measurements are performed at open circuit potential (ocp) and therefore near conditions of equilibrium.

The photocurrents were also measured over a potential range of 0.4 V to -1.2 V using linear sweep voltammetry (image not included). The highest photocurrent between the potentials of -0.2 V and 0.4 V comes from the samples sintered at 400°C and 500°C. The lowest photocurrents are measured from the unsintered and the 100°C sintered ITO/ZnO films. However, all samples displayed no photocurrent response at a potential of approx. -0.5 V. This potential indicates the potential when the CB of the ZnO gel comes in conjunction with the applied potential. This phenomenon has also been observed in the literature[138] and will be addressed in a later section.

In summary therefore it may be concluded that no real changes occur in the ZnO layers up to a sintering temperature of 300°C. At higher sintering tem-

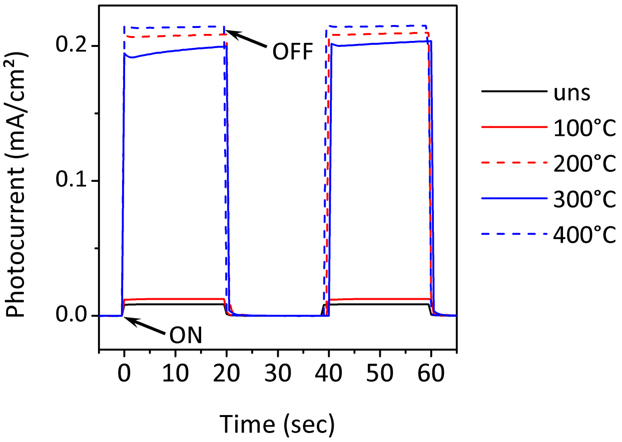

Figure 3.9: The photocurrent response of the ITO/ZnO film which were sintered at different temperatures (100°C to 400°C). The unsintered sample (uns) acts as reference. The illumination source has a maximum wavelength at 370 nm and the sample was radiated with a 20 sec on/off pulse.

peratures the optical, electrical and structural properties are strongly changed. Although the more highly tempered ZnO films generate the highest photocurrent and discharge electrons more efficiently. Furthermore, the more highly tempered samples are quite different to the ZnO synthesized gel. For that reason in the following studies the ITO/ZnO films have been sintered at 300°C and it is of some note that in the literature this temperature has often been reported as being used for sintering.

## 3.3 The Linker on the ITO/ZnO Film

### 3.3.1 The Linker Orientation on the ZnO layer

As knowledge concerning the attachment and orientation of the linker to the ZnO interface is of utmost importance for the attachment of the nanoparticles and impacts greatly on the charge carrier transfer rates, an FTIR-study of the attachment of the linker molecules to the ZnO was undertaken. The ITO/ZnO substrates were immersed in a solution of the linker and after immersion the FTIR-spectra of the ITO/ZnO/linker systems were taken and found to possess significant signals related to the alkyl and acid groups (see Figure 3.10). The

FTIR peak associated with thiol groups is expected to be in the region from 2600 to 2550 cm$^{-1}$. Most likely as a result of low concentration at the ZnO surface, which is expected to be at best monolayer coverage, and the generally low peak intensity associated with the thiol-group stretching signature, no signal for these functional groups was ascertainable in the FTIR-spectra (see Table 3.1 below for all expected signals and their associated vibrations).

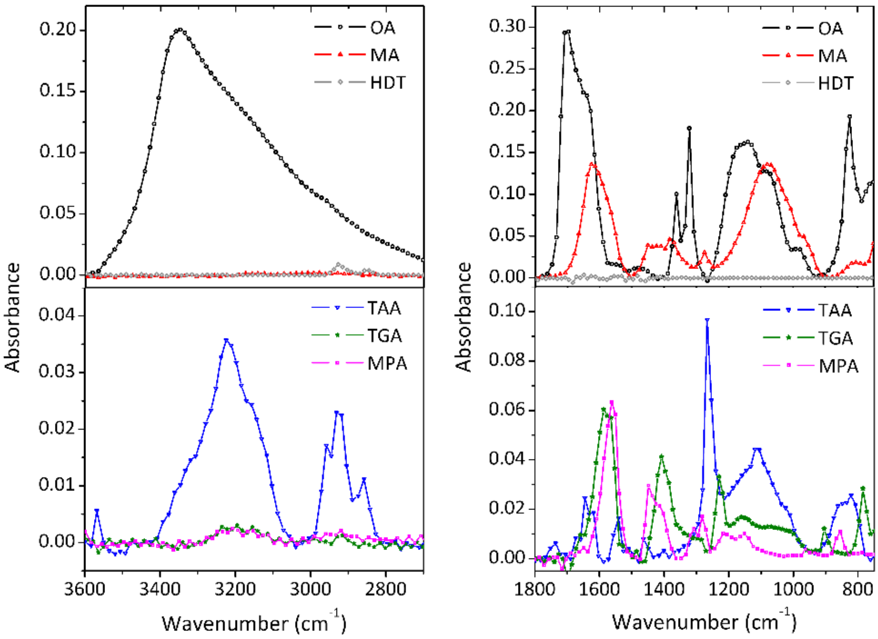

Figure 3.10: FTIR spectra, in the range 3600-2700 cm$^{-1}$ (right) and 1800-750 cm$^{-1}$ (left) of the linkers on the ZnO-layer.

In the region around 3200 cm$^{-1}$ broad bands were obtained from linker molecules containing acid groups. If the assumption that the carboxylic acid functional group is attached to the ZnO-surface and the second functional group is pendant into the solution is correct then it is possible that the non-bonded carboxylic acid groups of the dicarboxylic acids can form mutual H-bonds.[150] The H-bonds of the OA and MA molecules and the strong pH-dependence of their spectra have been well documented.[142] It is also documented in the literature which parts of the OA and MA acid group are bound to the surface of $TiO_2$[140], CrO[139] and kaloinite[143] and no deviances from the reported behavior are to be intuitively expected in this study. The connection of the dicarboxylic acids to the surface

| OA<br>[139–143] | MA<br>[144,145] | TAA<br>[146,147] | TGA<br>[148,149] | MPA<br>[150] | HDT<br>[151–153] | Assignment |
|---|---|---|---|---|---|---|
| 3347s/vb | - | - | - | - | - | $\nu$(OH) stretch |
| - | 3195vb | 3224vb | 3249vw | 3224vw | - | $\nu$(C-O-) bound |
| - | - | 3170sh | - | - | - | |
| - | - | 2958sh | 2917vw | 2939vw | - | $\nu$(CH) asymmetric |
| - | - | 2931m | - | - | 2927s | |
| - | - | 2858m | - | - | 2846s | $\nu$(CH) symmetric |
| 1709s | - | - | - | - | - | $\nu$C=O |
| 1639sh | 1626s | 1654m | 1658sh | 1565s | - | $\nu$COO$^-$, $\nu$C-O$^-$ |
| - | - | 1631sh | 1587s | - | - | |
| 1549vw | 1448m | - | 1408s | 1440m | - | $\nu$C-O |
| 1479vw | - | - | - | 1405sh | - | |
| - | 1421m | - | - | - | - | CH$_2$ bending |
| 1361m | 1381m | - | 1311sh | 1315m | - | $\delta$(OH) |
| 1321m | 1328sh | - | - | - | - | $\delta$(OH), $\nu$C-O |
| - | - | 1267s | 1230m | 1280m/b | - | CH$_2$ twisting+$\delta$(CH$_3$) |
| - | - | - | - | 1216m/b | - | |
| - | 1273m | 1189sh | 1160m/b | 1147m/b | - | CH$_2$+CH$_3$ wagging |
| - | - | 1159sh | - | - | - | |
| - | - | 1118m/b | - | - | - | |
| 1139m/b | - | - | - | - | - | $\delta$(OH), $\nu$C-O |
| - | - | - | - | 1045sh | - | |
| 1081sh | 1080s | 1014sh | 1092sh | 978w | - | $\nu$ C-C |
| 991sh | 966sh | - | - | 935sh | - | |
| - | - | 862sh | 905w | 853m | - | $\delta$(SH) |
| - | - | 822w | - | - | - | |
| 823m | 804sh | - | - | - | - | OCO bending |
| - | - | 756sh | 784,9m | 785vw | - | CH$_2$+CH$_3$ rocking |
| - | - | - | 714m | - | - | |
| 762w | 737m | - | - | - | - | $\tau$C-O, $\delta$(COOH) |
| - | - | - | - | 676m | - | $\nu$(C-S) |

Table 3.1: Observed FTIR-band positions (cm$^{-1}$) and their assignment: vs, very strong; s, strong; m, medium; w, weak; vw, very weak, b, broad, vb, very broad, sh, shoulder. The numbers in the header row refer to the relevant references.

of the ZnO as ions is further confirmed by the presence of bands at 1639, 1479 and 1361 cm$^{-1}$ in the case of OA[154] and 1628, 1448, 1421 and 1381 cm$^{-1}$ for MA (Figure 3.11(B)). Hanrahan et.al.[155] have ascribed the peak shift that arises for MA to be due to the dissociation of the carboxylic acid groups. Hence the peaks present at approx. 1600 cm$^{-1}$ may be attributed to that of COO$^{-}$-groups whereas the signature that appears at around 1700 cm$^{-1}$ are signatures associated with the COOH groups. The presence of a signal at 1709 cm$^{-1}$ in the case of OA (Figure 3.11(A)) also gives an indication that some carboxyl groups (e.g. the C=O bond) are still present.

The TAA molecules (Figure 3.11(C)) can link to the surface via the C=O functionality. The strong bands at 3200 cm$^{-1}$, 1654 cm$^{-1}$ and at 1631 cm$^{-1}$ are evidence of C-O- bonds (dissociated OH-groups) through which the linking to the surface occurs. Because the oxygen is bound to the oxide surface the vibration signal shows a slight shift compared to that of the C=O stretches of the TAA, which have been reported in the literature to occur at 3360 cm$^{-1}$ and 1696 cm$^{-1}$.[146,147] Also present are signals with a high intensity associated with the CH-stretching vibrations at 2900 and 2800 cm$^{-1}$ due to the presence of methyl-groups. By comparison to the $CH_3$-group present in the TAA, the CH-stretching vibrations of the HDT molecule can only be due to $CH_2$-groups as only these are present within the alkyl chain. TGA (Figure 3.11(D)) shows a dominant carboxylate linking to the surface which is confirmed through the presence of a weak signal at 3200 cm$^{-1}$. The signal at 1587 cm$^{-1}$ provides evidence of a dissociated acid group. The MPA (Figure 3.11(E)) linker which contains an even higher number of $CH_2$-groups than TGA is also attached to the ZnO only by the carboxylate group. This linker shows significant signals at 1562 cm$^{-1}$ for COO$^{-}$-groups and also has a weak signal at 3200 cm$^{-1}$. As expected it was not possible to observe the C-S signal at approx. 650 cm$^{-1}$ for the substrate covered with the HDT-linker (Figure 3.11(F)) due to its very weak intensity. As a result of the FTIR study it may therefore be proposed that the connection of the linkers to the ZnO surface is that as represented in Figure 3.11. In previous reports, the electron transfer of a number of linker molecules with various alkyl chain lengths were studied using STM, optical, kinetic and electrochemical measurements. It was demonstrated that the molecular interactions within the film, the type of assembly, the

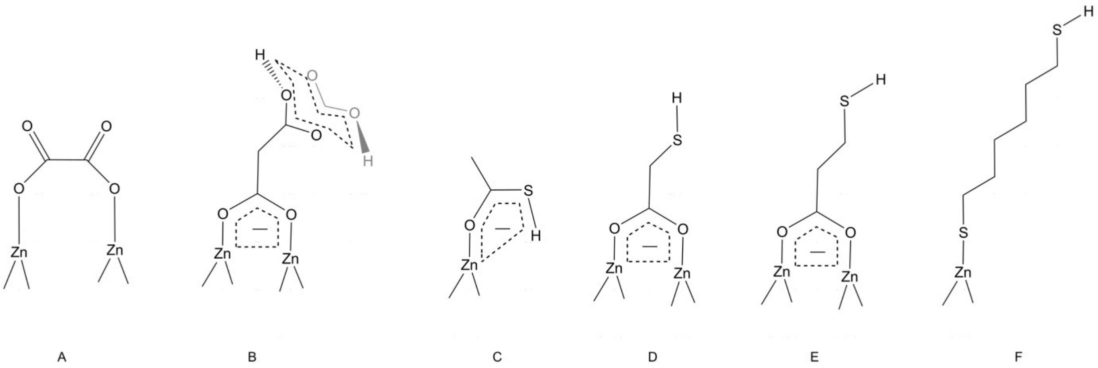

Figure 3.11: Schematic of the proposed linker bonding modes to the ZnO substrate: A: OA; B: MA, C: TAA; D: TGA; E: MPA and F: HDT.

molecular structures and the bond between substrate and linker have the most important influence on the electron transfer in the system.[132,156–160] Thus, the identification of the particular mode of attachment that the linkers employed in this study have and their influences, specifically on charge carrier transfer, is of some importance.

## 3.3.2 The Linker Interaction with the ZnO Gel

The presence of the linker on the ZnO surface could also be measured in the UV/Vis spectra of the ITO/ZnO/linker film (see Figure 3.12). In general the

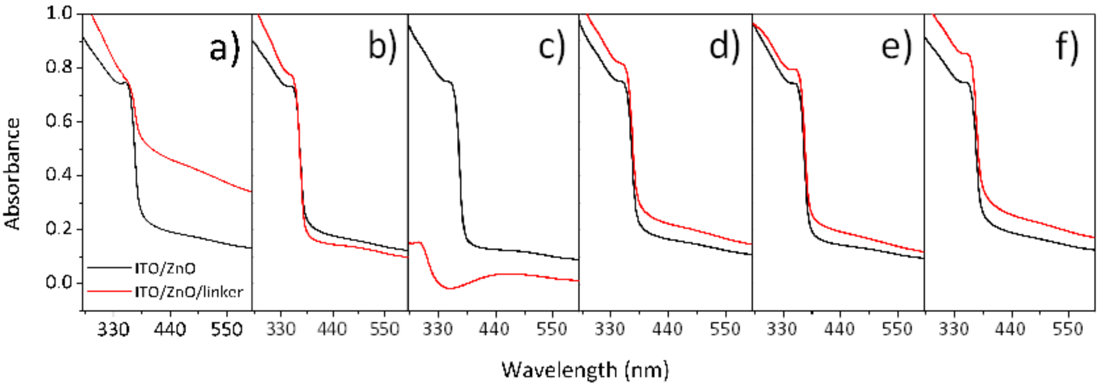

Figure 3.12: The absorbance spectra of the ITO/ZnO/linker films. The linkers are as follows: (a) OA (b) MA (c) TAA (d) TGA (e) MPA (f) HDT. Generally an increase in absorbance of the linker sensitized ZnO film compared to the pure ITO/ZnO film has been recorded. An ITO coated glass is employed as reference.

ITO/ZnO/linker films show an increase in absorbance over the complete absorption range compared to the ITO/ZnO film absorbance. This results and further experiments give an indication for some degree of electronic interaction between the linker and the ZnO surface. The TAA absorption profile changed dramatically in comparison to the ITO/ZnO film. It it likely that the ZnO layer has been destroyed which is also seen in the loss of the typical ZnO absorption bands. The solution containing the OA-linker was found to also have a very high interaction with the ZnO layer which was observed to be partially displaced from the ITO substrate during the immersion step and resulted in "crumb-like" agglomerates on the ITO.

Because of the different absorption properties of the ITO/ZnO and ITO/ZnO/linker films further optical studies of the ZnO in solution have been undertaken.

The UV/Vis spectra of the linker molecule solution have been determined and are presented in Figure 3.13. The TAA has a noticeable absorption which crossed over the absorption bands of the ZnO material at 350 nm. For this reason an additional TAA signal starting at 400 nm is to be expected for the ZnO-TAA mixture.

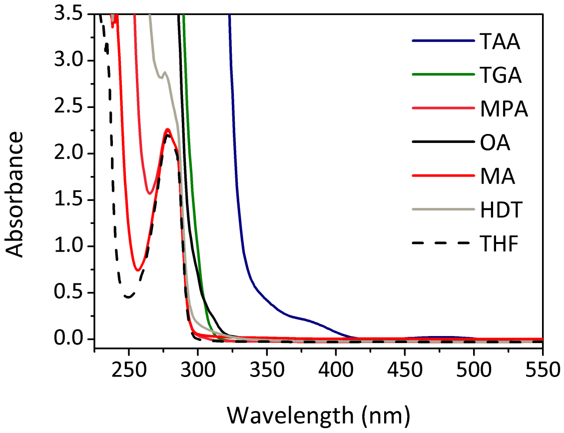

Figure 3.13: The absorbance spectra of each linker in THF. The THF spectrum has been added for comparison.

But in some cases the ZnO-THF solution containing the linker shows different absorption behavior and contrary to this assumption. Initially the absorbance of the ZnO gel diluted in THF was recorded whereas the pure THF solution was used as reference. This spectrum may then be taken as the starting point of the measurements at t=0. Then the linker was added to the ZnO-THF solution and the absorption recorded over a minimum time of four hours. This measurement was carried out for every linker using the same ZnO-THF solution and a linker concentration of 0.02 mM. In the case of MPA, TGA, MA and HDT the ZnO absorption increases with the attachment of the linker and is constant over time (Figure 3.14) analogous to the results for the ITO/ZnO substrate after the linker attachment. It was also noted that the absorption change is dependent on the amount of ligand. A sequential addition of the linker to the solution resulted in a proportional increase in the absorption. It may therefore be inferred that this effect is connected with the attachment of the linker to the ZnO surface. The more linker bound to the ZnO surface the higher the absorption of the ZnO/linker composite. Furthermore it was observed that the absorption stops if enough linker is present in the solution or rather at the ZnO surface. A further addition of the linker will bring about only a small absorption decrease but will eventually converge to a relative constant absorption of the ZnO composite, a behavior that is expected for a ZnO surface saturated with linker molecules.

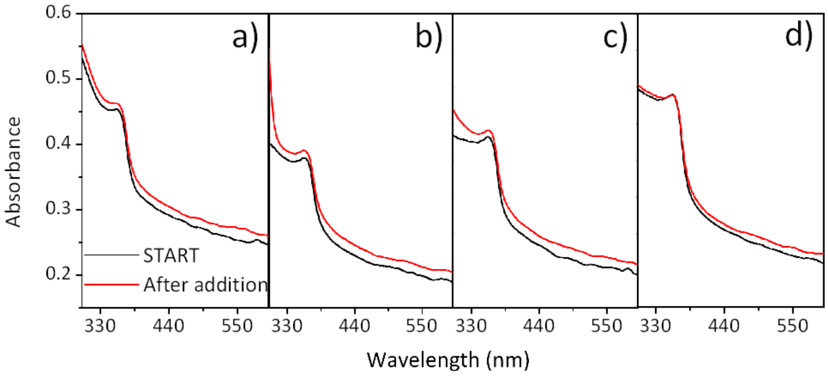

Figure 3.14: The absorption spectra of the pure ZnO dissolved in THF (black line) and ZnO in the presence of 0.02 mM linker a) MPA b) TGA c) HDT d) MA (red lines). An increase the absorption across all wavelengths can be determined.

This kind of interaction is not unusual when the dipole moments are considered. OA has a higher dipole moment compared to that of the thiol acids. TGA has a dipole moment of 2.28 D and MPA of 2.25 D[149], whereas HDT has a lower dipole moment because of the lower polarity of the C-S-H group compared to that of the C-O-H group. MA has a dipole moment of 2.64 D which is close to that of

OA whose dipole moment is 3 D.[161] This means that the electron distribution is located more at the functional groups, in the case of MA and OA which are stronger than that of the thiol acids, which increases the probability to inject these electrons into the ZnO surface states. In the literature a number of studies on $TiO_2$ report a shift in the $TiO_2$ band edge when a linker molecule absorbs at the surface. This has been explained by the fact that a ligand can increase the trap depth just through the strength of the Lewis-basicity. The stronger the basicity as well as the higher the dipole moment of the ligand the larger the increase in the energy of the $TiO_2$ surface states which causes them to converge towards the CB. For this reason the trap states become "lost" when charge injection occurs from a ligand which possesses a negatively polarized functional group (Figure 3.15).[129,130]

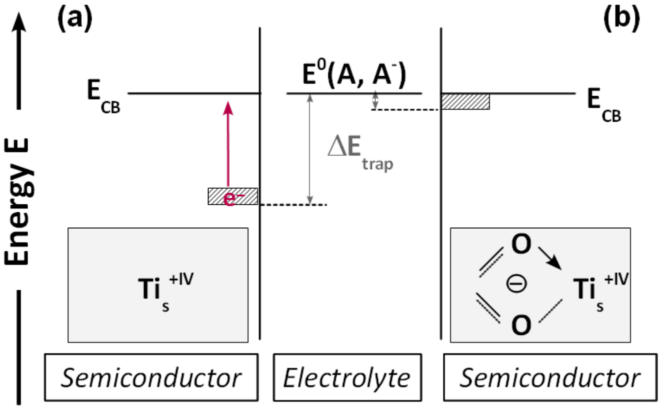

Figure 3.15: Energy schematic of the semiconductor-electrolyte interfaces for the $TiO_2$-electrolyte interface (a). The position of the trap states (striped box) is located far below the CB in the case of the $TiO_2$-electrolyte interface. The energy schematic for the $TiO_2$-electrolyte interface after a linker adsorption (b). A Ti-complexation with the functional moiety of the ligand occurs which results in an electron shifting into the $TiO_2$ and a decrease in the trap depth, $\Delta E_{trap}$, which is required to free a charge from the trap. Therefore the position of the unoccupied trap states (striped box) shifts to higher energies and the lower energetic trap states essentially disappeared.

In the same way the ZnO band edge structure may be altered resulting in an increase in the absorption. In contrast to the assumption that the linker attachment results an absorption increase it should also be mentioned that this effect may also be based on an additional scattering effect caused by a structural alteration or agglomeration of the ZnO gel after the linker attachment. However the same increase in the UV/Vis signal is also measured for the ITO/ZnO/linker substrate although a smaller degree of structure alteration is expected from an assembly in layer formation. In addition a change in the reflection of the ITO/ZnO/linker substrate may also be ruled out as the same magnitude increase was measured for THF solutions of the ZnO gel-linker. Therefore the comparison of the results obtained for the ITO/ZnO substrate and the ZnO gel solution suggests an absorption increase. Which particular mechanisms and processes are the causes of this increase cannot be clarified completely but may be connected with the trap depth alteration previously mentioned.

In some cases the electron interaction can be very strong resulting in the situation that more than surface state alteration may occur. For the linkers OA and TAA different absorption behaviors were observed. In the case of the addition of OA to the ZnO-THF solution a continuous decrease could be found (Figure 3.16(a)) until the ZnO absorption ceased. In earlier studies a strong acidic instability of ZnO was recorded.[162] Because of the strong acidity of the OA a complete disruption of the ZnO gel is to be expected. This is confirmed by the removal of the ZnO film from the ITO during the OA deposition (see above) and where the same flocculation was seen. This strong agglomeration had the appearance of the ZnO gel to the eye but the gel was no longer absorbing and became partially sticky.

A more complex interaction takes place between the ZnO and the TAA (Figure 3.16(b)). The original ZnO absorption maximum at 360 nm shifts quickly to approx. 340 nm and increases strongly in its absorption after the TAA addition. The expected TAA shoulder at around 400 nm is not seen for the mixture. From the beginning a second absorption maximum at 300 nm is observed to grow and disappear at the same time that the shifted ZnO maximum at 340 nm increases to a very strong peak over a period of approximately 240 minutes. A third peak at 400 nm is also observed. In the literature a reaction between ZnO and TAA to zinc sulfide (ZnS) at 60°C has been reported.[163] In comparison to that report the ZnO-TAA solution in this work was not temperature treated but the reaction is effected through the continuous irradiation by the spectrometer.

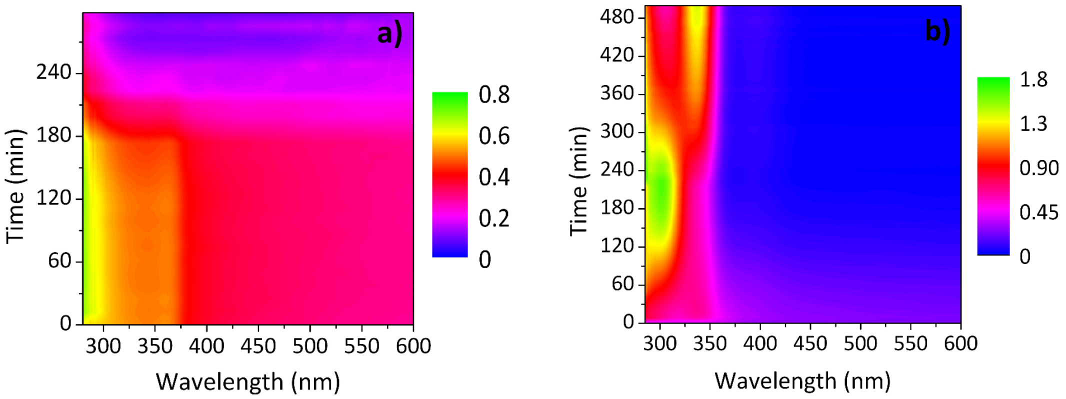

Figure 3.16: The spectrogram of the absorbance of the ZnO in the presence of a) OA and b) TAA. The abscissa shows the wavelength (nm), the ordinate the time (min) and the profile is associated with the absorbance. The intensity of the absorbance is shown through the color gradient (see color band at the right).

## 3.4 Conclusion

The preparation procedure for each sample has been shown to be reproducible so that direct comparison between the different samples can be made. It was shown that the ZnO thickness as well as the sintering temperature has a large influence on the ZnO properties. Further examination revealed that the same thickness of the ZnO with an absorbance of approx. 1 and a sintering temperature of 300°C are suitable to fabricate substrates with a high photoactivity while leaving the ZnO relatively unchanged in its structure compared to the unsintered ZnO film. Furthermore the linker attachment to the ZnO surface has been investigated using FTIR spectroscopy and the functional group most likely attached to the ZnO surface have been determined. The observation that an increase in the absorbance of the ITO/ZnO occurred after linker deposition prompted a further study of the system in which the linker was monitored by UV/Vis spectroscopy over a period of time after its addition to the ZnO solution. This result provided further evidence that the linker attachment has a large influence on the electronic structure of the ZnO material. It is expected that the increase in absorbance was due to the effect of electron transfer from the linker to the ZnO surface states because of the linker polarity. In addition it can be seen that the electron transfer influences the ZnO band edge and results in trap depth alteration which manifests itself as an absorption increase. In addition a strong electron interaction occurred such that a reaction or complete degradation of the ZnO was observed when the ligands are highly acidic.

# 4

# The PbS Sensitized ITO/ZnO/linker Substrate

## 4.1 Introduction

For the operation of an ISC an absorbing component is necessary. The search therefore for the best sensitizer, i.e. one which can efficiently absorb as much of the solar spectral output as possible while at the same time being electronically "well matched" to the substrate material, is an active area of research. In recent years the properties of narrow band gap semiconductors have attracted attention. In the case of nano-scaled semiconductors the absorption range is clearly tunable through tuning the width of the band gap. The control of the band gap down to 1 eV allows an absorption onset from the NIR down to the UV/Vis region of the spectrum because of the continuum of the NP electronic band structure. Amongst materials such as InAs[164–166], $Cd_3P_2$[167,168], PbSe[10,169–171] and PbTe[172,173] the lead chalcogenide PbS[174] is well suited to addressing this region of the spectrum. In addition the lead chalcogenides possess electronic and structural anomalies which make the materials attractive.[6,7,175] They also feature the possibility to exhibit multiple exciton generation (MEG)[19–22], i.e. the generation of more than one electron-hole pair by absorption of one high energy photon.[23–25] Thus these materials can be utilized to allow the harvesting efficiency of the solar spectrum to be increased if they are employed as absorbers in regions where dyes, up until now, have been unable to adequately address. Furthermore Vogel et.al.[2] have shown that sensitization of $TiO_2$ with PbS quantum dots of between 3 and 6 nm in size can be utilized to bring about the separation of the $e^{-}$-$h^{+}$ pair. Hence by tuning the PbS band gap i.e. stopping the growth of the NCs when they are in this size regime, the electron transfer to the substrate becomes energetically feasible. Therefore, all of the essential components for the fabrication of quantum dot sensitized solar cell (QDSSC) devices[104] exist and a number of such devices have been reported.[3]

In chapter 3 it was shown that linker attachment on the ZnO surface could be achieved. A strong influence on the ZnO optical properties because of electronic interaction between the ZnO surface and the linker could be observed. By the attachment of the PbS to the linker sensitized ZnO surface the electronic interaction between the linker and the PbS NPs could also be seen. Apart from the surface functionalization, an influence of the charge separation and the transport from the NP to the ZnO surface by charge tunneling plays an important role which has yet to be clarified. Slowinski et.al. have reported the charge transfer through a HDT molecule in a HDT film is by a chain to chain coupling which has a strong dependence on the film structure.[160] In addition in an earlier linker study the dependence of the electron transfer as a function of the distance between the QD and metal oxide are discussed.[131,132] Both authors noted the bridge mediated intramolecular electron transfer. Chidsey et.al.[176] also reports a slow electron transfer current through the long n-alkane monolayers which are impermeable to ions on a time scale of tens of seconds. The way in which the linker affects the (opto-)electrochemical properties of the ISC with an ITO/ZnO/linker/PbS structure is the subject of this chapter.

ITO is a TCO which is employed as the highly conductive, transparent component of the substrate. On the ITO is spin coated a nanoporous ZnO layer which is then sensitized by one of six different organic molecules. The linkers are varied in their alkyl chain length and the choice of either acid and/or thiol groups employed as the attachment moieties at the linker ends. The different linkers are oxalic acid (OA), malonic acid (MA), thioacetic acid (TAA), thioglycolic acid (TGA), 3-mercaptopropionic acid (MPA) and 1.6-hexandithiol (HDT). Each ITO/ZnO/linker sample has been covered with PbS NPs which have their absorption maximum at 1158 nm and therefore a band gap of approx. 1.08 eV. The typical construction has been shown in Figure 3.1 in chapter 3.

At first a general characterization of the ITO/ZnO/linker/PbS substrate will be presented. The evidence for the presence of PbS NPs on the ITO/ZnO/linker surface will also be addressed. Furthermore the complete substrate and the intermediate stages have undergone an extensive cyclic voltammogram study and the typical reaction and characteristics of the cyclic voltammogram profile will be discussed. In the end the evaluation of the chronoamperometry will be undertaken which allows an estimation of the linker dependence on the observed photocurrent.

## 4.2 The ITO/ZnO/Linker/PbS Substrate

### 4.2.1 Spectroscopic Evidence for PbS on the ITO/ZnO/Linker Substrate

Measurements to determine the presence of PbS on the ITO/ZnO/linker substrate surface were carried out. Attempts to measure the PbS nanoparticles after their attachment to the ZnO surface via XRD yielded diffractograms dominated by the intense diffraction peaks of the ITO, and therefore a clear XRD signal associated solely with the presence of the PbS could not be unambiguously recorded (Figure 4.1). However the UV/Vis/NIR spectra of a number of samples were found to

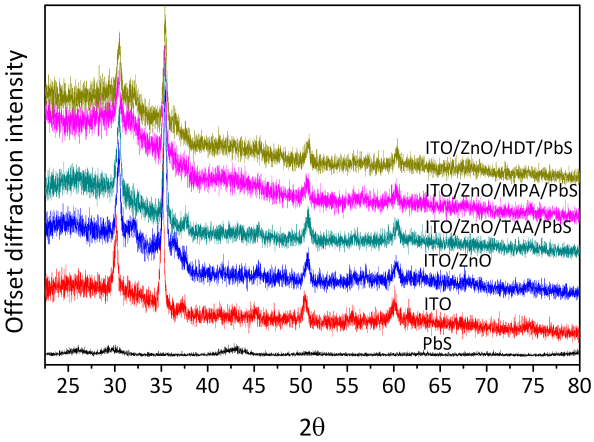

Figure 4.1: XRD diffractograms of a number of ITO/ZnO/linker/PbS substrates taken to detect the presence of PbS. The XRD diffractogram of PbS, ITO and ITO/ZnO act as references.

possess a low intensity PbS signal when a sufficient amount of the material was present.

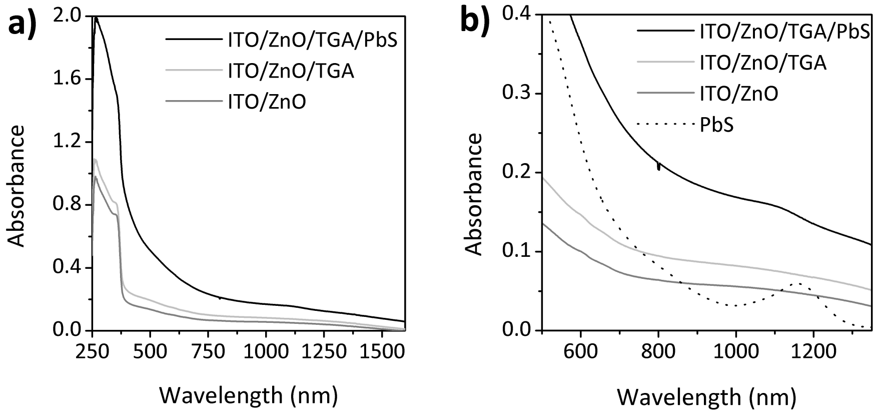

Figure 4.2: (a) UV/Vis spectra of ITO substrates coated with ZnO, ZnO/TGA and ZnO/TGA/PbS using a bare ITO substrate as reference. (b) as for (a) but in the wavelength range not dominated by the ZnO absorbance and with the inclusion of the absorbance of the PbS nanoparticle solution in tetrachlorethylene for comparison.

In Figure 4.2 the UV/Vis/NIR spectrum gained upon the addition of each layer is presented for the example of the TGA linker. For the ITO/ZnO/TGA/PbS substrate a weak absorption shoulder in the NIR can be observed that matches the position of the solution phase absorption maximum of the PbS nanoparticles. Similarly, it was by the visible changes in the ITO/ZnO/linker substrates that occurred after immersion into the nanoparticle solution that indications concerning the degree of PbS present after the coating procedure could be primarily derived. For the substrates with only linker molecules attached to the sintered ZnO-layer, there are no changes discernable by eye (top portion of substrates in Figure 4.3). The sintered ZnO-layers have been measured to have an absorbance of approx. 20 % when compared with a bare ITO substrate (see Figure 4.2(b)). After immersion of the substrates in the THF solution containing PbS nanocrystals (NC), the substrates were observed to show a clear color change from being almost transparent but possessing a slight tint to a distinct brown coloration (bottom portion of substrates in Figure 4.3). The degree of the coloration provides a visual aid as to the amount of PbS absorbed on the surface. However, it must be mentioned that the degree of coloration at the surface of the ZnO is not necessarily a trustworthy indicator of the level of the opto-electrochemical response that one measures under conditions of illumination, as will be more fully discussed below. In section 3.3.2 it was mentioned that a partial displacement of the ZnO gel from the ITO coated glass during the immersion step in the solution mixed with OA-linker occurred. This is the reason for the pointed marbling of sample A in Figure 4.3 after the PbS coating.

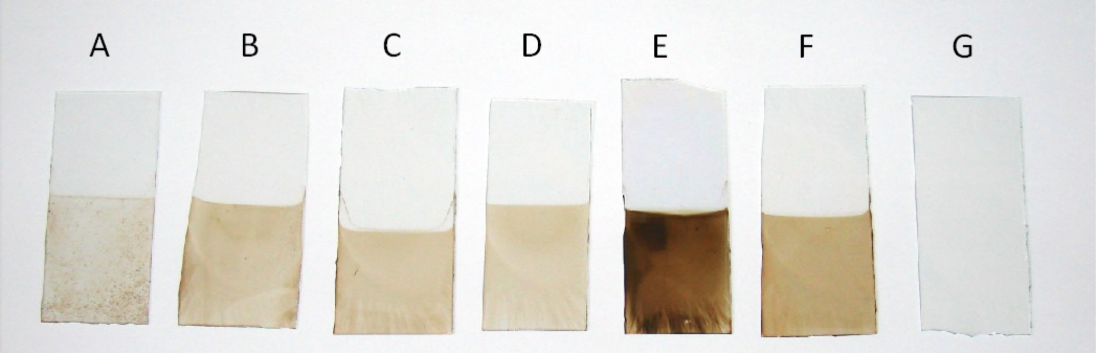

Figure 4.3: ZnO only (G) and ZnO-linker molecule-PbS (A-F, top portions) look similar and have a slightly reflective but predominantly transparent surface. In contact with the PbS the substrate color takes on a brown coloration from the PbS (A-F, bottom portions). The linker molecules are A: OA; B: MA; C: MPA; D: HDT; E: TAA and F: TGA.

It was shown that optical measurements are able to show the presence of PbS when it is present in large enough quantities. However, in the next section it will be demonstrated that cyclic voltammetry is a much more efficient tool to determine the PbS presence at low concentration.

### 4.2.2 The Cyclic Voltammetry Study on the Substrates

The use of dynamic electrochemical methods such as cyclic voltammetry provides a means to investigate surface species at the electrode electrolyte interface and hence was employed here to, amongst other things, confirm the presence of the PbS NC's. It is of utmost importance in electrochemical studies to determine at which potential any electrochemical reactions are occurring in the different layers and through this to establish a working potential range across which the data may be reasonably interpreted.

The electrochemical response for all of the ITO/ZnO/linker systems employed in this study was observed to result in a current of less than 5 $\mu$A/cm$^2$ across the potential range from -1.2 to 0.4 V using degassed 0.1 M sodium sulfite as background electrolyte. In $Na_2SO_3$ a linear decrease in the reduction current begins at -0.3 V and is similar for both the ITO and ITO/ZnO substrate (Figure 4.4).

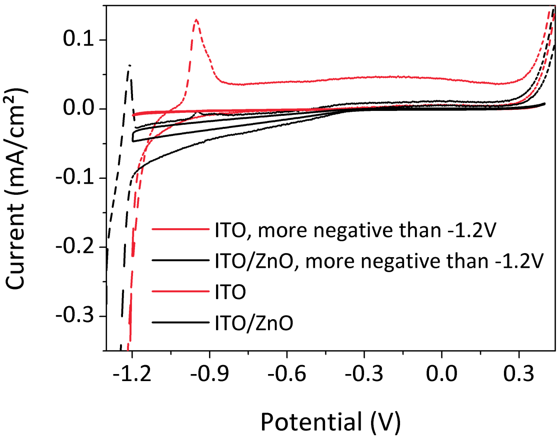

Figure 4.4: Cyclic voltammograms of ITO and ITO-ZnO surface in a 0.1M $Na_2SO_3$ solution. If the potential is scanned more negative than -1.2 V an oxidation peak is observed on the return scan (dashed line). CV's of the same substrate which has been scanned only to -1.2 V under the same conditions show no such oxidation peak (line).

In electrochemical studies in the dark and where scans more negative than -1.2 V were required the background electrolyte employed was sodium perchlorate due to its greater inertness at such negatively applied potentials. If the applied potential is scanned more negative than -1.2 V a reduction current is observed followed by the accompanying oxidation of the species formed at the ZnO surface at -1.091 V. This reaction can also be found for the blank ITO surface at approximately the same potential, but slightly shifted to more positive potentials, and has previously been reported for ITO and ZnO substrates.[177,178]

$$2SO_3^{2-} + 2H_2O + 2e^- \longrightarrow S_2O_4^{2-} + 4OH^- \tag{4.1}$$

$$SO_4^{2-} + H_2O + 2e^- \longrightarrow SO_3^{2-} + 2OH^- \tag{4.2}$$

These peaks were absent when sodium perchlorate ($NaClO_4$) was employed as background electrolyte and hence in electrochemical investigations where more negative potentials were applied the $NaClO_4$ was used in place of $Na_2SO_3$. Further reaction of $Na_2SO_3$ is not expected. The photolysis of $Na_2SO_3$ occurred in the UV range starting below 260 nm in solution at pH ∽9. The presence of oxygen as an impurity has a large influence on the photolysis.[179–181] The electrolyte used for these studies has been illuminated with wavelengths down to 370 nm only and has been stored in dark ambient conditions under Ar atmosphere which makes the photolysis of the $Na_2SO_3$ during a measurement and during storage insignificant. Also further electrochemical reactions can occur outside of the potential window used in these studies.

Rifai et al.[182] have previously published cyclic voltammetry studies on HDT where the presence of well defined signals was reported. However the oxidation of the linker samples observed in the present work is not as pronounced. The cyclic voltammetry also provided a clear indication that the coverage of the ZnO by the linker molecules was total, as for all ITO/ZnO/linker substrates the expected electrochemical signature for ZnO at -0.7 V and -1.15 V was completely suppressed (Figure 4.6(a)).

Upon deposition of the PbS NCs the CV profiles are observed to be dramatically altered. This influence can be seen in Figure 4.5 where the first sweep of the characteristic reactions of the complete ZnO/linker/PbS systems is illustrated for all linkers. The detailed electrochemical reactions of bulk PbS have previously been reported in the literature. Such studies focus primarily on bulk galena where a strong pH dependence of the signal position has been shown to exist.[183–187] Previous studies on quantum sized PbS[188] have ascertained the existence of the influence of the quantum size effect on the redox potential. Hence the presence of a wider band gap resulting from the decrease in the size of the PbS nanoparticles results in a shift to more negative potentials of the reduction peaks as a result of the differences in the electronic position of the conduction band. A complementary shift was observed for the anodic scan. The oxidation peak "A" in Figure 4.5 is obtained even if previously the reduction potential had not been passed through. The reaction therefore cannot be meditated via a previously reduced species and hence must be due to the direct oxidation of the PbS in the electrolyte. Experiments undertaken separately on an ITO/ZnO/linker substrate demonstrate that this oxidation peak is only observed when the PbS-layer is present. The oxidation reaction can be ascribed to the following reaction[183,185]:

$$PbS \longrightarrow Pb^{2+} + S^0 + 2e^- \tag{4.3}$$

Both manuscripts have commented on the fact that if a two-single-electron transfer reaction, i.e. sequential electron transfer, is assumed it will progress via a sulfur intermediate. However, the existence of such a two single electron transfer reaction presently remains a matter of speculation.

$$PbS \longrightarrow Pb^{2+} + (S^-)_s + e^- \tag{4.4}$$

$$(S^-)_s \longrightarrow S^0 + e^- \tag{4.5}$$

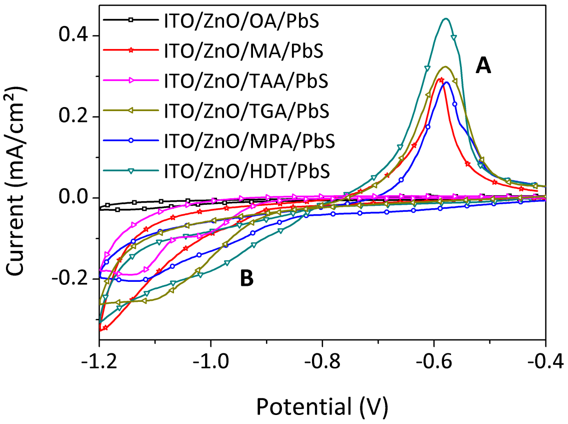

Figure 4.5: Cyclic voltammogram of the ZnO/linker/PbS system in $Na_2SO_3$ under conditions of non-illumination in the range from -1.2 till -0.4 V.

No such signal is detected for PbS systems where either the TAA or OA linker is present on the ZnO layer. As previously mentioned, during the OA coating procedure it was observed that the ZnO is at least partially removed from the ITO surface. There is therefore a smaller amount of ZnO present at the ITO surface which consequently results in a smaller amount of PbS being present. Also, if the linker molecules are attached as proposed in Figure 4.5, there is no acidic proton present to undergo dissociation and provide an attachment site for the PbS NCs. Unusually, as can be seen from Figure 4.3, the "blackest" substrate is that of the TAA derivatized ZnO and as such one would therefore have expected that the largest PbS related signature would be recorded for this sample but in fact for a number of such substrates this was consistently found not to be the case.

The potential shift of the redox reaction when compared to that of galena from the literature may be adequately explained by the quantum size effect[188] as well as a possible contribution associated with the influence of the linker contact. The reduction peak "B" in Fig. 4.5 at around -1.1 V is likewise decreased with each voltammetric sweep (seen in Figure 4.8a) and it was also noted that there is a linker dependence on the potential position of this peak. This reduction can be assigned to that of metallic lead and is analogous to the studies of Nicol et.al.[187] The corresponding weak signal at around -0.65 V is associated with the reduction of sulfide ion.

$$PbS + 2e^{-} \longrightarrow Pb^{0} + S^{2-} \tag{4.6}$$

$$S^{2-} + H^{+} \longrightarrow HS^{-} \tag{4.7}$$

A second low intensity oxidation peak between 0.05 and 0.15 V (this exact value being dependent on the linker present) can be determined only for the first cycle and is much more distinct for the presence of the TGA, HDT and MPA linker molecules. The product can be attributed to the presence of an impurity caused by the oxidation in air of the PbS species or by the partial stripping of the linker molecules. The large scale conversion of $Pb^{+}$ to $Pb(OH)_2$ can be ruled out due to the absence of a white precipitate in the vicinity of the electrode. This is further substantiated by the fact that during the measurement of the same samples in a solution of 0.1 M $NaClO_4$ at pH 12 the presence of small amounts of white $Pb(OH)_2$ was observed and which was accompanied by the presence of a third oxidation peak in the cyclic voltammogram at the expected potential (Fig. 4.6b).[184,189,190]

The reduction peak B which is explained by equations 4.4 and 4.5 can also be found in measurements taken of the same substrate measured in 0.1 M $NaClO_4$ at pH 12 at between -0.8 V and -0.6 V and hence are not related to the presence of the sulfite. The energy difference between the reduction "B" and oxidation "A" peaks in sodium sulfite (Figure 4.5) did not correspond to the magnitude of the PbS NC optical band gap, which is approx. 1.1 eV as determined from absorbance spectroscopy, an observation that has also been reported elsewhere for CdS[73] and

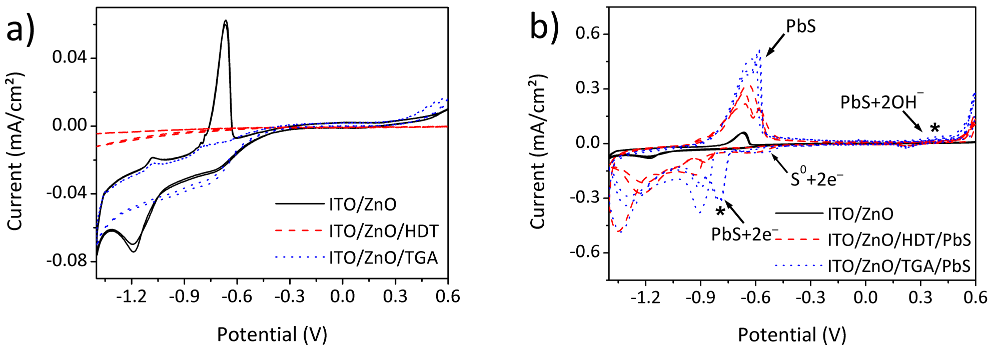

Figure 4.6: (a) Cyclic voltammogram of the ITO/ZnO, ITO/ZnO/HDT and ITO/ZnO/TGA in the range between -1.4 and 0.6 V in $NaClO_4$ solution (pH=12) for two voltammetric sweeps. (b) Cyclic voltammogram of the ZnO, ZnO/HDT/PbS and ZnO/TGA/PbS in the range between -1.4 and 0.6 V in $NaClO_4$ solution (pH=12) for three voltammetric sweeps. The asterisks mark the position of the reduction peak at approx. -0.8V and oxidation peak at approx. +0.4V associated with the CB and VB of the PbS NPs.

CdTe[191]. However, for CVs recorded using $NaClO_4$ as background electrolyte an inert electrochemical window between the most positively positioned oxidation peak and the first observed reduction peak, corresponding to a difference slightly larger than 1.1 eV was observed. The energy positions and width of this potential window were therefore examined to determine if they might be associated with the expected conduction and valance bands of the PbS NCs. The flat band potential window is located between -0.8 and 0.5 V. According to Xu et.al.[54] bulk PbS has the CB at -4.74 V and the VB at -5.11 V versus the vacuum level. The band positions of PbS NCs with a band gap of 1.1 eV and, as the effective masses of the electron and hole in PbS are equal, a symmetrical change in the band energies is expected whose positions can be calculated using the Brus-formula[5] (CB at -4.39 V; VB at -5.46 V). Using 1 M $K_3[Fe(CN)_6]/K_4[Fe(CN)_6]$ mixture 1:1 the potential of the Ag/AgCl/NaCl (3M) electrode used was determined to be 0.208 V vs. NHE, which corresponds to -4.808 V with respect to the vacuum (a value of -4.6 V[83] was used as the energetic level of the NHE with respect to the vacuum). Therefore the CB and VB of the PbS NCs were calculated to be -0.68 V and 0.42 V respectively vs. Ag/AgCl/NaCl (3M), values which are indeed in good agreement with the measured CV peaks and marked with asterisks in Figure 4.6(b). The difference observed (approx. 0.2 V) may be accounted for as the electrochemical band gap is larger than that of the optical band gap due to the extra energy required to transfer charge across the interface(s). The extra energy may be required due to the presence of barriers such as the organic molecules surrounding the PbS nanoparticles, the double layer and the Helmholtz layers at the semiconductor-electrolyte interface and may also have a contribution from the energy barrier to electron transfer from the PbS nanoparticles through the linkers to the back contact.

For evidence of this assumption the experimental results using PbS nanoparticle coated electrodes with different sizes of nanoparticles in 0.1 M $NaClO_4$ reveal a clear size dependence of the cyclic voltammogram peak positions. Two different sized PbS nanoparticles were used with absorption maxima at 1013 nm and 1345 nm (Figure 4.7(a)). The optical bandgaps of the PbS nanoparticles in eV are then 1.23 eV and 0.92 eV.

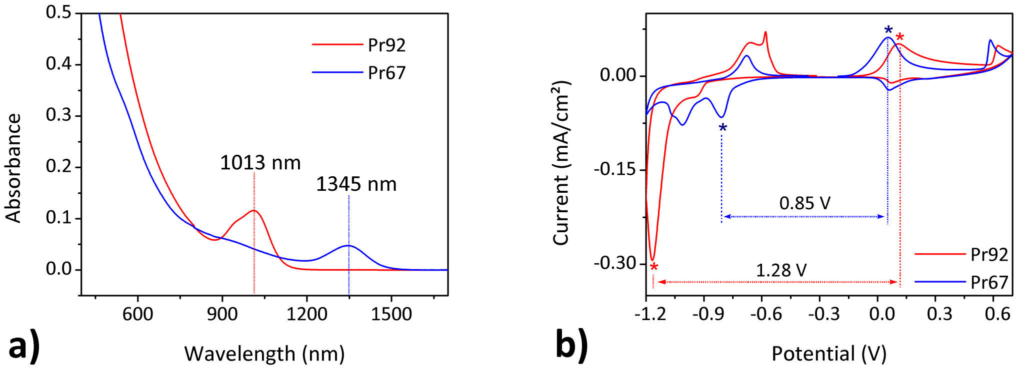

Figure 4.7: (a) Absorption spectra of PbS of two different sizes (Pr-x) in tetrachlorethylene (TCE) (b) first cycle of a cyclic voltammogram on an ITO/MPTMS/PbS substrate in the range between -1.4 and 0.6 V in $NaClO_4$ solution (pH=12).

The cyclic voltammograms obtained from these nanoparticles contain a number of size dependent signals (see Figure 4.7(b)). Most importantly, for this discussion, are the oxidation and reduction peaks marked with an asterisk, which can be observed to occur at almost the same energy difference as the optical band gaps (Pr92: 1.23 eV determined optical band gap compared to 1.28 V as determined from the electrochemistry, Pr67: 0.92 eV optically determined band gap compared to 0.85 V as determined from the electrochemistry). As one would expect if these peaks were to correspond to the conduction band and the valance band there is no evidence of any other signals to be found between the peaks (i.e. in the band gap) and the difference in the values observed correspond energetically very well (within experimental error) to the optically determined band gap. The existence of levels with higher energies (more negative potential) compared to the optically determined energies are reported in the literature.[192,193]

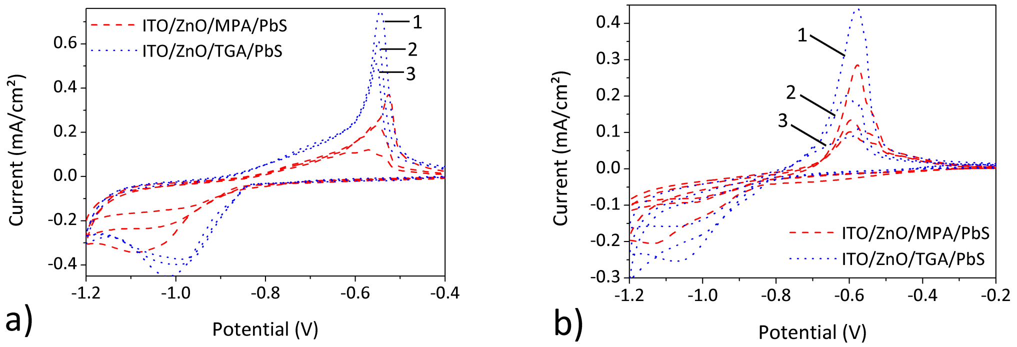

Figure 4.8: (Cyclic voltammogram of the ZnO/MPA/PbS and ZnO/TGA/PbS in the range of -1.2 to -0.4 V in $Na_2SO_3$ for three voltammetric sweeps under non-illuminated conditions (a) and under illumination with blue light (b).

The above CV measurements, which had been recorded in the dark, were repeated under conditions of illumination using a blue LED (peak = 470nm). Three voltammetric sweeps of ITO/ZnO/linker/PbS, for two different linkers, are presented. In this case differences in both the position and degree of oxidation and reduction are observed (Figure 4.8(a)+(b)). As can also be clearly observed the signal decreases with each successive voltammetric sweep in the oxidation potential direction as well as the reduction direction. The decrease in the CV profile may be explained by the degradation of a specific number of PbS nanoparticles at the substrate surface during each voltage sweep.

### 4.2.3 The Opto-Electrochemistry on the Substrates

The degree of photoactivity of each system was obtained by measuring its dc photocurrent response. An overview of the influence that the addition of each stage of the ITO/ZnO/linker/PbS system has on the photocurrent response is presented in Figure 4.9. The magnitude of the photocurrent for the ITO/ZnO substrates was found to be constant and reproducible having a value of $8{*}10^{-9}$ A/cm$^{-2}$. The highest photocurrents were recorded from the MPA, HDT and TGA linker-PbS systems and it is of interest that in these systems the linker itself also has a contribution to the sum of the photocurrent. Furthermore a photocurrent increase has been observed for the ITO/ZnO/linker substrates compared to those observed from the ITO/ZnO substrates. This kind of influence was already seen in the absorbance increase after the linker attachment to the ITO/ZnO in section 3.3.2. Both of these observations are as a result of the ability of the linker to increase the trap depth of the ZnO through the magnitude of its dipole moment. For further information see section 3.3.2. It was also observed that the photocurrents in all of the systems containing PbS reached the same upper value (a limiting value of the photocurrent under the conditions employed here). This fact is not intuitively expected given the possible differences in preparation: different linker molecule, differences in surface particle concentration etc.. In previous studies it was observed that the electron injection from a solution of ${SO_3}^{2-}$ was a slow process and therefore is likely to be amongst the contributive factors.[44]

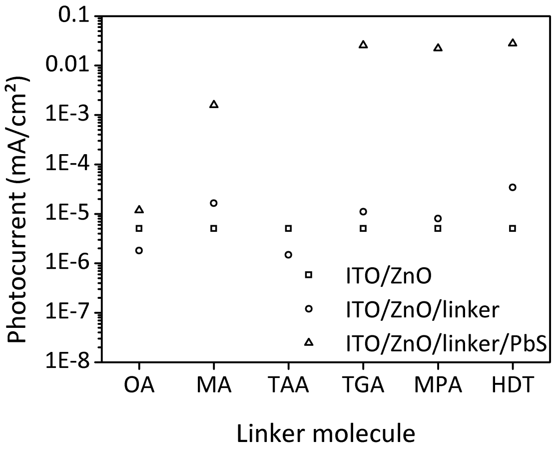

Figure 4.9: The role of the ZnO, linker and PbS in comparison to the complete ZnO/linker/PbS system.

The MA system also generates a comparable photocurrent which is in the 1 $\mu$A/cm$^2$ range. The photocurrent response from the OA system may be indicative of a number of the problems encountered in the coating procedure using this linker, a number of which have been previously mentioned. Although no significant photocurrent can be observed for the ZnO alone, ZnO/OA shows even less than this "background" photocurrent due to the dissolution of the ZnO during immersion in the linker solution. The TAA system is not presented in Figure 4.9 as the photocurrent obtained for ITO/ZnO/TAA/PbS was negative. The photocurrent measured for ITO/ZnO/TAA/PbS is -89.1 $\mu$A/cm$^2$. As is the case for the preceding results, the ZnO/TAA/PbS shows different trends in comparison to all of the other molecular systems used in this study. The different absorption spectra with a loss of the typical ZnO absorption bands, strong coloration after the PbS deposition step, negative photocurrents and the absence of the typical PbS signal in the cyclic voltammogram profile suggests the alteration of the materials which are in contact with TAA.

The photo-response profile to a steady state on/off dc illumination (Figure 4.10) shows a very quick increase followed by a slight exponential decrease of the signal during light irradiation and also a quick return to zero upon switching off the light. This optical response was found to be reproducible over many cycles therefore providing an indication of the stability of the PbS derived ZnO substrates.

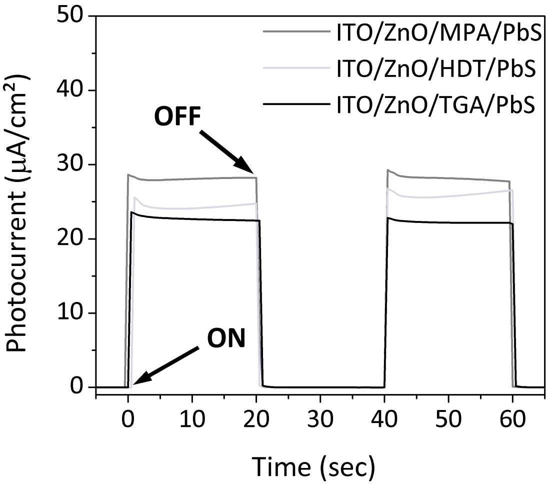

Figure 4.10: Typical photo-response profile for three ZnO/linker/PbS systems.

## 4.3 Conclusion

In summary the evidence for PbS attachment on the ITO/ZnO/linker substrate can be confirmed using UV/Vis/NIR spectroscopy if sufficient PbS material is attached to the surface. A more sensitive method is that of cyclic voltammetry. A number of signals in the voltagramm profile could be assigned to the PbS nanoparticles.

First cyclic voltammetry in sodium sulfite was employed to determine the potential range across which meaningful applied potential measurements could be performed. For ITO and ITO/ZnO substrates the background electrolyte underwent redox chemistry when a potential more negative than -1.2 V was applied using $Na_2SO_3$ as electrolyte. For that reason and for comparison purposes some samples were measured using $NaClO_4$ as electrolyte. An excellent linker coverage on the ZnO surface could be also recorded and seen in the cyclic voltammetry where it was observed that the typical ZnO signals are no longer present after the substrate has been immersed in the linker. For the ITO/ZnO/linker/PbS substrates the cyclic voltammograms in $NaClO_4$ displayed the rich electrochemistry associated with PbS. As a result a working potential window of approximately 1.3 V from -0.8 to +0.5 in the dark was determined and which corresponds well to the nanocrystal band gap as determined optically (1.1 eV). The electrochemical window for the NCs was wider than that associated with bulk galena which can be explained within the framework of quantum confinement. On a separate sample consisting of ITO/MPTMS/PbS with different PbS NP sizes CV was further employed to confirm the conduction and valance band positions and through this to confirm their size dependent response.

The photocurrent-response profile to a steady state on/off dc illumination showed a fast increase followed by a slight exponential decrease of the signal during light irradiation and also a quick return to zero upon switching off the light. This optical response was found to be reproducible over many cycles therefore providing an indication as to the stability of the PbS derived ZnO substrates. The electronic influence of the linker which had been seen in the absorption spectra of the ITO/ZnO/linker in chapter 3 was further confirmed from the photocurrent response. In accordance with the absorption an increase in the photocurrent could also be found.

In addition the results obtained from the TAA linker suggests the occurrence of a reaction between the linker and the ZnO as well as with the PbS NPs. The absence of the typical PbS signal in the CV profile, the negative photocurrent response and the alteration of the absorption spectra in chapter 3 are sufficient evidence to affirm that the properties of the MO semiconductor employed are changing once in contact with TAA. For this reason one expects a more complex process than a simple trap state filling through electron transfer between the semiconductors and the TAA to exist.

# 5

# The EIS Study of the ITO/ZnO/MPA/PbS Substrate

## 5.1 Introduction

Presently EIS and other techniques based in the frequency domain are increasingly being employed to clarify processes at polarisable surfaces for a wide variety of materials, and similarly such methods have experienced a resurgence in the field of photovoltaics, notably in the area of dye sensitized solar cells (DSSC).[27,30,31] This has proved to be a bonus in the electrochemical evaluation of all kinds of porous structures[194–197] and especially for nanoporous metal oxides in injection solar cells[29,32,34]. The theoretical work on the steady-state ac response in solid and liquid systems written by Jaffé et.al.[35] lead to the first basic understanding of electrochemical impedance spectroscopy and the mathematical framework within which to describe such systems was derived. Since these initial studies developments in the measurement technologies have enabled the researcher to attain a broader range of analysis. However it still remains a challenge to accurately interpret the results and especially to achieve a fit to the measured data using a theoretical model. MacDonald et.al.[78,79] further demonstrated a set of important rules concerning model handling and analysis. EIS, which is based on the detection of the ac current response under the application of a small ac potential is a powerful tool by which one may quantify the contribution to charge transport, through modelling the system as a set of in-series and parallel electrical components (primarily resistances and capacitances). Through the fitting of the frequency response data charge transfer processes, polarization effects, charge recombination and consequently limitations in device architectures can be uncovered and conclusions concerning chemical reactions, surface properties and interactions between the interfaces in the device may be drawn. In section 2.1.7 the theoretical details about impedance spectroscopy will be expanded and a more detailed background given.

The aim of this thesis is to present the electrochemical and opto-electrochemical analysis of each layer comprising an ISC and within this framework to determine the effects that each of the resulting deposition steps brings with it. In chapter 4 some of the fundamental (opto-)electrochemical techniques have been presented and a first assessment of the ITO/ZnO/linker/PbS and the role of each component layer in the ISC and the interactions between them made. The EIS measurement allows one to go deeper in detail concerning how the interfaces behave. For the EIS studies a standardized procedure with respect to experimental conditions and material quantities was employed for the preparation of each layer in the device namely FTO, FTO/ZnO, FTO/ZnO/MPA and FTO/ZnO/MPA/PbS. For this study the substrates were examined using flourine doped tin oxide (FTO) as the TCO component. The primary reason why the TCO has been changed was due to the lower thermal stability of ITO compared to FTO.[198] Furthermore in the literature it has been reported that ITO is prone to anodic corrosion[199] and to activation of the surface[200]. It was also shown that ITO undergoes a reaction with polymers when used together as components of an OLED (organic light emitting diode).[201] A further controversial point of discussion comprises whether the behavior of FTO is metallic[202] or semiconductor like when it is in contact with the metal oxide. In any case it can clearly be treated as a highly doped semiconductor and a number of articles may be found which demonstrate that the FTO does indeed act as a semiconductor.[203,204]

Each sequential layer of the ISC used for the EIS measurements was analyzed using UV/Vis/NIR spectroscopy, cyclic voltammetry and photocurrent transient analysis. This sequential layer formation and fitting sequence provides the opportunity to devise and subsequently adjust the model and enables one to use the results derived for each previously deposited layer as the foundation for understanding processes resulting in each successively more complex stage of the architecture. The influence and impact of all of the single layersteps will be presented and discussed.

In addition the measurements have been carried out at four different applied potentials which provide information concerning the rate of charge transport with respect to the different Fermi-level positions. In the present study the experiments were performed in the dark and for all PbS nanoparticle systems under illumination by red light (max = 630 nm). Illumination of the PbS nanoparticle containing systems was undertaken at longer wavelengths as at these wavelengths absorbance by the linker and ZnO is negligible. Hence it can be assumed that the optically induced generation of charge and their subsequent transfer effects are due exclusively to the excitation of the PbS nanoparticles. Although it can be assumed that the generation of excitons occurs only at the PbS NCs under illumination at a wavelength of 630 nm the system was also examined at the following illumination wavelengths: 370 nm (UV), 470 nm (blue) and 570 nm (yellow) and the way in which the ISC is affected at shorter wavelengths will be discussed. Additionally four different PbS particle sizes were employed and hence the influence of the nanoparticle size in these systems will also be addressed. The four different PbS sizes used have their absorption maximum at 868 nm (1.47 eV), 1033 nm (1.24 eV), 1169 nm (1.09 eV) and 1570 nm (0.8 eV). The linker employed for the attachment between PbS and the MO is MPA. MPA was one of the linkers which does not affect the ZnO surface as is the case with the acidic linkers. Furthermore it has shown one of the highest photocurrent responses and is not as long a molecule as HDT.

## 5.2 The Substrate Assembly

The complete system is composed of a transparent FTO glass, a nanoporous ZnO film and a monolayer of PbS nanoparticles which is linked to the ZnO surface by means of mercaptopropionic acid (MPA) analogous to that in Figure 3.1.

The assembly of the complete sample is built up layer-by-layer and upon the addition of each new layer the substrate characterized and the contribution of each addition determined. The skeletal structure of the substrate is composed primarily of the nanoporous structure of the ZnO gel on the FTO coated glass.

The large surface area and individual form of the ZnO NPs also persists after the deposition of the MPA and PbS nanoparticles.

As in the present study four different sizes of PbS NPs were used, four different complete FTO/ZnO/MPA/PbS substrates are listed, each of which is identified using a reference number, the number referring to the absorption maximum of the PbS NPs employed. As the PbS NPs have different sizes it can also be reasonably assumed that for the different sized NPs different amounts of PbS are present at the ZnO surface. In order to quantify this four samples were separately prepared for inductively coupled plasma-optical emission spectrometry (ICP-OES) and the ratio of the PbS coverage determined. The concentration of the $Pb^{2+}$ was measured after nanoparticle digestion and, as the particle sizes are known and therefore the number of atoms in the nanoparticle can be determined, the number of NPs present at the ZnO surface can be calculated. The number density was found to decrease in the following order: $PbS_{868} > PbS_{1033} > PbS_{1169} > PbS_{1570}$ and in the ratios of approx. $1 : 0.6 : 0.33 : 0.13$. It is worthy of note that the $PbS_{1570}$ result determined that the amount of NPs present on the ZnO substrate is one order of magnitude smaller than that of the $PbS_{868}$ NP sample present on the same surface area. These results assume particular importance for the opto-electrochemical results which are corrected for the area under illumination only and not corrected for the amount of NPs present.

## 5.3 The Substrate Characteristics

The UV/Vis/NIR spectra of the prepared substrates show a good coverage of the ZnO layer onto FTO. Using standardized protocols it was possible to coat all FTO substrates with the same thickness of ZnO. This was verified and monitored using UV/Vis spectroscopy during the preparation stage analogous to that of the metal oxide film preparation in earlier chapters. As expected, after the MPA deposition step an increase in the FTO/ZnO/MPA absorbance as compared to that of the FTO/ZnO absorbance is clearly observed (see Figure 5.1) which, as mentioned earlier, is due to the filling of the ZnO trap states, the electrons coming from the functional group of the linker (see also section 3.3.2 and section 4.3.1). After coverage of the FTO/ZnO/MPA with PbS nanoparticles the FTO/ZnO/MPA absorbance is overlain with the absorption of the nanoparticle continuum. The absorption maximum of the PbS cannot be observed in these samples due to the small amounts of PbS present at the surface. This is similar to the findings in the previous studies presented in section 4.2.1. The FTO/ZnO/MPA/PbS with a PbS absorption maximum at 1570 nm has the smallest absorption. The absorption of the substrates containing nanoparticles of other PbS sizes are quite similar in the UV range and show the higher absorption over the whole measured wavelength range.

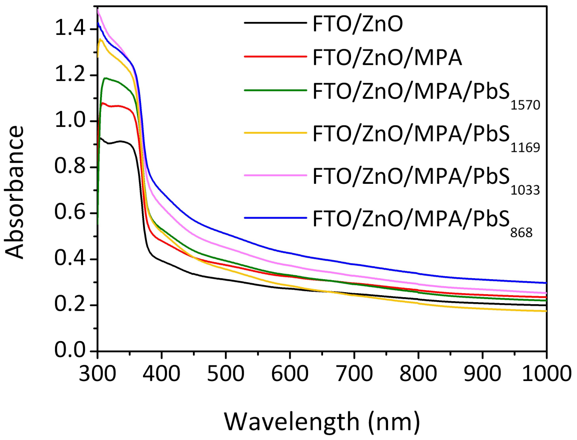

Figure 5.1: UV/Vis/NIR spectra of the samples used for the EIS study. The optically measured band gap of the ZnO is found to correspond to 3.28 eV (377 nm ). The amount of PbS present is insufficient to determine the absorption maximum associated with the PbS nanoparticles.

Using IPCE analysis the percentage of impinging photons that generate electrons which contribute to the photocurrent can be determined. IPCE measurements of the FTO/ZnO and FTO/ZnO/MPA have determined that effectively no photocurrents down to the band gap energy at 376 nm (3.29 eV) are generated, allowing the band gap value to be substantiated by the IPCE results (Figure 5.2). The substrate with the lowest measured photocurrent at 350 nm is coated with $PbS_{1570}$ NP. The smaller photocurrents observed from substrates containing $PbS_{1570}$ can be accounted for by the relatively lower amount of nanoparticles present at the surface (see above for the discussion pertaining to the relative degree of nanoparticle coverage). Also the alignment of the $PbS_{1570}$ band compared to the ZnO band is calculated to be disadvantageous because of its narrow band gap which results in the CB of the $PbS_{1570}$ being located near at the ZnO CB level. Furthermore the decrease of the photocurrent can be explained by the fact that the internal conversion by the nanoparticles is faster as the particle size increases. However, the size dependence of the nanoparticles used for the sensitisation of the substrates is seen for the photocurrents. The IPCE peak at approx. 700 nm can result from the second order light reflections of the monochromator which comes from the grating dispersion employed (600 grooves/mm with a blaze wavelength of 750 nm - values provided by the manufacturer). To remove this from the IPCE spectra a long bandpass optical filter, which shows low transmission for shorter wavelengths (blocking range) and high transmission at longer wavelengths (band pass range), may placed in the light path for later studies.

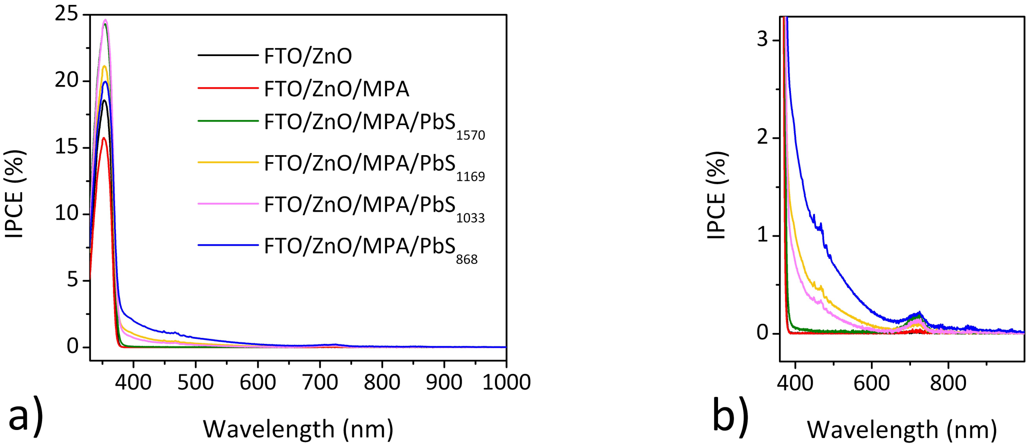

Figure 5.2: The IPCE spectra of the samples which were used for the EIS study. a) The IPCE spectra of the FTO/ZnO, FTO/ZnO/MPA and FTO/ZnO/MPA/PbS samples in the spectral range from 300 nm to 1000 nm. b) The IPCE as determined in a) but with the vertical axis zoomed to better highlight the PbS photocurrent.

At this point the EIS data obtained under red illumination will be discussed. By irradiating the substrates with red light it is assumed that the generation of charge carriers will occur only at the NPs, the largest band gap of which is 868 nm (1.47 eV). Opposite to the the substrate the bar FTO/ZnO substrate starts its charge carriers generation only from 376 nm (3.29 eV) which is near the band gap energy of ZnO and seen in the onset of the FTO/ZnO substrate at IPCE spectra. These results are also substantiated by the photocurrent transient profiles. In Figure 5.3 the photocurrent transients of the FTO/ZnO/MPA/PbS$_{868}$, FTO/ZnO/MPA and FTO/ZnO substrates are presented.

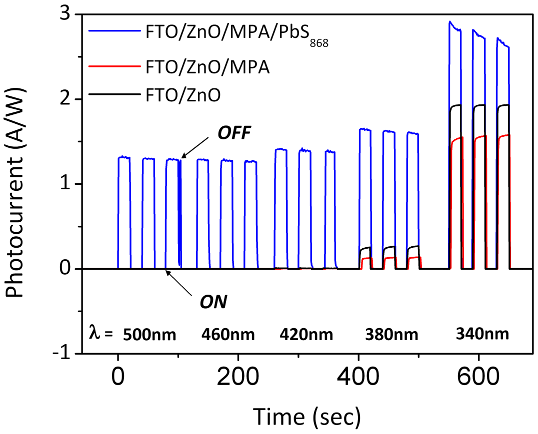

Figure 5.3: Photocurrent transient spectra of the FTO/ZnO (black), FTO/ZnO/MPA (red), FTO/ZnO/MPA/PbS$_{868}$ (blue) where five different wavelengths of monochromatic light have been employed. The sample was illuminated three times with a period of 20 sec on 20 sec off.

The results were obtained at open circuit potential with an illumination at five different wavelengths all of which pass through three on/off cycles. The measurement is first carried out at longer wavelengths and then changed stepwise to shorter wavelengths. The photocurrent is subsequently corrected for the intensity of the incoming light. It is seen that the photocurrent generated from the FTO/ZnO and FTO/ZnO/MPA substrates starts once an illumination wavelength of 380 nm has been reached. The photocurrent from the FTO/ZnO/MPA/PbS$_{868}$ sample shows a photoactivity at a longer wavelength which is due to the PbS NPs only. Once a wavelength of 380 nm or lower is reached the resulting photocurrent is the sum of the charge transfers that are derived from all processes coming from the excited states of ZnO gel and PbS NPs and all interacting processes between both. A weak photoresponse also occurred at wavelengths of 460 nm and 420 nm for the ZnO layer but is not seen at wavelengths of 500 nm or longer. The exciton generation which occurred under blue illumination and not only in the presence of UV light is unexpected as the energy of the blue LED is not sufficiently energetic for exciton generation in the ZnO (see Figure 5.4). However if the electronic structure of the ZnO were to be examined in greater detail then an energy level picture containing a band gap

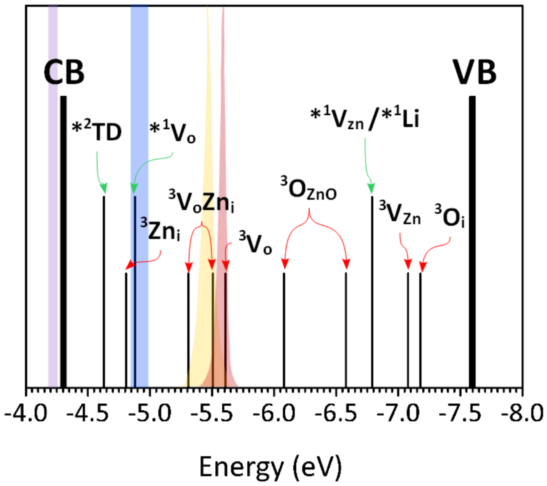

Figure 5.4: A schematic energy diagram versus the vacuum potential in eV, the CB and the VB of the ZnO used in this work. The red and the yellow lines are the emission spectra of the red ($\lambda_{max} = 630$ nm) and yellow ($\lambda_{max} = 570$ nm) LED used for the measurements. The light lila and the light blue portions show the half width band of the lila [UV] ($\lambda_{max} = 370$ nm) and blue ($\lambda_{max} = 470$ nm) LEDs. The emission spectra of both LEDs could not be measured because of the specific plug connector from the Zahner equipment. Furthermore the trap states found in the literature are added. The asterisks mark the trap states which result from experimental studies. $^1$ = Özgür et.al.[102], $^2$ = Casteleiro et.al.[205], $^3$ = Xu et.al.[206]

within which a number of trap states are to be found may emerge. In the literature some calculations of possible trap states and their positions are reported. The proposed trap states result primarily from crystalline defects. Possible defects that can be found are vacant zinc (V$_{Zn}$), vacant oxygen (V$_O$), interstitial zinc (Zn$_i$), interstitial oxygen (O$_i$), complexes of Zn$_i$ and V$_O$ (V$_O$Zn$_i$), complexes of Zn$_i$ and V$_{ZnO}$ (V$_{ZnO}$Zn$_i$) and substitution O and Zn positions (O$_{Zn}$).[206] A multitude of experimetal results are also available in the literature.[102] Casteleiro et.al.[205] have provided an account of trap states 0.32 eV under the CB band of the ZnO in which an electron is able to detrap into the CB. The detrapping mechanisms can be initiated through thermal activation (see also section 2.1.2). In Figure 5.4 the calculated CB and VB of the ZnO used in this thesis are depicted against their vacuum energy positions. The band gap was determined from the absorption spectra and the position of the ZnO CB was determined from linear sweep voltammetry (LSV).

In addition to the CB and VB of the ZnO used in our studies the trap states given in the literature are presented. It is to be noted that the ZnO band structure and band gap given in the literature can be, and most likely is, different from the ZnO used in this work. For that reason the trap states positions have to be assumed to be slightly shifted, insofar as the trap states can be assumed to really exist in the ZnO used here. On the other hand many other trap states can exist in the ZnO used in these studies. Therefore the scheme in Figure 5.4. may only be used to provide an indication as to whether it is possible to address such states rather than as a certainty that it will occur. Further more detailed discussions will be presented in sections 5.5.4.

## 5.4 The Model for the EIS Analysis

As mentioned any charge transfer observed from the FTO/ZnO/MPA/PbS samples under red illumination must emanate from within the PbS layer. The electron will be transferred into the conduction band (CB) of a ZnO particle at the outer edge of the ZnO film (the edge furthest from the FTO) having passed through the MPA molecules and transfer further through the ZnO film via a hopping mechanism to arrive at the ZnO/FTO interface. Once it reaches the FTO layer the electron will enter the electronic circuit (for more details see section 2.1.3). The hole, which is left on the PbS nanoparticles, will be removed by the hole scavenger (sodium sulfite). Generally the circuit may be completed if the oxidized species is reduced at the CE, but for the sulfite the back reaction is kinetically hindered and hence does not occur. Consequently the MPA, the ZnO, the FTO and the electrolyte will be termed as electron separating and transfer layers. The electronic properties of the ZnO layer are expected to remain constant, the only changes to this layer occurring at the ZnO/electrolyte interface when the ZnO is modified with MPA or MPA/PbS nanoparticles. Therefore the internal portion of the ZnO film (Figure 5.5[a] grey spheres with black outline) and the FTO/ZnO interface (Figure 5.5[a] grey spheres with light green outline) exhibit the same electrical properties when the MPA/PbS, just the MPA or neither are coated on the ZnO surface. The sole influence of the deposition processes is to be found in the outer part of the ZnO (Figure 5.5[a] grey spheres with dark green line). Based on this idea the model of the system and the measurements were carried out step by step based on a "brick by brick" methodology where each other brick which may be added later on the top of the substrate has to be added to the model. In Figure 5.5[b] the model for the complete FTO/ZnO/MPA/PbS substrate in contact with the electrolyte is shown. Corresponding to the box of bricks concept the model employed to fit the EIS data for the FTO/ZnO substrate will consist only of the FTO and ZnO components in contact with the electrolyte. Analogously the model employed to fit the EIS data of the FTO/ZnO/MPA will consist of the FTO/ZnO/MPA components in contact with the electrolyte.

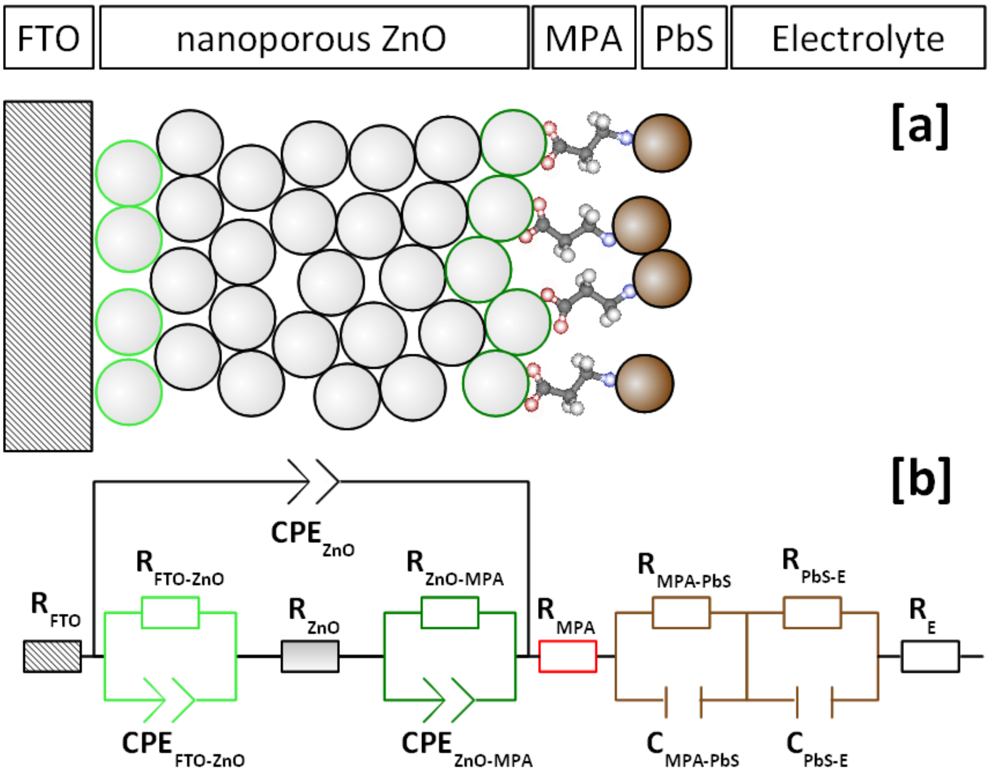

Figure 5.5: [a] The substrate assembly (top) composed of FTO/ZnO/MPA/PbS in contact with the electrolyte. [b] The EIS model (bottom) used to fit the complete substrate data.

A resistor in series with the interfacial circuitry is employed to describe the electrolyte. This electrolyte resistance ($R_E$) is constant for the same solution composition and concentrations and can be separately determined using a conductivity cell.[207] For the electrolyte solution (0.1 M $Na_2SO_3$) a resistance of 155 Ω was measured and this "unhindered" electrolyte resistance (that is to say with respect to unimpaired ion movement) was measured in order to check the cell geometry for the introduction of additional diffusion or other geometrically introduced resistances. Generally it is assumed that the electrolyte resistance in unobstructed geometries should be close to the resistance as measured in the cell geometry by EIS and it is for this reason that the electrolyte resistivity measurements were compared to the EIS measurements. Had significant differences been observed then this would have indicated that possible experimentally introduced artifacts were present. The measured electrolyte resistivity was close to the EIS measured values of the resistance (155 $\Omega$), the difference in the values being accounted for by the difference distance between the two plates in the resistivity setup (1 cm) and that of the working and reference electrodes in the cell ($< 1$ cm).[208] This check confirmed the assumption that no additional impedances due to obstructions in the electrolyte path between working electrode and reference electrode, which might have resulted from the cell geometry, existed. Generally, in an electrolyte resistance measurement the cell is calibrated against a known salt solution, such as KCl[178,209–211]. In accordance with the calibration the real (measured) electrolyte resistance of $Na_2SO_3$ has been determined to be 180 $\Omega$.

However for the EIS studies, two RC elements arranged in series are used to describe the charge separation of the generated exciton from the nanoparticle, similarly to previous studies.[46] The $R_{MPA-PbS}C_{MPA-PbS}$ elements in the circuit describe the electron injection process into the ZnO and the $R_{PbS-E}C_{PbS-E}$ element depicts the removal of the hole through an injection of an electron from the hole scavenger. The linker MPA is best represented by a simple resistor $R_{MPA}$. Generally $R_{MPA}$ may be considered to be constant for any one linker, a point which will be considered further in a later section of this chapter. The ZnO portion of the circuit is mechanistically the most complex part of the system. The processes which are required to be modeled are the electron entry at the outer ZnO particle film edge i.e. across the ZnO/MPA interface $R_{ZnO-MPA}CPE_{ZnO-MPA}$, the electron transfer into the FTO layer through the FTO/ZnO interface through the inner most layer of the ZnO particles $R_{FTO-ZnO}CPE_{FTO-ZnO}$ and the charge transport through the ZnO film, for example via a hopping process which can be described by a simple resistor $R_{ZnO}$. In the case where MPA has not been deposited onto the ZnO surface, as in the case of a FTO/ZnO substrate, the outer ZnO particle interface is represented as a ZnO/electrolyte interface given by $R_{ZnO-E}CPE_{ZnO-E}$. The FTO/ZnO interface and the outer ZnO particle film interface have a CPE-element instead of a capacitor C. The CPE must be used due to the highly inhomogeneous surface and porous nature of the ZnO layer.[80,212–214] In addition a further CPE element is placed across the complete layer. Often a high capacitance can occur due to the fact that the electrons cannot be discharged from the film. Thus the electron transport through the ZnO layer is also affected by the capacitance of the ZnO film as a whole. The electron then enters the external section of the circuit by transferring to the FTO layer. The FTO layer is represented by a simple resistor $R_{FTO}$ which normally results due the sheet resistance (SR) of the transparent conducting glass. The pure FTO substrate in contact with the electrolyte is not considered in the following analysis as from the moment the FTO is covered with a layer of ZnO the contact area between the FTO and the electrolyte is very small and may in fact be neglected. In the literature EIS treatments of transparent conductive oxides (TCO) in contact with electrolyte solutions have been discussed.[215–217] In all cases the models are quite complex and combine an electron transfer with a strong dependence on diffusion. Although the work of Strømme et.al. is concerned more with the diffusion process of lithium into the ITO electrode the reported model is an intricate one.[218] The often mentioned Warburg impedance and anomalous diffusion is considered in detail in the works of Bisquert et.al..[32,219]

## 5.5 The Results of EIS Data Fitting

### 5.5.1 The EIS Results of the FTO/ZnO Substrate

For the ZnO coated on the FTO a model representing the FTO/ZnO in contact with the electrolyte has been used. As previously mentioned the electrolyte resistance $R_E$ was taken as being constant the value of which was determined using a calibrated conductivity cell and, in the fitting, all other elements are left free to fluctuate (i.e. have no initial fixed value).

From modelling the EIS data the value of the FTO resistance $R_{FTO}$ was determined to be approx. 117 Ω under non illuminated conditions and 112 Ω under conditions of red illumination. These values are in good agreement with the measured value of the sheet resistance $R_{SR}$ of 110 Ω. The other resistances associated with the ZnO film show a typical trend in their dependence on the applied potential. In Figure 5.6 the dependence of the characteristic values of the FTO/ZnO interfacial resistance $R_{FTO-ZnO}$, the ZnO/electrolyte interfacial resistance $R_{ZnO-E}$ and the ZnO film resistance $R_{ZnO}$ on the potential are presented.

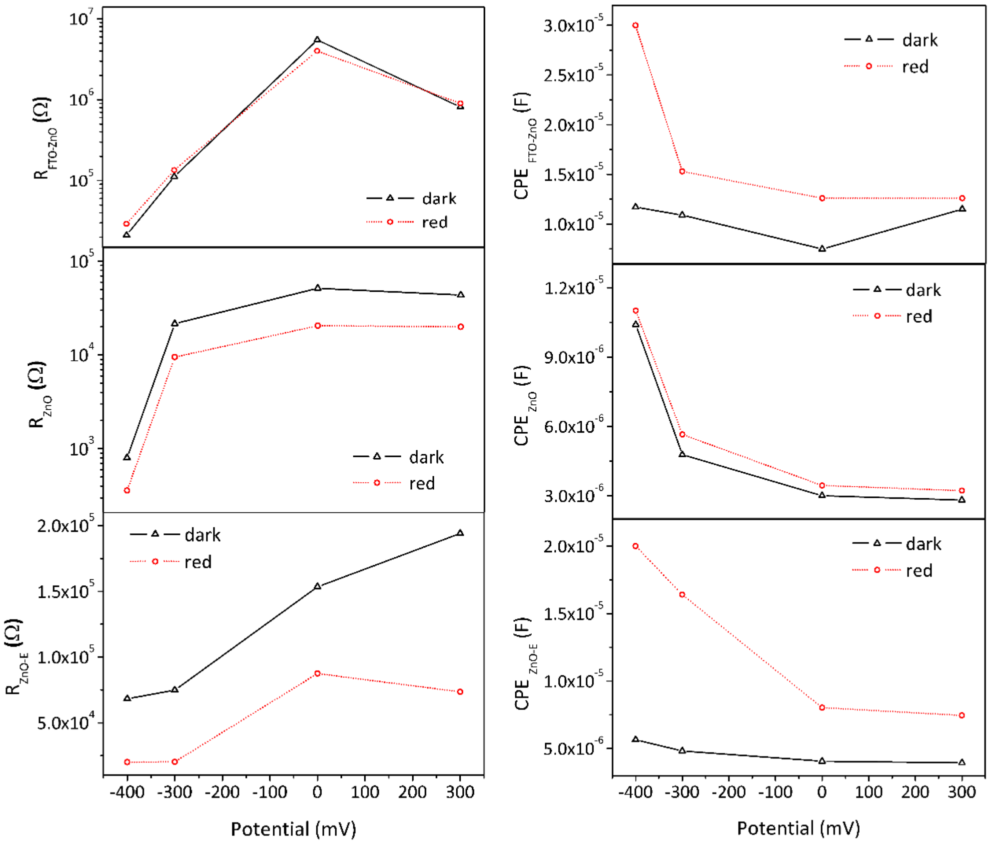

Figure 5.6: The calculated values of the FTO/ZnO/electrolyte system plotted against the applied potential. The FTO/ZnO interface with the $R_{FTO-ZnO}$ and the $CPE_{FTO-ZnO}$ (top), the ZnO film capacitance $CPE_{ZnO}$ and the ZnO film resistance $R_{ZnO}$ (middle) and The ZnO/E interface is given by $R_{ZnO-E}$ and $CPE_{ZnO-E}$ (bottom).

Generally the values determined for the FTO/ZnO/electrolyte system did not show large differences between conditions of red illumination and those of darkness. Their dependence on the applied potential also shows an almost equal trend. In further studies and in the literature the flat band potential of ZnO is estimated to be at approx. -0.5 V vs SCE at pH = 9.5 at single crystal facet

(0001).[138] The influence of the convergence of the applied potential to the band edge of the ZnO can be seen in the results obtained in this study, the closer the applied potential approaches to the band edge the lower the resistance and the higher the capacitance measured for the interfaces. The fits derived from the model describe the measured data quite well. The Nyquist and the Bode plots show a good agreement between the calculated and measured data (Figure 5.7 and Figure 5.8).

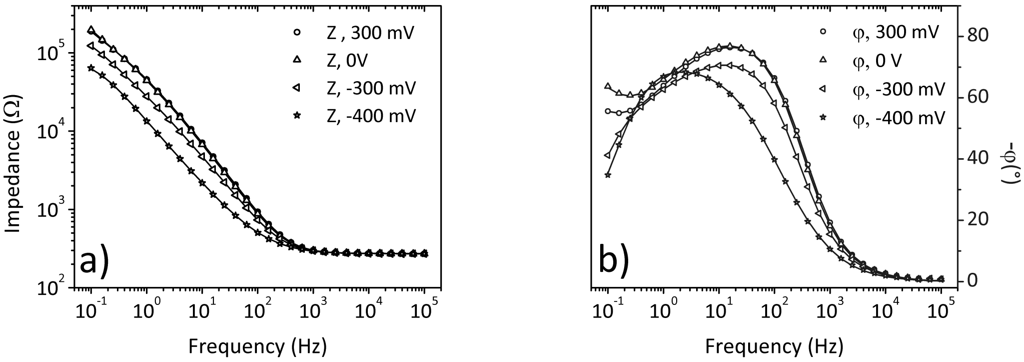

Figure 5.7: The Bode plot of the FTO/ZnO substrate under non-illuminated conditions at different applied potentials. The model (line) describes quite well the measured data (symbols) in the Bode magnitude (a) and in the Bode phase (b).

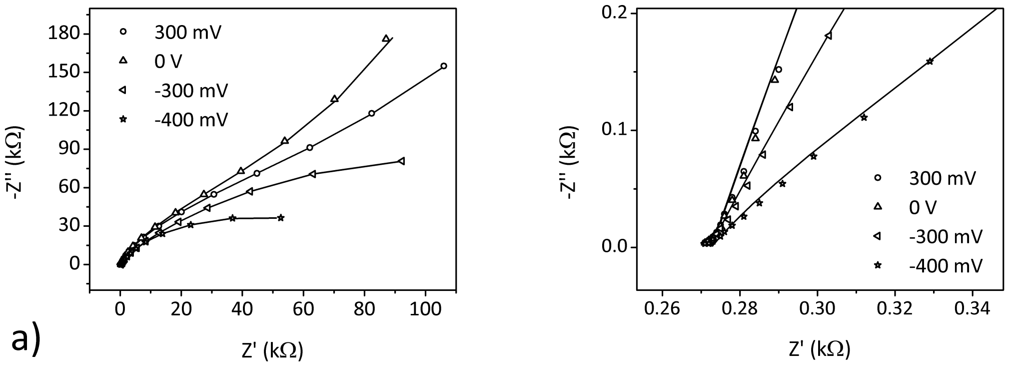

Figure 5.8: The Nyquist plot of the FTO/ZnO substrate under non-illuminated conditions at different applied potentials. The model (line) describes the measured data (symbols) in the low frequency range (a) and the high frequency range (b) very well.

For the data acquired under red illumination similar results have been obtained but are not shown here because the presented images are representative for all fits. As for the previous situation, when the EIS model was introduced, the processes at the FTO/ZnO interface and the processes in the interior of the ZnO film should remain unaffected by the linkage of the MPA to the outer edge of the ZnO particle film. Hence the results of the $R_{FTO-ZnO}$, $CPE_{FTO-ZnO}$ and $R_{ZnO}$ obtained in the previous section may also be used for modelling of the FTO/ZnO/MPA substrate.

### 5.5.2 The EIS Results of the FTO/ZnO/MPA Substrate

The data for the FTO/ZnO/MPA substrate were fit using the model for an FTO/ZnO/MPA substrate in contact with the electrolyte. As described in the previous section the results of the $R_{FTO-ZnO}$, $CPE_{FTO-ZnO}$ and $R_{ZnO}$ values were used for the modelling of the FTO/ZnO/MPA data. The fitting results of the $R_{FTO-ZnO}$, $CPE_{FTO-ZnO}$ and $R_{ZnO}$ values for the FTO/ZnO/MPA substrate differ by a maximum of 10% from the given values of the fitted FTO/ZnO model. However, in two cases a plot that fit the data well resulted with value differences of unfortunately just 30% from the given values derived from the FTO/ZnO model. The values of $R_{FTO}$ obtained from the previous FTO/ZnO fits have been employed here as a fixed value.

The calculated $R_{MPA}$ was set in dark conditions to be approx. 10 Ω and under red illumination to be 4 Ω which is close to the resistance values presented in the literature.[220,221] The MPA coverage at the ZnO surface affects the outer ZnO particle film and for this reason a change of the ZnO/MPA interface is to be expected in the modelling. The ZnO/MPA interface generates a small decrease in the resistance $R_{ZnO-MPA}$ and maintains similar dimensions in the values of the capacitance $CPE_{ZnO-MPA}$, the $CPE_{ZnO-E}$ under red radiation as well as a similar response for the capacitance of the ZnO film $CPE_{ZnO}$. Only under non-illuminated conditions does the $CPE_{ZnO}$ show 5E-6 higher values than in the other fittings, however the trend remains essentially the same (Figure 5.9).

The high degree of correlation between the experimental results and the fitting to the model in the Nyquist and Bode plots for the FTO/ZnO/MPA substrate are analogous to the plots presented in Figure 5.10 and Figure 5.11.

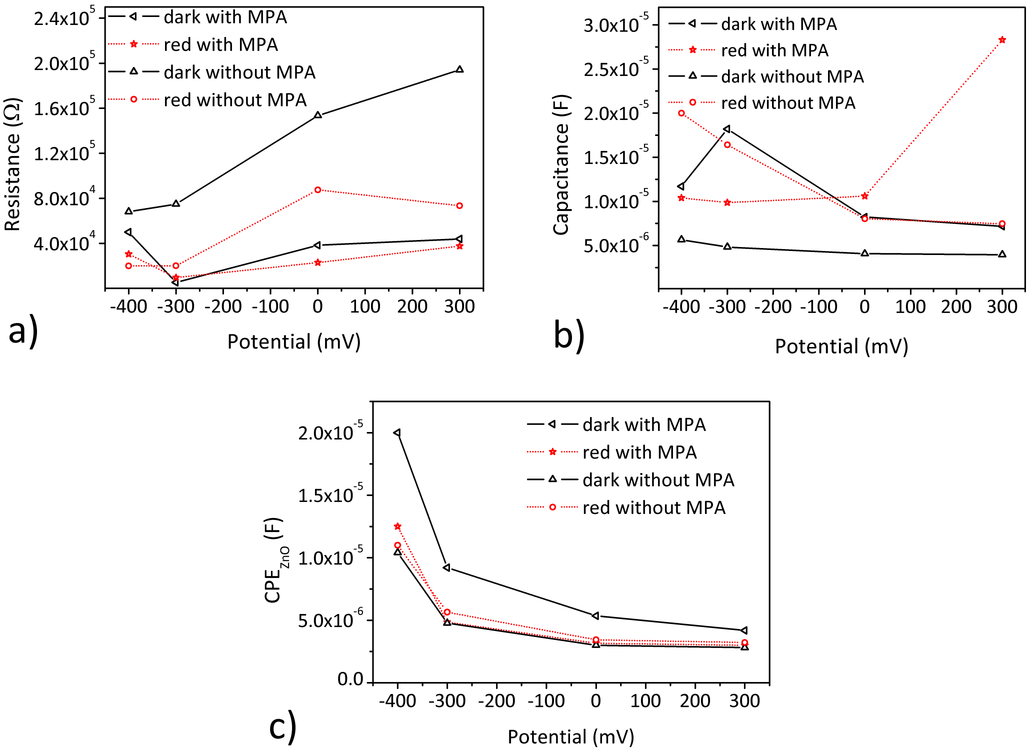

Figure 5.9: The resistance (a) and capacitance (b) fitting results for the FTO/ZnO/MPA system of the ZnO/MPA interface. (c) The ZnO film capacitance $CPE_{ZnO}$ in the dark (triangle with edge to the left) and under red illumination (star) compared to the results of the ZnO/E interface of the FTO/ZnO substrate (dark = triangle with edge on the top; under red illumination = circle).

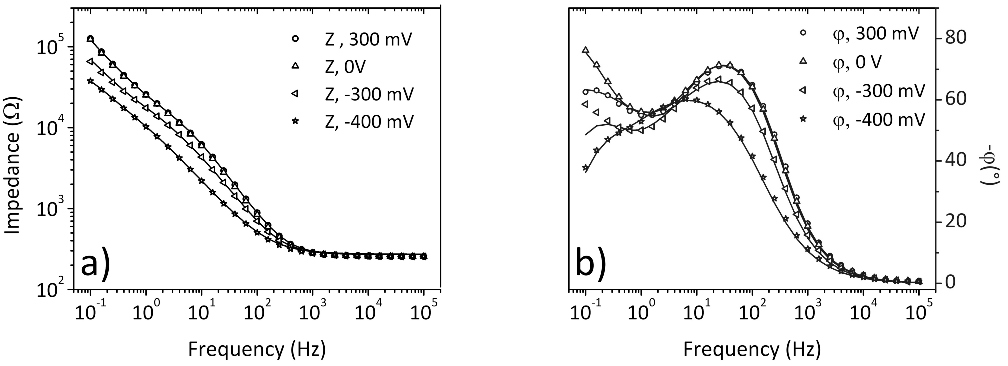

Figure 5.10: The Bode plot of the FTO/ZnO/MPA substrate under red irradiation at different applied potentials. The model (line) describes very closely the measured data (symbols) in the Bode magnitude (a) and in the Bode phase (b).

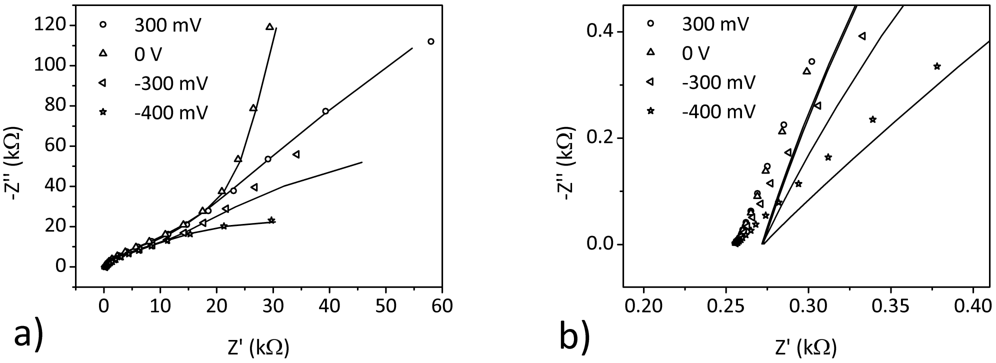

Figure 5.11: The Nyquist plot of the FTO/ZnO/MPA substrate under red irradiation at different applied potentials. The model (line) describes very closely the measured data (symbols) in the low frequency range (a) and the high frequency range (b)

In Figure 5.11(b) it can be seen that the calculated data at high frequencies does not fit the measured data. It was rarely observed that the serial resistance which consists of all in series resistances such as $R_{FTO}$ and $R_{MPA}$ are lower than the electrolyte resistance $R_E$. The reason for the decrease in the serial resistance could be caused by differences in the substrate quality or impurities but to achieve a clearer explanation further tests are required.

### 5.5.3 The EIS Results of the FTO/ZnO/MPA/PbS Substrate

For the FTO/ZnO/MPA/PbS system under conditions of darkness no charge carriers are generated on the PbS NPs. It is also expected that at the applied potentials used in these studies the Fermi-level positions of the electrode are located in the band gap or in the VB of the PbS NPs and hence the PbS particles cannot account for any of the current flowing in the system. The cyclic voltammograms of the ITO/PbS substrate presented in section 4.2.2 displayed band gaps located between -1,16 and 0,114 V for the $PbS_{1013}$ and for the $PbS_{1345}$ between -0,807 and 0,053 V which are in agreement with this assumption. Therefore, because of this assumption the FTO/ZnO/MPA model in contact with the electrolyte has also been used for modelling the substrates containing the PbS nanoparticles under dark conditions. The Bode and Nyquist plots of the FTO/ZnO/MPA/PbS substrate under dark conditions and fit using the FTO/ZnO/MPA model are shown in Figure 5.12 and in Figure 5.13.

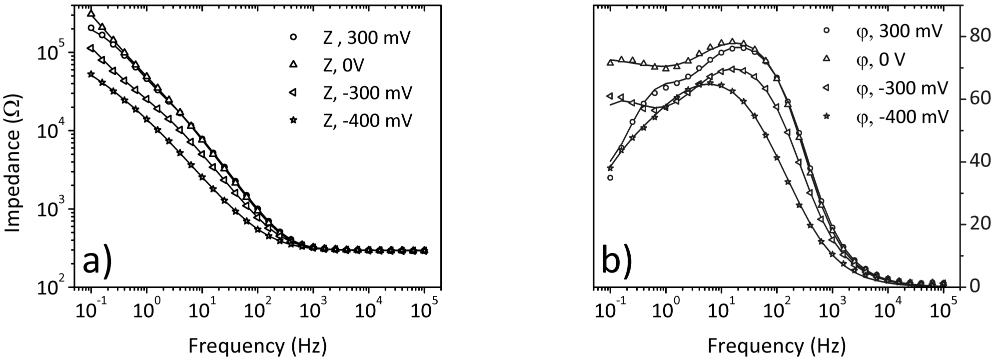

Figure 5.12: The Bode plot of the FTO/ZnO/MPA/PbS substrate with a PbS absorption maximum at 868 nm under non-illuminated conditions at different applied potentials. The model (line) describes quite well the measured data (symbols) in the Bode magnitude (left) and in the Bode phase (right).

As is apparent, good agreement is found when the measured data and the fitted results are compared. The following model which will be used to fit the system under red illumination does not fit the measured data measured in the dark.

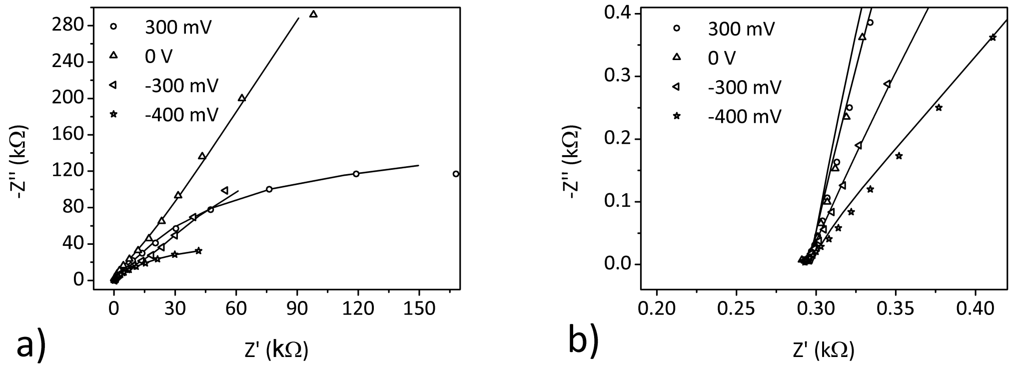

Figure 5.13: The Nyquist plot of the FTO/ZnO/MPA/PbS substrate with a PbS absorption at 868 nm under non-illuminated conditions and at different applied potentials. The model (line) describes the measured data (symbols) in the low frequency range (left) and the high frequency range (right) very well.

The complete model, with the PbS interfaces (Fig. 5.5[b],) are necessary to model the PbS sensitized substrate under incident light. Only in this case the impedance at the PbS interfaces can be measured due to exciton generation and subsequent charge separation. For this reason the complete model, has been used to fit the data set obtained for the FTO/ZnO/MPA/PbS substrate in contact with the electrolyte under red illumination. The electrolyte resistance $R_E$ was again set to 155 Ω for the reasons previously mentioned and the FTO resistance $R_{FTO}$ and the resistance of the MPA given by the previous calculation results were again employed as constant values for the modelling. Similar to the FTO/ZnO/MPA set up the values of the FTO/ZnO interface has been handled in the same way. For that reason the values of $R_{FTO-ZnO}$, $CPE_{FTO-ZnO}$ and $R_{ZnO-ZnO}$ were set to be constant and assigned the values as determined from the FTO/ZnO and FTO/ZnO/MPA calculations. The Bode and Nyquist plots of the FTO/ZnO/MPA/PbS substrate under red illumination are shown in Figure 5.14 and in Figure 5.15. Good agreement is also found for the measured data compared to the fitted results for the illuminated substrate. For all other substrates with different PbS sizes and irradiation conditions the plots are analogous to the presented images. The calculations result in $R_{MPA}$ values between 2 Ω and 7 Ω from the fittings irrespective of the kind of substrate employed. The $CPE_{ZnO}$ appears to be quite constant and equal to the value found for the

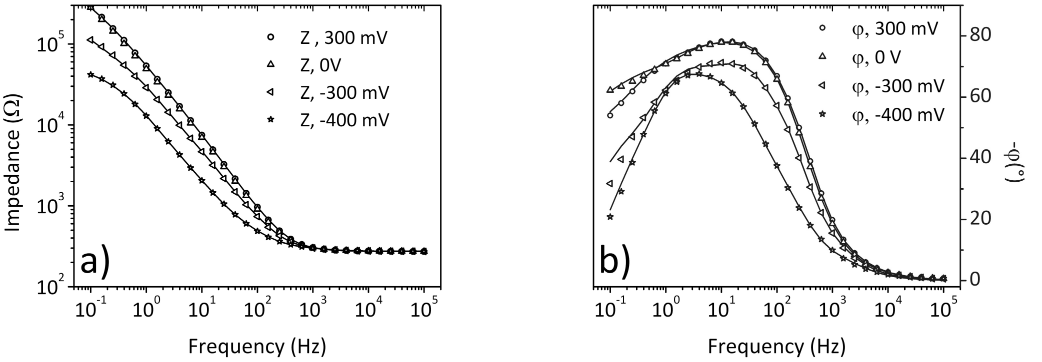

Figure 5.14: The Bode plot of the FTO/ZnO/MPA/PbS substrate with absorption maximum at 868 nm under red illumination at different applied potentials. The model (line) describes quite well the measured data (symbols) in the Bode magnitude (left) and in the Bode phase (right).

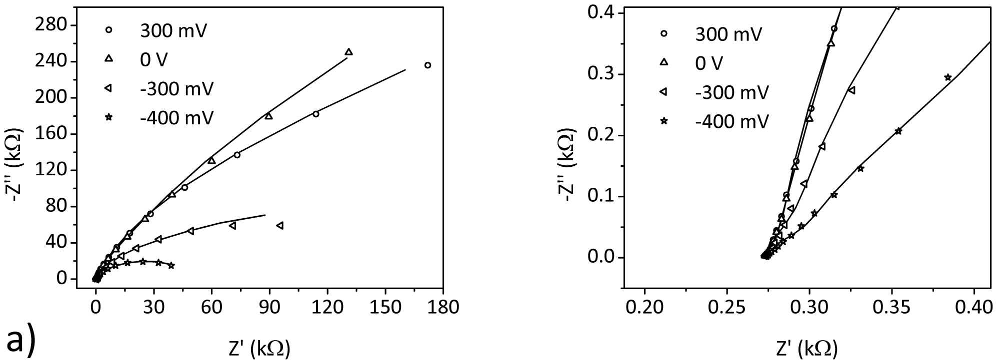

Figure 5.15: The Nyquist plot of the FTO/ZnO/MPA/PbS substrate with absorption maximum at 868 nm under red irradiation and at different applied potentials. The model (line) describes quite well the measured data (symbols) in the low frequency range (left) and the high frequency range (right)

FTO/ZnO/MPA substrate. Only in the case of an applied potential of -400 mV were lower values determined under red irradiation (Figure 5.16(a)). The capacitance of the ZnO/MPA interface CPE$_{ZnO-MPA}$ decreases when covered by PbS nanoparticles (Figure 5.16(b)) compared to the values of the data without PbS coverage.

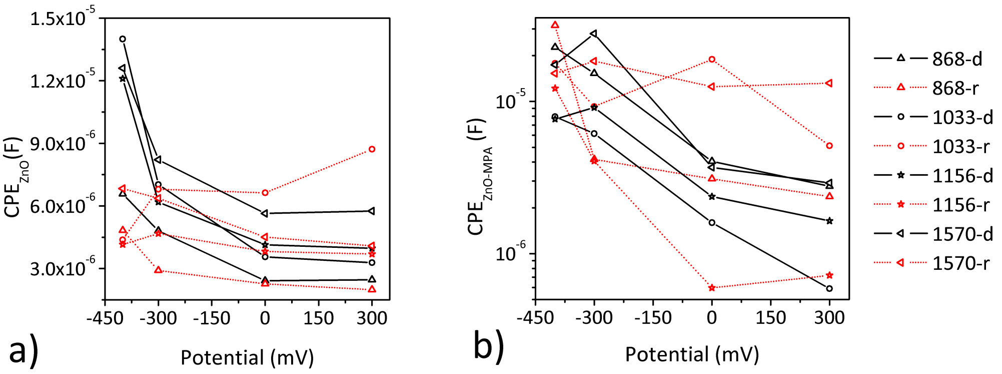

Figure 5.16: The ZnO film capacitance CPE$_{ZnO}$ (a) and the resulting capacitance of the ZnO/MPA interface CPE$_{ZnO-MPA}$ (b) of the FTO/ZnO/MPA system in the dark (line) and under red illumination (dotted line) and their dependence on different NP sizes which have absorption maxima at 868 nm (triangle with edge on the top), 1033(circle), 1156 nm (star) and 1570 nm (triangle with edge to the left).

By contrast the resistance of the ZnO/MPA interface R$_{ZnO-MPA}$ increases after coverage by the PbS nanoparticles at the ZnO/MPA surface, the highest resistance occurring under dark conditions (Figure 5.17).

As previously explained the PbS interface is determined just for the FTO/ZnO/MPA/PbS substrate under red irradiation. In Figure 5.18 the MPA/PbS and PbS/E interfaces are shown. The PbS size dependence can be more clearly seen in the resistance values as the capacitance values lie quite close together. Only the PbS nanoparticles with an absorption maximum at 868 nm show a clear and low capacitance at the PbS/E interface. In comparison to all other PbS NPs the band gap of PbS$_{868}$ is larger and may therefore be aligned more efficiently with the ZnO bands. The driving force to separate the charges might be stronger and because of the large band gap the back transfer of the electron be minimized which results in the total transfer of charge across the interface, so that the accumulation of charges in the PbS interface does not occur.

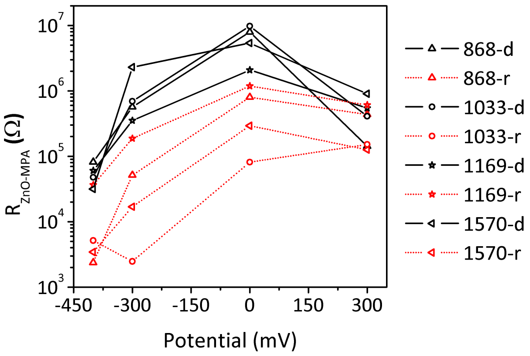

Figure 5.17: The resulting resistance for the ZnO/MPA interface $R_{ZnO-MPA}$ of the FTO/ZnO/MPA system in the dark (line) and under red illumination (dotted line) and their dependence on different NP sizes which have their absorption maxima at 868 nm (triangle with edge on the top), 1033(circle), 1156 nm (star) and 1570 nm (triangle with edge to the left).

This can be also seen in the lowest resistances $R_{MPA-PbS}$ and $R_{MPA-PbS}$ at both of the PbS interfaces of the $PbS_{868}$. The highest resistances occur using PbS with an absorption wavelength at 1033 nm. For the other two PbS nanoparticle sizes the values are located intermediate to these values. The potential dependence of the system for all interfaces presented above has been examined. Generally, between -300 mV and 300 mV the values of the resistances and capacitances remain approximately constant whereas at values of the potential of -300 mV the start of the changes in the trend which result from the convergence of the potential to the CB can be observed. The resistances of the MPA-PbS interface are lower compared to the resistances of the PbS-E interface. In section 4.2.3 it has been mentioned that the electron injection from solution by $SO_3{}^{2-}$ was a slow process and therefore is likely to be amongst the contributive factors for the increase in the resistances.[44]

### 5.5.4 The EIS Results for Shorter Illumination Wavelength

During the calculations there were a number of differences in the ease of fitting the data. The data set for the red (630 nm) illuminated and non-illuminated samples resulted in easily attained fit matches between the measured and the computed data. The fitting of the measured data obtained under yellow (570 nm) illumination was very time consuming because of the large variation in finding the

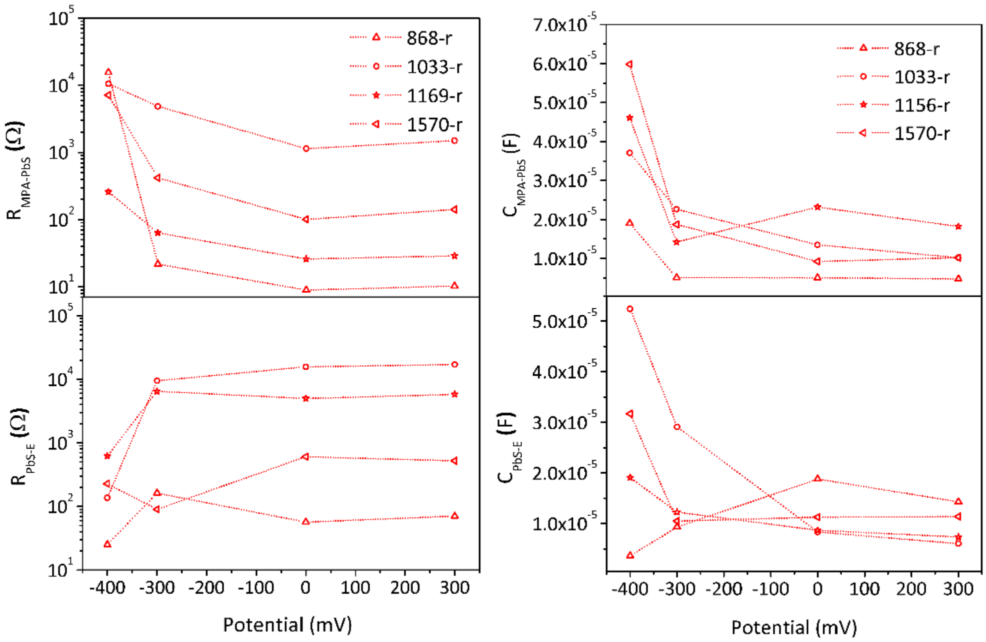

Figure 5.18: The results of the MPA/PbS and PbS/E interfaces of the FTO/ZnO/MPA system under red illumination (dotted line) and their dependence on the different NP sizes having their absorption wavelength maxima at 868 nm (triangle with edge on the top), 1033(circle), 1156 nm (star) and 1570 nm (triangle with edge to the left).

starting points as well as the calculation itself. Often the starting points employed did not result in a sufficient fit and gave high resistance and capacitance errors. Therefore it is necessary to find out starting points which yields acceptable fits and low errors. Easier processing was achieved in fitting the data for the samples under blue (470 nm) illumination while the calculated fits for the UV illumination (370 nm) were also not easy to obtain. Therefore the fitting of the results raises questions concerning the interpretation of these differences and the uniqueness of the model for sample illumination at shorter wavelengths. The handling of the measured data set and the modelling is analogous to the procedure presented above (section 5.5).

### The Modelling of the FTO/ZnO Substrate

The model in Figure 5.4(b) in section 5.5.1 gives fits which match the measured data at shorter illumination wavelengths. Only for the measurements at 0 V for the FTO/ZnO substrate under yellow illumination (Figure 5.19) and at 300 V for the blue illumination (Figure 5.20) an exiguous deviation in the low frequency range revealed. Under UV irradiation significant deviations occurred at a potential of 0 V (no Figure shown). For further analysis the data set received under blue irradiation is more useful so that all Bode and Nyquist plots will be shown.

The resulting resistances and capacitances of the data set obtained from samples under blue illumination show a similar trend compared to the results of the modelling for samples in the dark and under red illumination (Figure 5.21). The data from samples under yellow irradiation do not fit the trend. Especially the values of $R_{ZnO}$, $R_{ZnO-E}$, $CPE_{ZnO}$ and $CPE_{ZnO-E}$ differ from the data set measured under blue irradiation i.e. in contrast to the fit results the resistances under yellow irradiation are lower and the capacitances are higher when compared to the resistances and capacitances of the samples under blue illumination. This anomaly is also reflected in the error values. While the data errors under conditions of blue irradiation result in very good fits, errors upto 90%, and for two values errors upto 200%. For fittings which were less good the errors in these two values can increase to 400% whereas in the case of yellow illumination the errors could be upto twice as high as 400%. The same high errors as for the yellow illuminated fittings can be also determined for the data set obtained under UV

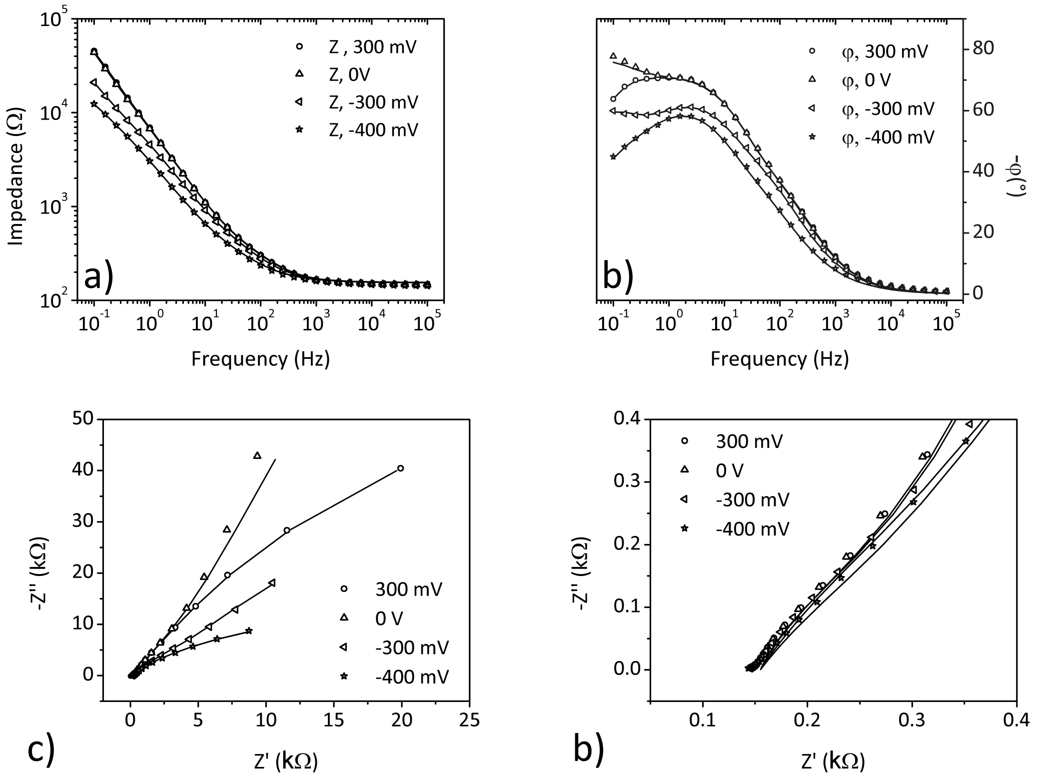

Figure 5.19: The Bode plot of the FTO/ZnO film under under yellow illumination at different applied potentials. The model (line) describes quite well the measured data (symbols) in the Bode magnitude (a) and in the Bode phase (b). The Nyquist plot shows the analogous fitting in the low frequency range (c) and the high frequency range (d)

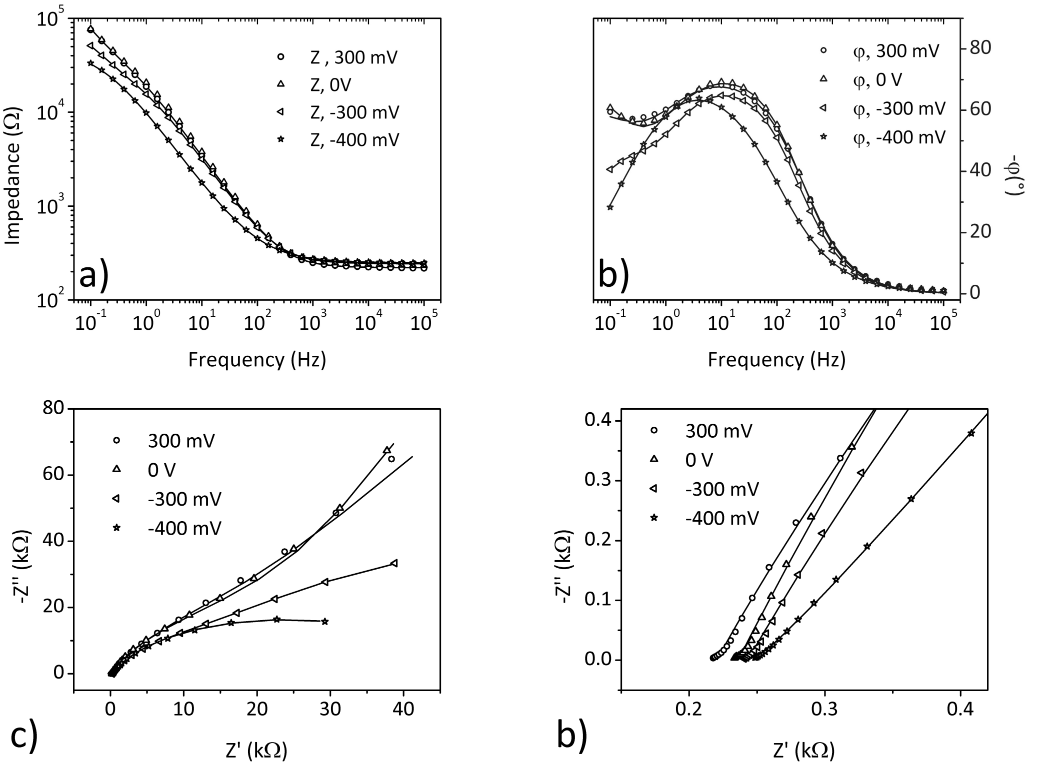

Figure 5.20: The Bode plot of the FTO/ZnO film under blue illumination at different applied potentials. The model (line) describes quite well the measured data (symbols) in the Bode magnitude (a) and in the Bode phase (b). The Nyquist plot shows the analogous fitting in the low frequency range (c) and the high frequency range (d)

illumination. The errors in the fits for samples under blue irradiation are also relatively high, but they are located just within the limits of acceptance. The reason for the difficult fittings under blue and yellow illumination are presented later in more depth.

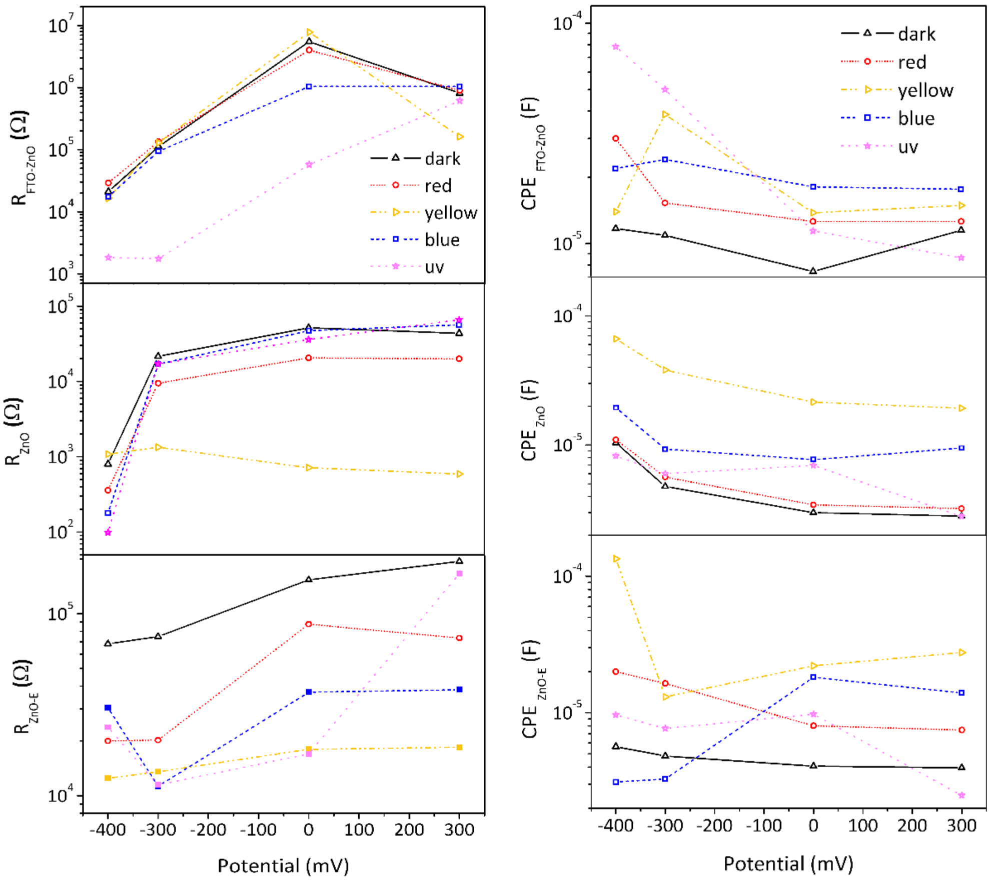

Figure 5.21: The calculated values of the FTO/ZnO/electrolyte system plotted against the applied potential and four different illumination wavelengths and under non-illuminated conditions (see the colors of the lines). The FTO/ZnO interface with the $R_{FTO-ZnO}$ and the $CPE_{FTO-ZnO}$ (top). The ZnO film capacitance $CPE_{ZnO}$ and the ZnO film resistor $R_{ZnO}$ (middle). The ZnO/E interface is given by $R_{ZnO-E}$ and $CPE_{ZnO-E}$ (bottom).

However, the obtained values from the fitting of the FTO/ZnO film, which have been used to obtain constant values for the FTO-ZnO interface after the linker attachment, seem to be in good agreement with the measured data. It should be mentioned that the ZnO portion of the model is symmetrical so that the positions of the calculated interfaces could be reversed. The implication is therefore that, if the values which have been kept constant and stand for the FTO-ZnO interface a fit of the FTO/ZnO/MPA data set cannot be achieved if the R-CPE element of the symmetrical model were mathematically intended for the ZnO-E interface. Nevertheless no significant problems were encountered. The Bode and Nyquist plots give a good fit to the calculated values of the measured data under blue illumination (Figure 5.22). Some drift in the calculated data (line) from the measured data (symbols) can occur in the low frequency range and the upper end of the high frequency range. In the case of samples measured under yellow irradiation the fits have quite a large deviation at potentials of -300 mV and -400 mV (not shown here) and are at the limit of acceptability.

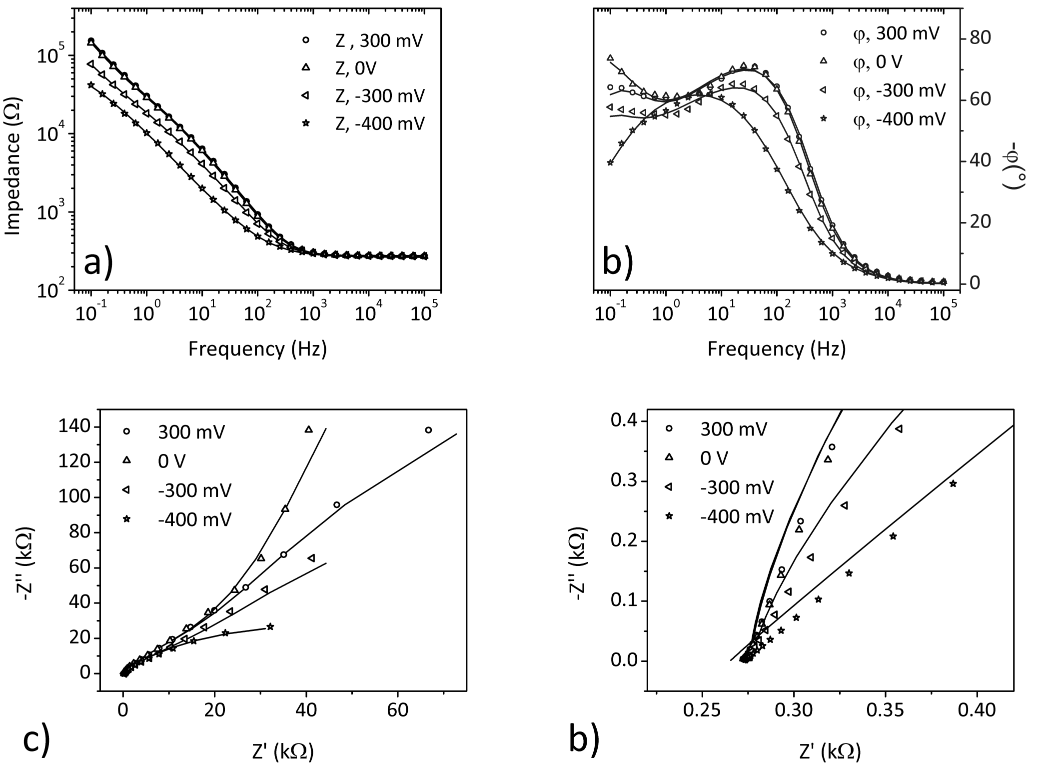

Figure 5.22: The Bode plot of the FTO/ZnO/MPA film under blue illumination at different applied potentials. The model (line) describes quite well the measured data (symbols) in the Bode magnitude (a) and in the Bode phase (b). The Nyquist plot shows the analogous fitting in the low frequency range (c) and the high frequency range (d)

After the linker attachment the values for the $\mathrm{CPE}_{ZnO}$ and the capacitance and resistance of the ZnO-MPA interface do not differ from the results measured for samples in the dark and under red illumination (not shown here). The values of $R_{ZnO-MPA}$ follow the trend for the values under dark and red conditions and gives values of the order of approx. $10^4$ Ω. The break at -300 mV in the value of $R_{ZnO-MPA}$ down to $10^3$ Ω can also be seen under shorter illumination wavelengths (see for comparison Figure 5.8(a)). The $CPE_{ZnO-MPA}$ values (see for comparison Figure 5.8(b)) under yellow irradiation are located above the highest values of the dark illumination with a value of 5E-5 F. The values under UV irradiation follow no specific trend and the values are distributed close to the values obtained for the other illumination wavelengths. The $CPE_{ZnO}$ values are extended over the range of 1E-6 up to 2E-5 F and increase at -400 mV analogous to the values in Figure 5.8(c). The errors in the values increase rapidly. For the yellow and UV irradiated samples errors from 30 up to 2000% were found. These high errors give rise to doubts concerning the correctness of these values and optional the model. Hence the errors in the calculations of the samples under conditions of blue irradiation are half of that but are nevertheless also beyond the limit of acceptable results. However it was considered to be worth to obtain the calculations for the complete FTO/ZnO/MPA/PbS substrate for the data set under blue irradiation in order to check for the existence of strong deviations compared to that of conditions under red illumination.

### The modelling of the FTO/ZnO/MPA/PbS Substrate

The modelling of the PbS size dependence was repeated only for the measured data for samples under blue irradiation. The values of the yellow and UV illumination data sets were also time consuming to fit so that the probability of finding the correct starting points, which must be keep constant, are extremely low. The Bode and Nyquist plots of the blue irradiated sample are presented in Figure 5.23. A well matching fit of the calculated data with the measured data can be observed.

The values of the MPA-PbS and PbS-E interface can be found in Figure 5.24. The capacitance of the ZnO film and the ZnO-MPA interface are presented in Figure 5.25(a) and Figure 5.25(b) as well as the resistance of the ZnO-MPA interface in Figure 5.26. Except from the increase in the values for $R_{ZnO-MPA}$ (Figure 5.26) the resistances $R_{MPA-PbS}$ (Figure 5.24 bottom left) and $R_{PbS-E}$

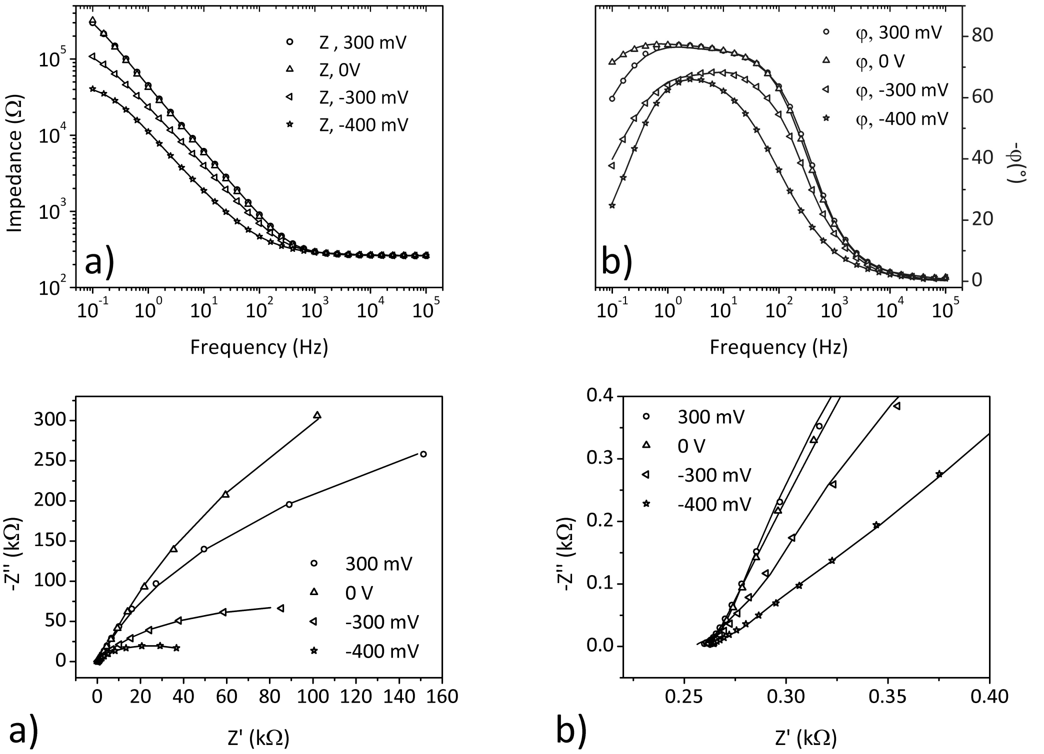

Figure 5.23: The Bode plot of the FTO/ZnO/MPA/PbS system under blue illumination at different applied potentials. The model (line) describes quite well the measured data (symbols) in the Bode magnitude (a) and in the Bode phase (b). The Nyquist plot shows the analogous fitting in the low frequency range (c) and the high frequency range (d)

(Figure 2.24 top left) are lower compared to the red illuminated PbS system. The capacitances of the ZnO (Figure 5.25(a)) and ZnO-MPA interface (Figure 5.25(b)) are quite similar to that of the capacitances for the red illuminated PbS system. A decrease can occur in the capacitance $C_{MPA-PbS}$ (Figure 5.24 top right) and a completely different trend compared to the results of the red illuminated PbS system are seen for the capacitance $C_{PbS-E}$ (Figure 5.24 bottom right). The maximum error recorded is around 400% and all other values are less at about 100%. For very good fits all values can also be found to possess errors below 10%. The additional two RC elements in the model used to account for the PbS interface in Figure 5.4 make the model quite complex. Generally it is agreed that the more complex the model the simpler it is to find a good fit of the plots with a low error in the resistance and capacitance values. But in the course of the modelling of the experimental data here this assertion is only partly true i.e., only in the case when all values are not fixed. The systems under study here are also quite complex and therefore an extremely simple model is not to be expected. Furthermore the values of the FTO-MPA interface and the $R_{ZnO}$ are employed as constant values so that the determination of the relatively low errors of all calculated values are noteworthy.

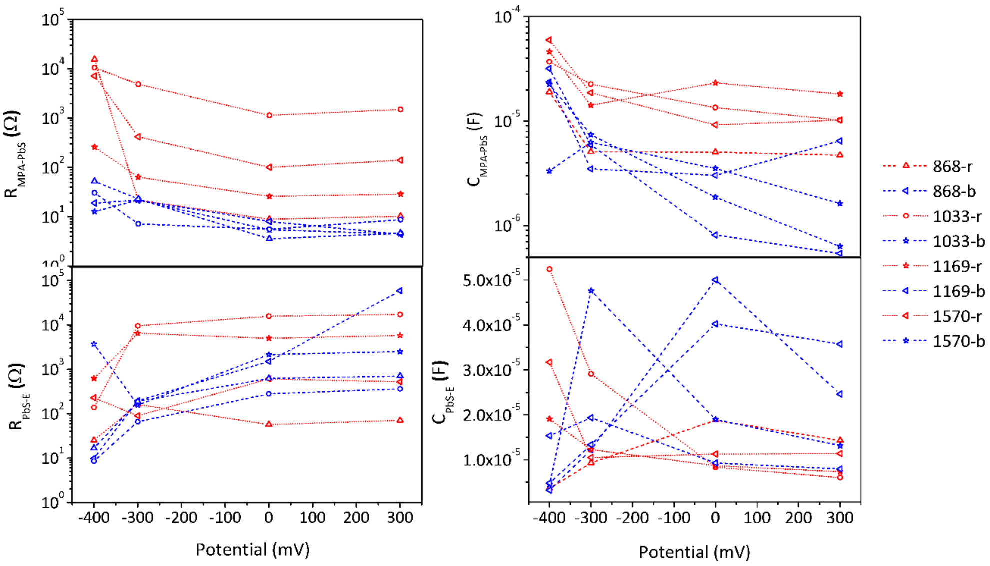

Figure 5.24: The results of the MPA/PbS and PbS/E interfaces for the FTO/ZnO/MPA system under blue illumination (dashed line) in comparison to the system under red illumination (dotted line) and their dependence on the different NP sizes having their absorption wavelength maxima at 868 nm (triangle with edge on the top), 1033(circle), 1156 nm (star) and 1570 nm (triangle with edge to the left).

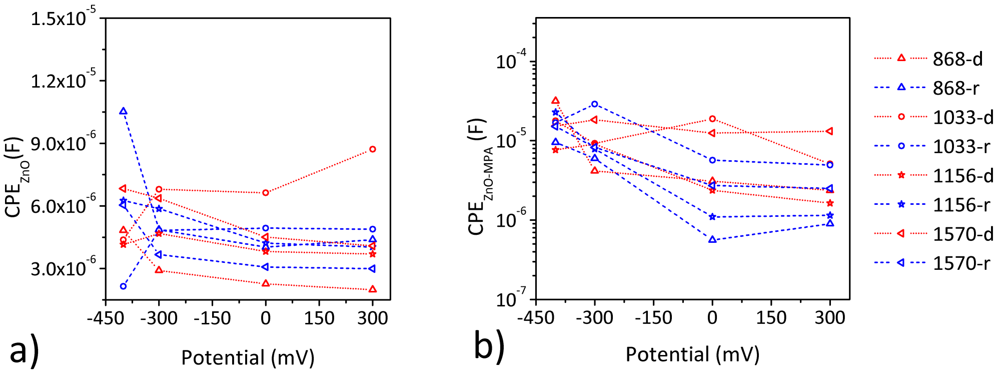

Figure 5.25: The ZnO film capacitance $CPE_{ZnO}$ (a) and the resulting capacitance of the ZnO/MPA interface $CPE_{ZnO-MPA}$ (b) of the FTO/ZnO/MPA/PbS system under blue illumination (dashed line) and under red illumination (dotted line) and their dependence on different NP sizes which have absorption maxima at 868 nm (triangle with edge on the top), 1033(circle), 1156 nm (star) and 1570 nm (triangle with edge to the left).

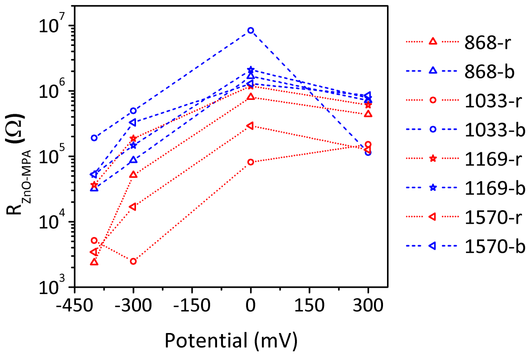

Figure 5.26: The resulting resistance of the ZnO/MPA interface $R_{ZnO-MPA}$ of the FTO/ZnO/MPA/PbS system under blue illumination (dashed line) and under red illumination (dotted line) and their dependence on different NP sizes which have their absorption maxima at 868 nm (triangle with edge on the top), 1033(circle), 1156 nm (star) and 1570 nm (triangle with edge to the left).

## Explanation of Results

Generally the computation of the measured FTO/ZnO/MPA/PbS system works well with the framework model presented in Figure 5.4. The capacitances of the ZnO interface are less affected by the PbS attachment and it appears to make no difference whether red or blue light irradiation is used. However, the resistances are affected much more. Whereas $R_{ZnO-MPA}$ increases strongly under blue illumination the resistance of the PbS decreases under blue illumination compared to that of red illumination. There is reason to believe that the proven exciton generation in the ZnO at wavelengths from the UV up to 460 nm hinder the electron transfer at the ZnO-MPA interface which may also be seen in the slight increase in the capacitance of this interface. The reason why the ZnO capacitance of the whole ZnO layer did not increase may be explained by the fast removal of the charges towards the FTO. At the beginning of the third chapter it was mentioned that ZnO has a high electron mobility of between 1 and 155 $cm^2/V{\cdot}s$[107] which would favour fast charge removal. Furthermore a directing force based on the relative band positions between the materials can be assumed because the ZnO CB is located in higher energies as the FTO CB.[203,204] Also a supportive force from the linker molecule cannot be ruled out.

In Figure 5.4 the position of the CB and the VB of the ZnO used in this thesis and the trap states found in the literature are presented. It could be shown that the light either red, yellow or blue used to illuminate the samples has enough energy to address existing inter band trap states. Which kind of trap states really exist in the ZnO cannot be clarified in this thesis. But it is possible to recognize possible processes in the ZnO that have, until this point in the discussion, not been taken into consideration.

At the PbS interfaces the trend as was observed under red illumination (section 5.5.3) could be found also during blue irradiation. Thereby the MPA-PbS interfaces have a lower resistance than the PbS-E interfaces. The total decrease in the resistances and $C_{MPA-PbS}$ under blue illumination should be noted. If the band positions of the materials used are considered in Figure 5.27 then the reason for a back reaction becomes clearer. Figure 5.27(a) shows the theoretically determined positions of the PbS sizes used for the EIS measurement compared to the ZnO band position as measured using CV and LSV and in Figure 5.27(b) the band positions measured by CV compared to the measured ZnO band positions are presented. It is clear that the PbS bands used for this study are slightly shifted to more negative potential i.e. to higher energies.

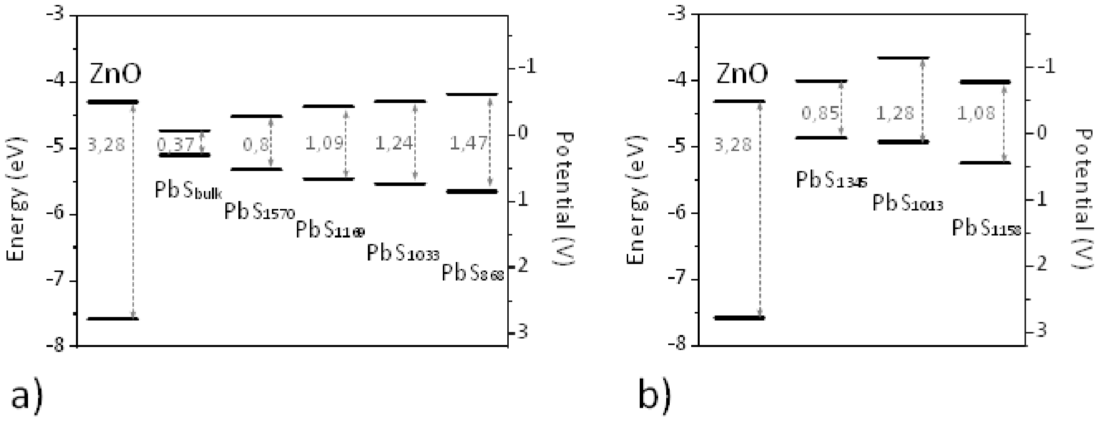

Figure 5.27: The band position of ZnO as determined from UV/VIS spectroscopy and LSV compared to (a) the theoretical determined band positions of PbS bulk, PbS NCs with an absorption wavelength of 1570 nm ($PbS_{1570}$), $PbS_{1169}$, $PbS_{1033}$, $PbS_{868}$ NCs and (b) compared to the PbS band positions determined from CV of ITO glass coated with $PbS_{1345}$ NCs and $PbS_{1013}$ NCs seen in Figure 4.7 and also of ITO/ZnO/MPA/PbS with $PbS_{1158}$ NCs seen in Figure 4.6(b).

The ZnO CB is located at approx. -4.31 eV whereas the CB of the $PbS_{1158}$

is positioned at -4.02 eV and the VB at -5.24 eV with respect to the vacuum level (Figure 5.27(b)). Consequently at an illumination wavelength of approx. 470 nm a generation of an exciton in the PbS VB and CB and the ZnO VB and surface states can occur (Figure 5.28(a)). In the case where suitable ZnO surface states are addressed a back electron transfer from the ZnO to the PbS VB could conceivably occur. On the one hand this results in a filling of the holes located in the PbS VB and hinders the recombination of the promoted e$^-$ from the PbS CB back to the PbS VB (Figure 5.28(b)). On the other hand in addition to the electrons generated in the PbS, the electrons that are thermally activated from the ZnO trap states closely below the ZnO CB can also be transferred.

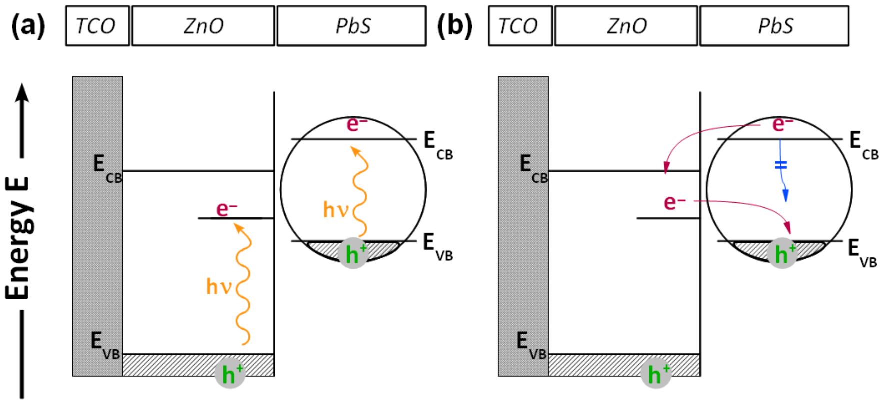

Figure 5.28: The processes which occur under blue illumination in a ITO/ZnO/MPA/PbS substrate. (a) The generation of electron-hole pairs in the PbS NC including VB and CB and the electron-hole pair generation of the ZnO using the VB and the surface trap state. (b) Back reaction of the e$^-$ from the ZnO surface state into the VB of the PbS NC which hinders the recombination of the promoted e$^-$.

Under red and yellow illumination these kinds of processes could also be possible. That the electronic band gaps are often larger than the optical ones is shown in section 4.2.2 because of the extra energy required to transfer charge across the semiconductor interface. This means that for red light this process can more or less be ruled out. For yellow light the probability for such back electron transfer is higher but it can also be seen that the trap states given in the literature do not possess an appropriate position to be addressed. It is also not mentioned whether this kind of trap state may be located at the surface, as only on the surface can an electron skip from one particle to another.

Returning to the yellow illumination data set the trap states in the ZnO might be detrimental for solar cell applications but might be beneficial for other approaches. In the literature it could be demonstrated that photoelectrical processes are far from the initial conditions of photocatalytic processes. Shi et.al.[222] have shown that the trap states in a doped material act as an "electron container". Such electrons "saved" in the trap states do not contribute to photoelectricity but do contribute to photocatalysis. If the results obtained from the EIS calculation are considered in this light then such an electron containment can be expected. Such electron storage results in a force which comes from inside of the ZnO particle and will not just have an influence on the electron transfer through the particle; it will also have an influence on the charging and surface properties of the ZnO particle. This could be a explanation for the strongly different values observed under yellow irradiation.

The different resistances and capacitances observed in the EIS data resulting from UV irradiation are also much easier to understand in this way. An exciton generation with an $e^-$ transfer to the CB and additional trap states and surface state filling processes can be assumed. For that reason the systems which were used in this thesis have more processes than visualized in Figure 2.4. Consequently the model shown in Figure 5.4 is not sufficient to explain such a complex course of events especially that of the $e^-$ behavior with known trap states positions as well as the electron back transfer to the PbS VB plus a lot of other competing processes.

When the PbS sizes are also included in the explanation then the band and trap state positions of the PbS NCs with respect to the ZnO gel are also necessary to consider. In section 5.5.3 an influence of the wider band gap of the $PbS_{868}$ NC concerning its lower resistances and capacitances at the interfaces compared to the larger PbS NCs could be shown. The additional optimal distances between the PbS CB and the ZnO CB results in an injection of the $e^-$ into the ZnO CB for which the possibility of a back transfer from ZnO CB into the PbS CB has to be minimized because of the clear potential step. When the NC size increases the band gap decreases and the PbS CB approaches that of the ZnO CB which allows more and more electron back transfer to occur. Therefore the driving force for the $e^-$ injection or back reaction is dramatically dependent on the distances of both bands. It is assumed that the possibility of such back reactions can be found in the following order: $PbS_{1570}>$ $PbS_{1169}>PbS_{1033}>PbS_{868}$. Another process involves the surface states of the ZnO and the irradiation wavelengths. The position of the PbS VB in comparison to the ZnO surface states are therefore important to consider because of back reaction of excited ZnO surface states into the PbS VB which also might be able to neutralise a hole located in the PbS VB (Figure 5.28). The larger the band gap of the PbS the more the back reaction is likely to happen. For smaller band gaps the possibility to approach such surface states are less conceivable, so that in the order $PbS_{1570}<PbS_{1169}<PbS_{1033}<PbS_{868}$ the PbS is able to use the advantages as outlined in Figure 5.28. For the $PbS_{868}$ NC such trend was mentioned in section 5.5.3. The reason why no significant differences in the resistances and capacitances at the interfaces could be seen in the case of $PbS_{1570}$, $PbS_{1169}$ and $PbS_{1033}$ may caused by the fact that the each processes which run at the same time may be cancel each other out.

### 5.5.5 The Resistance of the Linker

In Figure 5.4 the resistance $R_{MPA}$ was included which is related to the resistances which are associated with the linker itself. It was mentioned that for any one linker the resistance $R_{MPA}$ should possess its own characteristic resistance and should be constant. In this section this model was used for the fitting of the linker dependent substrates from chapter 3 and 4 where the EIS measurements were also undertaken and the data handling was based on the same rules as above. The EIS measurement determination of the linker resistances called here $R_{linker}$ is presented for each different linker in Figure 5.29. The resulting resistances of the linkers range go up to 30 Ω. For the MPA just one calculation point is presented as the measurements made under blue irradiation were problematic. From the previous section an MPA linker resistance of approx. 10 Ω under non-illuminated conditions was measured.

The highest resistance has been calculated for OA which is followed by TGA > HDT > MPA > TAA > MA. The error bars are given for the resulting errors in the $R_{linker}$ resistances. Some fluctuation in the values shows that the

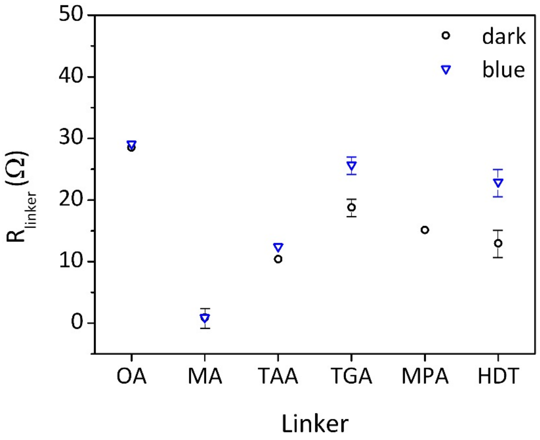

Figure 5.29: The comparison of the calculated linker resistances from the ITO/ZnO/linker substrate from chapter 3 and 4. The given error bars are to account for errors which result from the calculation. The errors of the non marked point are as large as the dimensions of the point itself.

EIS measurements are quite imprecise with respect to the absolute determination of resistances. But the fitting results show an approximate magnitude of the linker resistances. In summary the linker contributes only a small part to the total resistance and is limited in magnitude to values up to 30 Ω for the short linker used in chapter 3 and 4.

## 5.6 General Remarks on the Modelling

To find a model that matched the system well and provided a high level of understanding a lot of various models have been tested. For the following presented models the "()" stands for a parallel connected element and "[]" for a element which has been connected in series. For instance a normal electron transfer through the RC element in contact with electrolyte as shown in Figure 2.6 will be represented by [(RC)$R_E$]. To represent CPE elements a "Q" will be used.

The starting point for the system is the FTO substrate. Above, it was shown that FTO, although represented as a simple system, has a relatively complex electrochemical behavior. It was also mentioned above that the FTO can be considered as a highly doped semiconductor. For that reason quite complex electronic structures as well as electron processes, similar to those in ZnO, have to be taken into consideration. The FTO electrolyte contact has been neglected above because of the presence of very small pores in the ZnO which prevent the electrolyte from reaching the TCO interface. In these studies to fit the FTO EIS data an independently developed model has resulted which is similar to that of the model reported by Strømme et.al.[218] with:

$$[R_{FTO}(CR)_{FTO-E1}([RQ]Q)_{FTO-E2}R_E] \tag{5.1}$$

However, the idea behind this was a parallel process occurring at the FTO surface. One such process may be the normal e$^-$ transfer into the FTO CB and the other an e$^-$ transfer into the FTO defect states. Both should occur at the same time and should therefore be connected in parallel. But if one views the complete FTO area such that the first process happens at one place on the electrode surface and the second process at another place then the (RQ) and ([RQ]Q) elements connected in series can be seen as a sum of both processes. The model matched the data quite well at all four potentials and illumination wavelengths.

For the next view of modelling the intermediate states of the FTO/ZnO film the model has been treated in such a way that the FTO processes are located in parallel. This means that the additional contact between FTO and the electrolyte has been assumed here to occur in parallel to the ZnO/electrolyte contact. For that reason the standard ZnO model (also seen in Figure 5.4(b)):

$$[R_{FTO}(Q_{ZnO}[(QR)_{FTO-ZnO}R_{ZnO}(RQ)_{ZnO-E}])R_E] \tag{5.2}$$

has been connected in parallel with the FTO model in equation 5.1 to equation 5.3:

$$\begin{gathered}[R_{FTO}((Q_{ZnO}[(RC)_{FTO-E1}([RQ]Q)_{FTO_{E}2}])\\ [(RQ)_{FTO-ZnO}R_{ZnO}(QR)_{ZnO-E}])R_E]\end{gathered} \tag{5.3}$$

For the fit the calculated results of the pure FTO substrate were used and added into the FTO/ZnO model. The elements of the FTO interface which have an error of 0%<error<1% have selected and used as a constant value. All elements with higher errors than 1% have been selected in the fitting such that the errors are allowed to possess a maximum value of 10%, i.e. these parameters were not allowed to fluctuate completely freely during the modelling. For all fitting results the FTO-ZnO interface was similar to that of the blank FTO and gave reasonable results also for the modelling of the ZnO.

For the FTO/ZnO/MPA substrate the FTO has been handled in the same way as in the above fitting procedures and the FTO-ZnO interface values of $R_{FTO-ZnO}$ and $CPE_{FTO-ZnO}$ were handled according to the fittings in section 5.5.3 and 5.5.4. The $R_{MPA}$ resistor has also been added in the case of the FTO/ZnO/MPA substrate.

If the PbS interface in the FTO/ZnO/MPA part of the model were included then the calculation results did not longer match the measured data. The FTO/ZnO/MPA/PbS substrate conforms to the observations during the substrate measurements. It appears that the FTO/ZnO and the FTO/ZnO/MPA substrate act like a sponge, i.e. as if the electrolyte has been sucked into the layer. Generally the ZnO surface is comprised of a polar area with oxygen and zinc atoms and the MPA molecules have two hydrophilic functional groups and a short carbon chain. For that reason the hydrophilic surface property and, due to the presence of the mesoporous structure, capillary and hygroscopic actions may be assumed. After the PbS deposition the electrolyte stayed on the surface as a drop which indicates a hydrophobic effect. This effect is caused by the stabilizer of the PbS NCs such as trioctylphosphine and oleic acid. The long molecules consist mainly of carbon chains and partially unsaturated chemical compounds which result therefore in water-repellent surface properties. There is reason to believe that the FTO cannot be in contact with the electrolyte which would make the FTO/E model in parallel unnecessary in the case of the FTO/ZnO/MPA/PbS substrates. Certainly the last model is extremely complex and is in opposition to the principle of Occam's razor because the overall model also works without the inclusion of the FTO portion which can be seen from section 5.5. Occam's razor is a law of economy or parsimony which is encapsulated by the principle that the simplest explanation is most likely to be the correct one. The strict fitting rules and the multiplicity of constant values which are employed in any such fitting should always be presented. This result shows that a complex model cannot always fit all measured data.

Based on a different but quite similar idea one can devise the following model. It is known that the ZnO is well covered with the linker (see section 4.3.1). Another interesting approach is based on the fundamental idea that the attachment of the linker to the PbS is hindered by the available space so that not every linker is connected to a PbS NP. That means that free linker functional groups are also present at the interface. For that reason the FTO/ZnO/MPA model and the FTO/ZnO/MPA/PbS model have been connected in parallel. The sum of the resistance and capacitance can then be represented by equation 5.4

$$X = A \cdot X_{MPA} + B \cdot X_{MPA/PbS} \tag{5.4}$$

where A and B are some fraction representing the component of the current passing through each portion (MPA-electrolyte or PbS-electrolyte) of the interface. This model becomes enormously complicated:

$$\begin{aligned} &[R_{FTO}([(Q_{ZnO1}[(RQ)_{FTO-ZnO1}R_{ZnO1}(RQ)_{ZnO1-MPA1}])R_{MPA1}] \\ &\qquad [(Q_{ZnO2}[(RQ)_{FTO-ZnO2}R_{ZnO2}(QR)_{ZnO2-MPA2}]) \\ &\qquad\quad [R_{MPA2}(RC)_{MPA2-PbS}(RC)_{PbS-E}]])R_E] \end{aligned} \tag{5.5}$$

Thereby the calculations were undertaken for A$\cdot$ $X_{FTO/ZnO/MPA}$ with A : 1, 0.75, 0.5, 0.35, 0.3, 0.25, 0.2, 0.15, 0.1 as constant values being placed into the results of the FTO/ZnO/linker data set and with an open B$\cdot$ $X_{FTO/ZnO/MPA/PbS}$ term. The calculation results showed that 1, 0.75, 0.5, 0.2, 0.15 and 0.1 do not fit the data and are extremely different from the measured data set. In the case of 0.35, 0.3, 0.25 the shape of the measured data are presented but shifted to higher frequencies and with lower intensity. A convergence can be seen but not a complete overlapping of the calculated data with the measured data. From this point of view the model is also opposed to the principle of Occam's razor and should be simplified in further studies with the idea behind it being to find processes taking place in parallel which are related to each for the two parallel existing systems as a result of incomplete coverage. In all cases the basic model must be questioned as the execution may nevertheless be correct.

## 5.7 Conclusion

A model was found by which the non-illuminated and red illuminated data sets could be modelled. The results fit quite well and give reasonable trends in the values of the capacitance and resistance. At shorter illumination wavelengths a good fit has been also achieved. But the possibility of the existence of a more complex system has been shown to exist by the analysis of the results in which the ZnO exhibits a more complex electronic structure than expected. In addition a multiplicity of trap states directly under its CB including trap states (such as oxygen and zinc vacancies) exists. For that reason the treatment of ZnO as a wide band gap semiconductor where only the exciton separation occurs in the absorbing material is overly simplistic. In the highly doped ZnO an electronic structure arises where the defects in the ZnO crystalline structure may be viewed as an electron container. Whether an electron can be transferred to other particles is dependent on the number of surface states and the possibility to move within the ZnO crystal. The filling of these states can occur through electron promotion which results from electron excitation through absorbance of incoming light which has a smaller energy than the band gap energy. The resistances and the capacitances which result from each irradiation shows that the proposed model matches that of the measured results but gives impetus for further development especially with respect to the interpretation of the importance and action of trap states. The evidence for such trap states could be found in changes in the magnitude of photocurrent at excitation wavelengths whose energy is lower than the band gap of the ZnO. In total it could be shown that trap states are a very important consideration for the clarification of the processes in the ISC based metal oxide. However to obtain a clearer overview of such processes it is necessary to locate the trap states in the metal oxide. Particularly the question concerning the number of trap states within the particle or on the surface is very important to elucidate.

Furthermore it could be shown that each linker has its own linker resistances. But the determined resistance, having a value up to 30 Ω is very low in comparison to the total resistance, however an absolute determination cannot be undertaken using EIS measurements in such complex systems. In consideration of the principle of Occam's razor it could be shown that a complex model must not necessarily be invoked to fit the data. If the elements are completely or partially fixed in their values then also basic questions of experimental observations must be examined as for instance the existence of the FTO/electrolyte contact after the ZnO deposition.

# 6

# $TiO_2$ based Injection Solar Cell [1]

## 6.1 Introduction

In chapters 3 and 4 the unmistakable instability of the ZnO film in highly acidic milieu was commented upon. For this reason some questions concerning the reproducibility of the results received in the previous chapters in the case of the MOs and some missing electrochemical and opto-electrochemical datasets in the case of ISC including OA and TAA as ligand still remain to be answered. The results for the more stable metal oxide titanium dioxide ($TiO_2$) are reported. Often the lower efficiency of the ZnO ISC may be found to be due to its chemical instability in acidic environments.[112] Gerischer et.al.[223] explained the high instability compared to $TiO_2$ as being due to an anodic decomposition potential of the ZnO crystal which is located at more negative energies than the oxidation of water. This is not so in the case of $TiO_2$ for which the stability does not result from thermodynamic but rather kinetic reasons.

However, the wide band gap semiconductor $TiO_2$ has arguably become the most important substrate in solar cell research. A multitude of studies concerning its synthesis, especially that of highly transparent $TiO_2$, can be found in the literature.[224–230] Almost the same number of specialist literature publications concerning $TiO_2$ in connection with solar cell applications have been

---

[1] The results of this section were made within the framework of the scheduled research internship done by M. Sc. Clément Sieutat, a student of the european school of chemistry, polymers and materials science (ECPM) in Strasbourg (France), under mentoring from the author in the work group of Prof. A. Eychmüller at the TU Dresden.

published.[3,12,104,231–234] Vogel et.al.[2] first reported that charge separation in nanoparticles may be brought about by the contacting of nanoparticles with a wide band gap semiconductor material. The band positions between TiO$_2$ and the PbS NCs should be matched as is the case for the ZnO due to the similar band position and band gap sizes of TiO$_2$ compared to ZnO. In this way the attractive electronic and structural properties[7,8,10] can be exploited in the same or an even better way as for the ZnO composite. The use of PbS may be more efficient in a TiO$_2$ based ISC because of the increased stability and the possibility for such solar cell devices to exceed the Shockley-Queisser limit. Formerly Schockley and Queisser have calculated the theoretical maximum efficiency for p-n junction solar cells to be approx. 30% for an energy gap of 1.1 eV.[235] The limit originates because of the recombination processes, the spectral losses caused by the possibility of absorbing light in a material specific range and other energy losses which occur through the electron motion through the circuit. There are some possibilities by which this limit can be circumvented, including tandem solar cells and multiexciton assemblies[236], which can be afforded by PbS NPs.

A plurality of approaches using different assemblies, deposition techniques, nanoparticle shapes, nanoparticle sizes, composites and linkages of TiO$_2$-PbS assemblies may be found in the literature.[237–248] Both Dibbell et.al.[132] and Yank et.al.[249] have addressed the issue of the influence of the linker. Dibbell et.al. have examined in some detail the electron transfer dependency of the linker length using optical methods. The electron transfer rate constants and lifetimes observed by time-resolved emission spectroscopy and transient absorption spectroscopy in a TiO$_2$/linker/CdS suspension have been determined. Yang et.al. have studied the opto-electrochemical properties of OTE/TiO$_2$/-PbS/linker electrode systems. In their study, after the PbS synthesis was carried out directly on the TiO$_2$ substrate, the 1-thiol-linkers were coated onto the OTE/TiO$_2$/PbS substrate. The OTE/TiO$_2$/PbS substrate shows a photocurrent of 542 mA/cm$^2$ at an illumination wavelength of 400 nm. Three different thiols with C chain lengths of C$_3$, C$_6$ and C$_{12}$ have been used. The IPCE analysis, the open circuit photovoltage dependence of the incident light intensity and the stability of the photocurrent over the time were shown for the OTE/TiO$_2$/PbS/linker electrodes. These electrodes were also not stable over time and the sulfide modification as well as the particle growth onto the substrate was not fully developed.

The present work uses six different linkers which vary in their alkyl chain length or the choice of either acid and/or thiol groups. Each linker molecule was first attached to the $TiO_2$ and subsequently the PbS nanoparticles were deposited from solutions of THF and the complete assembly characterized by electrochemical and opto-electrochemical methods. The techniques of cyclic voltammetry and photocurrent spectroscopy were employed similarly to the work presented in chapter 3 and 4 in which ZnO was used as the wide band gap semiconductor. These methods may be used to provide information concerning the different interactions between the components, the exciton separation processes and device (material) instabilities. In addition characterisation of the substrate was carried out using UV/Vis/NIR-, X-Ray diffraction (XRD) spectroscopy and transmission electron microscopy (TEM). In the present work the linker dependence of the $TiO_2$ sensitized with PbS nanocrystals will be discussed and compared with the studies from the assembly using ZnO as the wide band gap semiconductor.

## 6.2 The ITO/$TiO_2$ Film

A colorless $TiO_2$ suspension was obtained from the $TiO_2$ synthesis. The $TiO_2$ was determined to be the anatase modification with an average diameter $d$ of 5.0 ± 0.5 nm as calculated from the XRD diffractograms (Figure 6.1) using the Debye-Scherrer relation[250]:

$$d = \frac{K \cdot \lambda}{\beta \cdot cos(\theta)} \tag{6.1}$$

where the shape factor $K$ assumes a value of 0.9 for spherical particles, $\lambda$ is the X-ray wavelength, $\beta$ the full width at half maximum of the reflexes and $\theta$ the diffraction angle. In addition the results from the size distribution histograms (Figure 6.2(b)) obtained using TEM images (Figure 6.2(a)) of the $TiO_2$ particles gives an average diameter of 5.1 ± 1.4 nm, both methods showing very good agreement and suggesting that the nanoparticles are primarily crystalline with little amorphous material being present. Suspensions of the $TiO_2$ nanoparticles are transparent and display a high stability over months.

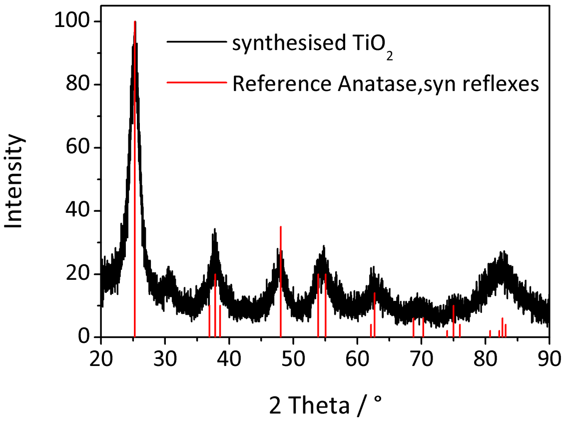

Figure 6.1: XRD-diffractogram of the synthesized $TiO_2$ measured on a silicon wafer

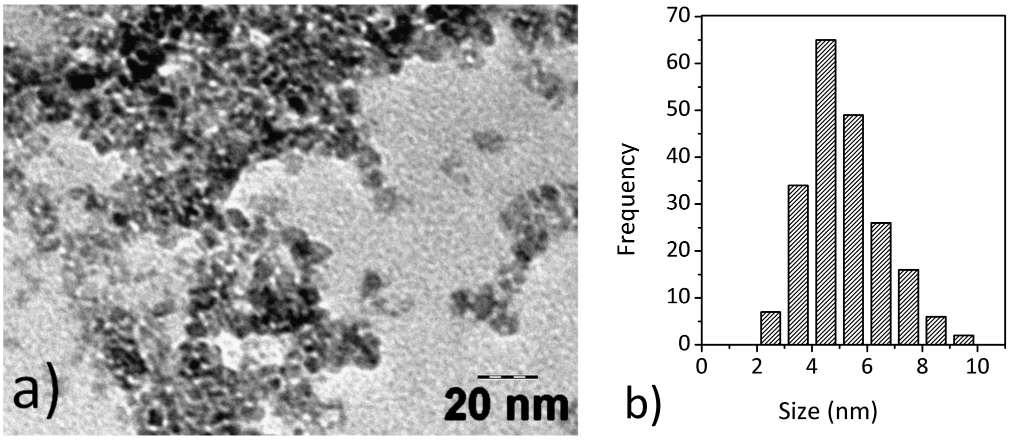

Figure 6.2: a) TEM image of the $TiO_2$ particles b) Size distribution of the $TiO_2$ determined through the TEM images.

Films made from the $TiO_2$ suspension show near complete transparency with almost no absorbance being measured across the NIR range and across the complete Vis range i.e. from 1500 nm down to 340 nm (Figure 6.3(a)). The optical properties of the films in the visual range remain intact even after the sintering process with only a slight red shift in the UV being observed. In accordance with our previous work the thickness of the films could be well controlled which was confirmed from the UV/Vis studies.

## 6.3 The Linker and PbS Attachment on the ITO/$TiO_2$ Substrate

The absorbance of the layers after each deposition step (i.e. ITO, $TiO_2$, linker, PbS) was also measured using UV/Vis spectroscopy (see Figure 6.3(b)) and one example, representative of all the samples measured, is presented here as variances within the sample sets were essentially inconsequential.

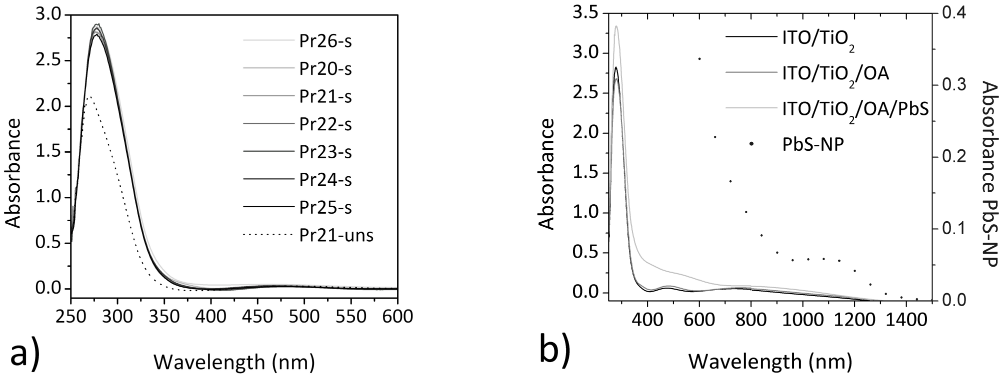

Figure 6.3: a) Absorbance spectra of the blank ITO/$TiO_2$ assemblies. Sintered Pr20-s till Pr26-s (line); unsintered Pr21-uns (points) b) Absorbance spectra after each deposition step (line) compared to the PbS NP solution spectrum (dotted line)

Slight differences in the spectra between the ITO/$TiO_2$ and the ITO/$TiO_2$/OA substrates can however be observed. Each $TiO_2$-linker assembly has almost the same transparency when compared to that of the blank $TiO_2$ film. At later times a strong influence on the photoactivity of the ITO/$TiO_2$/linker/PbS as well as the ITO/$TiO_2$/linker system can be seen. The successful deposition of a PbS nanoparticle layer on the TiO$_2$ substrate can be seen both by eye, due to the brown discoloration of the substrates after immersion in the PbS solution, and in the UV/Vis/NIR absorbance profile (Figure 6.3(b)). The transparency of the TiO$_2$ and the TiO$_2$/linker samples looks quite similar and the PbS attachment can be registered by the brown coloration (Figure 6.4)

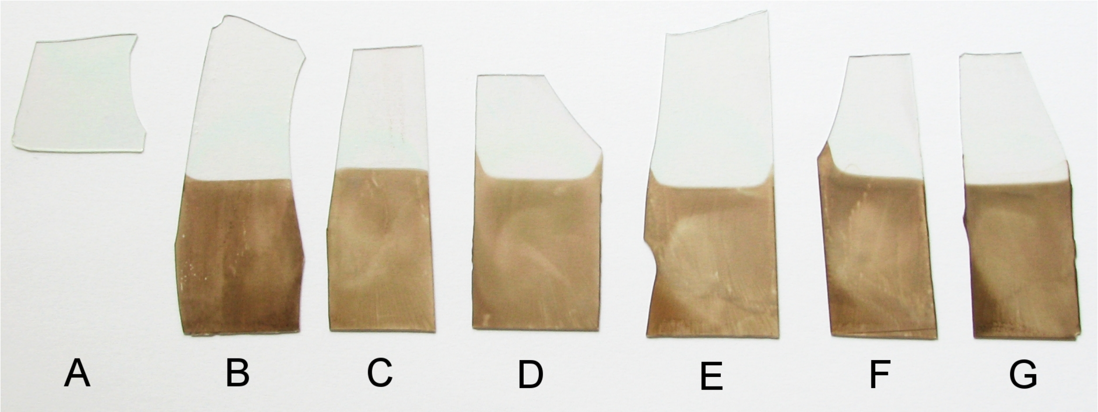

Figure 6.4: Sample A is the blank TiO$_2$ film. The top of B-G samples are loaded with different linkers and the bottom of the B-G samples is the complete TiO$_2$/linker/PbS substrates. The linker molecules are B: OA; C: MA; D: MPA; E: HDT; F: TAA; G:TGA

The attachment of the OA linker to the TiO$_2$ surface was again successful. The orientation of the OA on the surface has been well reported in the literature. The deprotonated carboxylic group is attached to the surface of the TiO$_2$ whereas the second carboxylic group lies pendant out into the electrolyte which may be protonated or deprotonated.[140,142] The carboxylic groups of the MA molecule which is not attached on the MO surface can build up a network of H-bonds with the carboxylic groups of the neighbouring MAs. In addition another bonding mode of MA with one carboxyl attachment and one monodentate attachment on the TiO$_2$ surface is possible.[251] As was mentioned in section 3.3.1 a similar conformation for the OA and MA attachment to CrO[139] and kaloinite[143] surfaces can be found. For the thiol acid and HDT the attachment has been assumed to be via the ZnO linkage.

# 6.4 The Cyclic Voltammetry Study on the Substrates

## 6.4.1 The Linker Sensitized ITO/$TiO_2$ Film

In Figure 6.5 the cyclic voltammogram of several ITO/$TiO_2$/linker assemblies under dark conditions (Figure 6.5(a)) and under illumination provided by a 470 nm LED (Figure 6.5(b)) are presented. The blank ITO/$TiO_2$ yields a distinctive profile in the negative potential range. Similar voltammetric profiles were observed and calculated in the previous works of Fabregat-Santiago et.al.[202] and Guijarro et.al.[14] In accordance with these the cathodic current at more negative potentials than -0.5 V can be attributed to a filling process by which the electrons fill an exponential distribution of trap states under the conduction band (CB) edge of the $TiO_2$. This additional charge is subsequently required to be neutralized by ionic species present in the electrolyte.

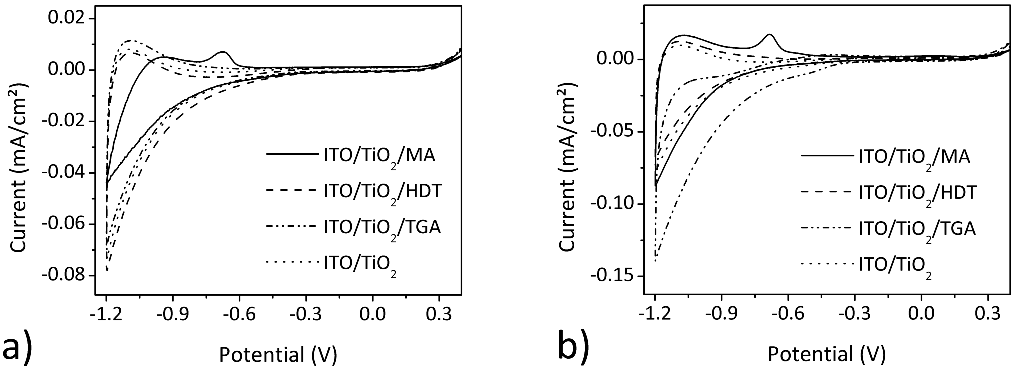

Figure 6.5: a) Second CV cycle of ITO/$TiO_2$/linker assemblies (line, dashed line, dash-dot-dot line) in the dark compared to the ITO/$TiO_2$ reference (dotted line) b) Second CV cycle of ITO/$TiO_2$/linker assemblies (line, dashed line, dash-dot-dot line) under illumination with light of 470 nm with the ITO/$TiO_2$ sample as reference (dotted line)

The peak position at -0.6 V, assumed in the works of Gujarro and Garza to be trap and surface state filling caused by the adsorption of linker molecules is recorded in the present study just for the ITO/$TiO_2$/OA system.[14,252] This sample displayed a weak peak at -0.54 V. The strong polarity and its structure are possible reasons for addressing these $TiO_2$ states with electrons during linking to the surface. In addition, OA has a higher dipole moment compared to the thiol acids. MA has a dipole moment of 2.64 D which is close to that of OA whose dipole moment is 3 D.[161] This means the electron distribution is more located at the functional groups in the case of OA which increases the probability to inject these electrons into the $TiO_2$ states. The different structure of the OA at the $TiO_2$ surface could also provide the reason for the sole peak position at approx. -0.6 V of the OA absorption. The complete OA molecule is a constructed $\pi$-system in which the electrons can be smoothly transferred. In both MA attachment modes which have been mentioned in sections 3.3.1 and 6.3 the continuous structure is disconnected due to the additional methyl group. Accordingly the OA can be stabilized by the system when the electron of the OA enters the trap and surface states of the $TiO_2$ which makes the probability for electron transfer higher.

Furthermore a shift in the $TiO_2$ band edge occurs when a linker molecule absorbs at the surface. This has been explained by the fact that a ligand can increase the trap depth through the strength of its polarity (see section 3.3.2). In most instances the $TiO_2$ substrates which were loaded with linker molecules give a similar response to that of the blank $TiO_2$ surface and suggest that the same processes are at work. In contrast to the other CVs the ITO/$TiO_2$/MA substrate possesses an oxidation peak at -0.68V in its CV profile (Figure 6.5 line). Furthermore the $TiO_2$/TGA system has a different onset under blue (470 nm) illumination. The trap state filling is shifted to more negative potentials and further redox processes in the range of -0.3 to -0.6 V can occur.

### 6.4.2 The ITO/$TiO_2$/Linker/PbS Substrate

The CVs in Figure 6.6 (line and dashed line) show the response of the complete ITO/$TiO_2$/linker/PbS substrate representative for all other systems. Two distinct oxidation peaks can be seen; the first located at approx. -0.89 V with the second lying in the potential range -0.64 V to -0.61 V in the dark and -0.61 V to -0.58 V under illumination. Another peak, this time associated with a reduction, can be found in the range -1.09 V to -1.05 V in the dark and -1.11 V to -1.09 V under blue illumination. The same processes were also determined to occur at the ZnO surface and are likely due to the same reaction, the peaks decreasing with every voltammetric sweep (see section 4.3.1).

The CV in case of the ITO/TiO$_2$/TGA/PbS substrate (Figure 6.6 dash-dot-dot line) gives an anomalous response. Two distinct oxidation peaks at -0.48 V in the dark and -0.4 V under illumination are observed and the response is present over a broader potential range. Under illumination in Figure 7(b) a crossover at -0.79 V and -0.97 V is also seen. The TGA-systems of ITO/TiO$_2$/TGA and ITO/TiO$_2$/TGA/PbS require further analysis in order to determine which additional reactions and/or electron transfers are occurring.

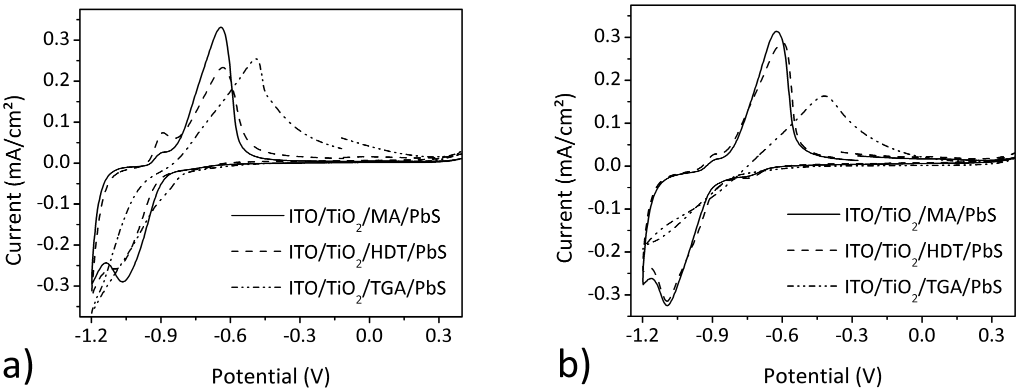

Figure 6.6: a) Selected second CV cycle of an ITO/TiO$_2$/linker/PbS substrate in the dark. b) Selected second CV cycle of an ITO/TiO$_2$/linker/PbS substrate under illumination with light of 470 nm.

## 6.5 The Opto-Electrochemistry on the Substrates

The photo response of each linker and linker-PbS substrate is considered in order to confirm the aforementioned phenomenon. The photocurrent response of the ITO/TiO$_2$/MA and ITO/TiO$_2$/OA substrate is in both cases negative. The ITO/TiO$_2$/MA substrate shows a current of -1.7E-7 mA/cm$^2$ and the ITO/TiO$_2$/OA of -3.9E-6 mA/cm$^2$. The negative current values reflect an electron transfer which goes from the TiO$_2$ to the electrolyte. It should be mentioned that the current observed from the ITO/TiO$_2$ and ITO/TiO$_2$/linker device comes from electrons generated in the TiO$_2$ layer. The negative direction is possible if the energy levels of the hole scavenger species are lower and quite close in energy to the TiO$_2$ CB. In the case of strong negative polar linker molecules such as OA and MA as mentioned in section 3.3.2 a shift in the trap depth of the TiO$_2$

to higher energy occurs and they move closer to the CB of $TiO_2$. Therefore the level of the highest filled states moves to higher energies and lies over and closer to that of the hole scavenger species and therefore can inject electrons in the opposite direction. If the PbS nanoparticles are connected via these linkers the photo transients are positive and have a value of approx. 0.001 mA/cm$^2$ (Figure 6.7) Accordingly it can be expected that the additional PbS states, especially that of the CB of the PbS, lie at higher energies than those of the $TiO_2$ CB and do not afford an electron transfer to the PbS as well as to the electrolyte. The increase in the photo response at the ITO/$TiO_2$/linker/PbS substrate shows the generation of electrons in the PbS NPs simultaneously with the electron generation in the $TiO_2$ layer. By comparison with the other linker-only systems the complete system of ITO/$TiO_2$/linker/PbS shows a similar photo response in the range between 0.0025 to 0.0007 mA/cm$^2$. The photo transient profiles are shown in Figure 6.8. The ITO/$TiO_2$/linker assemblies of TAA, TGA, MPA and HDT are positive and have a response between 1.6E-5 and 5.3E-5 mA/cm$^2$. The $TiO_2$ system shows a slower increase in the photocurrent profiles before reaching in a steady state (plateau region).

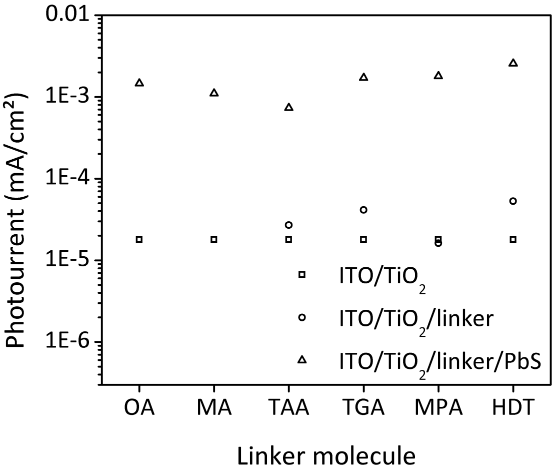

Figure 6.7: The role of the ZnO, linker and PbS in comparison to the complete $TiO_2$/linker/PbS system. The ITO/$TiO_2$/MA and ITO/$TiO_2$/OA substrate shows a negative photo response and cannot be shown using the logarithmic scale.

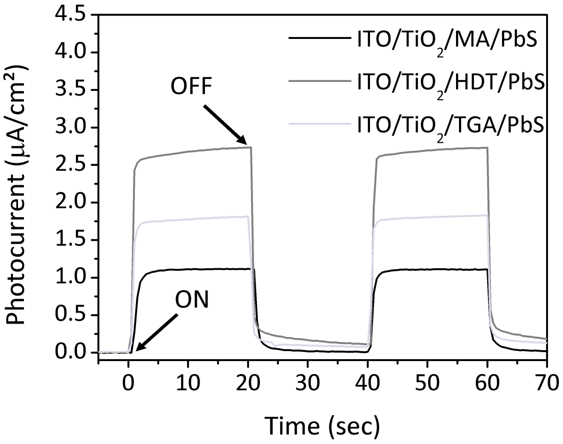

Figure 6.8: The photo transient profile of three representative ITO/TiO$_2$/linker/PbS substrates.

## 6.6 Comparison Between ZnO and TiO$_2$ Based ISCs

In chapter 3 and 4 it was demonstrated that due to the OA polarity the OA was able to affect the surface of the ZnO gel. This resulted in the loss of adhesion between the ITO and the ZnO particles. During the attachment of the OA to the TiO$_2$ surface no instability or degradation was observed to occur. From these studies we are able to conclude that TiO$_2$ is more stable with respect to polar media than ZnO but is affected in the same way with respect to the electron transfer from the linker into MO surface states. Also in earlier studies it could be shown that TiO$_2$ has a higher stability in the presence of OA compared to that of ZnO.[253] Hence (opto-)electrochemical techniques could be applied to the unaffected TiO$_2$ ISC substrate to examine the linker influence.

The instability with respect to the TAA molecule could also not be observed when the TiO$_2$ was in contact with the TAA molecule. The CV of the ITO/TiO$_2$/TAA/PbS has particularly confirmed the presence of the PbS by the typical PbS oxidation signals at approx. -0.6 V which are not seen for the ITO/ZnO/TAA/PbS CV profile (Figure 6.9). The presence of TiO$_2$ in contact with TAA could also be observed in the UV/Vis/NIR spectra. Whereas the absorbance of the TiO$_2$ NPs in contact with TAA are still recordable (Figure 6.10(a)) the absorbance of the ZnO in contact with the TAA dramatically changed (Figure 6.10(b)). Also after the PbS deposition the TiO$_2$ signal can be

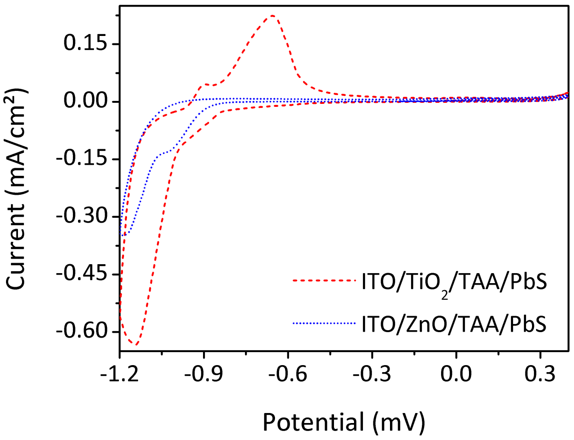

Figure 6.9: For the first cycles of the cyclic voltammogram the typical PbS oxidation peak at approx. -0.6 V of the ITO/$TiO_2$/TAA/PbS substrate compared to the ITO/ZnO/TAA/PbS substrate (red pointed line) no oxidation peaks can be seen. The reduction peaks of the ITO/ZnO/TAA/PbS substrate (blue dashed line) may be due to a reaction with the species present at the coated glass.

clearly recorded under the overlaid PbS absorption. The same absorption signal could also be determined for the OA linker on the $TiO_2$ surface. For the ITO/$TiO_2$/OA/PbS preparation steps the $TiO_2$ signal is quite strong (Figure 6.3(b) section 6.3) as compared to the ITO/ZnO/OA in Figure 3.12(a) in section 3.3.2 (or more specifically in Figure 3.15(a)).

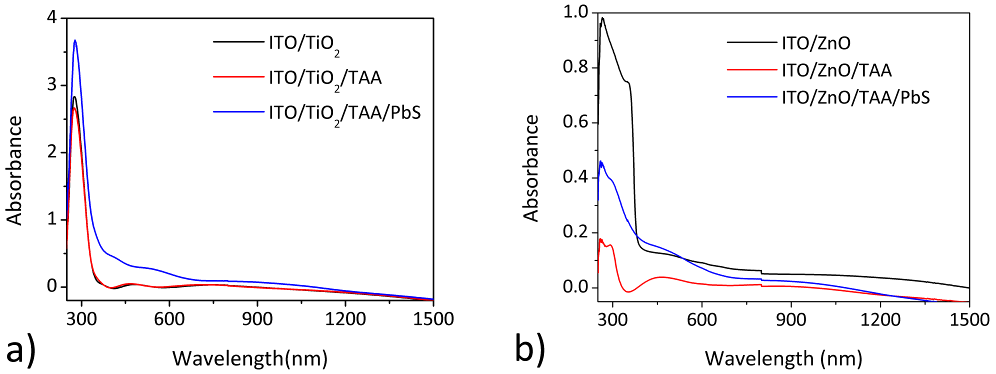

Figure 6.10: Absorption spectra of the ITO/$TiO_2$ (a) and ITO/ZnO (b) substrate during the deposistion steps of linker and PbS.

The shape of the $TiO_2$ photocurrent response profile is quite different from that of the ZnO substrate. In the case of the ZnO system a fast increase in the photocurrent is followed by a decrease which can occur before the photocurrent reaches a plateau (Figure 4.10). The $TiO_2$ system shows a slower increase in the photocurrent profile which directly reaches a steady state response (plateau region) (Figure 6.7). The shape of the photocurrent transient profile gives the first clues concerning the possible electron processes. Schwarzburg et.al. report a study on trap filling in polycrystalline $TiO_2$ and show a correlation between different kinds of processes of the photocurrent response.[254] For that reason different kinds of $e^-$ transfer processes can be expected. In addition a different electronic structure must be considered. The existence of trap states as well as their position is expected to be different in both metal oxides.

However, both metal oxide systems have a limit in their photocurrent magnitudes (see Figure 6.7 and 4.9). A slow electron injection process from the $Na_2SO_3$ electrolyte to the PbS was found to exist in earlier studies and is the most likely reason for the observed photocurrent limitation observed in these systems. Nevertheless the ITO/ZnO/linker/PbS substrate shows one decade higher photocurrent magnitude using the TGA, MPA and HDT molecules. The ITO/ZnO/MA/PbS shows the same magnitudes of photocurrent as the photocurrent of the other ITO/$TiO_2$/linker/PbS substrates. In an earlier discussion it was mentioned that ZnO has a higher charge mobility compared to that of $TiO_2$ but this must be applied with be caution. The materials are quite different and guarantee of having the same amount of the metal oxide on the ITO or surface porosity which can in turn affect the amount of PbS on the surface has not been quantified in this study. A number of other details with respect to the linker dependence within each ISC substrate can be found. It has also to be mentioned that a different amount of PbS being present on the linker sensitized substrate of each metal oxide is excluded. In the electrochemical studies in section 4.2.2 a high linker coverage on the ZnO surface was shown to exist. As mentioned in section 5.6 the linker molecules are smaller than the PbS NP which has the consequence that not every linker is connected to a NP or one NP may have more than one linker attached to its surface. At the end the amount of NPs present on the surface will be defined by the diameter of the nanoparticle itself as well as the exclusion volume of the PbS NP but not by the kind of linker used, hence a comparison between different linker systems is justified. It was mentioned above that the ISC substrate shows the highest photocurrent with the PbS connection to the ZnO surface being via TGA, MPA and HDT molecules. For these linkers the highest photocurrent was also observed to occur for the ITO/$TiO_2$/linker/PbS substrate whereas the $TiO_2$ and PbS NCs ISC gives the highest photocurrent with HDT as ligand. The MA has a smaller photocurrent compared to the OA, MPA, TGA and HDT linkers. A telling comparison is that of the MA with TGA as both have with the same C-chain length and same functional group attachment on the metal oxide surface. From this point of view the different functional group for the PbS NP linkage is the decisive factor for the photocurrent loss. Also the dipole moments of 2.28 D for TGA and 2.64 D for MA show a stronger intramolecular interaction in the MA which can hinder the $e^-$ transfer. There is also a reason to believe that the attachment of the thiol group to the PbS surface are more efficient with respect to the $e^-$ transfer and the linkage. This trend can be seen in both metal oxide systems (see Figure 6.7 and 4.9).

A different photocurrent for the MA/PbS systems compared to the OA linkage highlights the advantages of a constructed $\pi$-system in the case of the OA linker. The interruption of the $\pi$-system in the MA molecule, because of the additional $CH_2$ between the carboxylic groups, provides the $e^-$ with a higher barrier which must be to overcome. This barrier can be seen also in the lower photocurrents of the MA compared to the OA system (Figure 6.7). The OA-MA comparison can be seen just for the $TiO_2$ which provides one more piece of information which was unable to be addressed after the studies of the ITO/ZnO/linker/PbS substrate. Further additional results could be used to answer questions concerning the TAA attachment. In the order TAA, TGA and MPA the TAA has attained the least photocurrent. The TGA and the MPA molecules have shown a similar photo response so that only the shortest C-chain length, that of the TAA is disadvantageous for the $e^-$ transfer between the PbS and the $TiO_2$ surface.

If just the influence of the linker on the metal oxide surface without the PbS NP were to be considered then the MPA shows the lowest influence on the electronic structure of the metal oxide. The ZnO as well as the $TiO_2$ surfaces show the lowest photocurrent increases through the attachment of the MPA to the surface. The highest photocurrent increase after the linker attachment was determined for the HDT molecule at both metal oxide substrates. That is surprising because of the lower polarity of the thiol group compared to the carboxylic groups where a less directed $e^-$ transfer is expected. In addition one has to assume a slower $e^-$ transfer for that reason alone because of the longer C-chain length and which has to take place through a chain to chain coupling between the linker molecules on a highly porous metal oxide surface.[160]

## 6.7 Conclusion

In summary it could be shown that $TiO_2$ based ISCs with six different linkers could be prepared. The linker dependence was examined and presented through differences in their cyclic voltammetric profile and photo transient measurements. The stability of $TiO_2$ with respect to TAA has also been demonstrated. All chosen linkers did not chemically affect the $TiO_2$. The linkers do however affect the electronic properties of the $TiO_2$ by alteration of the trap depth and band edges. The aim of the study designed to answer the open question concerning the linker dependence which results from the ZnO based ISC have been achieved. Consistently reproducible results between the ZnO based and $TiO_2$ based ISC substrate could be found. The typical electrochemical PbS related signals in the cyclic voltammograms have been also recorded for all ITO/$TiO_2$/linker/PbS substrates. The photocurrent response of each ITO/$TiO_2$/linker/PbS substrate and intermediate state of the substrates as well as the comparison with the ZnO based substrates made possible the first clear observations concerning the linker influences on the electron transfer between the PbS and the metal oxide surface for all six linkers. Therefore the supporting effects of the electron transfer through a constructed $\pi$-system within the linker, the thiol group as connector on the PbS attachment side and the existence of the C-chain whereas a detrimental effect as expected for a longer linker length could be shown.

# 7

# ZnO/Eosin Y Injection Solar Cell [2]

## 7.1 Introduction

The material, homogeneity and the technical expertise for the preparation of thin films especially on large areas are the most common challenges for the economic development of solar cells. In earlier chapters the metal oxides have been synthesised by sol-gel methods and spin coated onto TCO coated glass. This procedure is quite time consuming for large areas, specific thicknesses and larger numbers of substrates.

Electrodeposition provides a simple, low temperature technique for the preparation of homogenous, large area films. In the beginning and middle of the last century the first studies of electrodeposition with alloys and metals were published.[255–257] In the meantime the fabrication techniques for electrodepositing films using semiconductive materials were well studied.[258] Electrochemically deposited films composed of ZnO are of particular relevance for the present study. In the literature an abundance of shapes and techniques is reported[259–261] but the most interesting feature of such deposited layers are the higher efficiencies of the electron transport through such films. Compared with the particular ZnO which was prepared according to the sol-gel technique by Spanhel et.al.[85] the electrodeposited ZnO has a higher crystallinity and more preferential orientation. This is

---

[2] The results of this section were made within the framework of the bachelor thesis written by B. Sc. Elisabeth Schreyer under mentoring of the author in the work group of Prof. A. Eychmüller at the TU Dresden .

caused by a lower amount of grain boundaries and less trap processes which yield a higher effective diffusion of the electron through the layer.[47,48]

In this study a ZnO film which is electrodeposited with the dye, eosin Y will be used. This kind of ZnO film is well characterized in the literature.[47,262–264] The prepared thin film is highly porous and exhibits the aforementioned electron transport properties. These qualities were taken advantage of in the preparation of the PbS nanoparticle (NP) sensitized injection solar cell. The structured ZnO substrate which is deposited onto FTO coated glass acts as the wide band gap metal oxide. The PbS nanoparticles used act as the light absorber and have an absorption maximum at 1056 nm and therefore a band gap energy of 1.17 eV. The PbS NPs have been linked to the ZnO surface through the linker molecule MPA. Although the highly porous structure provides a high surface area the assembly may nevertheless be considered as a layer-by-layer structure (Figure 7.1).

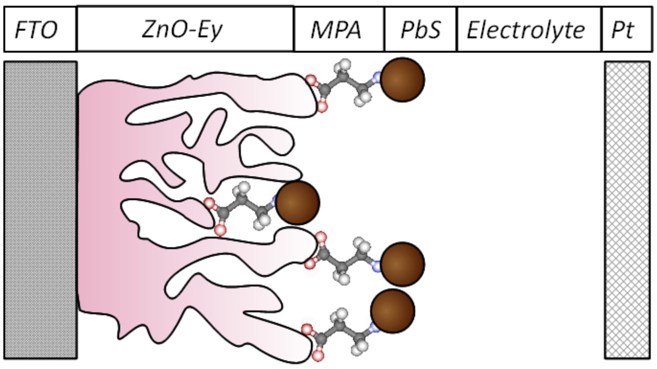

Figure 7.1: The substrate made up of a layer-by-layer structure. On the transparent conducting FTO glass is the ZnO film structured by using the dye eosin Y. The eosin Y acts as a placeholder during the electrodeposition and will be desorbed at the end. The ZnO-Ey film is sensitized by PbS nanoparticles which are linked to the ZnO-Ey surface through the MPA layer. The ZnO-Ey has a highly porous structure and the PbS and MPA also enter the pores.

For that reason the characterization was carried out in the following preparation step order i.e. every additional layer: FTO, FTO/ZnO-Ey, FTO/ZnO-Ey/MPA and FTO/ZnO-Ey/MPA/PbS was measured.

In the present study the solar cell assembly is characterized using electrochemical and opto-electrochemical methods. Cyclic voltammetry (CV), linear sweep voltammetry (LSV), photocurrent transients (PT) and incident photon-to-electron conversion (IPCE) spectroscopy will be used as well as scanning electron microscopy (SEM) to provide information concerning the influence of each layer in the complete injection solar cell. Furthermore the impact of the ZnO-Ey system will be discussed and compared to the systems from earlier studies which were fabricated using the ZnO gel. The studies were done under different applied potentials and under four different irradiation wavelengths.

## 7.2 The FTO/ZnO-Ey Film

In the framework of the collaboration the ZnO-Ey film are made in the working group of Professor M. Wark (University of Bochum). The layer has largely been characterized using a variety of methods and published elsewhere.[47,262–264]

The ZnO-Ey layer has a preferential orientation and an amount of less than 2% eosin Y is present after the desorption step compared to the eosin Y amount before the desorption step. To what extent or whether the eosin Y remainder and material orientation affects the injection solar cell will be discussed in the following sections.

## 7.3 The PbS Attachment to the FTO/ZnO-Ey Film

In chapter 3 it was noted that a direct contact between ZnO and PbS is neither efficient nor stable enough which necessitated the use of special linker molecules. It was experienced that the attachment of the PbS nanoparticles is very low if a linker has not been used. A similar experiment could be used to show whether the ZnO structure and embedded eosin Y molecules changes the ZnO functionalization and the PbS attachment. In Figure 7.2 the photograph of the pure FTO/ZnO-Ey substrate (Figure 7.2(C)) and the PbS attachment on the FTO/ZnO-Ey substrate by the MPA molecule used (Figure 7.2(A)) and the PbS attachment without any use of linking molecules (Figure 7.2(B)) are presented.

By eye it can be seen that the FTO/ZnO-Ey substrate shows a slightly rose-pink color because of the eosin Y remainder in the naturally colorless ZnO. It is clear to see that the use of the linker molecule strongly influenced the color depth of the sample. To clarify whether the weak PbS color on substrate B in Figure 7.2 is caused by interaction with the FTO/ZnO-Ey film or caused by the

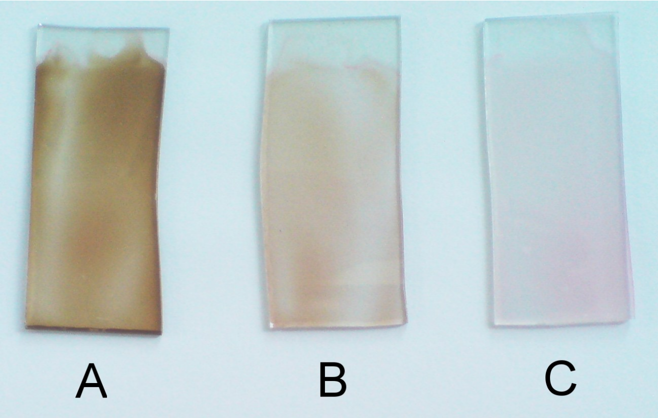

Figure 7.2: A photograph of FTO/ZnO-Ey substrate (C) in comparison to the substrate which (B) is deposited with pure PbS nanoparticle (FTO/ZnO-Ey/PbS) and (A) is first deposited with MPA and than with PbS NPs (FTO/ZnO-Ey/MPA/PbS)

smaller amount of PbS particles a number of LSV measurements were undertaken on the substrates. The results, seen in Figure 7.3, show the highest photoactivity at the FTO/ZnO-Ey/MPA/PbS substrate. In contrast the FTO/ZnO-Ey/PbS substrate shows only a weak photocurrent signal. As reference the pure FTO/ZnO-Ey film can be seen to have no photocurrent in the scale divisions

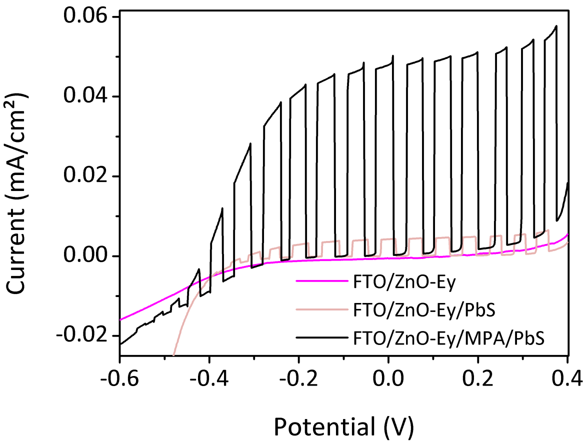

Figure 7.3: The LSV profile of the FTO/ZnO-Ey film (pink line), the FTO/ZnO-Ey/PbS substrate (light rose line) and the FTO/ZnO-Ey/MPA/PbS substrate (pink line). The FTO/ZnO-Ey/PbS substrate shows a low photocurrent activity over the entire potential range so that a small amount of PbS particles result in the light color of the substrate as seen by eye. The LED with the wavelength maximum at 630 nm was used for the excitation.

shown in the Figure 7.3. However, the stronger coloration of the FTO/ZnO-Ey/MPA/PbS substrate and the high photocurrent density in the potential range from -0.6 to 0.4 V effectively confirms the higher PbS nanoparticle concentration on the ZnO surface through the use of the MPA linker. For this reason MPA was used as the linker for such kinds of metal oxide substrates.

From the SEM images of FTO/ZnO-Ey a highly porous structure is recorded (Figure 7.4(a)). The porous surface is frequently crossed by larger gaps which result from the growth of ZnO crystals (Figure 7.4(b)). It is assumed that the small pores as well as the larger gaps extend partially down to the FTO surface or close to it. After the attachment of the MPA molecule and PbS nanoparticles a complete coverage of the ZnO-Ey surface can be seen in the SEM image (Figure 7.4(c)). Upon closer examination the pores and the gaps are also observed to

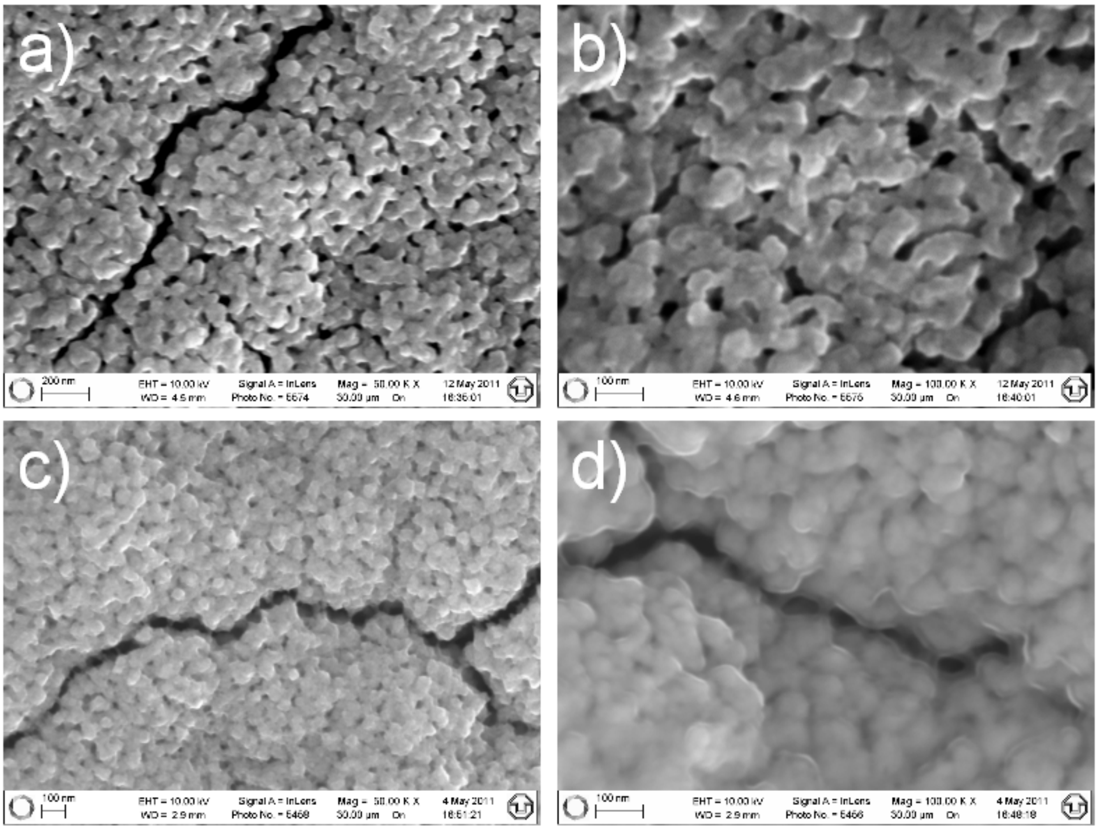

Figure 7.4: The SEM images of the pure FTO/ZnO-Ey film (a) and (b). After the MPA and PbS deposition the ZnO-Ey shows a complete covering on the surface (c) as well as also in the pores (d).

be filled with PbS NPs and therefore also with MPA molecules (Figure 7.4(d)). Hence the highly porous skeleton of the ZnO-Ey surface still persists.

The direct determination for the existence of PbS NPs at the surface using UV/Vis/NIR spectroscopy was not possible. The FTO coated glass shows interferences over the complete UV/Vis/NIR range which did not disappear after the deposition of the ZnO layer onto the FTO. These signals cannot be differentiated from the interferences hence an unambiguous interpretation of the signal is not possible (Figure 7.5).

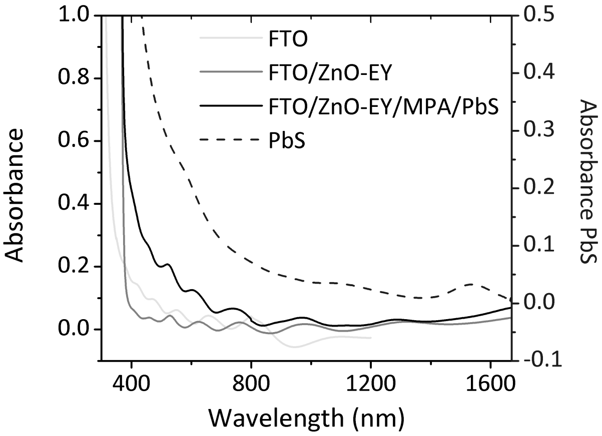

Figure 7.5: The UV/Vis spectra after the substrate of each deposition step (lines) in comparison to a PbS nanoparticle solution (dashed blue line). The FTO shows interferences which are still seen after the attachment of the ZnO-Ey film and also after the MPA and PbS deposition.

## 7.4 The Cyclic Voltammetry Study on the Substrates

As previously demonstrated the presence of PbS can be evidenced by using electrochemical techniques. In earlier chapters it could be seen that specific signals in the cyclic voltammogram can be associated with electrochemical reactions of the PbS nanoparticles. These kinds of signals could also be found when the FTO/ZnO-Ey/MPA/PbS substrate has been measured using CV. In Figure 7.6(b) an oxidation peak at approx. -0.6 V can be seen and also a reduction peak at approx. -1.1 V can be observed. Analogous to equations 4.3 and 4.6 in section

4.2.2 the PbS redox reaction can be discerned as can the oxidation of $S^{2-}$ to $S^0$ and the reduction of $Pb^{2+}$ to $Pb^0$.

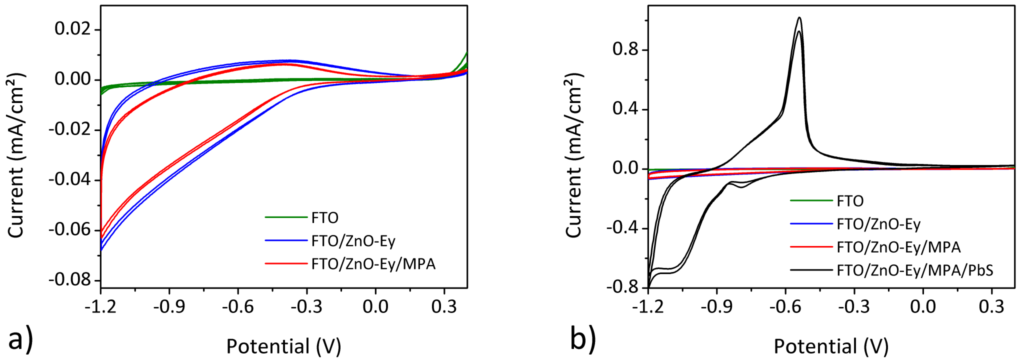

Figure 7.6: The cyclic voltammogram of the 2nd and 3rd cycle of the FTO/ZnO-Ey, FTO/ZnO-Ey/MPA and FTO/ZnO-Ey/MPA/PbS substrate. The CV was recorded under non-illuminated conditions.

The pure FTO coated glass gives almost no current response under non-illumination conditions (Figure 7.6(a)) nor under UV illumination (Figure 7.7(a)). In the $Na_2SO_3$ electrolyte the FTO/ZnO-Ey film shows an analogous behavior to the ZnO gel (Figure 4.4. in section 4.2.2) a very weak current signal in the I-V curve (Figure 7.6(a)). But under UV irradiation the cyclic voltammetric profile of the FTO/ZnO-Ey film yields an additional resistance of the ZnO-Ey surface after the MPA attachment. This is seen in the increasing slope in the potential range between -0.3 up to 0.1 and in the greater hysteresis (Figure 7.7(a)).

The FTO/ZnO-Ey/MPA shows a gentler slope i.e. higher resistance compared to the FTO/ZnO-Ey film under UV irradiation. This reversible effect seems to begin as soon as the UV region is reached. In earlier IPCE studies a lower photocurrent in the case of the MPA covered system (see Figure 5.2. in section 5.3), which is normally higher for the MPA attachment compared to the pure ZnO substrate, has been recorded. Therefore the effect on the photocurrent comes from the linker. The only possible process which can affect the charge transfer is the hole regeneration in the ZnO layer. Because of the loss of the direct ZnO/electrolyte contact the electron transfer onto the ZnO surface must occur through the linker. Hence the regeneration of the hole in the ZnO layer

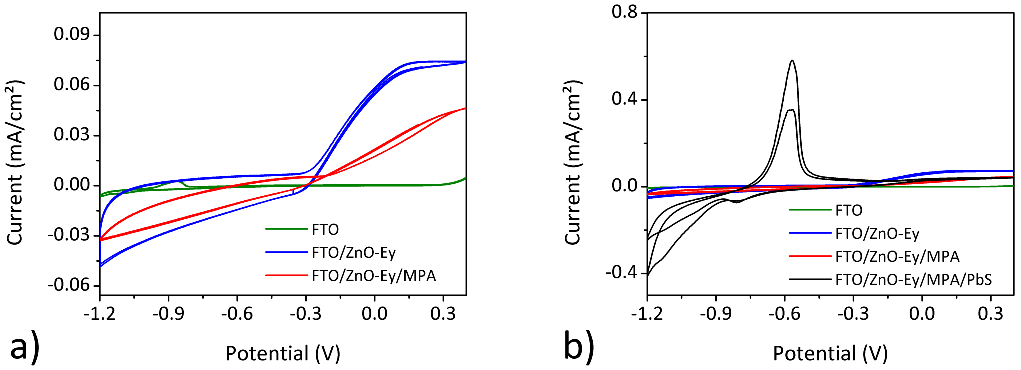

Figure 7.7: The cyclic voltammogram of the 2nd and 3rd cycle of the FTO/ZnO-Ey, FTO/ZnO-Ey/MPA and FTO/ZnO-Ey/MPA/PbS substrate is demonstrated. The CV was recorded under UV-illuminated conditions.

over the linker molecule might be an additional limiting process which affords such behavior.

## 7.5 The Opto-Electrochemistry on the Substrates

### 7.5.1 The Linear Sweep Voltammetry (LSV) Study on the Substrates

A hindering of the hole regeneration initiated through the linker can also be seen over the whole potential range between -0.5 up to 0.4 in the LSV diagram under UV radiation in Figure 7.8(a). The ZnO-Ey shows a higher photocurrent than the MPA covered ZnO-Ey film.

So far a higher photocurrent can be observed at longer wavelengths in the LSV spectra (Figure 7.9). Under UV irradiation the FTO/ZnO-Ey/MPA system is less efficient compared to the FTO/ZnO-Ey and FTO/ZnO-Ey/MPA/PbS substrate. However, in all LSV measurements (Figure 7.8 and 7.9) a complete photocurrent decline at a potential of -0.5 V which is associated with the approach of the applied potential to the ZnO CB as mentioned in earlier chapters is seen.

Furthermore it should be noted that a photocurrent from the FTO/ZnO-Ey and the FTO/ZnO-Ey/MPA films has been recorded using monochromatic light with a wavelength maximum at 630 nm (Figure 7.9(a)). Under yellow illumination (570 nm) (not shown here) and blue illumination (470 nm) (Figure 7.9(b)) a

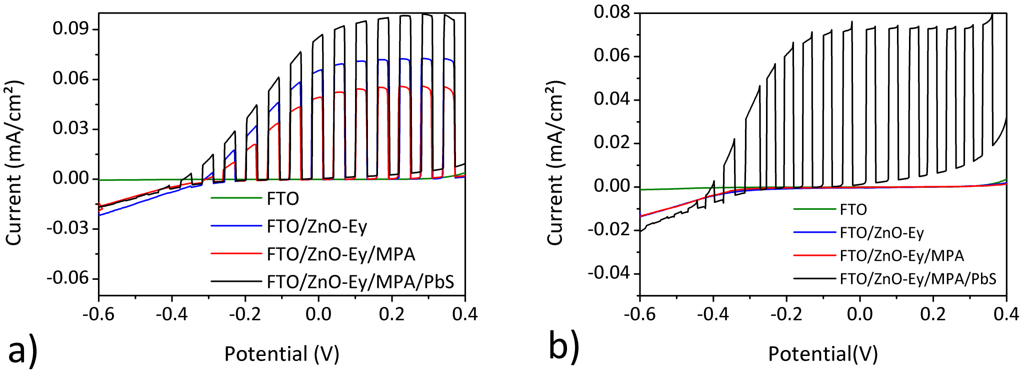

Figure 7.8: The LSV profile recorded from the substrate after each deposition step (a) under UV illuminated conditions and (b) under red radiation.

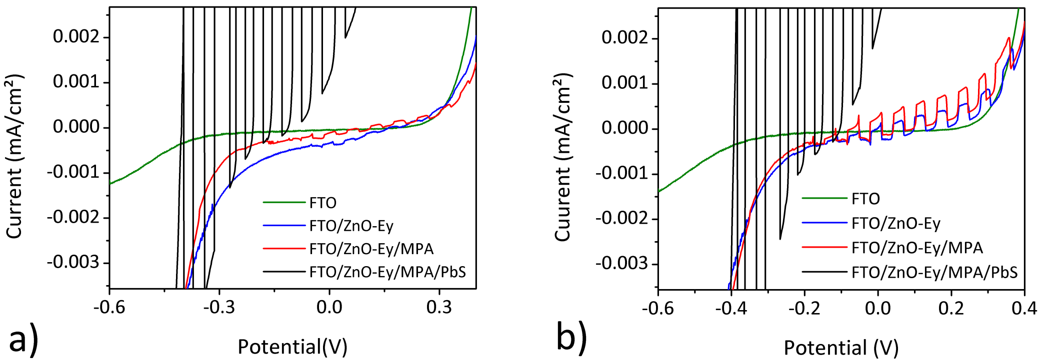

Figure 7.9: The magnified view of the LSV profile which was recorded from the substrate after each deposition step (a) under conditions of red illumination and (b) under blue irradiation. A photocurrent response can be seen for the pure FTO/ZnO-Ey film at blue and red illumination.

photoactivity can also be observed. This may be due to the eosin remainder and interaction with the ZnO material.

### 7.5.2 The IPCE Measurements on the Substrates

The wavelength dependent photoactivity of the FTO/ZnO-Ey, FTO/ZnO-Ey/MPA and the FTO/ZnO-Ey/MPA/PbS samples can be seen in Figure 7.10. The photoactivity of the eosin Y in the ZnO-Ey film can also be confirmed by the IPCE diagrams of each sample. A clear signal at wavelengths between 400 and 600 nm is seen in Figure 7.10(b) which is associated with eosin Y absorbance. An analogous absorbance spectrum of pure eosin Y can be found in the work of Brahimi et.al.[238]. The different intensity of the IPCE peak might be due to the concentration dependence of the signal. In Figure 7.2 the inhomogeneity of the sample could be observed by eye from the different coloration across the complete surface area. This concentration influence may also be the reason for the strong intensity variation in the ZnO IPCE signal between the wavelengths of 300 and 400 nm measured at the FTO/ZnO-Ey/MPA/PbS substrate which has a value of approx. 34% compared to the FTO/ZnO-Ey film with a value of approx. 58%. In the case of the FTO/ZnO-Ey/MPA substrate with an IPCE of approx. 26% the same effect could explain the strong decrease in the IPCE signal (analogous to Figure 5.2 in section 5.3).

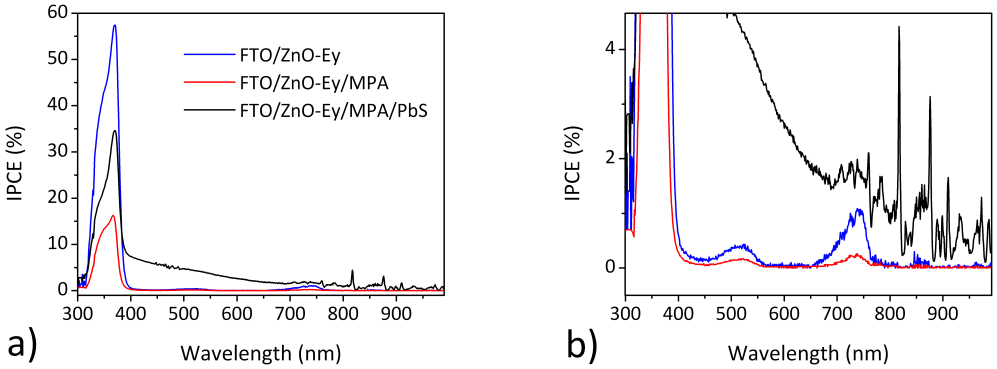

Figure 7.10: The IPCE spectra of the substrate after each deposition step. In (a) the complete IPCE range is presented. The pure FTO/ZnO-Ey shows an IPCE of approx. 60%. To illustrate the small signals at longer wavelengths a larger magnification of the spectrum is presented (b).

The signal from approx. 700 up to 770 nm is, as previously mentioned is a result of charge carrier generation caused by the second order of the monochromatic light coming from the monochromator.

### 7.5.3 The Photo Transient Measurements on the Substrates

The phototransient spectra were undertaken at four different wavelengths for each sample that resulted from every deposition step. Over longer times a decrease in the photocurrent could be measured. The maximum photocurrent (FTO/ZnO-Ey/MPA/$PbS_{max}$) and the photocurrent at steady state response (FTO/ZnO-Ey/MPA/PbS) is shown in Figure 7.11.

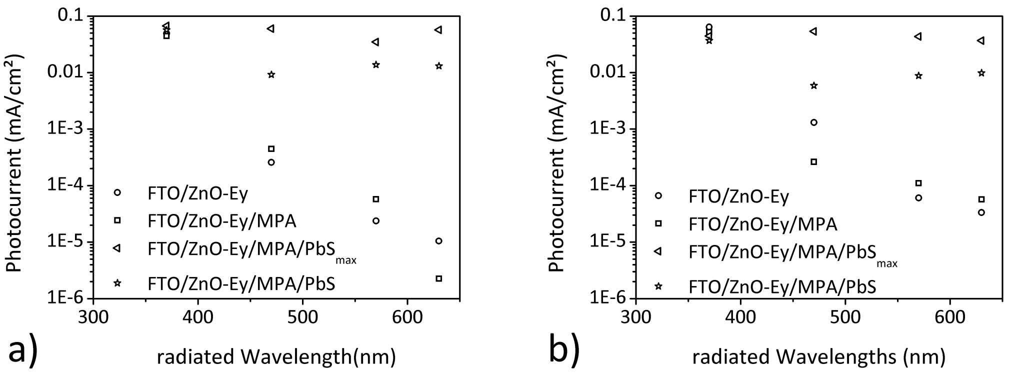

Figure 7.11: The role of the MPA and the PbS photo reponse in comparison to the complete system FTO/ZnO-Ey/MPA/PbS (a) at an applied potential of 0 V and (b) at a potential which shows the highest photocurrent in the LSV measurements.

The measurements were undertaken at two different potentials, at 0 V (Figure 7.11(a)) and at the potential which gives the highest photocurrent in the LSV measurements (Figure 7.11(b)). The difference in the applied potential makes no difference to the intensity of the photocurrent in the case of the FTO/ZnO-Ey/MPA/PbS substrate. The FTO/ZnO-Ey/MPA and FTO/ZnO-Ey substrates have a significantly lower photocurrent at 0 V. Therefore the limitations in the photocurrent, which was mentioned also in section 4.2.2 and 6.5, cannot be due to the material properties. In all three systems with different metal oxides just one component, i.e. the electrolyte, was constant. The repeated occurrence of the upper photocurrent limit is more or less a clear indication that this limitation is caused by the electrolyte.

An influence of the linker which increases the photocurrent at longer wavelengths could also be found. But also in these measurements the inhomogenity of the FTO/ZnO-Ey film cannot be neglected and therefore the responses of the FTO/ZnO-Ey film under red illumination at 0 V and blue illumination at the potential with highest photocurrent in the LSV needs to be further clarified.

## 7.6 Comparison between ZnO and ZnO-Ey based ISC

In summary the ISC based on our particular ZnO and the ISC based on ZnO-Ey shows typical behaviors which are expected from the ZnO material. Therefore the reactions over almost the complete potential range as well as the properties under different irradiation conditions are similar and reproducible. Similar CV profiles of FTO/ZnO-Ey/MPA/PbS (Figure 7.5) compared to the ITO/ZnO/MPA/PbS (Figure 4.8) under non-illuminated conditions could be found and are largely equal if light of UV and longer wavelengths is used. The CV profiles of the ITO/ZnO/MPA/PbS system show more shoulders which is an indication of a more complex interaction of the band states. The pure ITO/ZnO and the ITO (see Figure 3.8(b) in section 3.2.2) shows a equal behavior and almost no hysteresis compared to the FTO/ZnO-Ey film and the FTO (see Figure 7.6 and 7.7).

However, in all LSVs of each FTO/ZnO-Ey samples (Figure 7.8 and 7.9) a complete photocurrent decline at a potential of -0.5 V is seen which is associated with the CB edge of the ZnO. The same metal oxide edge position was also found for the pure ZnO gel material in earlier chapters so that a similar metal oxide CB band position is fundamentally guaranteed in both of these ZnO based ISCs.

In contrast to the results in section 5.3 for FTO/ZnO a generation of the photocurrent begins at an illumination wavelength of approx. 500 nm. Consequently the photocurrent under yellow and red irradiation could not occur for the ZnO gel film. In the case of the FTO/ZnO-Ey sample a photocurrent was measured with illumination wavelengths up to 630 nm. The same was also observed for the FTO/ZnO-Ey/MPA samples. The generation of the excitons and discharge of the charges in the circuit at such wavelengths can be caused by the excess eosin Y in the FTO/ZnO-Ey film. The eosin Y has a band gap energy of 2.4 eV[238] so that a direct electron generation in the eosin is not to be expected. When the eosin Y energy level positions are considered a possible explanation can be found. In Figure 5.4 in section 5.3 the band gap of the ZnO has been given with respect to the vacuum potential. During the evaluation of the FTO/ZnO-Ey films by LSV a cessation of the photocurrent at a potential of approx. -0.5 V equal to that of the pure ZnO gel film could also be found. Hence the CB position of both ZnO materials might be at the same potential with respect to the vacuum of -4.308 eV. According to Brahimi et.al.[238] the NHE potential in the vacuum[83] and the lowest unoccupied molecular orbital (LUMO) of the eosin Y is located at approx. -3.35 eV and the highest occupied molecular orbital (HOMO) is likely to be at approx. -5.75 eV. The assumption that some ZnO of the ZnO-Ey film also has trap and surface states within the band gap and so an electron intercrossing transfer process between ZnO and eosin Y can be expected. Therefore in the FTO/ZnO-Ey/MPA/PbS system two kinds of photovoltaic processes may be relevant. On the one hand the PbS exciton generation and PbS-ZnO electron injection has to be taken into account and additionally the eosin Y-ZnO intercrossing electron transfer has to be considered.

But generally the photocurrent response is of the same magnitude and shows the same trend as in the case of the ZnO and the ZnO-Ey based ICS. Admittedly the linker attachment to the ZnO surface contributes its part in both kinds of systems. Under UV irradiation the linker decreases the photocurrent of the ZnO which may be the result of its ability to limit the electron transfer during the hole regeneration. At longer wavelengths this influence is not as pronounced as under UV irradiation. Rather it is the electron which comes from the linker functional group which moves to the ZnO surface state and contributes to the photocurrent increase (see in section 4.2.3 and 3.3.2). The regeneration process seems to be negligibly small because of the lower probability of exciton generation which in general depends on the existence of trap states and their band gap position as well as the position of the Fermi-level. Under UV irradiation a high rate of exciton generation in the ZnO can occur which requires a concomitant increase in hole regeneration to close the circuit.

However, in both cases the upper limit of the photocurrent was measured in the photo transients for the metal oxides so that a clear indication for a slow electron transfer from the electrolyte could be surmised.

Another similarity of the ZnO based ISCs was the decrease in the photo transient signal to a constant photocurrent. At this stage it cannot be said whether it is a ZnO based material behavior or as a result of unconnected PbS within the pores which becomes lost. In the case of $TiO_2$ during the measurements no degradation was observed to occur but the magnitude of the photocurrents are far from the ZnO based ISC. Furthermore the degree of porosity may also be different. Hence in this case further analysis has to be undertaken in order to understand this behavior.

In general a lot of similar results could be measured for the ZnO and ZnO-Ey based ISC and their intermediate substrates. In the end a clear advantage for using the directed crystalline structure of the FTO/ZnO-Ey based ISC could not be found. Also better electron transport through the film with respect to the ZnO gel related films could not be seen in these studies. The difficulty in seeing any differences could be caused by the electrolyte employed. It has previously been mentioned that a limitation in the charge transfer processes has been attributed to this electrolyte.

## 7.7 Conclusion

In this chapter it was shown that another modification of the ISC can be achieved by the structuring of the metal oxide material. The use of electrodeposited ZnO is also able to act as an electron separator. In many cases a large number of similarities in the electrochemical and opto-electrochemical behaviors are found compared to the particular ZnO used in chapters 3 to 5. The postulated advantages of the preferential crystal orientation which should increase the electron transfer and therefore the photo efficiency could not be validated in these studies. The electrolyte used was found to play an important role. Because of the limitation in the electron transfer during the hole regeneration an upper limit of the photocurrent in the linker systems could be recorded. For that reason to achieve its supposed advantages the ZnO-Ey should be examined in the presence of a faster hole scavenger.

Another important remark is in relation to the eosin Y remainder. This small amount of embedded eosin Y has a relatively small influence on the FTO/ZnO-Ey/MPA/PbS substrate but a larger influence in the case of the FTO/ZnO-Ey/MPA and FTO/ZnO-Ey. The eosin Y shows a photoactivity which can be recorded in the IPCE across its specific absorption range. Furthermore an intercrossing electron transfer between ZnO and eosin Y which the ZnO also allows to generate as well as a transfer of electrons at illumination wavelengths up to 630 nm could be measured. That means that such electron transfer is still far away from the typical exciton generation from the VB into the CB of the metal oxide and away from thermally activated processes.

# 8

# Injection Solar Cell meets Photonic Crystal [3]

## 8.1 Introduction

Polymers, glasses and semiconductor materials are able to interact strongly with electromagnetic radiation the absorbance of which is not only a property of the material itself. In addition to radiation absorbance which is controlled by the material, a directed reflection and control of the radiation within the material can be realized if the material is arranged in a periodic dielectric structure. These kinds of structured assemblies are better known as photonic crystals.[265–268] Opal is a naturally occurring mineral with very colorful reflections and is where the name opalescence stems from. The opalescence results from photon reflection from the periodically arranged spheres. Which photons and which specific frequencies are influenced is specified by the material from which the spheres, which make up the periodic structure, are composed and their diameter. The arrangement of a periodic crystal affords a photonic band structure with a formation of a photonic band gap. Analogous to electron interaction through the band gap in the electronic band structure the photons are controlled by the photonic band gap in the photonic band structure. The photonic band gap can be calculated using a combination of both Braggs-law and Snells-law.[269] However, the so-called stop

---

[3] The results of this chapter were made within the framework of the bachelor thesis written by B. Sc. Susann Kittler under mentoring of the author in the work group of Prof. A. Eychmüller at the TU Dresden .

band allows the dispersion of the radiation along specific crystal axes for a specific frequency range which is comparable to X-ray scattering in atomic crystals. Whereas the full band gap affords the dispersion of the radiation in all crystallographic directions at any angles for a specific frequency range. The last effect can be realized only through the use of a high refractive index difference between the crystal material and the material composing the space between.[267,270–272] Analogous to the electronic bands some defects in the photonic band gap arise when contaminations or irregularities are built into the periodic structure.[272–274]

In a preceding section (2.1.3) the mode of action of a photovoltaic cell was described in detail. The impinging electromagnetic radiation has to be absorbed. But how can it be that the reflection properties of photonic crystals are not in contradiction to the absorbance requirements for photovoltaic application?

Nishimura[275] recognized a spectral effect in the UV/Vis/NIR range analogous to the Borrmann effect for X-rays. Electromagnetic radiation may be regarded as a standing wave. Whereas the wave maxima are positioned in the high dielectric part of the band gap edge at longer wavelengths, the wave maxima on the band gap edge at shorter wavelengths can be found in the low dielectric part of the photonic crystal. This means the light waves are localized in different parts of the structure. The semiconductors which are used in the ISC have a higher dielectric constant compared to that of air and water.[178] Moreover the inverse opal structure for photovoltaic applications will be used. For that reason the conditions for a photonic crystal with a full band gap are given. The absorbing material in an inverse photonic structure contains the high dielectric part. This results in a stronger interaction between the absorbing material and the longer wavelengths close to the stop band of the inverse photonic crystal. Finally the absorbing material, the semiconductors, will have gained an absorption increase at longer wavelengths and may contribute to an increase in the total ISC efficiency. In the literature such ISCs with dye molecules[275–277] are reported. For ISC applications inverse photonic structures combined with nanoparticles can also be found but these arise only in research undertaken in the last few years.[278–281] The pure inverted opals are already common for photovoltaic applications.[276,278,281]

In the following sections this topic is discussed and initial suggestions for further research are made. The ISC assembly characterization were undertaken using UV/Vis/NIR spectroscopy, linear sweep voltammetry (LSV), photo transient techniques, cyclic voltammetry, IPCE and EIS. But first, the chapter will open with the preparation of the opal and inverse opal as well as the results of their variable angle specular reflectance accessory (VASRA), optical microscopic and SEM characterization.

The final assembly is based on the construction of solar cells in the preceding chapters but with a metal oxide as an inverse opal structure (Figure 8.1). The inverse opal used consisted of the $TiO_2$ gel which has been used in chapter 6. The attempt to infiltrate the ZnO gel into the opal structure did not work because of the larger sizes of the ZnO particles and may also be because of the surface charge interaction of the ZnO particles with the opal spheres compared to that of the $TiO_2$ particles. The absorbing material used are PbS nanoparticles with an absorption maximum at 1084 nm and therefore a band gap at approx. 1.14 eV. The linkage between $TiO_2$ and PbS NP has been realized using MPA.

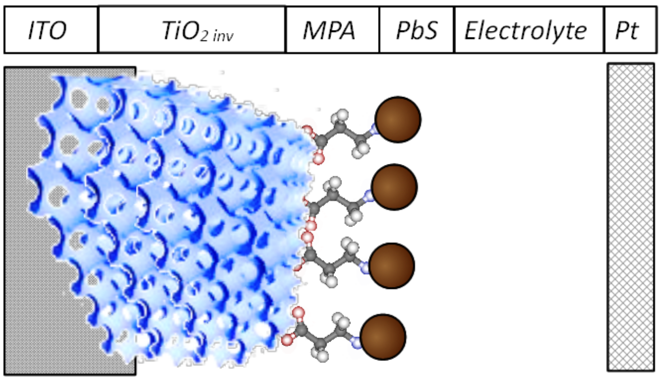

Figure 8.1: The schematic assembly of the injection solar cell used is shown. The TCO is an ITO coated substrate. On the ITO an inverse opal structure consisting of $TiO_2$ has been placed. The absorbing component is represented by PbS nanoparticles which are linked to the $TiO_{2inv}$ though MPA as the linker. The MPA and PbS may also be expected to be found inside of the inverse opal structure but is not explicitly included in the above scheme.

## 8.2 The Opal

There are a number of different methods for the construction of opals. A distinction is drawn between driving forces using field-induced, flow-induced and volume decrease methods.[271,282] In the present work vertical deposition through vaporization of the liquid phase was used. This flow induced self assembly method was carried out using polystyrene latex spheres (PS) on ITO coated glass.[270,271]

The preparation is a common procedure and works quite well if the preparation parameters such as concentration of the polystyrene latex solution, vaporization time, temperature and a vibration-free space can be controlled (for further details of the procedure see section 2.2.4). The resulting opals show a quite homogenous arrangement of the spheres. In Figure 8.2(c) such ordered periodic structures of polystyrene latex with sphere sizes of 535 nm are recorded using SEM. From the SEM image it can be noticed that the dimensions of the latex spheres are not congruent with the dimension specified by the manufacturer. This is primarily due to the fact that polymers are able to swell and shrink and in this case the tendency of the polymer latex to evaporate in the electron beam causes the spheres to shrink.[283,284] The final opal packing after the drying process must also be kept in consideration but generally such a large shrinkage effect is not seen by drying under atmosphere conditions which may be distinguished in the VASRA measurements and the following calculation of the stop band edge.

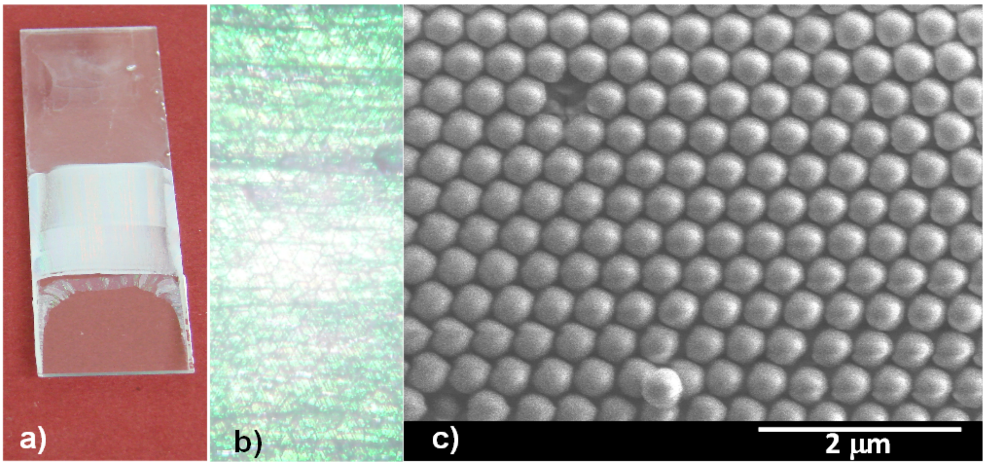

Figure 8.2: The self-assembled opal structure on ITO coated glass consisting of packed PS latex spheres with a diameter of 535 nm. The images were taken by a) camera b) optical microscope and c) SEM

In the introduction it was mentioned that the reflection wavelength $\lambda_R$ which is related to the photonic band gap edge can be determined by using the Bragg relation modified by Snells-law. The resulting relationship is:

$$\lambda_R = \frac{2 \cdot d_{hkl} \cdot \sqrt{n_{eff}^2 - \sin^2(\theta)}}{n} \tag{8.1}$$

where the space between the interplane distance is given by:

$$d_{hkl} = d \cdot \sqrt{\frac{2}{3}} \tag{8.2}$$

and the effective refraction index of the colloidal crystal is:

$$n_{eff}^2 = \sqrt{f_{fcc} \cdot n_{PS}^2 + (1 - f_{fcc}) \cdot n_{air}^2} \tag{8.3}$$

Generally the opals will self-assemble into a face-centered cubic (fcc) packing (also called cubic close packing (ccp)).[267] The fcc packing has a packing density of $f_{fcc} = 0.7405$.[285] The interplanar distances $d_{hkl}$ have been taken along [111], so that $d_{hkl} = d_{111}$. The refractive index of air is $n_{air} \approx 1.0$[178] and for PS spheres $n_{PS} = 1.59$ (value provided by the manufacturer). The diameter of the spheres is d = 535 nm, the diffraction angle was chosen to be $\theta = 20°$ and the diffraction order is n = 1. The reflection wavelength of the photonic crystal with spheres of a diameter of 535 nm can be found at $\lambda_R = 1050$ nm. To a good approximation the reflection spectra in Figure 8.2 shows a reflection onset starting at approx. 1090 nm. When the diameter used for the $\lambda_R$ calculation is that which has been measured in the SEM images ($\approx$ 400 nm) than a reflection at approx. 780 nm results. This is far away from the VASRA measured value and supports the assumption that the spheres have shrunk in the SEM beam.

Upon examination of the photograph in Figure 8.2(a) the homogenous reflection of blue and green light with wavelengths in the range of approx. 530 down to 475 nm can be seen. But the green reflection is not the wavelength which is related to the calculated photonic band gap in the NIR range. This reflection can be explained as being the reflection wavelength of the second order. By using the modified Bragg relation 8.1 the second order reflections have been determined to be at approx. 525 nm which is in good agreement with the reflection seen in the photograph. Also this reflection can be seen under the optical microscope in Figure 8.2(b) and can be optically detected through the reflection peak in the

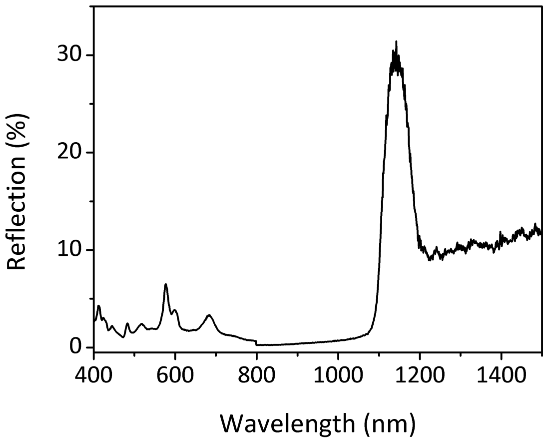

Figure 8.3: The VASRA spectrum of the opal substrate on the ITO coated glass using PS latex spheres with a diameter of 535 nm. The measured reflection onset is given at approx. 1090 nm.

VASRA spectrum at wavelengths in the visual range seen in Figure 8.3. In this section a high quality of the opal structure with a diameter of 535 nm could be shown.

## 8.3 The Inverse Opal

The inverse opal has been achieved through the infiltration of an opal similar to that which is shown in section 8.2. For the final (opto-)electrochemical characterization of inverse opal based ISCs polystyrene spheres with diameters of 535 and 471 nm have been used for the preparation of the opal substrates. To ensure that enough ISC substrates were available for the electrochemical characterization the best inverted opals have been used. Inverse opals with similar diameters have been employed for further characterization. A size dependent correlation has not been carried out.

The infiltration solution consisted of a diluted $TiO_2$ gel in a water/ethanol mixture with a ratio of 8:2. The infiltration technique has been optimized by using different mixture ratios. Pure water has a too high surface tension and results in a strong interaction with the opal surface at the $TiO_2$ solution meniscus. As a result the opal peels away from the ITO surface. At ethanol concentrations higher than 20% a less effective infiltration could be observed. During the infiltration, capillary forces are necessary and this effect may be decreased by a low surface tension of the solution. Also the alteration of the solution polarity has an effect on the polymer surface charge which will impact on the attachment of the $TiO_2$ to the polymer spheres. Due to the $TiO_2$ surface charges which are also stabilized by the particle itself the charge on the polymer spheres and their interaction with the $TiO_2$ charge is very important for the attachment and infiltration processes.

It was also observed that an intermediate heat treatment of the opal structure was advantageous. As the opal network is a self assembling structure of polystyrene spheres if this network is heated up to near the glass temperature of the polymer the latex spheres become slightly viscous and stick together at the point of the sphere-to-sphere contact which strengthens the network structure.

Furthermore the amount of infiltration cycles and the drying methods employed after the infiltration will also affect the quality of the inverse opal. A first heating to 50°C dries the complete opal-infiltrated $TiO_2$. By an additional heating process up to the sintering temperature of 450°C the removal of the PS spheres and the sintering of the $TiO_2$ structure with less drying cracks will be achieved. The preparation procedure which resulted in the best inverse opals is given in section 2.2.4 and is applied for the following samples which are used for the characterisation.

In Figure 8.4 the photograph (a), the micrograph (b) and the SEM images (c) and (d) of such inverse opals are presented. The base opal used for structuring of the inverse opal had spheres with a diameter of 471 nm. Normally the inverse opal should be transparent but shows a white colour which can be caused by the large amount of crystal defects. In the micrograph this kind of furrow which is mentioned above can be seen. The disruption is caused by pulling the whole inverse opal structure through whereas smaller splits are also pronounced in Figure 8.4(c) and (d). The inverse opal network is only open at the splits and everywhere else is closed by a coverage of $TiO_2$. The dimension of the holes is almost that of the diameter of the excluded polystyrene spheres. Furthermore, as expected, the desired residual volume structure (RVS) can be seen. Other inverse opal structures are the shell structure (ShS) and the skeleton structure (SkS).[286]

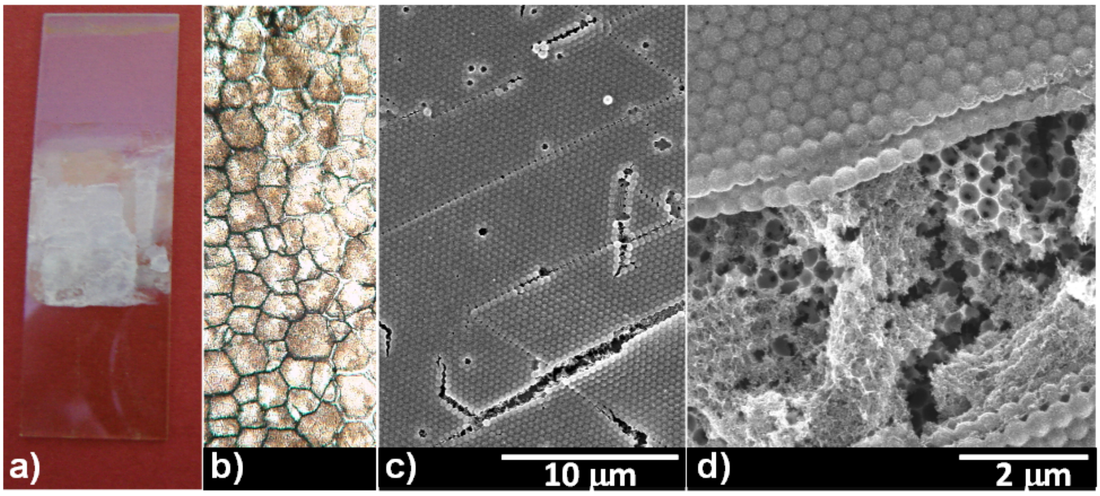

Figure 8.4: The inverse opal prepared by the infiltration of $TiO_2$ into an opal network with packed PS latex spheres with a diameter of 471 nm. The images were taken by a) camera b) optical microscope and c)+d) SEM

The opal which was used for the infiltration shows a well matched reflection onset at approx. 970 nm (Figure 8.5) compared to the Bragg relation 8.1 calculated from the reflection wavelength $\lambda_R = 925$ nm. For the band edge calculation of the $TiO_2$ inverse opal at a sintering temperature of 450°C a refractive index of $n_{TiO_2} \approx 2.0$[287–290] has been used. The calculation of $n_{eff}$ has to be undertaken in reverse to that of the case for an opal. That means the most volume is occupied by the air and the spaces between are filled by $TiO_2$. In doing so the calculated wavelength of the stop band edge is $\lambda_R = 804$ nm. The VASRA spectrum measured shows a broad reflection band whose reflection can be seen from approx. 840 nm up to the NIR (1400 nm) (see Figure 8.5). For that reason the modified Bragg relation 8.1 is also in good agreement with all data obtained using the VASRA. The deviations within the measured data could be caused by the defects in the inverse opal structure. The permanent slits in the continuous crystal disturb the interference of the reflecting light in the crystal plane. The slits may cause a slightly different position of the crystal planes at neighboring opal domains which affects the interference and the wavelength distribution of the reflecting light. In Figure 8.4(d) it is seen that the inverse structure is distorted which also results in an effect on the reflected light wavelength. Such problems with the instability of the inverse opal have been reported in the literature. The

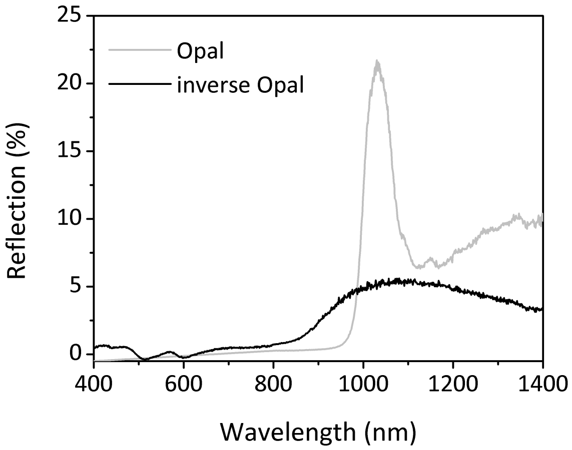

Figure 8.5: The VASRA spectrum of the opal substrate on the ITO coated glass and the $TiO_2$ inverted opal prepared with latex spheres with a diameter of 471 nm. The measured opal reflection onset is given at approx. 970 nm. The inverse opal shows a broad band across the NIR down to the inverse opal onset at approx. 840 nm. All VASRA measurements were done at an angle of 20°.

alteration and the decrease in the quality in their photoactivity and efficiency could be observed.[279]

## 8.4 The Inverse Opal based ISC

### 8.4.1 The Substrate Characteristics

In section 8.2 and 8.3 the successful structuring of the $TiO_2$ to an inverse opal could be shown. The next step for the ISC is the deposition of the MPA and PbS nanoparticles. By eye the ITO/$TiO_{2\ inv}$/MPA/PbS is characterized through a strong brown coloration whereas the substrate itself looked relatively homogenous to the eye (Figure 8.6(a)). In the Figure is also seen that a part of the $TiO_2$ substrate has split off which occurred during the infiltration step. The dipping of the opal substrate into the $TiO_2$ infiltration solution can lead to a detachment generally on the lower dip edge of the opal.

The absorption spectra of the periodically structured $TiO_2$ with PS spheres with a diameter of 471 nm shows a maximum absorption peak at approx. 450 nm (Figure 8.6(b)). This absorption peak also persists after the deposition of the MPA and PbS nanoparticles. As expected the MPA attachment has a small influence on the absorption, and because of the material interaction the results should be the same as those in chapter 6. But the PbS coverage shows a large increase in the absorption but also in the range were the PbS is not absorbing anymore. The PbS absorption in solution has also been added to Figure 8.6(b) for comparison. In the range in which the PbS shows a decrease between the absorption maximum and the absorption of the continuum the absorption spectra of the ITO/$TiO_{2inv}$/MPA/PbS displays an absorption increase. This absorption increase is exactly located at longer wavelengths of the inverse opal stop band edge at approx. 840 nm. But an increase in the absorption at longer wavelength as expected from the report by Nishimura[275] cannot be verified. The standard UV/Vis spectroscopy is also measuring the reflection behaviors of the substrate. For a clear evidence of such absorption increase it requires a measurement using the integrating sphere.

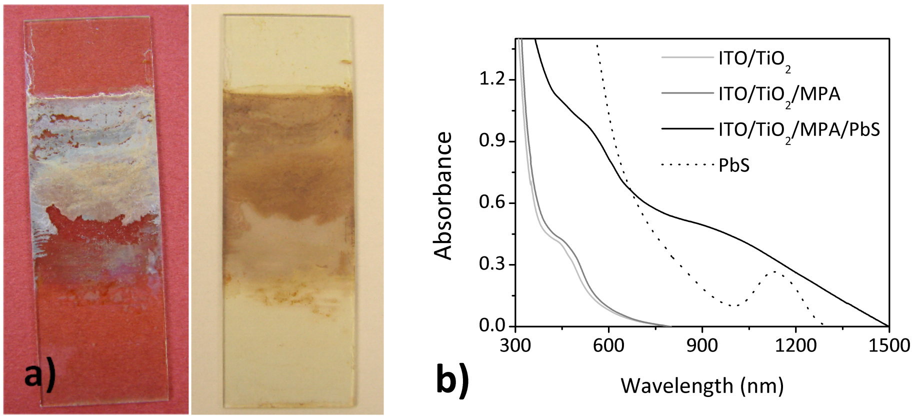

Figure 8.6: The ITO/$TiO_2$ $_{inv}$/MPA/PbS substrate prepared with latex spheres with 471 nm diameter shows a brown coloration at photograph (a) whereas the presence of highly absorbing components are evidenced through the absorption spectra of each deposition step (b).

## 8.4.2 The Cyclic Voltammetry

As was demonstrated in earlier chapters a typical oxidation peak at -0.7 V can be observed when PbS exists on the $TiO_2$ substrate. The absence of this peak in the ITO/$TiO_2$ $_{inv}$/MPA/PbS is very remarkable. But another small peak at approx. -0.8 V is present (Figure 8.7). Under non-illuminated conditions a second oxidation peak at approx. 0.1 V and a reduction peak at approx. -0.9 V can also be seen. By contrast the blue illuminated samples show no further oxidation peak at positive potentials but a slightly shifted reduction peak at more negative potentials than approx. -1.0 V. The shift in the peak has its cause again in the structuring. In the absorption spectra a material alteration or at least an electronic alteration in the material could be observed. It could be shown that the peak position has shifted from -0.6 to -0.7 V just through the exchange of the ZnO layer by the $TiO_2$ layer. The special structuring of the $TiO_2$ changed the surface texture and could alter the electronic surface of the material which is seen by the change in the CV profile. By eye it seems that enough PbS material exists at the surface but the promoted electrons in the PbS cannot transferred into the circuit.

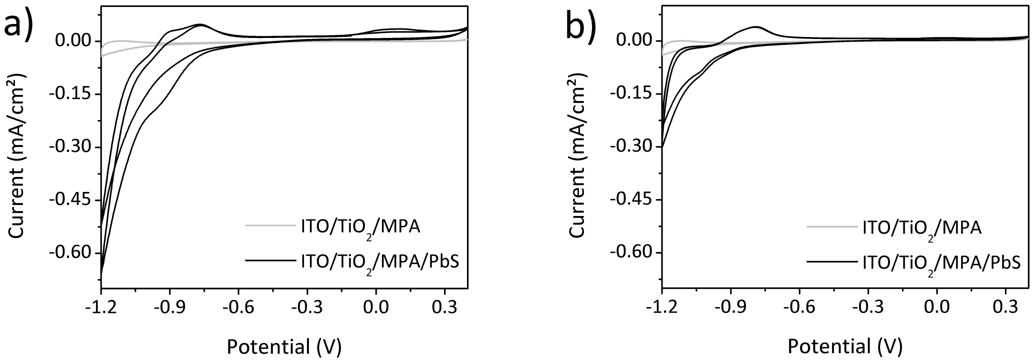

Figure 8.7: The first two cycles of the cyclic voltammetry profile are presented. The behaviors of the ITO/$TiO_2$ $_{inv}$/MPA/PbS and the ITO/$TiO_2$ $_{inv}$/MPA substrate a) under non-illuminated and b) blue-illuminated ($\lambda_{max}$ = 470 nm) conditions in 0.1 M $Na_2SO_3$ solution.

### 8.4.3 The Opto-Electrochemistry

The photoactivity of the ISC substrate is very low. Linear sweep voltammetry (LSV) shows a very low photocurrent in the potential range of 0.4 down to -0.8 V (Figure 8.8(a)). From the phototransient measurements a photocurrent at approx. 1E-5 mA/cm$^2$ could be observed (Figure 8.8(b)). From the LSV profiles of the MPA coated ITO/$TiO_2$ $_{inv}$ only a very large resistance can be seen in the form of the slope of the I-V curve. The pure ITO/$TiO_2$ $_{inv}$ also contains such a feature alluding to its high resistance (not shown here). In chapter 6 it was reported that this kind of material combination generates excitons and can discharge the electron into the circuit. Through photo-transient measurements photocurrents whose magnitude is approx. 0.01 mA/cm$^2$ have been recorded for the ITO/TiO$_2$/MPA/PbS system (see chapter 6). For that reason the decrease in the photocurrent can be explained by structuring of the TiO$_2$ and it is conceivable that the high resistance could also be caused by the structured surface. The highly twisted and convoluted TiO$_2$ layer has an influence on the charge flow through the electrolyte in the deposited inverse opal structure. It is also possible that the area of contact between the substrate surface and electrolyte varies strongly. In one place the inverse opal structure is strongly cracked as seen in Figure 8.4(b) and in other parts of the substrate the electrolyte accumulated only on the surface because of a small number of splits (Figure 8.4(c)). The same problem could occur on the samples at different deposition steps so that for observations at the microscopic level the strongly homogenous deposition can occur mainly at the furrows. The PbS is more distributed on the surface inside the furrow and on the cover but may not be distributed in the cavities of the TiO$_2$ inverse structure.

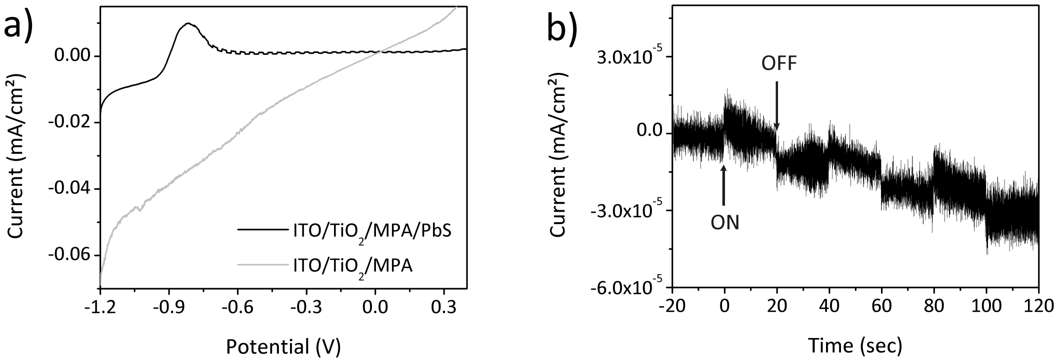

Figure 8.8: a) The linear sweep voltammetry profile of the complete ITO/TiO$_2$ $_{inv}$/MPA/PbS and the ITO/TiO$_2$ $_{inv}$/MPA substrate in the potential range between -1.2 V up to 0.4 V. The PbS coated ISC substrate shows a photocurrent down to -0.8 V. b) The phototransient response of the ITO/TiO$_2$ $_{inv}$/MPA/PbS at ocp. The other deposition steps did not show any photoresponse. The opto-electrochemical techniques have been carried out in a 0.1 M Na$_2$SO$_3$ solution.

The IPCE presented in Figure 8.9 shows a similar decrease. No photoresponse is seen at above 370 nm which is the band gap edge of the $TiO_2$ material. Hence the influence of the stop band edges of the photonic crystal could not be demonstrated electrochemically. Furthermore a decrease in the IPCE of the $TiO_{2inv}$ absorption range can be observed. The reason for this decrease may result from the layer itself. The layers are often quite different although a homogenous distribution can be observed by eye. No methods have been used to check the thickness and/or the amount of the $TiO_2$ until now. Even if it can be assumed that the opal is prepared always under the same conditions, it cannot be guaranteed that the same thickness always occurs in the final inverse opal because of the relatively unpredictable infiltration step. For that reason a strong variation in the inverse opal structure itself cannot be excluded.

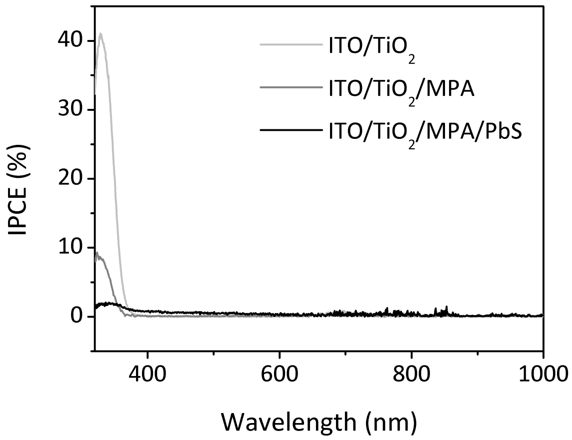

Figure 8.9: The IPCE of the substrate after each deposition step ITO/$TiO_{2\ inv}$/MPA/PbS, ITO/$TiO_{2\ inv}$/MPA and ITO/$TiO_{2\ inv}$ in 0.1 M $Na_2SO_3$ solution at ocp.

### 8.4.4 The EIS Measurements

The Nyquist and the Bode plots as well as the magnitude of the resistances and capacitances are different from the results shown in chapter 5. The whole system is distinguished by a significantly lower impedance which makes it possible to observe two semicircles in the Nyquist plot (Figure 8.10(b)). EIS measurements on the normal ITO/$TiO_2$/linker/PbS analyzed in chapter 6 have shown the same high impedances and similar plots (not shown) as presented in chapter 5. The possibility that an electrolyte contact to the ITO results in such a decrease in the system impedance can be neglected. Measurements on the pure ITO coated glass also show quite a high impedance up to a total impedance of over 100 kΩ. Therefore the decrease can be explained only by the structuring of the $TiO_2$ material to form an inverse opal. The EIS measurements were carried out at different potentials and under non-illuminated and blue illuminated conditions. In comparison with the absorption spectra in Figure 8.6 it could be seen that the illumination with light at the wavelength maximum of 470 nm overcomes the band gap energy of the structured $TiO_2$ material. It has to be mentioned that the pure $TiO_2$ gel shows an absorption band at approx. 340 nm which shifts to longer wavelength after the structuring.

In Figure 8.10 the Nyquist and the Bode plots of the pure ITO/$TiO_{2inv}$ substrate under dark conditions and at an applied potential of 0 V are presented. The same model presented in Figure 5.5 and the fitting of the measured data has been handled in the same way as in earlier chapters.

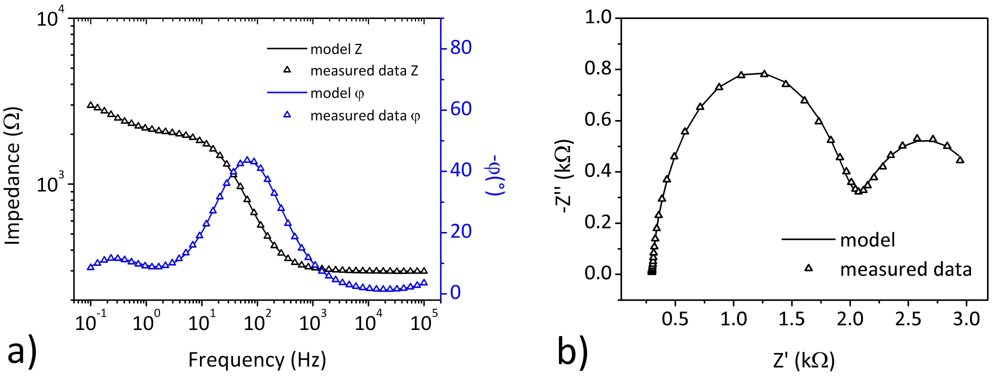

Figure 8.10: (a) Bode and (b) the Nyquist plot of the pure ITO/$TiO_{2inv}$ substrate under dark conditions at an applied potential of 0 V.

Therefore the calculated magnitudes for the ITO-$TiO_2$ interface are $R_{ITO-TiO2}$ = 1720 Ω and $CPE_{ITO-TiO2}$ = 5.5E-6 F, for the $TiO_2$-E interface $R_{TiO2-E}$ = 1312 Ω and $CPE_{TiO2-E}$ = 6.6E-4 F as well as the $CPE_{TiO2}$ = 4.2E-9 F and $R_{TiO2}$ = 83 Ω. Compared to the EIS results from the $TiO_2$ gel system shown in chapter 6 the resistances are one or two decades smaller and the capacitance one decade higher. In the case of the $CPE_{TiO2}$ it is not clear how trustworthy the value is. Analogous to the plot presented the substrate covered with MPA and MPA/PbS displays similar responses and similar dimensions in the impedance. For what reason such a strong interface alteration appears is presently not clear. To obtain a greater understanding of the process responsible first inverse opals of high quality have to be prepared in a reproducible manner and then further deeper analysis using (opto-)electrochemistry and frequency modulated techniques can be applied in order to achieve a fuller understanding of these processes. Here the aim is to demonstrate the strong property changes in the solar cell substrate brought about by structuring of the wide band semiconductor.

## 8.5 Conclusion

In this chapter a successful preparation of an opal network on an ITO coated glass could be shown. Furthermore the preparation of the inverse opal by using infiltration methods could be demonstrated. At this point in time the infiltration steps are not sufficiently controlled making a comparison between each deposition steps quite difficult. In addition a very low photocurrent could be measured for the ITO/$TiO_{2\ inv}$/MPA/PbS. The PbS oxidation signal in the cyclic voltammetry is of a very low magnitude. Also very different results for the ITO/$TiO_{2\ inv}$ were recorded by EIS compared to that of the ITO/$TiO_2$ film. Because of a significant decrease in the impedance it was possible to measure two semicircles in the Nyquist for the first time due only to the structuring of the metal oxide. It seems that the promoted electrons in the PbS nanoparticle become "lost" in the structured film and do not contribute to the circuit. In summary the whole ISC assembly is not sufficiently improved yet and further progress has still to be made. At first a method must be found for the controllable and reproducible preparation of the inverse opals because of structure defects over the complete inverted photonic crystal. Through the use of the VASRA very good reflection spectra with a photonic band edge which is in good agreement with the modified Bragg-relation could be recorded.

# 9

# Overall Conclusion

At the end of the day any device, solar cells included, is only as good as the selection of the materials used in its construction and their interactions. Every component within the system has its specific properties which affect and control the behaviour of the during application. In the present studies an injection solar cell constructed from a transparent conductive metal oxide (TCO)/metal oxide ($MO_x$)/linker/PbS nanoparticles has been analysed. ITO and FTO were used as TCO. The FTO, which was employed for more complex analysis such as the EIS studies, shows a higher stability when compared to the ITO. Overall the ITO and FTO glasses have shown many similarities in their conductivity and in their interfacial interaction. The TCO subsequently had another wide band gap metal oxide such as ZnO gel, $TiO_2$ gel or an electrodeposited ZnO/eosin Y deposited onto it. The PbS nanoparticles employed as the light absorbing component have been linked to the metal oxide (MO) surface through a linker molecule. The use of linker molecules was determined to be necessary as the photoresponse from the device when the PbS was merely physisorbed to the MO was inefficient and unstable. In the studies the influence of the six different linkers; oxalic acid (OA), malonic acid (MA), thioacetic acid (TAA), thioglycolic acid (TGA), 3-mercaptopropionic acid (MPA) and 1.6-hexandithiol (HDT) has been investigated.

The linker analysis of the systems shows that a $\pi$-system present within the linker, the thiol group as connector on the PbS surface and the existence of a C-chain are beneficial to electron transfer whereas a detrimental effect is expected from longer linker chain lengths. Precisely how long the C-chain has to be before a detrimental effect could be observed was not be shown as no measurements specifically concerning the chain length limits were done. Generally the linker increases the absorbance of the MO only when they were attached onto the MO surface. The magnitude of the absorbance is limited and dependent on the amount of linker present at the MO surface. Linkers with a large dipole moment have the ability to shift electrons from their functional moieties to the MO surface states which results in filling of the surface states. Therefore an increase of the MO trap depth and shift of the highest occupied surface state to higher energies can occur insofar as the highest occupied states converge towards the CB resulting in the trap states becoming "lost".[129,130] Furthermore a similar effect could be found for the photoactivity. The photo-transient measurements of the TCO/MO/linker substrate have shown a higher magnitude response compared to that of the TCO/MO substrate. Certainly the increase in the efficiency caused by the linker attachment to the MO surface is limited when the energy of the irradiation is higher than the energy of the MO band gap. At this stage the rate of exciton generation is very high because the promotion of electrons to the MO CB may occur. The hole regeneration initialized from the electrolyte cannot inject electrons into the hole located in the MO VB quickly enough due to the additional barrier caused by the linker molecule at the MO surface. For that reason a smaller photocurrent magnitude may be recorded for the TCO/MO/linker substrate as compared to the TCO/MO substrate.

However, in the case of the ZnO as MO strongly acidic linkers such as OA and TAA initiate a reaction between the ZnO and the linker molecules and, given enough time, cause a complete degradation of the ZnO. Due to the chemical instability of ZnO in acidic milieus the studies on the ZnO based ISC with OA and TAA as ligand were limited. Therefore comparable studies concerning the linker dependence and the reproducibility of the (opto-)electrochemical results for other MOs have been undertaken successfully using a $TiO_2$ based ISC. Furthermore the orientation of the linker at the ZnO surface using FTIR measurements could be shown. In addition the photoelectric response of the ZnO gel as a function of the film thickness and the sinter temperature could be demonstrated.

During the EIS measurements of a ZnO based ISC a strong interaction of the ZnO MO with light of different wavelengths could be achieved. In addition to the CB, photoactive states of the ZnO which need an energy of 3.27 eV (in UV range) to be addressed and additionally photoactive states between the ZnO conduction and valance bands, which may be addressed with lower energies, could be determined. These "midgap" photoactive states could be addressed by using wavelengths up to 500 nm, for instance blue light of $\lambda_{max}$=470 nm, which corresponds to an energy of 2.26 eV. The photoactivity of such states is dependent on a thermally activated promotion which allows the detrapping of the electrons from the so called trap states into the ZnO CB. In the ZnO trap states may also be addressed by using wavelengths longer than 500 nm, for instance yellow ($\lambda_{max}$=570 nm) and also red ($\lambda_{max}$=630 nm) light. However, such trap states do not contribute to the photocurrent. Unfortunately these trap states may act as an electron "container"[222] and have an influence on the capacitances and resistances of the ZnO interfaces and therefore alter the behaviour of the layer. More complex electron transfer processes in the ISC may be caused by such trap states and have to be considered. A back electron transfer from the ZnO trap states into the PbS VB at blue illumination may be occurred using EIS.

In addition a model which fits the measured EIS data quite well could be formulated. The effect of illuminating the ISC at different wavelengths as well as a significant effect when the applied potential converged to the CB of the ZnO could be identified. During the convergence of the applied potential (the TCO Fermi-level) to the CB of the ZnO a slight increase in the capacitances and decrease in the resistances of the FTO and ZnO interfaces have been determined. The loss of the driving force for the electron transfer as well as the convergence of the Fermi-level to the FTO CB (located at -4.85 eV[203]) may be the reason for this effect. From the EIS measurement data taken at different illumination wavelengths evidence is provided suggesting a complex set of interactions are present in the ISC amongst which are trap state filling and a back electron transfer from the ZnO to the PbS NPs as mentioned above.

Evidence for PbS being present at the ZnO surface has been determined by cyclic voltammetry. The specific signals in the cyclic voltammometric profile have been indentified to be associated with the attached PbS. In addition the specific oxidation and reduction peaks recorded show a size dependence which allows determining the band position and the band gap of the PbS nanoparticles using cyclic voltammetry. This size dependence was confirmed using theoretical calculations.

In addition the effect that the size of the PbS nanoparticles have on the relative band positions has been recorded. It could be shown that the magnitude of the IPCE and the absorbance of the smallest PbS nanoparticles, with an absorption maximum at 868 nm, is larger compared to that of the largest PbS nanoparticle used, which has an absorption maximum at 1570 nm. The $PbS_{1570}$ NPs have been shown to have one decade lower surface coverage than the $PbS_{868}$ NPs due to their size exclusion. But in addition to the lower surface coverage, the band gap decrease and therefore the resulting band shifts of these NPs may also contribute to the magnitude decrease. Generally a significant limit to the efficiency of the ISC can be assumed at a PbS NP absorption maximum of approx. 1500 nm which has low driving force for an electron transfer. The NPs employed with an absorption maximum of up to 1200 nm may be sufficient and have the best matching band positions to maintain the driving force between the ZnO CB and the PbS CB at an acceptable level.

A better charge carrier transfer through the ZnO film caused by a lower amount of grain boundaries may be utilized by using a higher crystalline and more preferentially orientated ZnO. Such ZnO was prepared by using an electrodeposition method in the presence of the dye eosin Y which acts as a place holder and has been used to fabricate a ZnO/Eosin Y based ISC. The ZnO itself generally shows approximately the same behaviour as the film deposited from the particulate ZnO gel. Unfortunately, the eosin Y desorption did not take place completely leaving a small amount of eosin Y in the structured ZnO film. Therefore the FTO/ZnO-Ey substrate shows a photoactivity up to a wavelength of 630 nm (1.96 eV). But the eosin Y LUMO-HOMO band difference is 2.4 eV, energetically higher than 630 nm, and therefore an intercrossing electron transfer between the ZnO and the eosin Y can be assumed.

In these studies the electrolyte represents the limiting part of the system. Unfortunately the electrolyte limitation has quite a strong effect on the system with the result that no significant differences between particulate ZnO and the preferentially orientated ZnO/Eosin Y substrate could be occurred. In addition the linker dependence of MPA, TGA and HDT, could not be estimated.

Another study, in which the MOs have been structured as photonic crystal, has been undertaken. The structuring has been predicted to increase the efficiency of the PbS light absorbance through the interaction of the optically active material with the band gap of the photonic architectures. The successful preparation of the opal could be shown and its typical reflection properties measured by VASRA and theoretically verified using the Bragg-Snells relation. It was not possible to achieve an inverse opal with a reproducible thickness and homogeneity which resulted in a non-reproducibility and non-comparability of the (opto-)electrochemical results. A very low photoactivity and a wide distribution in the trends of the results are recorded. For the first time in these studies it was possible to measure a Nyquist plot with two semicircles caused by the very low impedance which resulted from the structuring of the inverted $TiO_2$ material. In contrast for EIS measurements on unstructured MO based ISC in general high impedances have been recorded.

In summary the preparation of a working ZnO gel, $TiO_2$ gel and ZnO/Eosin Y based injection solar cell (ISC) could be demonstrated. This thesis has dealt with the basic research of such an injection solar cell and has provided a wide variety of interesting findings concerning the optical and opto-electrochemical responses which are dependent on the type of linker and their orientation on the surface, the structuring of the metal oxide employed, the sizes of the PbS nanoparticles as well as the wavelengths employed for irradiation and the applied potential. New benchmarks concerning the assembly properties and the interactions within the materials employed in its construction could be shown. The behavioural and material properties have been estimated so that the next steps for improvements can now be initiated.

# 10

# Outlook

This thesis consists of the results of basic research which provide our insights concerning processes which occur in injection solar cells. It would not be possible to provide a complete comprehension of the myriad of processes occurring within the ISC between the covers of one thesis alone and hence further work is necessary in order to confirm the assumptions and to answer further questions which arose during these studies.

In this thesis many indications as to how such layered systems behave have been obtained. One of the most important insights obtained is the need to exchange the electrolyte for one containing a faster hole scavenger or redox species. On the one hand during the redox process the reduced species may be able to oxidize not only at the counter electrode but also onto the ISC substrate. This disadvantage necessitated the search for a redox species with a matching energy distribution within respect to the band positions of the materials employed for the ISC. The most common redox species in the literature is the iodine/iodide mixture but in the case of PbS nanoparticles this cannot be used as the redox couple due to reaction of PbS with the iodine to from PbI (this result was obtained in house). Another possibility is the use of complexes. One family of promising complexes are the cobalt containing complexes. A multiplicity of cobalt containing complexes for photovoltaic applications have been reported in the literature.[13,291–293] Generally a change to non-solvent based materials such as conductive polymers[294,295] and/or direct metal as well as alloy contacts[296] are conceivable. In that way it may be possible to achieve the forcasted efficiency increase for the FTO/ZnO-Ey substrate compared with that of the particulate ZnO gel films. In such a way the linker dependence in an ITO/ZnO/linker/PbS or ITO/$TiO_2$/linker/PbS substrate could be amplified in the case of the TGA, MPA and HDT linker molecules.

During the EIS and photo-transient measurements the ISC behaviour is significantly dependent on the band structure. From each material employed the trap state and band positions must be examined. An overview of every existing energetically-localized state allows considerations concerning the interaction of the states among each other and any additional processes after they have been addressed using light with defined energy. For the localization of trap states, including thermally active trap states, the thermally stimulated current (TSC) may be determined. In this technique the energy level is first filled by optical or electronical injection at relatively low temperatures and then the electrons are measured as they are emitted when the temperature is increased. The spectrum which consists of the emitted current vs. the temperature gives information concerning the energy levels in the semiconductor.[205] The flat band potential of the TCO in a solar cell assembly can be measured using interference reflection microscopy (IRM). Turrion et.al.[203,204] reported on the behaviour of FTO in contact with a $TiO_2$ substrate. The VB and all other occupied levels of a material employed in the solar cell can be determined using UV photoelectron spectroscopy (UPS) and X-ray photoelectron spectroscopy (XPS), however the unoccupied states such as the CB are not recorded using these methods.[297–300] To determine the CB the X-ray emission spectroscopy should be used. However, generally these methods are used to localize states in a single material. However for the examination of the band positions in the sample as an assembled layer and therefore the states of every material with respect to one another XPS and UPS are rather unfeasible methods. This may be justified by the fact that a known Fermi-level is applied on the system. In a material assembly the alteration of all states present will be with respect to this Fermi-level, i.e. the work function of each material, and not against to the vacuum level, which is the benchmark generally used. Specifically, the technique of near edge X-ray absorption fine structure (NEXAFS) could be an effective way to define the band structure of each material with respect to the other materials. The band gap and CB, against the vacuum level can be obtained which then allows the calculation of the VB position.[301] For a comparison of each band structure in the ISC composite a significantly different position of the core bands must be assumed. In the case where the signals are overlaying the signal cannot be assigned to a specific material. Evans et.al.[302] have also presented a possibility to determine the band bending and VB offset which is caused by the presence of an inorganic-organic interface such as is the case of the ZnO-linker system in this thesis. This technique may be used to probe such trap filling processes such as those initiated by the linker attachment. This method might also be helpful to find out more about the electron transfer between the eosin Y dye and the ZnO in the ZnO-Ey based ISC. Furthermore scanning tunnelling microscopy (STM) offers another possibility to determine the position of the states in a material with respect to each of the other materials present. Through the application of a potential and the shifting of this potential the electron transfer through the bands of the materials by a current signal may be followed. In this way the band position of every material with respect to each other might be measureable indirectly. In principle it is possible to determine the band positions and trap states of every single layer shown by the list of possible techniques mentioned above. However the interacting band positions in the assembly are more difficult to quantify caused by the more complex system. For that reason by this choice of techniques the responses, which caused by the material properties and the properties of the complete system, should not overlay for a clear determination of states. Last but not least it has to be mentioned that trap states and surface states can also be located in the PbS which can be analyzed analogous to the metal oxide states mentioned above.

To answer the questions concerning multiple exciton generation (MEG) a further measurement can be added. In this experiment the absorption of the sample has to be measured and any reflections excluded using an integrating sphere, therefore allowing just the absorption of the sample to be determined. If the incident photon to current conversion efficiency (IPCE) data is divided by the absorbance the internal quantum efficiency (IQE) is ascertainable. The IQE describes the number of absorbed electrons injected into the semiconductor per photon absorbed[303] and gives evidence as to the presence of MEG in the system.

In addition the second order of the monochromatic light necessitates the use of a filter during the IPCE measurements in order to eliminate disturbing signals.

Generally measurements using an integrating sphere expose the real absorption of a substrate without any reflection. For this reason the substrates especially the substrate with the photonic crystal structure have to measured using such a tool to determine the real absorption and determine the contribution of every preparation step to the whole system.

For further identification of the electron transfer processes and their kinetics intensity modulated photocurrent spectroscopy (IMPS) is a very useful tool. A number of measurements have been done under the same conditions employed for the EIS studies but this data has yet to be fully analyzed. A typical semicircle could be measured at all illumination wavelengths and applied potentials (under conditions analogous to the EIS measurements). The simplest model given in section 2.1.8 did not match the measured data, which is expected as these systems are very complex and contain interacting trap states and intercrossing electron transfer processes. For that reason the search for a suitable model is still in progress. It should also be mentioned that the FTO/ZnO/MPA/$PbS_{1570}$ substrate shows a circle at an applied potential of -0.4 V under illumination by yellow and red light. Therefore a back recombination is expected which has been mentioned in earlier chapters. If a model is found which fits the IMPS data, kinetic information concerning processes in the ISC may be divulged which support the interpretation of the photo-transient profile of the $TiO_2$ and ZnO based ISC.

Similar to the modelling of the IMPS data some notable changes in the EIS model were also mentioned in chapter 5. In the model formulated only the generation of excitons in the PbS NPs and an electron separation and transfer, analogous the scheme presented in section 2.1.3, were included. In addition the question of how meaningful the models are for the interpretation of processes which integrate trap states while considering the exciton generation may be posed.

Finally all information which has been interpreted it will make it possible to improve the solar cell. The substrates used and which have been characterised were freshly prepared every time and the electrolyte stored under conditions of inert gas and darkness. For a complete exclusion of oxidation and other such alteration effects due to the atmosphere it would be better to encapsulate the solar cell substrate or work generally under inert gas conditions. Some characteristic parameters such as the extinction coefficients have been taken from the literature. But the actual values can be determined by elemental analysis and concentration dependent absorption measurements of the pure materials.[304] That would allow ITO/ZnO and ITO/$TiO_2$ substrates with the same amount of material to be accurately prepared.

For evidence that equal amounts of PbS NPs are present on the MO surface when different linkers are used for the PbS attachment inductively coupled plasma-optical emission spectrometry (ICP-OES) is the tool of choice. The PbS concentration present on the substrate, even of very low amounts of materials, can thus be determined.

To avoid typical problems concerning processes which are caused by trap states, a MO single crystal could be used. The single crystal should only have a small amount of defects and the minimization of effects of the trap states is therefore possible. The unadulterated signal, and through this a clearer picture of the mechanism present in the ISC presented in section 2.1.3. might be measureable through the use of single crystals.

Research into the influence of photonic crystal architectures on the solar cell efficiency should be continued. At first a more efficient method must be found to prepare stable metal oxide inverse opals on a large area. Chemical vapour deposition[305] and electrodeposition techniques[306] might be more useful tools for such applications. After a successful reproducible substrate preparation has been achieved standard (opto-)electrochemical as well as the frequency modulated experiments should be repeated especially to determine the photonic effect near the stop band edges. Afterwards analysis of the photonic effect and its dependence on the sphere size used for the inverse opal preparation would be of great interest. In particular the influence of the PbS absorption and the effect of the (opto-)electrochemistry on the ISC should be clarified.

After improvement of the ISC the typical specifications of the solar cell should not be forgotten. The determination of the efficiency, the fill factor (FF) and the I-U characteristics must be measured under standard test conditions (STC) of: irradiance $G_{STC}$=1000 W/$m^2$, radiation spectrum of AM1.5 and solar cell temperature of 25°C.[307–309]

# Bibliography

[1] B. O'Regan, M. Grätzel, *Nature* **1991**, *353*, 737–740.

[2] R. Vogel, P. Hoyer, H. Weller, *The Journal of Physical Chemistry* **1994**, *98*, 3183–3188.

[3] P. V. Kamat, *The Journal of Physical Chemistry C* **2007**, *111*, 2834–2860.

[4] P. E. Lippens, M. Lannoo, *Physical Review B* **1989**, *39*, 10935–10942.

[5] L. E. Brus, *The Journal of Chemical Physics* **1984**, *79*, 5566–5571.

[6] S.-H. Wei, A. Zunger, *Physical Review B* **1997**, *55*, 13605–13610.

[7] G. E. Tudury, M. V. Marquezini, L. G. Ferreira, L. C. Barbosa, C. L. Cesar, *Physical Review B* **2000**, *62*, 7357–7364.

[8] S.-H. Wei, S. B. Zhang, A. Zunger, *Journal of Applied Physics* **2000**, *87*, 1304–1311.

[9] S. J. Lade, M. D. Uplane, C. D. Lokhande, *Materials Chemistry and Physics* **2001**, *68*, 36–41.

[10] K. K. Zhuravlev, *Physica B: Condensed Matter* **2007**, *394*, 1–7.

[11] Q. Shen, T. Sato, M. Hashimoto, C. Chen, T. Toyoda, *Thin Solid Films* **2006**, *499*, 299–305.

[12] A. Kongkanand, K. Tvrdy, K. Takechi, M. Kuno, P. V. Kamat, *Journal of the American Chemical Society* **2008**, *130*, 4007–4015.

[13] H. J. Lee, J.-H. Yum, H. C. Leventis, S. M. Zakeeruddin, S. A. Haque, P. Chen, S. I. Seok, M. Grätzel, M. K. Nazeeruddin, *The Journal of Physical Chemistry C* **2008**, *112*, 11600–11608.

[14] N. Guijarro, T. Lana-Villarreal, I. Mora-Seró, J. Bisquert, R. Gómez, *The Journal of Physical Chemistry C* **2009**, *113*, 4208–4214.

[15] R. S. Singh, V. K. Rangari, S. Sanagapalli, V. Jayaraman, S. Mahendra, V. P. Singh, *Solar Energy Materials and Solar Cells* **2004**, *82*, 315–330.

[16] J. A. Seabold, K. Shankar, R. H. T. Wilke, M. Paulose, O. K. Varghese, C. A. Grimes, K.-S. Choi, *Chemistry of Materials* **2008**, *20*, 5266–5273.

[17] G.-Y. Lan, Z. Yang, Y.-W. Lin, Z.-H. Lin, H.-Y. Liao, H.-T. Chang, *Journal of Materials Chemistry* **2009**, *19*, 2349–2355.

[18] H. J. Lee, D.-Y. Kim, J.-S. Yoo, J. Bang, S. Kim, S.-M. Park, *Bulletin of Korean Chemical Society* **2007**, *28*, 953–958.

[19] R. J. Ellingson, M. C. Beard, J. C. Johnson, P. Yu, O. I. Micic, A. J. Nozik, A. Shabaev, A. L. Efros, *Nano Letters* **2005**, *5*, 865–871.

[20] A. Shabaev, A. L. Efros, A. J. Nozik, *Nano Letters* **2006**, *6*, 2856–2863.

[21] V. I. Klimov, *Annual Review of Physical Chemistry* **2007**, *58*, 635–673.

[22] R. D. Schaller, M. Sykora, J. M. Pietryga, V. I. Klimov, *Nano Letters* **2006**, *6*, 424–429.

[23] J. H. Werner, S. Kolodinski, H. J. Queisser, *Physical Review Letters* **1994**, *72*, 3851–3854.

[24] A. De Vos, B. Desoete, *Solar Energy Materials and Solar Cells* **1998**, *51*, 413–424.

[25] D. Oron, M. Kazes, I. Shweky, U. Banin, *Physical Review B* **2006**, *74*, 115333–115338.

[26] T. Hoshikawa, M. Yamada, R. Kikuchi, K. Eguchi, *Journal of Electroanalytical Chemistry* **2005**, *577*, 339–348.

[27] Q. Wang, J.-E. Moser, M. Grätzel, *The Journal of Physical Chemistry B* **2005**, *109*, 14945–14953.

[28] L. Bay, K. West, *Solar Energy Materials and Solar Cells* **2005**, *87*, 613–628.

[29] F. Fabregat-Santiago, J. Bisquert, G. Garcia-Belmonte, G. Boschloo, A. Hagfeldt, *Solar Energy Materials and Solar Cells* **2005**, *87*, 117–131.

[30] I. Mora-Seró, J. Bisquert, F. Fabregat-Santiago, G. Garcia-Belmonte, G. Zoppi, K. Durose, Y. Proskuryakov, I. Oja, A. Belaidi, T. Dittrich, R. Tena-Zaera, A. Katty, C. L'evy-Clément, V. Barrioz, S. J. C. Irvine, *Nano Letters* **2006**, *6*, 640–650.

[31] J. van de Lagemaat, N.-G. Park, A. J. Frank, *The Journal of Physical Chemistry B* **2000**, *104*, 2044–2052.

[32] J. Bisquert, G. Garcia-Belmonte, F. Fabregat-Santiago, N. S. Ferriols, P. Bogdanoff, E. C. Pereira, *The Journal of Physical Chemistry B* **2000**, *104*, 2287–2298.

[33] F. Cao, G. Oskam, G. J. Meyer, P. C. Searson, *The Journal of Physical Chemistry* **1996**, *100*, 17021–17027.

[34] A. Pitarch, G. Garcia-Belmonte, I. Mora-Seró, J. Bisquert, *Physical Chemistry Chemical Physics* **2004**, *6*, 2983–2988.

[35] H.-C. Chang, G. Jaffe, *The Journal of Chemical Physics* **1952**, *20*, 1071–1077.

[36] L. M. Peter, *Chemical Reviews* **1990**, *90*, 753–769.

[37] E. Ponomarev, L. Peter, *Journal of Electroanalytical Chemistry* **1995**, *397*, 45–52.

[38] E. Ponomarev, L. Peter, *Journal of Electroanalytical Chemistry* **1995**, *396*, 219–226.

[39] P. E. de Jongh, D. Vanmaekelbergh, *Physical Review Letters* **1996**, *77*, 3427–3430.

[40] P. E. de Jongh, D. Vanmaekelbergh, *The Journal of Physical Chemistry B* **1997**, *101*, 2716–2722.

[41] G. Franco, L. M. Peter, E. A. Ponomarev, *Electrochemistry Communications* **1999**, *1*, 61–64.

[42] L. M. Peter, K. G. U. Wijayantha, *Electrochemistry Communications* **1999**, *1*, 576–580.

[43] L. Dloczik, O. Ileperuma, I. Lauermann, L. M. Peter, E. A. Ponomarev, G. Redmond, N. J. Shaw, I. Uhlendorf, *The Journal of Physical Chemistry B* **1997**, *101*, 10281–10289.

[44] S. G. Hickey, D. J. Riley, *Electrochimica Acta* **2000**, *45*, 3277–3282.

[45] S. G. Hickey, D. J. Riley, *The Journal of Physical Chemistry B* **1999**, *103*, 4599–4602.

[46] E. P. A. M. Bakkers, E. Reitsma, J. J. Kelly, D. Vanmaekelbergh, *The Journal of Physical Chemistry B* **1999**, *103*, 2781–2788.

[47] T. Oekermann, T. Yoshida, H. Minoura, K. G. U. Wijayantha, L. M. Peter, *The Journal of Physical Chemistry B* **2004**, *108*, 8364–8370.

[48] V. M. Guerin, C. Magne, T. Pauporté, T. Le Bahers, J. Rathousky, *ACS Applied Materials & Interfaces* **2010**, *2*, 3677–3685.

[49] C. G. B. Garrett, W. H. Brattain, *Phys. Rev.* **1955**, *99*, 376–387.

[50] R. H. Wilson, *Critical Reviews in Solid State and Materials Sciences* **1980**, *10*, 1–41.

[51] A. W. Bott, *Current Seperations* **1998**, *17*, 87–91.

[52] H. J. Lewerenz, *Tailoring of Interfaces for the Photoelectrochemical Conversion of Solar Energy*, Vol. 12 of *Advances in Electrochemical Science and Engineering*, R. C. Alkire, D. M. Kolb, J. Lipkowski, P. Ross (Eds.), Wiley-VCH Verlag GmbH, **2010**.

[53] A. Kumar, W. C. A. Wilisch, N. S. Lewis, *Critical Reviews in Solid State and Materials Sciences* **1993**, *18*, 327–353.

[54] Y. Xu, M. A. Schoonen, *American Mineralogist* **2000**, *85*, 543–556.

[55] M. Grätzel, *Nature* **2001**, *414*, 338–344.

[56] E. Becquerel, *Les Comptes Rendus de l'Académie des sciences* **1839**, *9*, 561–567.

[57] C. Brattain, W.H.; Garrett, *Bell System Technical Journal* **1955**, *34*, 129–176.

[58] L. M. Peter, D. Vanmaekelbergh, *Time and Frequency Resolved Studies of Photoelectrochemical Kinetics*, Wiley-VCH Verlag GmbH, **2008**.

[59] J. Q. Chambers, *Journal of Chemical Education* **1983**, *60*, 259–261.

[60] A. J. Nozik, *Annual Review of Physical Chemistry* **1978**, *29*, 189–222.

[61] T. Soga, U. Planning, *Nanostructured materials for solar energy conversion*, Elsevier, **2006**.

[62] G. Hodes, I. D. J. Howell, L. M. Peter, *Journal of The Electrochemical Society* **1992**, *139*, 3136–3140.

[63] J. Bisquert, A. Zaban, P. Salvador, *The Journal of Physical Chemistry B* **2002**, *106*, 8774–8782.

[64] R. van de Krol, H. L. Tuller, *Solid State Ionics* **2002**, *150*, 167–179.

[65] R. V. Latham, *High Voltage Vacuum Insulation: Basic Concepts and Technological Practice*, Academic Press, **1995**.

[66] P. Cox, *Transition Metal Oxides - An Introduction to their Electronic Structure and Properties*, of *27*, Oxford Science Puplications, **1992**.

[67] W. A. Harrison, *Solid State Theory*, Dover Publications, **1980**.

[68] N. Metropolis, *Los Alamos Science* **1987**, *15*, 125–130.

[69] M. Tamor, *Solid State Communications* **1987**, *64*, 141–144.

[70] J. E. B. Randles, *Trans. Faraday Soc.* **1948**, *44*, 327–338.

[71] R. S. Nicholson, I. Shain, *Analytical Chemistry* **1964**, *36*, 706–723.

[72] E. Kuçur, J. Riegler, G. A. Urban, T. Nann, *The Journal of Chemical Physics* **2003**, *119*, 2333–2337.

[73] S. K. Haram, B. M. Quinn, A. J. Bard, *Journal of the American Chemical Society* **2001**, *123*, 8860–8861.

[74] L. Peter, J. Li, R. Peat, *Journal of Electroanalytical Chemistry and Interfacial Electrochemistry* **1984**, *165*, 29–40.

[75] S. G. Hickey, D. J. Riley, E. J. Tull, *The Journal of Physical Chemistry B* **2000**, *104*, 7623–7626.

[76] V. Noack, H. Weller, A. Eychmüller, *The Journal of Physical Chemistry B* **2002**, *106*, 8514–8523.

[77] J. M. Macák, H. Tsuchiya, A. Ghicov, P. Schmuki, *Electrochemistry Communications* **2005**, *7*, 1133–1137.

[78] J. R. Macdonald, *Journal of Electroanalytical Chemistry* **1987**, *223*, 25–50.

[79] J. R. Macdonald, D. R. Franceschetti, *The Journal of Chemical Physics* **1978**, *68*, 1614–1637.

[80] J.-B. Jorcin, M. E. Orazem, N. Pébère, B. Tribollet, *Electrochimica Acta* **2006**, *51*, 1473–1479.

[81] M. E. Oraze, B. Tribollet, P. Pintauro, *Tutorials in Electrochemical Technology: Impedance Spectroscopy*, Vol. 13 of *Ecs Transactions*, Electrochemical Society (Ecs), **2008**.

[82] E. Barsoukov, J. R. Macdonald, *Impedance Spectroscopy: Theory, Experiment, and Applications 2nd ed.*, Wiley-VCH Verlag GmbH, **2005**.

[83] A. J. Bard, L. R. Faulkner, *Electrochemical Methods: Fundamentals and Applications 2nd ed.*, New York: Wiley, **2001**.

[84] K. Lunze, *Theorie der Wechselstromschaltungen 5th ed.*, VEB Verlag Technik Berlin, **1982**.

[85] L. Spanhel, M. A. Anderson, *Journal of the American Chemical Society* **1991**, *113*, 2826–2833.

[86] E. A. Meulenkamp, *The Journal of Physical Chemistry B* **1998**, *102*, 5566–5572.

[87] K. Srikanth, M. M. Rahman, H. Tanaka, K. M. Krishna, T. Soga, M. K. Mishra, T. Jimbo, M. Umeno, *Solar Energy Materials and Solar Cells* **2001**, *65*, 171–177.

[88] C. Boeckler, T. Oekermann, M. Saruban, K. Ichinose, T. Yoshida, *physica status solidi (a)* **2008**, *205*, 2388–2391.

[89] B. H. Juárez, C. Lápez, C. Alonso, *The Journal of Physical Chemistry B* **2004**, *108*, 16708–16712.

[90] S. Krüger, S. G. Hickey, S. Tscharntke, A. Eychmüller, *The Journal of Physical Chemistry C* **2011**, *115*, 13047–13055.

[91] R. P. Doherty, S. G. Hickey, D. Riley, E. J. Tull, *Journal of Electroanalytical Chemistry* **2004**, *569*, 271–274.

[92] D. Fermín, E. Ponomarev, L. Peter, *Journal of Electroanalytical Chemistry* **1999**, *473*, 192–203.

[93] L. M. Peter, D. J. Riley, E. J. Tull, K. G. U. Wijayantha, *Chem. Commun.* **2002**, 1030–1031.

[94] W. Beyer, J. Hüpkes, H. Stiebig, *Thin Solid Films* **2007**, *516*, 147–154.

[95] H. Hartnagel, A. L. Dawar, A. K. Jain, C. Jagadish, *Semiconducting Transparent Thin Films 1st ed.*, Institute of Physics Publishing, Bristol (UK) and Philadelphia (Pa), **1995**.

[96] X. Li, M. W. Wanlass, T. A. Gessert, K. A. Emery, T. J. Coutts, *Applied Physics Letters* **1989**, *54*, 2674–2676.

[97] J. Martinez-Pastor, A. Segura, J. L. Valdes, A. Chevy, *Journal of Applied Physics* **1987**, *62*, 1477–1483.

[98] K. Schulze, B. Maennig, K. Leo, Y. Tomita, C. May, J. Hupkes, E. Brier, E. Reinold, P. Bauerle, *Applied Physics Letters* **2007**, *91*, 073521.

[99] J. Y. Kim, K. Lee, N. E. Coates, D. Moses, T.-Q. Nguyen, M. Dante, A. J. Heeger, *Science* **2007**, *317*, 222–225.

[100] M. D. Irwin, D. B. Buchholz, A. W. Hains, R. P. H. Chang, T. J. Marks, *Proceedings of the National Academy of Sciences* **2008**, *105*, 2783–2787.

[101] K. Chopra, S. Major, D. Pandya, *Thin Solid Films* **1983**, *102*, 1–46.

[102] U. Özgür, Y. I. Alivov, C. Liu, A. Teke, M. A. Reshchikov, S. Dogan, V. Avrutin, S.-J. Cho, H. Morkoc, *Journal of Applied Physics* **2005**, *98*, 041301.1–041301.103.

[103] M. Grätzel, *E&I Elektrotechnik und Informationstechnik* **1997**, *114*, 579–586, 10.1007/BF03159082.

[104] P. V. Kamat, *The Journal of Physical Chemistry C* **2008**, *112*, 18737–18753.

[105] A. J. Frank, N. Kopidakis, J. van de Lagemaat, *Coordination Chemistry Reviews* **2004**, *248*, 1165–1179.

[106] L. M. Peter, *The Journal of Physical Chemistry Letters* **2011**, *2*, 1861–1867.

[107] E. M. Kaidashev, M. Lorenz, H. von Wenckstern, A. Rahm, H.-C. Semmelhack, K.-H. Han, G. Benndorf, C. Bundesmann, H. Hochmuth, M. Grundmann, *Applied Physics Letters* **2003**, *82*, 3901–3903.

[108] B. S. Ong, C. Li, Y. Li, Y. Wu, R. Loutfy, *Journal of the American Chemical Society* **2007**, *129*, 2750–2751.

[109] T. Dittrich, E. A. Lebedev, J. Weidmann, *Physica Status Solidi (A)* **1998**, *165*, R5–R6.

[110] Z. Xie, V. M. Burlakov, B. M. Henry, K. R. Kirov, H. E. Smith, C. R. M. Grovenor, H. E. Assender, G. A. D. Briggs, M. Kano, Y. Tsukahara, *Phys. Rev. B* **2006**, *73*, 113317(1)–113317(4).

[111] A. C. Arango, L. R. Johnson, V. N. Bliznyuk, Z. Schlesinger, S. A. Carter, H.-H. Hörhold, *Advanced Materials* **2000**, *12*, 1689–1692.

[112] T. P. Chou, Q. Zhang, G. Cao, *The Journal of Physical Chemistry C* **2007**, *111*, 18804–18811.

[113] L. L. Hench, J. K. West, *Chemical Reviews* **1990**, *90*, 33–72.

[114] O. Salvadogo, *Thin-Film Semiconductors Deposited in Nanometric Scales by Electrochemical and Wet Chemical Methods for Photovoltaic Solar Cell Apllications*, Vol. 12 of *Advances in Electrochemical Science and Engineering*, R. C. Alkire, D. M. Kolb, J. Lipkowski, P. Ross (Eds.), Wiley-VCH Verlag GmbH, **2010**.

[115] D. Schubert, T. Dunkel, *Materials Research Innovations* **2003**, *7*, 314–321.

[116] K. Norrman, A. Ghanbari-Siahkali, N. B. Larsen, *Annual Reports Section C: Physical Chemistry* **2005**, *101*, 174–201.

[117] P. Sigmund, *Nuclear Instruments and Methods in Physics Research Section B: Beam Interactions with Materials and Atoms* **1987**, *27*, 1–20.

[118] M. Hezam, N. Tabet, A. Mekki, *Thin Solid Films* **2010**, *518*, e161–e164.

[119] P. S. Patil, *Materials Chemistry and Physics* **1999**, *59*, 185–198.

[120] K. Krunks, O. Bijakina, V. Mikli, T. Varema, E. Mellikov, *Physica Scripta* **1999**, *1999*, 209–212.

[121] K. L. Choy, *Progress in Materials Science* **2003**, *48*, 57–170.

[122] T. Maruyama, J. Shionoya, *Journal of Materials Science Letters* **1992**, *11*, 170–172.

[123] R. Pandey, S. Sahu, S. Chandra., *Handbook of semiconductor electrodeposition 1st ed.*, Marcel Dekker inc New York, **1996**.

[124] T. Yoshida, D. Komatsu, N. Shimokawa, H. Minoura, *Thin Solid Films* **2004**, *451-452*, 166–169.

[125] H.-P. Boehm, *Angewandte Chemie* **1966**, *78*, 617–628.

[126] S. G. Hickey, N. Gaponik, A. Eychmüller, *Photonics and Nanostructures - Fundamentals and Applications* **2007**, *5*, 113–118.

[127] K. Doblhofer, J. Figura, J. H. Fuhrhop, *Langmuir* **1992**, *8*, 1811–1816.

[128] D. Qu, K. Uosaki, *The Journal of Physical Chemistry B* **2006**, *110*, 17570–17577.

[129] J. Moser, S. Punchihewa, P. P. Infelta, M. Grätzel, *Langmuir* **1991**, *7*, 3012–3018.

[130] S. Rühle, M. Greenshtein, S. G. Chen, A. Merson, H. Pizem, C. S. Sukenik, D. Cahen, A. Zaban, *The Journal of Physical Chemistry B* **2005**, *109*, 18907–18913.

[131] D. F. Watson, *The Journal of Physical Chemistry Letters* **2010**, *1*, 2299–2309.

[132] R. S. Dibbell, D. F. Watson, *The Journal of Physical Chemistry C* **2009**, *113*, 3139–3149.

[133] P. Sagar, P. K. Shishodia, R. M. Mehra, H. Okada, A. Wakahara, A. Yoshida, *Journal of Luminescence* **2007**, *126*, 800–806.

[134] O. F. Schirmer, D. Zwingel, *Solid State Communications* **1970**, *8*, 1559–1563.

[135] V. Noack, A. Eychmüller, *Chemistry of Materials* **2002**, *14*, 1411–1417.

[136] S. Sepeur, *Nanotechnology: Technical Basics and Applications*, Vincentz Network, **2008**.

[137] E. Mittemeijer, P. Scardi, *Diffraction Analysis of the Microstructure of Materials*, of *Springer Series in Materials Science*, Springer-Verlag, **2004**.

[138] H. Gerischer, *Journal of Electroanalytical Chemistry and Interfacial Electrochemistry* **1983**, *150*, 553–569.

[139] J. Degenhardt, A. J. McQuillan, *Chemical Physics Letters* **1999**, *311*, 179–184.

[140] S. J. Hug, B. Sulzberger, *Langmuir* **1994**, *10*, 3587–3597.

[141] E. M. S. Macoas, R. Fausto, M. Pettersson, L. Khriachtchev, M. Rasanen, *The Journal of Physical Chemistry A* **2000**, *104*, 6956–6961.

[142] R. L. Redington, T. E. Redington, *Journal of Molecular Structure* **1978**, *48*, 165–176.

[143] C. H. Specht, F. H. Frimmel, *Journal of Molecular Structure* **2001**, *3*, 5444–5449.

[144] M. J. Schmelz, I. Nakagawa, S.-I. Mizushima, J. V. Quagliano, *Journal of the American Chemical Society* **1959**, *81*, 287–290.

[145] A. Syamal, *Transition metal chemistry* **1978**, *3*, 292–296.

[146] M. Cefola, S. S. Peter, P. S. Gentile, R. A. V. Celiano, *Talanta* **1962**, *9*, 537–540.

[147] N. Sheppard, *Transactions of the Faraday Society* **1949**, *45*, 693–697.

[148] B. D. Saksena, P. H. Trevedi, *Transactions of the Faraday Society* **1962**, *58*, 2082–2089.

[149] N. Saraswathi, S. Soundararajan, *Journal of Molecular Structure* **1969**, *4*, 419–433.

[150] T. Imae, H. Torii, *The Journal of Physical Chemistry B* **2000**, *104*, 9218–9224.

[151] P. Kohli, K. K. Taylor, J. J. Harris, G. J. Blanchard, *Journal of the American Chemical Society* **1998**, *120*, 11962–11968.

[152] E. M. S. Macoas, R. Fausto, J. Lundell, M. Pettersson, L. Khriachtchev, M. Rasanen, *The Journal of Physical Chemistry A* **2000**, *104*, 11725–11732.

[153] N. Öztürk, c. c. Çırak, S. Bahçeli, *Zeitschrift für Naturforschung* **2005**, *60*, 633–636.

[154] T. A. Shippey, *Journal of Molecular Structure* **1980**, *65*, 71–86.

[155] E. S. Hanrahan, *Spectrochimica Acta* **1966**, *22*, 1243–1244.

[156] L. A. Bumm, J. J. Arnold, T. D. Dunbar, D. L. Allara, P. S. Weiss, *The Journal of Physical Chemistry B* **1999**, *103*, 8122–8127.

[157] R. E. Holmlin, R. F. Ismagilov, R. Haag, V. Mujica, M. A. Ratner, M. A. Rampi, G. M. Whitesides, *Angewandte Chemie International Edition* **2001**, *113*, 2378–2382.

[158] J. J. Sumner, K. S. Weber, L. A. Hockett, S. E. Creager, *The Journal of Physical Chemistry B* **2000**, *104*, 7449–7454.

[159] V. Ganesh, V. Lakshminarayanan, *Langmuir* **2006**, *22*, 1561–1570.

[160] K. Slowinski, R. V. Chamberlain, C. J. Miller, M. Majda, *Journal of the American Chemical Society* **1997**, *119*, 11910–11919.

[161] P. T. Narasimhan, *Proceedings of NISI A (Physical Sciences)* **1957**, *24*, 121–129.

[162] M. Valtiner, S. Borodin, G. Grundmeier, *Langmuir* **2008**, *24*, 5350–5358.

[163] V. Krishnan, D. Camozzo, L. Armelao, H. Bertagnolli, E. Tondello, S. Gross, *Zeitschrift für Physikalische Chemie* **2008**, *222*, 655–669.

[164] A. A. Guzelian, U. Banin, A. V. Kadavanich, X. Peng, A. P. Alivisatos, *Applied Physics Letters* **1996**, *69*, 1432–1434.

[165] A. L. Efros, M. Rosen, *Annual Review of Materials Science* **2000**, *30*, 475–521.

[166] U. Banin, C. J. Lee, A. A. Guzelian, A. V. Kadavanich, A. P. Alivisatos, W. Jaskolski, G. W. Bryant, A. L. Efros, M. Rosen, *The Journal of Chemical Physics* **1998**, *109*, 2306–2309.

[167] P. O. Brien, N. Pickett, *Strategies for the Scalable Synthesis of Quantum Dots and Related Nanodimensional Materials*, Wiley-VCH Verlag GmbH & Co. KGaA, **2005**, chapter 2, pp. 12–30.

[168] R. Xie, J. Zhang, F. Zhao, W. Yang, X. Peng, *Chemistry of Materials* **2010**, *22*, 3820–3822.

[169] D. Cui, J. Xu, T. Zhu, G. Paradee, S. Ashok, M. Gerhold, *Applied Physics Letters* **2006**, *88*, 183111.

[170] H. Du, C. Chen, R. Krishnan, T. D. Krauss, J. M. Harbold, F. W. Wise, M. G. Thomas, J. Silcox, *Nano Letters* **2002**, *2*, 1321–1324.

[171] R. D. Schaller, V. I. Klimov, *Physical Review Letters* **2004**, *92*, 186601–186604.

[172] J. E. Murphy, M. C. Beard, A. G. Norman, S. P. Ahrenkiel, J. C. Johnson, P. Yu, O. I. Mićić, R. J. Ellingson, A. J. Nozik, *Journal of the American Chemical Society* **2006**, *128*, 3241–3247.

[173] J. J. Urban, D. V. Talapin, E. V. Shevchenko, C. B. Murray, *Journal of the American Chemical Society* **2006**, *128*, 3248–3255.

[174] J. J. Peterson, T. D. Krauss, *Physical Chemistry Chemical Physics* **2006**, *8*, 3851–3856.

[175] H. Yokoi, S. Takeyama, O. Portugall, N. Miura, G. Bauer, *Physica B: Condensed Matter* **1993**, *184*, 173–177.

[176] C. E. D. Chidsey, D. N. Loiacono, *Langmuir* **1990**, *6*, 682–691.

[177] C. A. S. Brevett, D. C. Johnson, *Journal of The Electrochemical Society* **1992**, *139*, 1314–1319.

[178] D. R. Lide, *CRC Handbook of Chemistry and Physics*, TF-CRC, **2007**.

[179] R. B. Mason, J. H. Mathews, *The Journal of Physical Chemistry* **1926**, *30*, 414–420.

[180] O. P. Chawla, N. L. Arthur, R. W. Fessenden, *The Journal of Physical Chemistry* **1973**, *77*, 772–776.

[181] E. Hayon, A. Treinin, J. Wilf, *Journal of the American Chemical Society* **1972**, *94*, 47–57.

[182] S. Rifai, G. P. Lopinski, T. Ward, D. D. M. Wayner, M. Morin, *Langmuir* **2003**, *19*, 8916–8921.

[183] R. L. Paul, M. J. Nicol, J. W. Diggle, A. P. Saunders, *Electrochimica Acta* **1978**, *23*, 625–633.

[184] A. P. Davis, C. P. Huang, *Langmuir* **1991**, *7*, 803–808.

[185] J. R. Gardner, R. Woods, *Journal of Electroanalytical Chemistry* **1979**, *100*, 447–459.

[186] Y. Mikhlin, *Journal of applied electrochemistry* **2004**, *34*, 37–46.

[187] M. J. Nicol, R. L. Paul, J. W. Diggle, *Electrochimica Acta* **1978**, *23*, 635–639.

[188] S. Ogawa, K. Hu, F.-R. F. Fan, A. J. Bard, *The Journal of Physical Chemistry B* **1997**, *101*, 5707–5711.

[189] I. V. Chernyshova, *Russian Journal of Electrochemistry* **2001**, *37*, 579–584.

[190] T. Pauporté, D. Schuhmann, *Journal of Electroanalytical Chemistry* **1996**, *404*, 123–135.

[191] S. K. Poznyak, N. P. Osipovich, A. Shavel, D. V. Talapin, M. Gao, A. Eychmüller, N. Gaponik, *The Journal of Physical Chemistry B* **2005**, *109*, 1094–1100.

[192] I. Kang, F. W. Wise, *Journal of the Optical Society of America B: Optical Physics* **1997**, *14*, 1632–1646.

[193] L. Cademartiri, E. Montanari, G. Calestani, A. Migliori, A. Guagliardi, G. A. Ozin, *Journal of the American Chemical Society* **2006**, *128*, 10337–10346.

[194] H. Keiser, K. D. Beccu, M. A. Gutjahr, *Electrochimica Acta* **1976**, *21*, 539–543.

[195] R. De Levie, *Electrochimica Acta* **1965**, *10*, 113–130.

[196] J. Gunning, *Journal of Electroanalytical Chemistry* **1995**, *392*, 1–11.

[197] C. Hitz, A. Lasia, *Journal of Electroanalytical Chemistry* **2001**, *500*, 213–222.

[198] B. Russo, G. Cao, *Applied Physics A: Materials Science &amp; Processing* **2008**, *90*, 311–315.

[199] G. Folcher, H. Cachet, M. Froment, J. Bruneaux, *Thin Solid Films* **1997**, *301*, 242–248.

[200] D. J. Milliron, I. G. Hill, C. Shen, A. Kahn, J. Schwartz, *Journal of Applied Physics* **2000**, *87*, 572–576.

[201] M. Herold, J. GmeinerR, C. DrummerR, M. Schwoerer, *Journal of Materials Science* **1997**, *32*, 5709–5715.

[202] F. Fabregat-Santiago, I. Mora-Seró, G. Garcia-Belmonte, J. Bisquert, *The Journal of Physical Chemistry B* **2003**, *107*, 758–768.

[203] M. Turrión, B. Macht, H. Tributsch, P. Salvador, *The Journal of Physical Chemistry B* **2001**, *105*, 9732–9738.

[204] M. Turrión, J. Bisquert, P. Salvador, *The Journal of Physical Chemistry B* **2003**, *107*, 9397–9403.

[205] C. Casteleiro, H. L. Gomes, P. Stallinga, L. Bentes, R. Ayouchi, R. Schwarz, *Journal of Non-Crystalline Solids* **2008**, *354*, 2519–2522.

[206] P. S. Xu, Y. M. Sun, C. S. Shi, F. Q. Xu, H. B. Pan, *Nuclear Instruments and Methods in Physics Research Section B: Beam Interactions with Materials and Atoms* **2003**, *199*, 286–290.

[207] L. Scribner, T. Ray, *The Measurement and Correction of Electrolyte Resistance in Electrochemical Tests*, American Society for Testing and Materials, **1990**.

[208] M. R. Wright, *An Introduction to Aqueous Electrolyte Solutions*, Wiley-VCH Verlag GmbH, **2007**.

[209] C. Wu, F. Koch, W. Pratt, *Proposed new electrolytic conductivity primary standards for KCl solutions*, *Vol. 96*, National Institute of Standards and Technology, Gaithersburg, MD, ETATS-UNIS, **1991**.

[210] C. Wu, F. Koch, W. Pratt, *Proposed new electrolytic conductivity primary standards for KCl solutions*, *Vol. 99*, National Institute of Standards and Technology, Gaithersburg, MD, ETATS-UNIS, **1994**.

[211] K. W. Pratt, W. F. Koch, Y. C. Wu, P. A. Berezansky, *Pure and Applied Chemistry* **2001**, *73*, 1783–1793.

[212] T. Pajkossy, *Solid State Ionics* **2005**, *176*, 1997–2003.

[213] R. Kötz, M. Carlen, *Electrochimica Acta* **2000**, *45*, 2483–2498.

[214] R. L. Hurt, J. R. Macdonald, *Solid State Ionics* **1986**, *20*, 111–124.

[215] A. Hassanzadeh, M. Habibi, A. Zeini-Isfahani, *Acta Chimica Slovenica* **2004**, *51*, 507–527.

[216] M. Metikos-Hukovic, S. Omanovic, *Journal of Electroanalytical Chemistry* **1998**, *455*, 181–189.

[217] H. R. Fallah, M. Ghasemi, A. Hassanzadeh, *Physica E: Low-dimensional Systems and Nanostructures* **2007**, *39*, 69–74.

[218] M. Strømme, J. Isidorsson, G. A. Niklasson, C. G. Granqvist, *Journal of Applied Physics* **1996**, *80*, 233–241.

[219] J. Bisquert, A. Compte, *Journal of Electroanalytical Chemistry* **2001**, *499*, 112–120.

[220] N. Gu, D. Wei, L. Niu, A. Ivaska, *Electrochimica Acta* **2006**, *51*, 6038–6044.

[221] X. Chen, Y. Wang, J. Zhou, W. Yan, X. Li, J.-J. Zhu, *Analytical Chemistry* **2008**, *80*, 2133–2140.

[222] J. Shi, H. Cui, Z. Liang, X. Lu, Y. Tong, C. Su, H. Liu, *Energy & Environmental Science* **2011**, *4*, 466–470.

[223] H. Gerischer, *Journal of Electroanalytical Chemistry and Interfacial Electrochemistry* **1977**, *82*, 133–143.

[224] B. Guo, Z. Liu, L. Hong, H. Jiang, J. Y. Lee, *Thin Solid Films* **2005**, *479*, 310–315.

[225] C. Vautey, M. Burgos, M. Langlet, *Thin Solid Films* **1999**, *347*, 184–194.

[226] M. Sasani Ghamsari, A. R. Bahramian, *Materials Letters* **2008**, *62*, 361–364.

[227] M. Burgos, M. Langlet, *Journal of Sol-Gel Science and Technology* **1999**, *16*, 267–276.

[228] Y. Fu, Z. Jin, W. Xue, Z. Ge, *Journal of the American Ceramic Society* **2008**, *91*, 2676–2682.

[229] M. Murayama, E. Yamazaki, N. Nishikawa, N. Hashimoto, *Japanese Journal of Applied Physics* **2006**, *45*, 7917–7921.

[230] J. Yu, X. Zhao, J. C. Yu, G. Zhong, J. Han, Q. Zhao, *Journal of Materials Science Letters* **2001**, *20*, 1745–1748.

[231] V. Subramanian, E. E. Wolf, P. V. Kamat, *Journal of the American Chemical Society* **2004**, *126*, 4943–4950.

[232] J. Yu, J. C. Yu, X. Zhao, *Journal of Sol-Gel Science and Technology* **2002**, *24*, 95–103.

[233] K. Shankar, J. Bandara, M. Paulose, H. Wietasch, O. K. Varghese, G. K. Mor, T. J. LaTempa, M. Thelakkat, C. A. Grimes, *Nano Letters* **2008**, *8*, 1654–1659.

[234] I. Robel, V. Subramanian, M. Kuno, P. V. Kamat, *Journal of the American Chemical Society* **2006**, *128*, 2385–2393.

[235] W. Shockley, H. J. Queisser, *Journal of Applied Physics* **1961**, *32*, 510–519.

[236] A. J. Nozik, *Quantum Dot Solar Cells: Preprint*, **2001**.

[237] S. Günes, K. P. Fritz, H. Neugebauer, N. S. Sariciftci, S. Kumar, G. D. Scholes, *Solar Energy Materials and Solar Cells* **2007**, *91*, 420–423.

[238] R. Brahimi, Y. Bessekhouad, A. Bouguelia, M. Trari, *Journal of Photochemistry and Photobiology A: Chemistry* **2008**, *194*, 173–180.

[239] P. Hoyer, R. Könenkamp, *Applied Physics Letters* **1995**, *66*, 349–351.

[240] B.-R. Hyun, Y.-W. Zhong, A. C. Bartnik, L. Sun, H. D. Abruña, F. W. Wise, J. D. Goodreau, J. R. Matthews, T. M. Leslie, N. F. Borrelli, *ACS Nano* **2008**, *2*, 2206–2212.

[241] Y. Sun, E. Hao, X. Zhang, B. Yang, J. Shen, L. Chi, H. Fuchs, *Langmuir* **1997**, *13*, 5168–5174.

[242] Y. Sun, E. Hao, X. Zhang, B. Yang, M. Gao, J. Shen, *Chemical Communications* **1996**, 2381–2382.

[243] H. C. Leventis, F. O'Mahony, J. Akhtar, M. Afzaal, P. O'Brien, S. A. Haque, *Journal of the American Chemical Society* **2010**, *132*, 2743–2750.

[244] R. Plass, S. Pelet, J. Krueger, M. Grätzel, U. Bach, *The Journal of Physical Chemistry B* **2002**, *106*, 7578–7580.

[245] P. Wang, L. Wang, B. Ma, B. Li, Y. Qiu, *The Journal of Physical Chemistry B* **2006**, *110*, 14406–14409.

[246] W. Lee, J. Lee, S. K. Min, T. Park, W. Yi, S.-H. Han, *Materials Science and Engineering: B* **2009**, *156*, 48–51.

[247] R. Patil, C. Lokhande, R. Mane, T. Gujar, S.-H. Han, *Journal of Non-Crystalline Solids* **2007**, *353*, 1645–1649.

[248] B. Ma, F. Luo, L. Wang, X. Wu, C. Zhan, Y. Qiu, *Japanese Journal of Applied Physics* **2007**, *46*, 7745–7748.

[249] S.-m. Yang, Z.-s. Wang, C.-h. Huang, *Synthetic Metals* **2001**, *123*, 267–272.

[250] E. V. Dirote, *Nanotechnology at the Leading Edge*, Nova Science Publishers, **2006**.

[251] I. Dolamic, T. Bürgi, *The Journal of Physical Chemistry B* **2006**, *110*, 14898–14904.

[252] L. de la Garza, Z. V. Saponjic, N. M. Dimitrijevic, M. C. Thurnauer, T. Rajh, *The Journal of Physical Chemistry B* **2006**, *110*, 680–686.

[253] J.-M. Herrmann, M.-N. Mozzanega, P. Pichat, *Journal of Photochemistry* **1983**, *22*, 333–343.

[254] K. Schwarzburg, F. Willig, *Applied Physics Letters* **1991**, *58*, 2520–2522.

[255] A. Brenner, *Electrodeposition of Alloys: Principle and Practice*, of *Volume I General Survey, Principles, and Alloys of Copper and of Silver*, Academic Press, New York and London, **1963**.

[256] A. Brenner, *Electrodeposition of Alloys. Principle and Practice*, of *Volume II Principles and Practice Practical Considerations and Specific Information*, Academic Press, New York and London, **1963**.

[257] W. Blum, G. B. Hogaboom, *Journal of the Society of Chemical Industry* **1924**, *43*, 791–792.

[258] D. Lincot, *Thin Solid Films* **2005**, *487*, 40–48.

[259] L. Xu, Q. Chen, D. Xu, *The Journal of Physical Chemistry C* **2007**, *111*, 11560–11565.

[260] Z. Chen, Y. Tang, L. Zhang, L. Luo, *Electrochimica Acta* **2006**, *51*, 5870–5875.

[261] T. Yoshida, M. Tochimoto, D. Schlettwein, D. WÃűhrle, T. Sugiura, H. Minoura, *Chemistry of Materials* **1999**, *11*, 2657–2667.

[262] T. Yoshida, K. Terada, D. Schlettwein, T. Oekermann, T. Sugiura, H. Minoura, *Advanced Materials* **2000**, *12*, 1214–1217.

[263] T. Oekermann, T. Yoshida, C. Boeckler, J. Caro, H. Minoura, *The Journal of Physical Chemistry B* **2005**, *109*, 12560–12566, doi: 10.1021/jp051394p.

[264] K. Nonomura, D. Komatsu, T. Yoshida, H. Minoura, D. Schlettwein, *Physical Chemistry Chemical Physics* **2007**, *9*, 1843–1849.

[265] E. Yablonovitch, *Journal of the Optical Society of America B* **1993**, *10*, 283–295.

[266] S. John, *Physical Review Letters* **1987**, *58*, 2486–2489.

[267] F. Fleischhaker, R. Zentel, *Chemie in unserer Zeit* **2007**, *41*, 38–44.

[268] J. D. Joannopoulos, P. R. Villeneuve, S. Fan, *Nature* **1997**, *386*, 143–149.

[269] T. Ruhl, P. Spahn, H. Winkler, G. P. Hellmann in *Mesophases, Polymers, and Particles*, Vol. 129 of *Progress in Colloid and Polymer Science*, G. Lagaly, W. Richtering (Eds.), Springer Berlin / Heidelberg, **2004**, pp. 93–100.

[270] M. Egen, R. Zentel, P. Ferrand, S. Eiden, G. Maret, F. Caruso, *Preparation of 3D Photonic Crystals from Opals*, Wiley-VCH Verlag GmbH & Co. KGaA, **2006**, pp. 109–131.

[271] B. Lange, F. Fleischhaker, R. Zentel, *Functional 3D Photonic Films from Polymer Beads*, Wiley-VCH Verlag GmbH & Co. KGaA, **2008**, pp. 39–61.

[272] J. D. Joannopoulos, R. D. Meade, J. N. Winn, *Photonic Crystals - Molding the Flow of Light*, Princeton University Press, **1995**.

[273] R. D. Meade, K. D. Brommer, A. M. Rappe, J. D. Joannopoulos, *Physical Review B* **1991**, *44*, 13772–13774.

[274] R. D. Meade, A. M. Rappe, K. D. Brommer, J. D. Joannopoulos, O. L. Alerhand, *Physical Review B* **1993**, *48*, 8434–8437.

[275] S. Nishimura, N. Abrams, B. A. Lewis, L. I. Halaoui, T. E. Mallouk, K. D. Benkstein, J. van de Lagemaat, A. J. Frank, *Journal of the American Chemical Society* **2003**, *125*, 6306–6310.

[276] H. Míguez, F. Meseguer, C. Lápez, F. Lápez-Tejeira, J. Sánchez-Dehesa, *Advanced Materials* **2001**, *13*, 393–396.

[277] L. I. Halaoui, N. M. Abrams, T. E. Mallouk, *The Journal of Physical Chemistry B* **2005**, *109*, 6334–6342.

[278] I. Rodriguez, P. Atienzar, F. Ramiro-Manzano, F. Meseguer, A. Corma, H. Garcia, *Photonics and Nanostructures - Fundamentals and Applications* **2005**, *3*, 148 – 154.

[279] M. El Harakeh, L. Halaoui, *The Journal of Physical Chemistry C* **2010**, *114*, 2806–2813.

[280] L. J. Diguna, M. Murakami, A. Sato, Y. Kumagai, T. Ishihara, N. Kobayashi, Q. Shen, T. Toyoda, *Japanese Journal of Applied Physics* **2006**, *45*, 5563–5568.

[281] A. Mihi, M. E. Calvo, J. A. Anta, H. Miguez, *The Journal of Physical Chemistry C* **2008**, *112*, 13–17.

[282] F. Marlow, Muldarisnur, P. Sharifi, R. Brinkmann, C. Mendive, *Angewandte Chemie* **2009**, *121*, 6328–6351.

[283] M. Cermola, W.-H. Schreil, *Journal of Electron Microscopy Technique* **1987**, *5*, 171–179.

[284] K. S. Lim, S. B. Kwon, K. W. Lee, M. C. Kim, *Aerosol Science and Technology* **2002**, *36*, 1003 – 1011.

[285] G. D. Scott, D. M. Kilgour, *Journal of Physics D: Applied Physics* **1969**, *2*, 863–866.

[286] W. Dong, H. Bongard, B. Tesche, F. Marlow, *Advanced Materials* **2002**, *14*, 1457–1460.

[287] H. Imai, K. Awazu, M. Yasumori, H. Onuki, H. Hirashima, *Journal of Sol-Gel Science and Technology* **1997**, *8*, 365–369.

[288] T. Nishide, M. Sato, H. Hara, *Journal of Materials Science* **2000**, *35*, 465–469.

[289] T. Nishide, F. Mizukami, *Thin Solid Films* **1999**, *353*, 67–71.

[290] C. J. Huang, K. C. Liao, Y. K. Su, *Key Engineering Materials* **2008**, *368-372*, 1465–1467.

[291] H. Nusbaumer, S. M. Zakeeruddin, J.-E. Moser, M. Grätzel, *Chemistry - A European Journal* **2003**, *9*, 3756–3763.

[292] S. A. Sapp, C. M. Elliott, C. Contado, S. Caramori, C. A. Bignozzi, *Journal of the American Chemical Society* **2002**, *124*, 11215–11222.

[293] H. Nusbaumer, J.-E. Moser, S. M. Zakeeruddin, M. K. Nazeeruddin, M. Grätzel, *The Journal of Physical Chemistry B* **2001**, *105*, 10461–10464.

[294] W. Ma, C. Yang, X. Gong, K. Lee, A. Heeger, *Advanced Functional Materials* **2005**, *15*, 1617–1622.

[295] W. U. Huynh, J. J. Dittmer, A. P. Alivisatos, *Science* **2002**, *295*, 2425–2427.

[296] V. K. Kapur, A. Bansal, P. Le, O. I. Asensio, *Thin Solid Films* **2003**, *431-432*, 53–57.

[297] D. J. Asunskis, L. Hanley, *Surface Science* **2007**, *601*, 4648–4656.

[298] K. H. Tam, C. K. Cheung, Y. H. Leung, A. B. Djurišić, C. C. Ling, C. D. Beling, S. Fung, W. M. Kwok, W. K. Chan, D. L. Phillips, L. Ding, W. K. Ge, *The Journal of Physical Chemistry B* **2006**, *110*, 20865–20871.

[299] D. Morris, R. Dixon, F. H. Jones, Y. Dou, R. G. Egdell, S. W. Downes, G. Beamson, *Phys. Rev. B* **1997**, *55*, 16083–16087.

[300] A. K. See, M. Thayer, R. A. Bartynski, *Phys. Rev. B* **1993**, *47*, 13722–13729.

[301] J. Solomon, R. Madix, J. Stöhr, *Surface Science* **1991**, *255*, 12–30.

[302] D. A. Evans, H. J. Steiner, A. R. Vearey-Roberts, A. Bushell, G. Cabailh, S. O'Brien, J. W. Wells, I. T. McGovern, V. R. Dhanak, T. U. Kampen, D. R. T. Zahn, D. Batchelor, *Nuclear Instruments and Methods in Physics Research Section B: Beam Interactions with Materials and Atoms* **2003**, *199*, 475–480.

[303] E. W. McFarland, J. Tang, *Nature* **2003**, *421*, 616–618.

[304] W. W. Yu, L. Qu, W. Guo, X. Peng, *Chemistry of Materials* **2003**, *15*, 2854–2860.

[305] M. Wang, X. Wang, *Solar Energy Materials and Solar Cells* **2008**, *92*, 357–362.

[306] B. Juárez, P. García, D. Golmayo, A. Blanco, C. López, *Advanced Materials* **2005**, *17*, 2761–2765.

[307] H.-J. Lewerenz, H. Jungblut, *Photovoltaik -Grundlagen und Anwendungen*, Springer Verlag, **1995**.

[308] D. Meissner, *Solarzellen - Physikalische Grundlagen und Anwendungen der Photovoltaik*, Vieweg&Teubner, **1993**.

[309] U. Rindelhardt, *Photovoltaische Stromversorgung 1st ed.*, B.G. Teubner Verlag, **2001**.

# A

# Acknowledgement

My sincere thanks are expressed to Prof. Dr. Alexander Eychmüller for the provision of this very interesting and complex topic and the go-ahead I received to undertake a research trip abroad. Also I would like to exceedingly thank him for his ability to motivate, encourage and challenge plus the new approaches to problems that he endowed.

In equal measure I would like to acknowledge Dr. Stephen Hickey for the very fruitful, critical and instructive mentoring. I wish to express my appreciation for the chance he gave me to go to London. I am especially deeply thankful for his attempts at preservation of his mother tongue. I am at a loss for English words to express my gratefulness.

Furthermore, I am gratefully thankful to Dr. Jason Riley for his consent in allowing me to do a part of my practical work in his group at Imperial College London. I am also grateful for his critically specialist advice.

I would like to express my appreciation for the work of my bachelor students B. Sc. Elisabeth Schreyer and B. Sc. Susann Kittler. My thanks also go to M. Sc. Clément Sieutat, Dipl. Chem. Céline Vervacke, Dipl. Chem. Alexander Klein, Dipl. Chem. Christoph Ziegler and Dipl. Chem. Sebastian Paulik for all their practical help.

For the synthesis of lead sulfide I am indebted to Dipl. Chem. Stefanie Tscharntke and M. Sc. Lydia Liebscher.

Many thanks go to Dr. Tobias Otto for the ingenious ideas and discussions, the little projects, the patent and further pieces of wisdom. I would also like to thank M. Sc. Jan Poppe for all our discussions, the superb electrotechnical and other technical help and the support for the ligand exchange technique used for the PbS particles.

My thanks go to Ms. Ellen Kern and PD Dr. Ellen Hieckmann for the SEM images, to Ms. Anja Bensch for the XRD diffractograms and to Ms. Renate Schulze for the ICP-OES measurements. Thanks to Dr. René Luther for the instruction and the authorisation to use the FTIR-spectrometer.

Not to be forgotten, my thanks go also to technician Matthias Gestrich, all the workshops and technicians of the Royal School of Mines at Imperial College for their many kinds of technical aptitudes and their patience with me.

Certainly, I would like to say thank you to Prof. Dr. Michael Wark, Dr. Thorsten Öckermann, Dr. Cathrin Boeckler and Dipl. Chem. Christian Dunkel from the University of Hannover for the collaboration with the porous eosin Y zinc oxide substrates.

I am thankful to the DFG for funding through project No. Hl 1113/3-1.

My thanks also go to the combined Eychmüller and Bund groups as well as the complete Riley group for the warm reception I received from the groups, the lovely ambience, the helpful discussions, the internal and, most notably, the external academic get-together.

Certainly my heartfelt thanks also go to the most discerning person I know, Olaf Krömer. I thank him for the last (almost) decade filled with all the rough edges and sphericity of our relationship, for the suggestions and criticisms he has given me and the backing at any time it was needed.

Last but not least I really greatly appreciate my lovely parents and my wonderful brother for all the help and being the wind at my back at every time of my life. I am deeply thankful for their support, willing ear, suggestions at any time, factual criticism and quite simply their presence.

# B

# Erklärung

Hiermit versichere ich, dass ich die vorliegende Arbeit ohne unzulässige Hilfe Dritter und ohne Benutzung anderer als der angegebenen Hilfsmittel angefertigt habe; die aus fremden Quellen direkt oder indirekt übernommenen Gedanken sind als solche kenntlich gemacht. Die Arbeit wurde bisher weder im Inland noch im Ausland in gleicher oder ähnlicher Form einer anderen Prüfungsbehörde vorgelegt.

Diese Dissertation wurde im Zeitraum August 2007 bis September 2011 an der Technischen Universität Dresden unter der wissenschaftlichen Betreuung von Prof. Dr. rer. nat. habil. Alexander Eychmüller angefertigt.

Es existieren keine früheren Promotionsverfahren.

Ich erkenne hiermit die Promotionsordnung der Fakultät Mathematik und Naturwissenschaften an der Technischen Universität vom 23.02.2011 an.

Dresden, 23.09.2011

Susanne Krüger